CANDE-2007
Culvert Analysis and Design
Solution Methods and Formulations

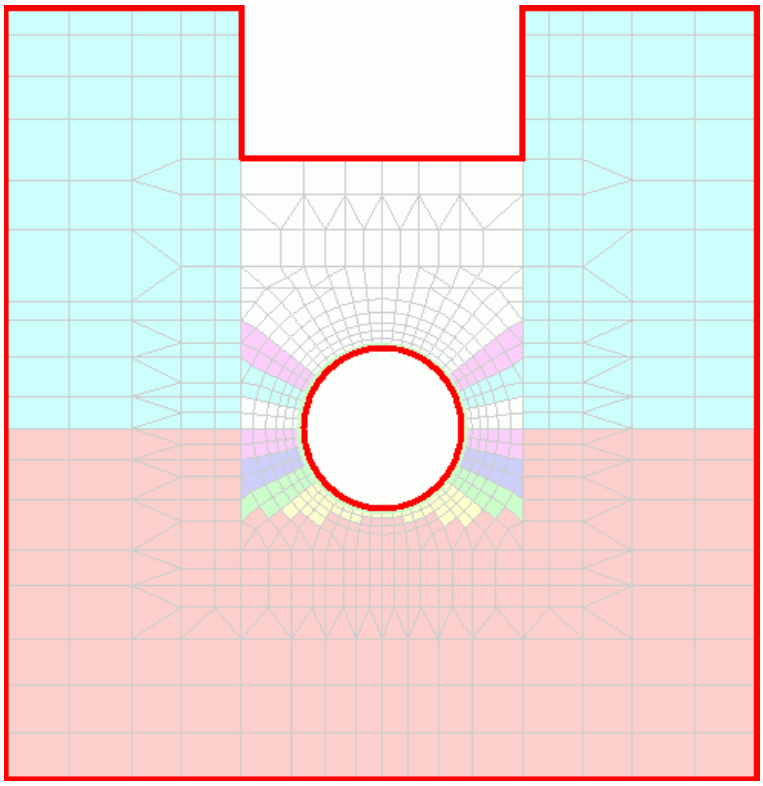

Developed under National Cooperative Highway Research Project NCHRP 15-28

CANDE-2007
Culvert Analysis and Design
Solution Methods and Formulations

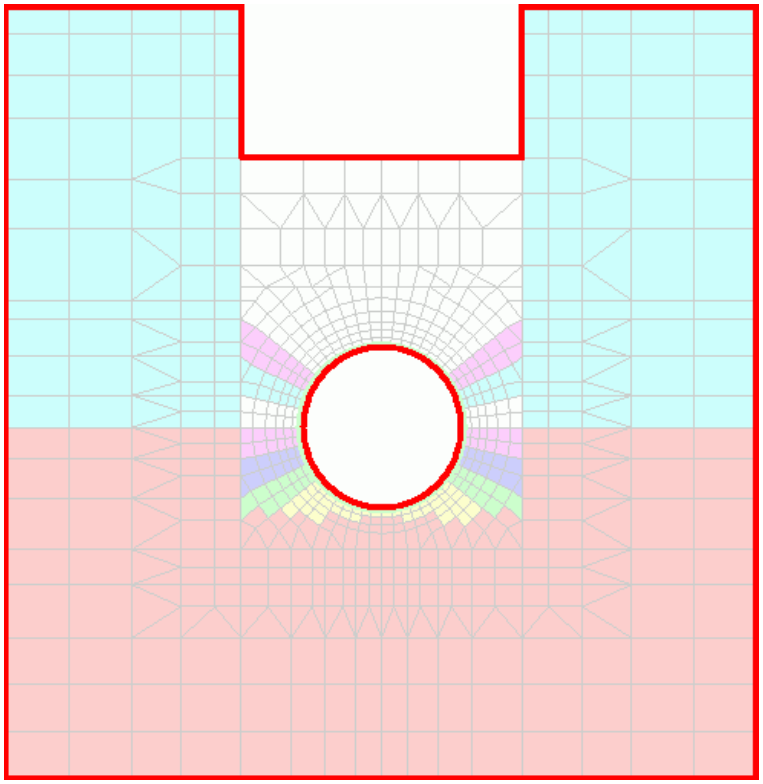

Developed under National Cooperative Highway Research Project NCHRP 15-28

Michael G. Katona – Consultant
Gig Harbor, WA

Mark Mlynarski – Michael Baker Jr. Inc.
Moon Township, PA

Timothy J. McGrath – Simpson, Gumpertz & Heger Inc.
Arlington, MA

(This page intentionally left blank)

Table of Contents:

(This page intentionally left blank)

1 SOLUTION LEVELS AND ASSUMPTIONS

This document focuses on the engineering mechanics and methods that lie behind the capabilities in CANDE-2007. Each chapter is essentially a stand-alone reference that describes the theory and engineering approximations used for the solution methods and nonlinear models employed in the program. The reader is referred to *CANDE-2007 User Manual and Guideline* for an overall understanding of CANDE capabilities and architecture from a user's perspective.

Two distinct solution methods are contained in CANDE. The first is called Level 1and is an extension of a closed-form elasticity solution by Burns and Richard (Reference 7). The second is a finite element methodology modified and extended from Herrmann (Reference 8). Input for the finite element method has two input options called Level 2 and Level 3. Level 2 offers a completely automated mesh generation scheme but it is restricted to basic culvert shapes and symmetric installations, whereas Level 3 is virtually unrestricted in modeling capability, but requires the user to define the mesh topology.

Fundamental to both the closed form solution and the finite element methodology is the assumption of plane strain geometry, two-dimensional loading, and real-time independence. Naturally, the elasticity solution is more restrictive than the finite element solutions for Levels 2 and 3. Detailed capabilities and restrictions of the solution methods are discussed in the following sections.

1.1 Elasticity Solution

The elasticity formulation provides an exact solution for an elastic cylindrical conduit encased in an isotropic, homogeneous, infinite, elastic medium (soil) with a uniformly distributed pressure acting on horizontal planes at an infinite distance. Thin-shell theory is assumed for the conduit, and continuum elastic theory is employed for the surrounding infinite medium. The conduit-medium interface is modeled with a choice of two boundary conditions: bonded interface, where both normal and tangential forces are transmitted across the interface, and frictionless interface, where only normal forces are transmitted across the interface. Table 1.1-1 identifies the parameters that describe the idealized boundary value problem and summarizes the elasticity solutions of key structural responses for the two interface assumptions. Key structural responses, including radial and tangential soil pressure on conduit, radial and tangential displacements of conduit wall, along with moment, thrust and shear resultants are given as a function of the angle theta measured counterclockwise from the springline. The solutions in Table 1.1-1 are expressed in terms of the dimensionless parameters alpha and beta. Alpha is a measure of the conduit's hoop stiffness relative to the soil's ability to resist uniform compression, and beta is a measure of the conduits bending stiffness relative to the soil's ability to resist ovaling deformation. The expressions in Table 1.1-1 are developed in References 9 and 10.

1.1.1 Conceptual model

At first encounter, the applicability of the infinite regions described above to model culvert systems with finite burial depths may seem questionable. However, it has been shown that the interaction between conduit and medium (or pipe and soil) occurs primarily within a three-radius area of the pipe center. Beyond this area the soil response is practically unaffected by the pipe inclusion for overburden loading. Therefore, the pipe-soil system can be visualized with the finite boundaries and overburden loading as shown in Figure 7.1.1. In this representation, P_o is the equivalent overburden pressure of the fill soil above the pipe given by $P_o = \gamma H$, where the parameters are identified in the figure. The elasticity solution becomes progressively less valid when H, the depth of cover, is less than 3R and should not be used for cover depths less than 2R.

Table 1.1.1-1 Elasticity parameters and solutions for bonded and frictionless interfaces.

Elasticity Solution Parameters		
Soil Properties • P_0 = Overburden pressure • G = Shear modulus • K = Lateral pressure coeff. $K = \mu/(1-\mu)$, where μ is Poisson ratio of soil	**Pipe Properties** • R = Average radius • A = Wall thrust area per unit length • I = Wall moment of inertia per unit length • E = Young's modulus in plane strain form $E = E_{pipe}/(1-\mu_{pipe}^2)$	**Dimensionless Parameters** • θ = Angle in polar coord. • $\alpha = EA/(2GR)$ (Relative hoop stiffness) • $\beta = EI/(2GR^3)$ (Relative bend stiffness)

Bonded Interface: Structural Response Solutions		
Structural Response 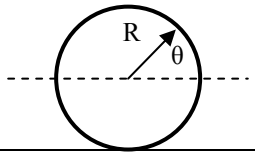	Common Factor	Bonded Interface – Expression to be multiplied by common factor Denominator term: $D = (1+K) + 3(5-K)\beta + (3+K)\alpha + 12(3-K)\alpha\beta$
Radial pressure on pipe	P_o	$\alpha/(1+\alpha) - \{(1-K)(-2\alpha + 18\beta + 24\alpha\beta)/D\}\cos 2\theta$
Tangential pressure on pipe	P_o	$0 + \{(1-K)(4\alpha + 24\alpha\beta)/D\}\sin 2\theta$
Radial displacement of pipe	$P_o R/(2G)$	$1/(1+\alpha) - \{(1-K)(2 + 4\alpha)/D\}\cos 2\theta$
Tangential displacement of pipe	$P_o R/(2G)$	$0 + \{(1-K)(2 + 2\alpha + 6\beta)/D\}\sin 2\theta$
Moment in pipe wall per unit length	$P_o R^2$	$\beta/(1+\alpha) + \{(1-K)(6\beta + 12\alpha\beta)/D\}\cos 2\theta$
Thrust force in pipe wall Per unit length	$P_o R$	$\alpha/(1+\alpha) + \{(1-K)(2\alpha + 6\beta + 24\alpha\beta)/D\}\cos 2\theta$
Shear force in pipe wall per unit length	$P_o R$	$0 - \{(1-K)(12\beta + 24\alpha\beta)/D\}\sin 2\theta$
Frictionless Interface: Structural Response Solutions		
Structural Response 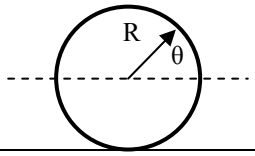	Common Factor	Frictionless Interface -- Expression to be multiplied by common factor Denominator term: $D = (1+K) + 3(5-K)\beta$
Radial pressure on pipe	P_o	$\alpha/(1+\alpha) - \{(1-K)(18\beta)/D\}\cos 2\theta$
Tangential pressure on pipe	P_o	0.0
Radial displacement of pipe	$P_o R/(2G)$	$1/(1+\alpha) - \{(1-K)2/D\}\cos 2\theta$
Tangential displacement of pipe	$P_o R/(2G)$	$0 + \{(1-K)/D\}\sin 2\theta$
Moment in pipe wall per unit length	$P_o R^2$	$\beta/(1+\alpha) + \{(1-K)(6\beta)/D\}\cos 2\theta$
Thrust force in pipe wall Per unit length	$P_o R$	$\alpha/(1+\alpha) + \{(1-K)(6\beta)/D\}\cos 2\theta$
Shear force in pipe wall per unit length	$P_o R$	$0 - \{(1-K)(12\beta)/D\}\sin 2\theta$

Figure 1.1.1-1 Conceptual view of elasticity solution with finite boundaries.

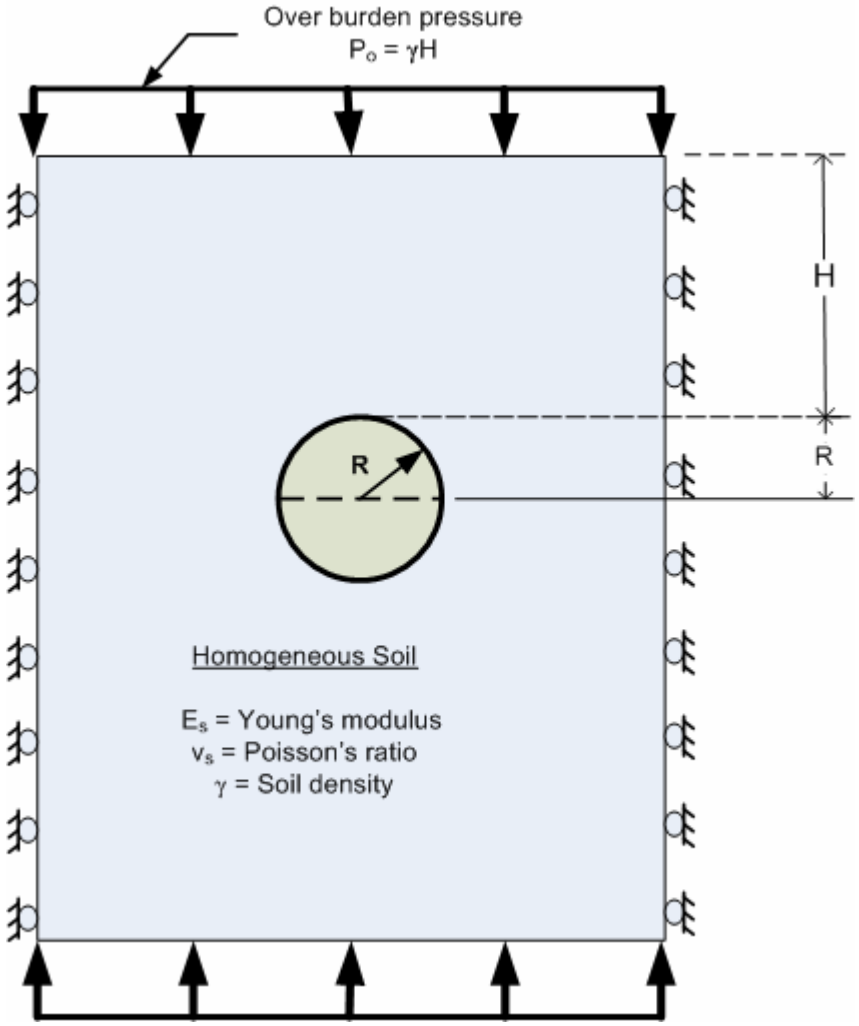

1.1.2 Nonlinear aspects

Although Level 1 is based on a linear elasticity solution, a fair degree on nonlinear modeling is achieved for both soil and pipe in the following manner. First the overburden pressure, P_o, may be divided into "n" load increments, ΔP_i, for i = 1 to n, and each load increment is applied in a series of load steps. During each load step the material properties of the soil may be redefined in accordance with current overburden pressure. The structural responses as presented in Table 1.1-1, with P_o replaced by ΔP_i, are summed in a running total thereby providing a load-deformation history record. The concept of overburden-dependent soil properties is elaborated in a later chapter on soil models.

With regard to nonlinear behavior of the pipe, each pipe type model (discussed later) can create changes in the effective bending stiffness EI and the effective hoop stiffness EA at each point around the pipe periphery. These modified properties are used directly to predict stress and strain at each pipe point based on the moment, thrust and shear at that point. However, an average value of the modified properties is used in the closed-form equations to predict the primary unknowns (displacements, moment, thrust, and shear) at each point on the pipe periphery.

1.1.3 Utility of Level 1

The Level 1 approach does not have the versati1ity and generality of the Level 2 and 3 counterparts. Nonethe1ess its efficiency and app1icabi1ity particularly for design is quite remarkable. From a design viewpoint, the exact nature of

the soil system, loading and boundary conditions may not be known with enough certainty to warrant a finite element solution. Thus the simplifying assumptions of Level 1 are often commensurate with knowledge of the design problem. It follows that the simple data preparation and quick computer time make Level 1 an attractive and powerful design tool for routine applications for deep burial loading.

1.2 Finite Element Methodology

As previously mentioned Level 2 and Level 3 share a common finite element solution program and differ only with respect to the mode of input: automatic or user-defined. Although the development and formulation of the finite element method is well established in the literature, an overview will be given herein as it applies to culvert installations.

A static, displacement-based finite element formulation is developed based on incremental virtual work. Incremental virtual work is ideally suited for characterizing buried structures problems because the load may be applied in a series of steps representing increments of overburden pressure, temporary construction loading and live loads from vehicles. In the case of culvert-soil systems, the incremental approach takes on a larger meaning than just incremental load steps. To wit, not only the load, but also the structural system may be assembled in increments. This process is termed the "incremental construction" technique and is the mathematical analogue of the physical process of constructing the soil system in a series of compacted layers or lifts. The structural predictions from an incremented system are more realistic than an equivalent monolith system. Another advantage of the incremental virtual work formulation is the relative ease of incorporating and solving various nonlinear models, which are discussed throughout this document.

For a general structural-continuum system, incremental virtual work may be expressed in matrix notation as:

$$\int_V \delta\varepsilon^T \Delta\sigma \, dV = \int_S \delta u^T \Delta\tau \, dS + \int_V \delta u^T \Delta f \, dV \qquad \text{Equation 1-1}$$

Where, σ = stress vector
ε = strain vector
u = displacement vector
τ = surface-traction vector
f = body-force vector
δx = small virtual variation of any vector x, δ is an operator
$\Delta x = x_{i+1} - x_i$, incremental change in any vector x from load step i to i+1, Δ is an operator
S = surface area of traction loads at load step i + 1
V = volume of structural system at load step i + 1

The physics behind the above incremental virtual work statement is as follows. We assume that the structural system is in equilibrium at load step i, and we are in the process of applying incremental loads to reach load step i + 1. With this understanding, Equation 1-1 states, "The increment of internal virtual-strain-energy is equal to the increment of external virtual work of body and traction loads as the system undergoes a virtual movement compatible with the kinematical constraints of the system."

To express the virtual work statement in a displacement formulation, the stress vector is expressed in terms of strains by using an incremental constitutive relationship, symbolized as ;

$$\Delta\sigma = \underline{C}\Delta\varepsilon \qquad \text{Equation} \qquad 1\text{-}2$$

Where, $\underline{C}$ is the constitutive function (matrix) that relates stress and strain increments from load step i to load step i + 1. In general, the coefficients may be nonlinear and dependent on the total stress and strain history.

Next, the strain increments are expressed in terms of displacement increments as;

$$\Delta\varepsilon = \Delta\underline{Q}(u) = \underline{Q}(\Delta u) \qquad \text{Equation 1-3}$$

where, $\underline{Q}$ is an operator matrix composed of partial derivatives. For small-deformation theory, the operator matrix contains linear operations so that $\underline{Q}$ is commutative with Δ and δ operators. In a later section of this chapter, the strain-displacement operator is extended to include large deformations, however for present purposes small-deformation theory is assumed.

Using the above relationships, the incremental virtual work may be expressed in terms of displacement fields over the entire domain as;

$$\int_V \underline{Q}(\delta u)^T \underline{C}\, \underline{Q}(\Delta u)\, dV = \int_S \delta u^T \Delta\tau\, dS + \int_V \delta u^T \Delta f\, dV \qquad \text{Equation 1-4}$$

The components of $\underline{C}$ and $\underline{Q}$ are dependent on element type, material behavior, and kinematical assumptions. Later, a nonlinear form of the $\underline{Q}$ operator is used to formulate large deformation analysis. The specific forms will be developed in subsequent chapters, for now, the concern is with the general formulation.

At this juncture, the finite element approximation is introduced by subdividing the domain V into a discrete set of elements interconnected at common nodal points. The unknown displacement fields within each element are approximated with prescribed functions such that continuity is maintained at the nodes and along the boundaries between elements. The assemblage of elements and nodes is termed the finite element mesh or topology.

The unknown displacement fields within each element are approximated by specified interpolation functions with unknown nodal-point displacements values, symbolically expressed as;

$$u_e = \underline{N}\hat{u}_e \qquad \text{Equation 1-5}$$

where , u_e = displacement vector-field within element

$\underline{N}$ = matrix of prescribed interpolation functions (spatial variables)

$\hat{u}_e$ = nodal-point displacement vector (unknown degrees of freedom)

The subscript "e" implies the above relationship holds within a given element. The form of the interpolation matrix and nodal displacement vector is dependent on element type.

1.2.1 Element types

The heart of any finite element formulation is the description of the elements themselves. There are three basic element types employed in the CANDE program.

- Quadrilateral and triangular elements: for in-situ soil, bedding material, fill soil, pavement, etc.
- Interface element: for interfaces such as between pipe and soil.
- Beam-column element: for culvert structure like pipes, boxes, arches, etc.

The ***quadrilateral*** element is a nonconforming element developed by Herrmann (Reference 11) that has superior qualities in all basic deformation modes. The quadrilateral is composed of two triangles with complete quadratic interpolation functions initially specified within each triangle. Upon applying appropriate constraints and static condensation procedures a four-node quadrilateral with an 8 x 8 stiffness matrix is formed, wherein each node has two degrees of freedom representing horizontal and vertical displacements. Associated with the quadrilateral/triangle element are four choices for material characterization: (1) linear elastic, isotropic or anisotropic; (2) incremental elastic, dependent on overburden pressure; (3) hyperbolic soil models by Duncan and Duncan & Selig, and (4) variable

modulus soil model by Hardin. Specific derivations of the quadrilateral/triangular element are given in Section 7.3 in conjunction with the constitutive models for soil.

The ***interface*** element allows consideration of two subassemblies meeting at a common interface such that under loading the subassemblies may slip relative to each other with Coulomb friction, or separate, or re-bond. A natural application of this element is simulating the pipe-soil interface, other applications include trench soil-to-in-situ soil interface. The interface element is composed of two nodes, each associated with one subassembly and initially meeting at a common contact point. Each contact node has two degrees of freedom, horizontal and vertical displacement. In addition, a third node is assigned to the "interior" of the contact point to represent normal and tangential interface forces. The three nodes produce a 6 x 6 element "stiffness" matrix in a mixed formulation. Actually, the element stiffness is a set of constraint equations with Lagrange multipliers. Constraint equations impose conditions on normal and tangential displacements, and Lagrange multipliers are interface forces. The interface element derivation is presented in Chapter 4

Lastly, the ***beam-column*** element is the familiar structural-matrix element for two-dimensional bending and axial deformation. It is defined by two nodes with three degrees of freedom per node, horizontal and vertical displacement and a rotation. Bending deformation is approximated by a cubic interpolation function and axial deformation is represented by a linear interpolation function. The beam-column element derivation employs a general nonlinear stress-strain model that is specialized to the material behavior of different pipe types. Specifically, elastic-plastic behavior for corrugated metal, tensile cracking and compressing yielding for reinforced concrete, and local buckling of wall profile elements for thermoplastic pipes. The beam-column element derivation is presented in Chapter 2 for each pipe type.

With the above background on specific element types, we continue with the general finite element formulation, wherein the global integrations expressed in Equation 1-4 may now be obtained as a summation of all element integrations. Specifically, within each element we replace the global displacement vector Δu by $\underline{N}\Delta\hat{u}_e$ and δu by $\underline{N}\delta\hat{u}_e$. Since $\Delta\hat{u}_e$ and $\delta\hat{u}_e$ are nodal-point parameters, they may be factored out of the element integrations. Thus, the element integrations are performed over known interpolation functions resulting in the so-called element stiffness matrix and load vector, expressed as;

$$\underline{k}_e = \int_{V_e} \underline{Q}(\underline{N})^T \underline{C}\, \underline{Q}(\underline{N})\, dV_e \qquad \text{Equation 1-6}$$

$$\Delta p_e = \int_{S_e} \underline{N}^T \Delta\tau\, dS_e + \int_{V_e} \underline{N}^T \Delta f\, dV_e \qquad \text{Equation 1-7}$$

Where, k_e = element stiffness matrix

V_e = volume of element

Δp_e = element load vector

S_e = surface of element where traction is applied

1.2.2 Global assembly and incremental construction.

Each element is assigned a construction increment number, which corresponds to the load step number that the element stiffness matrix and load vector is assembled into the global system. Once an element stiffness enters the system it remains active for all subsequent load steps (there is no element death option). Of course, the element body-load vector is only applied during the load step corresponding to the element construction increment number; it is not reapplied on subsequent load steps. Similarly, surface pressure and/or point loads (i.e., force boundary conditions) are also assigned a particular construction increment number and are only applied during the corresponding load step. Likewise, displacement boundary conditions are applied during the load step they are specified and remain fixed for all subsequent load steps.

To facilitate the global assemblage of elements, the current list of all active nodal degrees of freedom are aligned in a particular sequence order corresponding to the numerical sequence of the number-tag assigned to each node. Each active node is assigned two sequential positions in the global list for the horizontal and vertical nodal degrees of freedom. For those nodes that have a beam-column element attached, a third sequential position is assigned to the global list for the rotational degree of freedom. The global displacement vector, $\hat{u}_G$, represents the ordered list of all active degrees of freedom.

With the above understanding, the finite-element equivalent of Equation 1-4 is obtained by summing all active element contributions and assembling them into the global incremental virtual work statement. Since $\delta\hat{u}_G$ is an arbitrary virtual movement of all active degrees of freedom, the virtual work statement requires that the following set equilibrium equations be satisfied for each load step.

$$\underline{K}_G \Delta\hat{u}_G = \Delta P_G \qquad \text{Equation 1-8}$$

where, $\underline{K}_G = \sum_{\text{elements}} \underline{k}_e$ = incremental global stiffness matrix

$\Delta P_G = \sum_{\text{elements}} \Delta p_e$ = incremental global load vector

$\Delta\hat{u}_G$ = increment of global displacement vector (unknown degrees of freedom)

If the global system is linear, (that is, linear models are selected for the pipe materials, soil zones, interface conditions, and deformation theory), then the global stiffness matrix is directly calculable and constant for each load step. With this simplifying assumption, Equation 1-8 represents a set of linear algebraic equations that may be solved by standard methods such as Gauss Elimination to obtain $\Delta\hat{u}_G$. The running summation of each $\Delta\hat{u}_G$ over all load steps provides the total solution for the global displacement vector. Unfortunately, most culvert problems exhibit some type of nonlinear behavior so that the global stiffness matrix is not constant during the load step, requiring a nonlinear solution strategy discussed next.

1.2.3 Nonlinear solution strategy

CANDE employs a solution strategy known as the direct iterative method, or more simply called trial and error. This method has proven to be robust and readily accommodates the wide variety of nonlinear models such as tensile cracking and elastic-plastic behavior of pipe models, hyperbolic constitutive laws for soil models, frictional sliding and separation for interface models, and geometric nonlinearity for large deformation analysis. Most importantly, the solution accuracy is not dependent on the magnitude of load increments; that is, a large load increment will produce essentially the same results as the case where the load increment is divided into two or more sub-increments.

To illustrate the strategy, we start with the assumption that a valid (converged) solution is in hand for load step i, and we seek to increment the solution from load step i to i+1. That is, we know the mechanical responses (displacements, stresses, strains, etc.) at load step i and we seek to update the mechanical responses at load step i+1. The global set of equations for load step i+1 is expressed with an iteration counter *k* as;

$$\underline{K}_{Gk} \Delta\hat{u}_{Gk} = \Delta P_{Gk} \qquad \text{Equation 1-9}$$

where, $\underline{K}_{Gk}$ = global stiffness matrix for iteration k, (assembly of active elements)

$\Delta\hat{u}_{Gk}$ = increment of global displacement vector for iteration k (active dof)

ΔP_{Gk} = incremental global load vector for iteration k

k = iteration counter; 1, 2, 3, …

For the first iteration k =1, the global stiffness matrix is assumed to remain the same as computed at the end of the previous iteration cycle for the step i, except for the addition of new elements entering the system for the first time at load step i+1. Note, if load step i+1 happens to be the first step, meaning the initial configuration, then the global stiffness matrix is constructed based on unloaded, linear-elastic elements belonging to the initial configuration prior to loading.

With the above understanding, the set of linear-like equations (Equation 1-9 for k = 1) is solved by a standard Gauss elimination scheme for the first trial solution $\Delta\hat{u}_{G1}$. The trial solution is temporarily added to the known mechanical responses at load step i to form a new and better estimate of the displacements, stresses and strains at load step i+1. Next, all the nonlinear models for each element are re-evaluated based on current estimate of mechanical response for load step i+1, typically requiring small modifications to the elements stiffness matrices.

The process is repeated for k = 2, 3, 4 … until convergence is witnessed. That is, iteration k produces a trial solution $\Delta\hat{u}_{Gk}$ that is based on the revised stiffness matrix from the previous iteration $\Delta\hat{u}_{G\,k-1}$. When two consecutive iterations produce the same stiffness matrices for all elements within small error limits, then the solution has converged and we proceed to the next load step. The mechanics behind updating each element stiffness during the iteration cycle depends on the particular nonlinear model, discussed in subsequent chapters.

Once a converged solution increment has been found, all the mechanical responses are updated based on the last iteration solution, all intermediate iteration solutions are discarded. Thus prior to starting the next load step, the mechanical responses are permanently updated as symbolically shown below

$$q_{i+1} = q_i + \Delta q \qquad \text{Equation 1-10}$$

where q stands for all structural responses such as displacements, stresses, strains, moments, thrusts, etc. The data is saved in the program and the output file thereby providing a load-response history record.

As a final comment, it must be recognized that convergence is never guaranteed to occur. Sometimes convergence does not and should not occur because the system or portion of the system is physically incapable of carrying additional loading (singular system). In the normal default mode, CANDE will terminate on non-convergence with a message describing what nonlinear models are not converging. However, CANDE also offers the user control over the number of iterations with a special command to continue processing load steps even after a non-convergence load step has been encountered. In this way the user may inspect the post-convergent results to ascertain the cause of the problem.

2 BEAM-COLUMN ELEMENTS – PIPE TYPE MODELS

Presented in this section is a complete development of the beam-column elements used for modeling corrugated metal, reinforced concrete and thermoplastic pipe materials (or any two-dimensional structure). The initial development is focused on the general finite-element formulation that is applicable to all pipe-type material models. Subsequent developments describe specific stress-strain models that distinguish one pipe-type material from another.

2.1 General Form

The major assumptions and limitations used for the beam-column element are listed below:

1. Two-dimensional framework in a plane strain formulation.
2. Bernoulli-Euler beam kinematics without shear deformation.
3. Small deformation theory (this restriction removed in a subsequent chapter).
4. Material nonlinearity is a function of normal stress and strain and their history.
5. Incremental virtual work formulation with incremental stress-strain relationships.

2.1.1 Beam kinematics.

Based on the assumption that cross-sectional planes remain plane in bending and axial deformation, the Bernoulli-Euler assumption for displacement increments Δu at any station x along the beam length and at any point y in the beam's cross section may be expressed as an increment from load step i to i+1 as,

$$\Delta u(x, y) = \Delta a(x) + (y^*-y)\Delta v' \qquad \text{Equation} \qquad 2\text{-}1$$

where, $\Delta u(x,y)$ = displacement in x direction from column and bending deformation.

$\Delta a(x)$ = uniform displacement in x direction from column action, independent of y.

$\Delta v(x)$ = displacement in y direction as function of x, independent of y.

$\Delta v' = d(\Delta v)/dx$, derivative of Δv with respect to x (local deformation slope).

y^* = reference plane in the beam cross-section at y = y*, yet to be specified.

$\Delta q = q_{i+1} - q_i$ = incremental change in any function q from load step i to i+1.

The Bernoulli-Euler assumption states that Δu at any point in the cross-section may be described by a uniform displacement Δa plus a rotational-like motion due to the slope of the transverse displacement increment. Note that the axis, y*, is not specifically fixed in cross-section under these assumptions. Figure 2.1.1-1 illustrates the beam-column element in local beam coordinates, wherein x is aligned with the longitudinal axis and y is in the transverse direction locating positions in the beam's cross section.

Figure 2.1.1-1 Local coordinates for beam element and cross section.

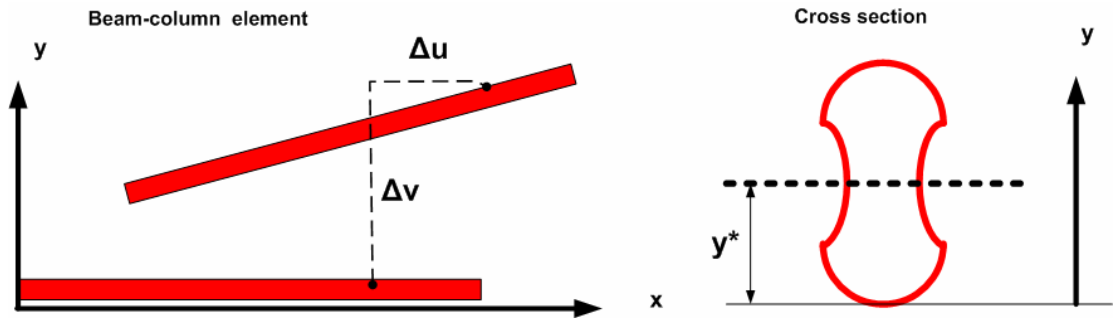

Applying small strain theory to the above displacement functions produces one non-zero strain component, which is the strain normal to the beam cross section, $\Delta\varepsilon = d(\Delta u)/dx$. In terms of the Bernoulli-Euler functions, the incremental normal strain function is given by:

$$\Delta\varepsilon(x,y) = \Delta a' + (y^*-y)\Delta v'' \qquad \text{Equation 2-2}$$

where $(\ )' = d(\ )/dx$, prime symbol denotes derivative of any quantity with respect to x.

2.1.2 Incremental stress-strain model

The nonlinear stress-strain laws used in CANDE are specific to each pipe material such as corrugated metal, reinforced concrete, and profile plastic pipe, which are presented in subsequent sections. However, all pipe materials stress-strain models conform to the same generic form expressed as;

$$\Delta\sigma = E_c\Delta\varepsilon \qquad \text{Equation 2-3}$$

where, $\Delta\sigma$ = increment of axial stress from load step i to i + 1, ($\Delta\sigma = \sigma_{i+1} - \sigma_i$)
$\Delta\varepsilon$ = increment of axial strain from load step i to i + 1, ($\Delta\varepsilon = \varepsilon_{i+1} - \varepsilon_i$)
E_c = chord modulus of total stress-strain curve from load step i to i + 1

The chord modulus is dependent on the type of material and is generally dependent on the history of stress and strain throughout all loading steps. It is determined iteratively during each load step by repeating the solution process until the value of E_c converges for each point within the element to a small tolerance of error. The chord modulus is illustrated in Figure 2.1.2-1 for a generic, nonlinear stress-strain relationship.

Replacing $\Delta\varepsilon$ in Equation 2-3 with Equation 2-2, the fundamental stress-displacement relationship may be expressed as,

$$\Delta\sigma = E_c(\Delta a' + (y^*-y)\Delta v'') \qquad \text{Equation 2-4}$$

Next, we will use the above equation to define the internal thrust and internal moment acting on the cross section at any station x.

Figure 2.1.2-1. Generic incremental stress-strain relationship.

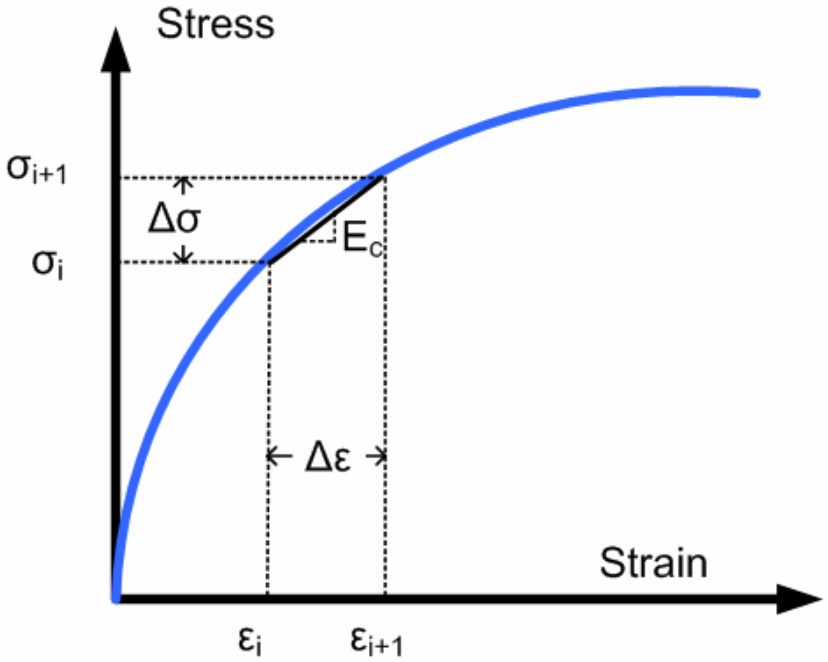

2.1.3 Internal thrust and moment increments

As is customary, we define the thrust increment as the integral of Δσ over the cross section area A, and the moment increment as the integral of Δσ (y*-y) over the cross section area A. Specifically,

$$\Delta N = \int_A \Delta\sigma \, dA = \int_A E_c(\Delta a' + (y^*-y)\Delta v'') \, dA \qquad \text{Equation 2-5}$$

$$\Delta M = \int_A \Delta\sigma (y^*-y) dA = \int_A E_c(\Delta a' + (y^*-y)\Delta v'')(y^*-y) dA \qquad \text{Equation 2-6}$$

where, ΔN = thrust increment from load step i to i + 1, ($\Delta N = \Delta N(x)$)
ΔM = moment increment from load step i to i + 1, ($\Delta M = \Delta M(x)$)
dA = b(y)dy, a differential area of cross section where b(y) is the width

Figure 2.1.3-1 shows the incremental thrust and moment resultants for an arbitrary cross-section with the coordinate y measured from bottom.

Figure 2.1.3-1 Thrust and moment increments from integration of stress distribution

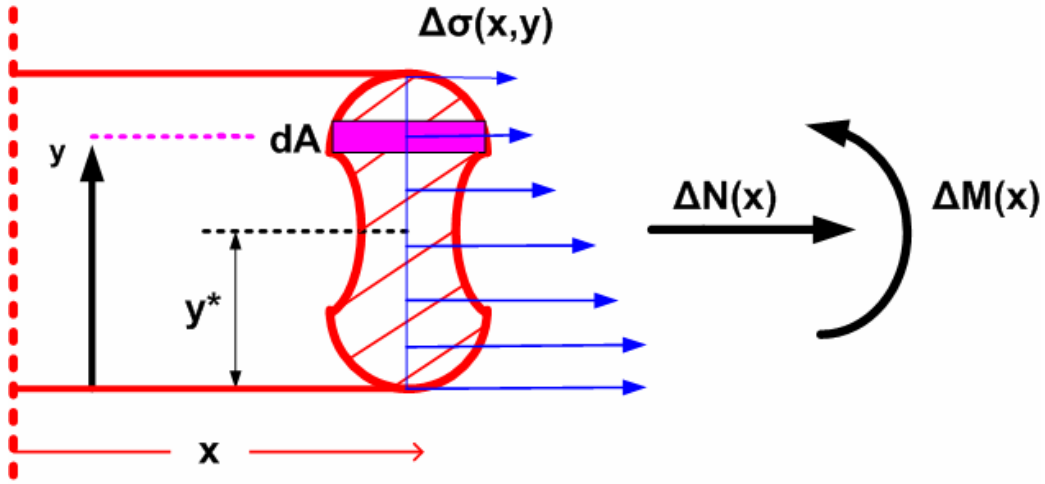

.

The location of the arbitrary reference position y* is now conveniently selected so that the first moment of integration is zero, i.e.,
$\int_A E_c\,(y^*-y)\,dA = 0$. Therefore, the location of y* measured from the bottom of the cross section is,

$$y^* = \left(\int_A E_c\, y\, dA\right) / \left(\int_A E_c\, dA\right) \qquad \text{Equation 2-7}$$

With the above definitions for y*, the thrust and moment increments simplify to the following equations,

$$\Delta N = EA^* \Delta a' \qquad \text{Equation 2-8}$$

$$\Delta M = EI^* \Delta v'' \qquad \text{Equation 2-9}$$

where, $EA^* = \int_A E_c\, dA$ = effective axial stiffness of beam element

$EI^* = \int_A E_c \left(y^*-y\right)^2 dA$ = effective bending stiffness of beam element .

In the above equations, the thrust expression is written in the familiar linear form as the product of axial stiffness and column strain; likewise, the moment expression is written in the familiar form as the product of bending stiffness and beam curvature. Although the equations for thrust and moment increments may appear linear-like, the integrals defining y*, EA*, and EI* depend on the nonlinear chord modulus, which in turn depends on the stress-strain state at each point in the cross-section in advancing from load step i to i+1.

From an analytical viewpoint, the only difference between one nonlinear pipe material and another is calculation of y*, EA*, and EI* along with the associated convergence criteria. Except for these calculations, the fundamental beam-column formulation is identical for all pipes as presented in the remainder of this section.

2.1.4 Beam-column virtual work.

The general framework of incremental virtual work as previously presented is now specialized for the beam-column element. Specifically, the increment of internal virtual-strain-energy is written as,

$$\delta\Delta U_e = \int_V (\delta a' + (y^*-y)\delta v'')\Delta\sigma \, dV \qquad \text{Equation 2-10}$$

where the virtual strain is expressed in terms of the Bernoulli-Euler functions prescribed in Equation 2-2, and V represents the volume of the beam-column element.

Separating the volume integral into area and length integrals, dV = dAdx, we arrive at,

$$\delta\Delta U_e = \int_x \{\delta a' \int_A \Delta\sigma dA + \delta v'' \int_A \Delta\sigma (y^*-y) dA\} \, dx \qquad \text{Equation 2-11}$$

Since the two area integrals in the above expression have been identified as ΔN and ΔM, the above expression may be equivalently written as,

$$\delta\Delta U_e = \int_x \{\delta a'\Delta N + \delta v''\Delta M\} \, dx \qquad \text{Equation 2-12}$$

Lastly, replacing ΔN and ΔM by Equations 2-8 and 2-9, we arrive at the desired displacement form for internal virtual strain energy of the beam-column element,

$$\delta\Delta U_e = \int_x \{\delta a' EA^* \Delta a' + \delta v'' EI^* \Delta v''\} dx \qquad \text{Equation 2-13}$$

In a similar manner, the incremental external virtual work for body loads is specialized for the beam-column element as,

$$\delta W_e = \int_x (\delta a \Delta F_x + \delta v \Delta F_y) dx \qquad \text{Equation 2-14}$$

where, $\Delta F_x = \int_A f_x dA$ = axial body force per unit beam length in local x-direction,

$\Delta F_y = \int_A f_y dA$ = transverse body force per unit beam length in local y-direction.

The body force per unit volume is assumed to be generated by gravity acting in the global vertical direction so that f_x and f_y are the component body forces per unit volume in local beam coordinates. Recall that all surface tractions and pressures are incorporated in the system at the global level, not at the element level.

2.1.5 Finite element interpolation functions.

To utilize the internal and external virtual work expressions in a finite element formulation for the beam-column, elements, we introduce specific interpolation functions for the displacement functions that become exact as the element lengths become small. The interpolation functions are expressed in terms of unknown nodal variables shown in the sketch below.

where, Δu_a, Δu_b = incremental nodal displacements in x direction at nodes a and b

Δv_a, Δv_b = incremental nodal displacements in y direction at nodes a and b

$\Delta \theta_a$, $\Delta \theta_b$ = incremental nodal rotations in counter-clockwise direction at nodes

The incremental axial displacement function is approximated with a linear interpolation function given by,

$$\Delta a(x) = \varphi_1(x)\, \Delta u_a + \varphi_2(x)\, \Delta u_b \qquad \text{Equation 2-15a}$$

Or in vector notation,

$$\Delta a(x) = \langle \varphi_1\ \varphi_2 \rangle \langle \Delta u_a\ \Delta u_b \rangle^T \qquad \text{Equation 2-15b}$$

where, $\varphi_1(x) = 1 - x/L$ = first interpolation function defined over beam length L.

$\varphi_2(x) = x/L$ = second interpolation function defined over beam length L.

The incremental vertical displacement function is approximated by a cubic polynomial, known as a Hermetian interpolation function, and is expressed in vector notation by,

$$\Delta v(x) = \langle \gamma_1\ \gamma_2\ \gamma_3\ \gamma_4 \rangle \langle \Delta v_a\ \Delta \theta_a\ \Delta v_b\ \Delta \theta_b \rangle^T \qquad \text{Equation 2-16}$$

where, $\gamma_1(x) = 1 - 3\,(x/L)^2 + 2\,(x/L)^3$ = Hermetian interpolation function one,

$\gamma_2(x) = L\,(1 - x/L)^2\ x/L$ = Hermetian interpolation function two,

$\gamma_3(x) = 3\,(x/L)^2 - 2\,(x/L)^3$ = Hermetian interpolation function three,

$\gamma_4(x) = L\,(1 - x/L)\,(x/L)^2$ = Hermetian interpolation function four.

The above interpolation functions for axial deformation and bending lead to the element stiffness matrices developed next.

2.1.6 Element stiffness matrices

Taking the necessary derivatives of the interpolation functions for $\Delta a(x)$ and $\Delta v(x)$ and inserting them into the two internal virtual work terms of Equation 2-13, we arrive at the following expressions for internal virtual work in terms of axial virtual work and bending virtual work.

$$\delta \Delta U_e = \delta \langle \Delta u_a \Delta u_b \rangle \underline{K}_a \langle \Delta u_a \Delta u_b \rangle^T + \delta \langle \Delta v_a \Delta \theta_a \Delta v_b \Delta \theta_b \rangle \underline{K}_b \langle \Delta v_a \Delta \theta_a \Delta v_b \Delta \theta_b \rangle^T$$

where, $\underline{K}_a = (EA^*) \int_0^L [\langle \varphi_1'\ \varphi_2' \rangle^T \langle \varphi_1'\ \varphi_2' \rangle] dx$ (axial stiffness) Equation 2-17

and, $\underline{K}_b = (EI^*) \int_0^L [\langle \gamma_1''\ \gamma_2''\ \gamma_3''\ \gamma_4'' \rangle^T \langle \gamma_1''\ \gamma_2''\ \gamma_3''\ \gamma'' \rangle] dx$ (bending stiffness) Equation 2-18

Performing the integrations with respect to x over the element length L, we arrive at the final evaluation for the axial stiffness and bending stiffness as recorded below.

$$\underline{K}_a = (EA^*/L)\begin{pmatrix} 1 & -1 \\ -1 & 1 \end{pmatrix} \qquad \text{Equation 2-19}$$

$$\underline{K}_b = (EI^*/L)\begin{pmatrix} 12/L^2 & 6/L & -12/L^2 & 6/L \\ 6/L & 4 & -6/L & 2 \\ -12/L^2 & -6/L & 12/L^2 & -6/L \\ 6/L & 2 & -6/L & 4 \end{pmatrix} \qquad \text{Equation 2-20}$$

For linear materials EA* and EI* are constant and remain the same through out the analysis. For nonlinear materials the stiffness factors EA* and EI* are determined iteratively for each load step wherein the factors are computed from the average moment and thrust at the center of the element. This implies that the elements will be sufficiently small so that thrust and moment do not vary substantially over any one element.

The above two matrices are combined into a single 6 x 6 matrix by re-grouping the nodal unknowns into a single vector as expressed below

$$\Delta\hat{u}_e = < \Delta u_a \; \Delta v_a \; \Delta\theta_a \; \Delta u_b \; \Delta v_b \; \Delta\theta_b >^T \qquad \text{Equation 2-21}$$

where, $\Delta\hat{u}_e$ is a vector of the six nodal unknowns in element coordinates. Accordingly, the 6x 6 element stiffness matrix is formed from the adding $\underline{K}_a$ and $\underline{K}_b$ to get the complete element stiffness matrix, $\underline{K}_e$.

$$\underline{K}_e = EA^*\begin{pmatrix} 1 & 0 & 0 & -1 & 0 & 0 \\ 0 & 0 & 0 & 0 & 0 & 0 \\ 0 & 0 & 0 & 0 & 0 & 0 \\ -1 & 0 & 0 & 1 & 0 & 0 \\ 0 & 0 & 0 & 0 & 0 & 0 \\ 0 & 0 & 0 & 0 & 0 & 0 \end{pmatrix} + EI^*\begin{pmatrix} 0 & 0 & 0 & 0 & 0 & 0 \\ 0 & 12/L^2 & 6/L & 0 & -12/L^2 & 6/L \\ 0 & 6/L & 4 & 0 & -6/L & 2 \\ 0 & 0 & 0 & 0 & 0 & 0 \\ 0 & -12/L^2 & -6/L & 0 & 12/L^2 & -6/L \\ 0 & 6/L & 2 & 0 & -6/L & 4 \end{pmatrix}$$

2.1.7 Transformation to global coordinates.

The last step before adding the element's contribution into the entire system is to transform the nodal variables from local coordinates to global coordinates.

Let β = angle from global X-axis to local x-axis, then the local nodal variables may be expressed as global nodal variables by,

$$\Delta\hat{u}_e = \underline{T}\,\Delta\hat{u}_E \qquad \text{Equation 2-22}$$

where, $\Delta\hat{u}_e = < \Delta u_a \; \Delta v_a \; \Delta\theta_a \; \Delta u_b \; \Delta v_b \; \Delta\theta_b >^T$ = local nodal variables for element

$\Delta\hat{u}_E = < \Delta u_A \; \Delta v_A \; \Delta\theta_A \; \Delta u_B \; \Delta v_B \; \Delta\theta_B >^T$ = global nodal variables for element

$$\underline{T}=\begin{pmatrix} \cos\beta & \sin\beta & 0 & 0 & 0 & 0 \\ -\sin\beta & \cos\beta & 0 & 0 & 0 & 0 \\ 0 & 0 & 1 & 0 & 0 & 0 \\ 0 & 0 & 0 & \cos\beta & \sin\beta & 0 \\ 0 & 0 & 0 & -\sin\beta & \cos\beta & 0 \\ 0 & 0 & 0 & 0 & 0 & 1 \end{pmatrix} \quad = \text{transformation matrix}$$

With the above transformation matrix, the global element stiffness matrix may be expressed in global coordinates as,

$$\underline{K}_E = \underline{T}^T \underline{K}_e \underline{T} \qquad = \text{global element stiffness matrix} \qquad \text{Equation 2-23}$$

It should be clear that lower-case subscripts are used for element quantities that are in expressed in local coordinates, whereas upper-case subscripts are used for element quantities that are in expressed in global coordinates.

The element load vector due to body weight may be directly expressed in global coordinates because gravity operates in the global Y direction (negative). Thus the element's weight is divided equally to both nodes and acting in the -Y direction associated with Δv_A and Δv_B as expressed below.

$$\Delta p_E = -\rho AL \begin{pmatrix} 0 \\ 1/2 \\ 0 \\ 0 \\ 1/2 \\ 0 \end{pmatrix} \qquad = \text{global element load vector} \qquad \text{Equation 2-24}$$

where, ρ is the density of the beam-column material, A is the cross-sectional area and L is the length. The element stiffness matrix K_E and load vector Δp_E are in the proper form for global assembly.

2.1.8 Equation solving and recovery of structural responses.

After the entire set of elements is assembled and solved by Gauss elimination as described in Sections 1.2.2 and 1.2.3, the solution (or trial solution) gives numerical results for the incremental displacements at all nodes. Using these results, other key structural responses of the beam-column element are calculated (recovered) based the previously developed relationships. Key responses include internal thrust, moment and shear resultants and stress and strain distributions. .

First, the internal force and moment increments at the ends of the beam-column element are recovered by multiplying the element stiffness matrix by the calculated incremental displacements (transformed to local coordinates) as shown below.

$$< \Delta N_a \ \Delta Q_a \ \Delta M_a \ \Delta N_b \ \Delta Q_b \ \Delta M_b >^T = \underline{K}_e \, \Delta \hat{u}_e \qquad \text{Equation 2-25}$$

.

where, ΔN_a, ΔN_b = thrust force increments (local x_i direction) at nodes a and b

ΔQ_a, ΔQ_b = shear force increments (local y_i direction) at nodes a and b

ΔM_a, ΔM_b = moment increments at nodes a and b (invariant to x-y coordinates)

The fact that the incremental end forces can be recovered by multiplying the current element stiffness matrix times the incremental displacements is a direct result of applying incremental virtual work to a free-body beam-column element cut just short of the end nodes. Said another way, the incremental forces and moments at the cut ends are the additional end forces that are required to hold the free-body element in equilibrium as a result of the incremental load. As a result of the assumed interpolation functions, thrust and shear forces are constant within the element and the moment varies linearly from end to end. Thus, ΔN and ΔM are known at every point x along the element length.

Next, the incremental strain, defined by Equation 2-2, may be evaluated at any point (x,y) by using Equation 2-8 to evaluate the constant axial strain increment ($\Delta a' = \Delta N/EA^*$) and Equation 2.9 to evaluate the bending curvature ($\Delta v'' = \Delta M/EI^*$) as shown below. The strain distribution over any cross-section is always linear irrespective of the material stress-strain model.

$$\Delta\varepsilon(x,y) = \Delta N/EA^* + (y^*-y)\Delta M/EI^* \qquad \text{Equation 2-26}$$

Knowing the strain distribution, the stress increment at any point (x,y) may be calculated using the incremental stress-strain relationship (chord modulus) defined by Equation 2-3, which is dependent on the particular type of material.

$$\Delta\sigma(x,y) = E_c\,\Delta\varepsilon(x,y) \qquad \text{Equation 2-27}$$

where, $E_c = E_c(\sigma(x,y))$ = chord modulus as a function of total stress and stress history

Unlike the linear strain distribution, the incremental stress distribution is, in general, nonlinear over the cross-section because the chord modulus is dependent on the total stress magnitude and history.

After the incremental structural responses have been computed, the total structural responses at load step i + 1 are computed by adding the incremental values to the values of previous load step as indicated below.

$$q_{i+1} = q_i + \Delta q \qquad \text{Equation 2-28}$$

where q stands for any structural responses such as displacements, stresses, strains, moments, thrusts, and so on. If the solution represents a converged load step (or a linear system), then the q_{i+1} values are printed to the output file and permanently stored in the computer in preparation for the next load step. On the other hand, if the solution has not converged, the q_{i+1} values are used temporarily to compute improved estimates of the element stiffness matrices and then discarded.

2.1.9 Nonlinear solution strategy

The key section properties, EA*, y* and EI*, are the heart of the nonlinear algorithm, and they are computed at every node for every iteration. Shown below is a summary of the key section property definitions.

$$EA^* = \int_A E_c\,dA \qquad \text{= effective axial stiffness of beam element} \qquad \text{Equation 2-29a}$$

$$y^* = \left(\int_A E_c\,y\,dA\right) / \left(\int_A E_c\,dA\right) \text{ = reference axis} \qquad \text{Equation 2-29b}$$

$$EI^* = \int_A E_c \, (y^*-y)^2 dA \quad = \text{effective bending stiffness of beam element} \qquad \text{Equation 2-29c}$$

To perform the above area integrations, the chord modulus, E_c, must be estimated at each point in the cross-section. As previously illustrated in Figure 2.1.2-1, the chord modulus for nonlinear materials is dependent on the known stress-strain state at load step i and the unknown stress-strain at load step i + 1, thereby requiring an iterative solution strategy as outlined below.

1. For the first iteration, the chord moduli are assumed to remain unchanged from the converged results of load step i. Thus, the key section properties and element stiffness also remain the same as they were. Based on these known element stiffness matrices, the first trial solution is obtained for the new incremental load vector from load step i to load step i+1.

2. Using the first trial solution, the recovery process discussed above provides estimates for σ_{i+1} and ε_{i+1}, which, in turn, provides new estimates for the chord moduli depending on the particular stress-strain model assigned to the element.

3. Knowing the new estimates for the chord moduli, the area integrations in Equations 2-29a,b,c are performed to provide new estimates for the key section properties, EA*, y* and EI*, and hence, revised element stiffness matrices.

4. After assembling the revised element stiffness matrices, the next trial solution is obtained, which leads to new estimates for σ_{i+1} , ε_{i+1}, and E_c, for each point in the cross-section. Once again, the area integrals are evaluated to provide better estimates of the key section properties at each nodal location, and so on.

5. The above process is repeated for each iteration until two successive solutions produce essentially the same section properties for every element within 1% relative difference. When this occurs, the solution is said to have converged and all the updated structural responses are printed and saved for the next load step.

The area integrations for section properties, EA*, y* and EI*, are accomplished in each pipe-type subroutine. In some cases, the integrations are done numerically and in other cases the integrations are accomplished in a semi-analytical manner depending on the stress-strain model of the pipe material. In subsequent sections of this chapter the calculation procedure to obtain EA*, y* and EI* for each pipe material are presented for each pipe-type material.

2.2 Corrugated Metal

2.2.1 Overview of corrugated metal pipe type

Corrugated metal applies to both corrugated steel and corrugated aluminum. Both metals are represented by the same fundamental models and differ only with respect to the numerical values of key parameters such as modulus and yield stress. Wall properties of corrugated metal are characterized by cross-sectional area, moment of inertia and section modulus, which represent the geometry of the corrugation's waveform per unit length. The aluminum pipe-type subroutine and the steel pipe-type subroutine have built-in tables for commercially available corrugation sizes as well as realistic default values for all linear and nonlinear material properties. Steel and aluminum material behavior is simulated with a bilinear stress-strain model with an initial elastic response up to yield stress followed a hardening plastic response, identical in tension and compression. All unloading is assumed linear elastic.

2.2.2 Design criteria for corrugated metal

Design criteria for corrugated metal includes strength limits for thrust stress against material yielding in hoop compression, global buckling and seam strength rupture. A new strength criterion is a limit on the amount of plastic penetration through the cross section. Finally, a performance limit on the allowable defection completes the set of design criteria. The design criteria are summarized in the following table.

TABLE 2.2.2-1 Corrugated Metal Design Criteria.

Design Criterion (Strength limits)	**Demand**	**Capacity**
(1) Thrust stress (psi)	$\sigma_{max} = N_{max}/A$	f_y = yield strength
(2) Global Buckling (psi)	$\sigma_{max} = N_{max}/A$	f_b = buckling capacity
(3) Seam strength (psi)	$\sigma_{max} = N_{max}/A$	f_s = seam strength
(4) Plastic Penetration *(%)	pp = computed % plastic	failure = 100%
(Performance Limits) (at Service Load)		
(5) Allowable deflection *(%)	Δ_{max} =computed deflect %	Allowable = 5% (Long Spans = 2%)

The above design criteria are equally applicable to working stress or LRFD design methodologies. For the working stress approach, the demand and the capacity quantities are unfactored, and the design evaluation is given by safety factors defined as capacity divided by demand. Typically safety factors on the order of 2.0 are desirable for strength-related criteria. For the LRFD approach the demand and the capacity quantities are factored (see Chapter 6), and the design evaluation is given by ratios of demand-to-capacity. Demand-to-capacity ratios less than or equal to 1.0 are acceptably safe. Further discussion on the design criteria is provided below.

1. *Thrust stress*. Thrust-stress demand is determined by finding the element with the largest thrust force, N_{max}, and dividing by the cross-sectional area. The corresponding yield-strength capacity is typically 33,000 psi for steel and 24,000 psi for aluminum.

2. *Global buckling*. For the buckling-strength capacity, CANDE-2007 offers the user two choices; (1) an approximate and generally conservative estimate based on the simplified AASHTO LRFD equations 12.7.2.4-1-2, and (2) a much more accurate solution based on CANDE's large deformation formulation with linearized buckling prediction.

3. *Seam strength*. If longitudinal seams are present in the corrugated metal culvert, the seam-strength capacity is typically less than the material yield strength. In the absence of experimental test data, seam-strength capacity is often specified as 67% of material yield-strength capacity.

4. *Plastic penetration*. On the demand side, the percentage of the cross-section that is strained into the plastic range from thrust and bending is calculated directly from the nonlinear corrugated metal model. The limit of plastic penetration is100% of the cross section, meaning cross section is incapable of carrying any additional load. Note that some amount of plastic yielding is expected to occur in the outer fibers of most well designed corrugated metal culverts under service loading. The plastic penetration design criterion is a precaution against full 100% yielding of the entire cross section, not against moderate outer fiber yielding.

5. *Allowable deflection*. Computed deflection is the relative vertical movement between the top and bottom of the culvert structure, and the percent deflection is relative the vertical distance. The service load limit for allowable deflection is generally taken as 5% for all corrugated metal structures except long spans, which are usually limited to 2% of the vertical rise.

2.2.3 Nonlinear model for corrugated metal

The one-dimensional stress-strain relationship for metal is approximated by a bilinear curve as shown in the figure below.

Figure 2.2.3-1 Stress-strain relationship for metal culverts

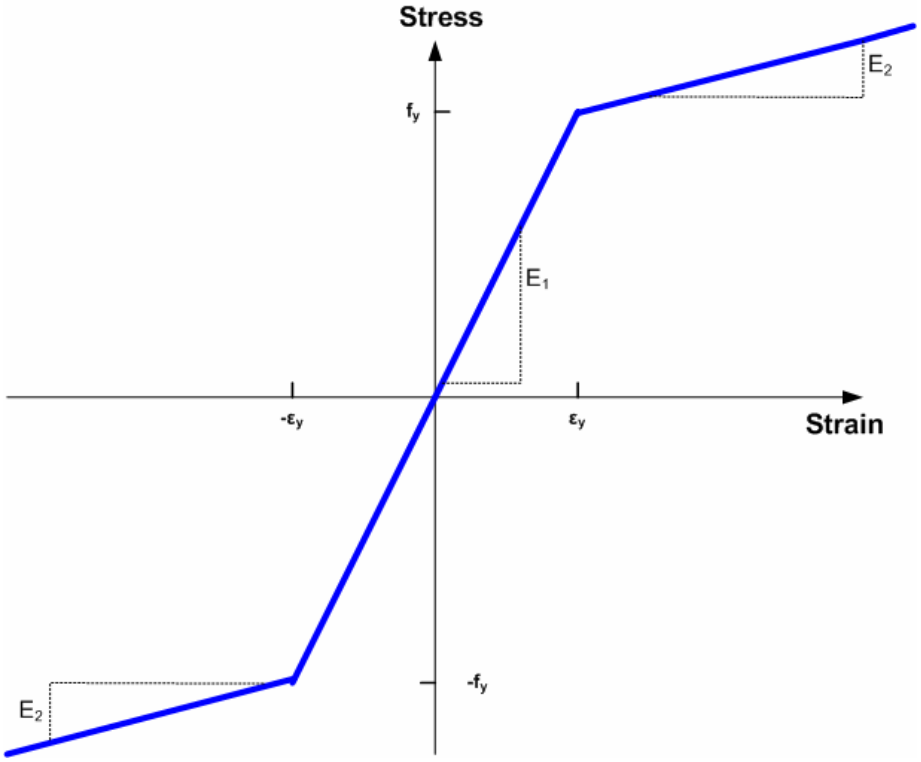

The model is identical in tension and compression and applies to both steel and aluminum, which differ only in parametric values as shown in the table below.

Table 2.2.3-1 Typical material parametric values for steel and aluminum

Metal type	Yield strength psi	Elastic Young's modulus, E_1 psi	Upper curve modulus, E_2 psi
Aluminum	24,000	10,000,000	500,000
Steel	33,000	29,000,000	0.0

The following material constants are used for plane strain conditions:

$E_e = E_1/(1-\nu^2)$ = Effective plane strain modulus in elastic zone

ν = Poisson ratio of metal

$r = E_2/E_1$ = Ratio of upper-curve modulus to initial modulus

$r E_e$ = Effective plane strain modulus for upper-curve zone.

Initial section properties are defined (input) as follows:

A_0 = Cross-sectional area of corrugation per unit length

I_0 = Moment of inertia of corrugation about mid-height

$S_0 = I_0/(h/2)$ = Section modulus of corrugation

h = Total height of corrugation

Within the framework of the general nonlinear model, the objective is to determine the integral quantities EA*, y*, and EI* defined by Equations 2-29a,b, & c. To accomplish this, the chord modulus E_c must be determined consistently with the bi-linear model, and, secondly, the area of integration must be defined. With regard to the latter, a manageable integration area can be obtained by approximating the actual corrugation geometry by a saw-tooth pattern, such that the same area A_0 and depth of section h is preserved, as shown in Figure 2.2.3-2

Figure 2.2.3-2 Saw-tooth approximation of corrugation for integrating in nonlinear range

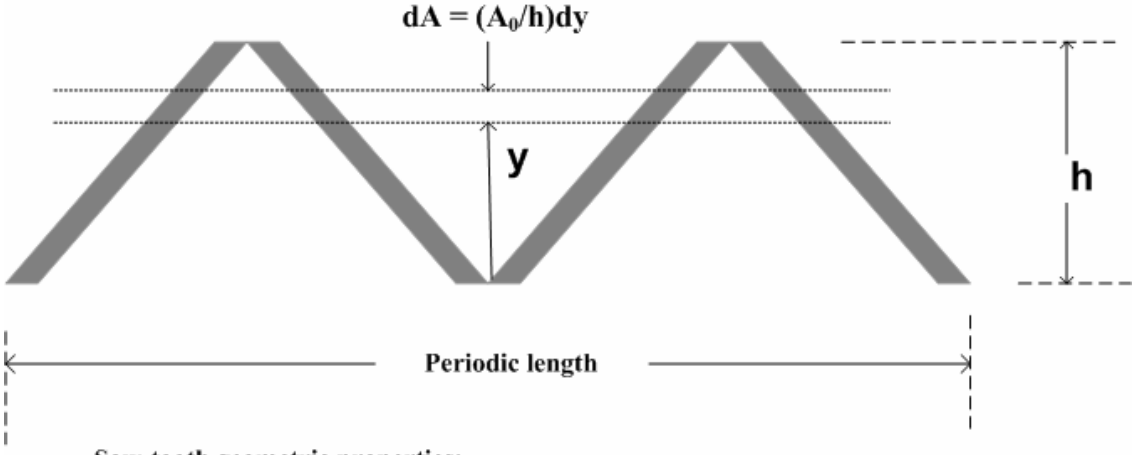

Saw-tooth geometric properties:

Area = $(A_0/h)\int_h dy = A_0$

Centroid = $(A_0/h)\int_h y\,dy / A_0 = h/2$

Moment inertia = $(A_0/h)\int_h (y-h/2)^2\,dy = A_0h^2/12$

Correction factor for moment of inertia:

$C_0 = I_0 / (A_0h^2/12)$

Moment inertia = $C_0 (A_0/h)\int_h (y-h/2)^2\,dy = I_0$

As shown in the above figure, integration of the saw-tooth approximation yields the correct area and centroid location, however, the moment of inertia = $A_0h^2/12$ is an approximation of actual corrugations, which are more rounded at the top and bottom than the saw-tooth approximation. By inspecting sectional properties of standard corrugation tables the moment of inertias from the saw-tooth approximation are 5 to 10% lower than the reported moment of inertia values. To correct for this discrepancy, integrations for the effective bending stiffness will be multiplied by the correction factor C_0 defined in the above figure in order to reproduce the correct moment of inertia. Of course if the metal is not yielding anywhere in the cross section, the chord modulus has the constant value E_e and may removed from inside the integral and integrations need not be performed since the section properties are already known.

Recalling the chord modulus relates increments of stress to increments of strain, $\Delta\sigma = E_C\,\Delta\varepsilon$, the bilinear model results in three distinct zones as illustrated in Figure 2.2.3-3. Case 1occurs when the strain increment lies entirely in the elastic zone, bounded by the yield strain, as illustrated by $\Delta\varepsilon_1$. Case 2 occurs when the strain increment starts in the elastic

region and exceeds the yield strain, as illustrated by $\Delta\varepsilon_2$. Finally Case 3 occurs when the strain increment starts at a strain greater than yield strain and ends at a greater value, as illustrated by $\Delta\varepsilon_3$. All other cases wherein the strain increment start from a large strain value and ends with a smaller strain value is elastic unloading and treated the same as Case 1.

Figure 2.2.3-3 Illustration of strain increments in three zones; elastic, transition and plastic

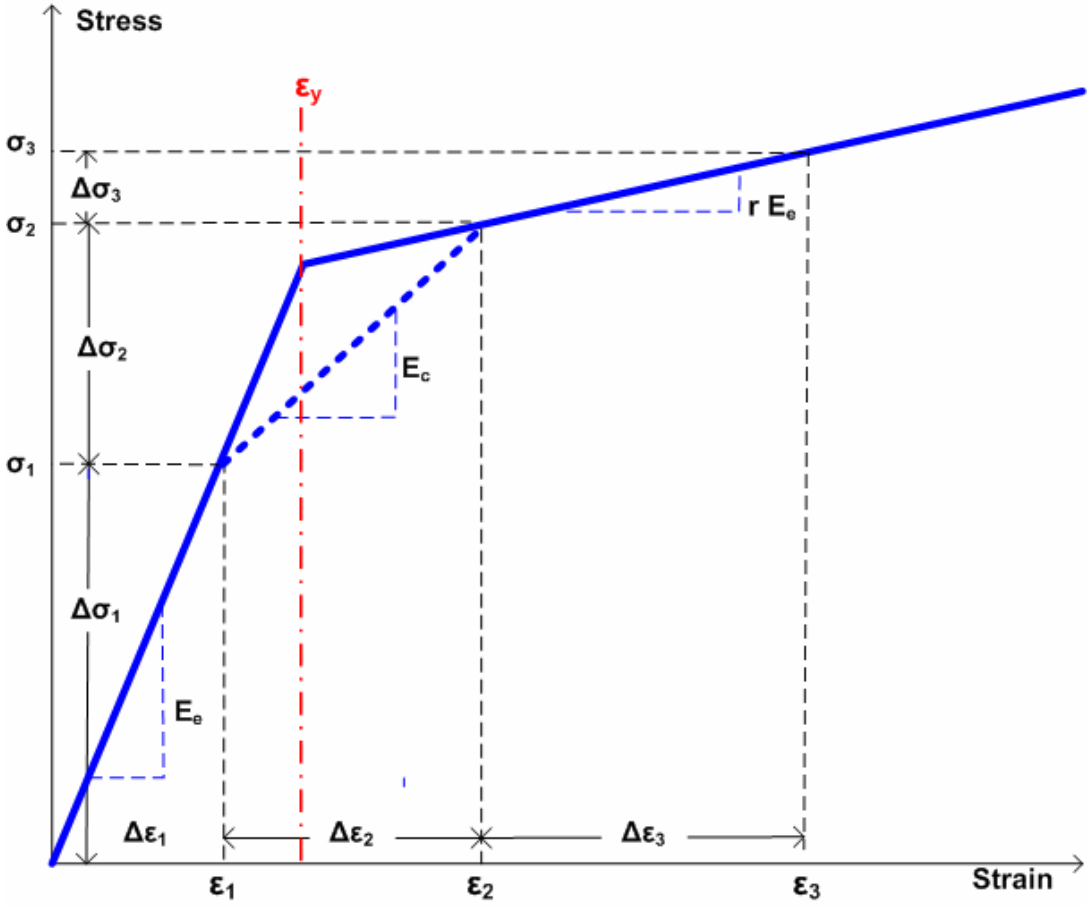

With the above understanding the general chord modulus can be defined in term of the bilinear model for the elastic, transition and plastic zones as follows;

$E_C = E_e$ (Elastic zone) Equation 2.2-1a

$E_C = E_e[(\varepsilon_y - \varepsilon_i)/(\Delta\varepsilon_{i+1}) + r(\varepsilon_{i+1} - \varepsilon_y)/(\Delta\varepsilon_{i+1})]$ (Transition zone) Equation 2.2-1b

$E_C = r E_e$ (Plastic zone) Equation 2.2-1c

In the above, the transition zone chord modulus is defined generally from load step i to i+1 where $\varepsilon_i < \varepsilon_y < \varepsilon_{i+1}$.

The foregoing considered the stress-strain relationship at a point. To obtain EA*, y*, and EI*, the stress-strain relationship must be defined over the cross-sectional area. To this end we take great advantage of the fact the strain profile always remains linear due to Bernoulli-Euler kinematics. Figure 2.2.3-4 illustrates two typical strain distributions at load step i and at load step i+l. The cross-section depth is divided into the regions elastic, transition, and plastic. The elastic region is that portion which remains totally elastic during the load step. The transition region is the zone that begins elastic and becomes plastic during the load step. And finally, the yield region signifies the zone where the material remains plastic.

Figure 2.2.3-4 Typical strain profiles and resulting zone descriptions

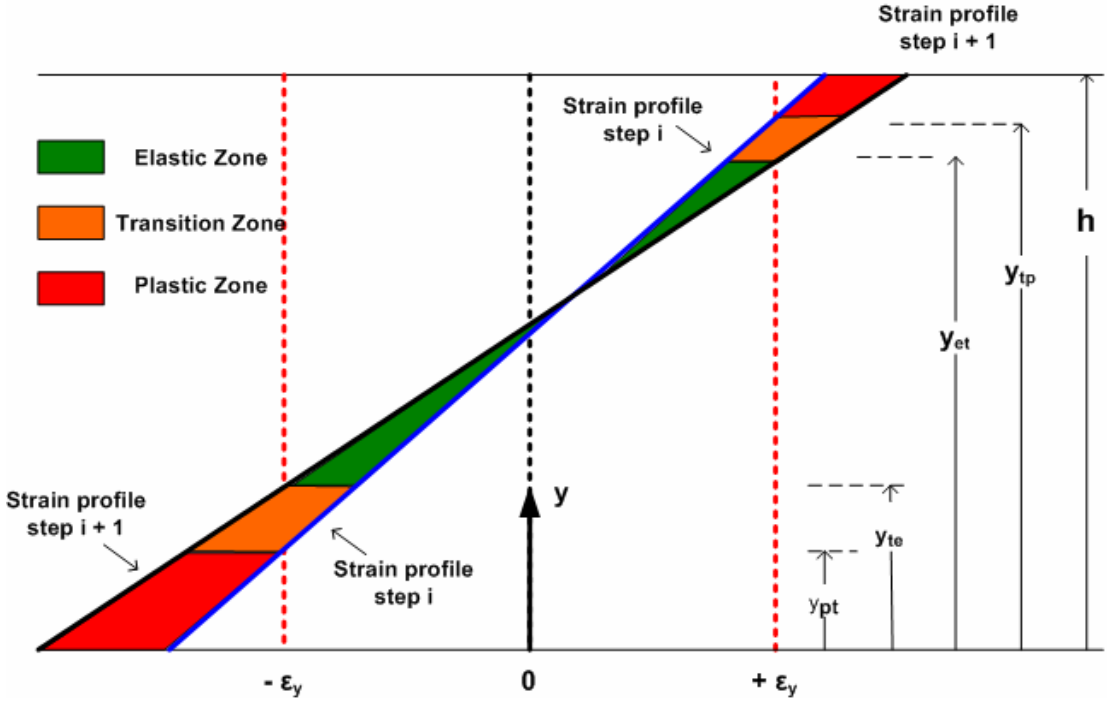

Knowing the strain profile at step i and having obtained a trial strain profile at step i+1, it is a simple matter to locate the elastic-transition boundaries and the transition-plastic boundaries using straight-line equations as indicated in the above figure. The elastic-transition boundaries are located where the strain profile at step i+1intersects the yield strain limits, and the transition-plastic boundaries are located where the strain profile at step i intersects the yield strain limits.

The chord modulus in the elastic and plastic zones is a constant value, however in the transition zones, the chord modulus varies with y because the strain increments vary with y. To simplify the integrations of the chord modulus in the transition zones, an average value of E_C is computed from Equation 2.2-1b based on the strain increment in the center of the transition zones. Letting z_{t1} and z_{t2} be the y-distance to the centroid of the lower and upper transition zones and computing the strain increments at these levels, we can express the chord moduli as,

$$E_{C1} = \alpha_1 E_e \quad \text{Average chord modulus in lower transition zone} \qquad \text{Equation 2.2-2a}$$

$$E_{C2} = \alpha_2 E_e \quad \text{Average chord modulus in upper transition zone} \qquad \text{Equation 2.2-2b}$$

where, $\alpha_1 = [(\varepsilon_y - \varepsilon_i)/(\Delta\varepsilon_{i+1}) + r(\varepsilon_{i+1} - \varepsilon_y)/(\Delta\varepsilon_{i+1})]$, with $\Delta\varepsilon_{i+1}$ evaluated at z_{t1}
$\alpha_2 = [(\varepsilon_y - \varepsilon_i)/(\Delta\varepsilon_{i+1}) + r(\varepsilon_{i+1} - \varepsilon_y)/(\Delta\varepsilon_{i+1})]$, with $\Delta\varepsilon_{i+1}$ evaluated at z_{t2}

The alpha terms are constants and are within the range, r < alpha < 1.0, depending on the transition zone boundaries, which may be truncated at the top and bottom of the cross-section. This transition zone integration technique has proven to be very accurate. The following table summarizes the data that is required to compute the key section properties.

Table 2.2.3-2 Zone integration parameters to compute key section properties

Zone Number	Zone Description	Zone Thickness	Distance to zone centroid	Zone weight due to nonlinear modulus
1	Elastic	Δh_1	z_1	$w_1 = 1.0$
2	Lower transition	Δh_2	z_2	$w_2 = \alpha_1$
3	Upper transition	Δh_3	z_3	$w_3 = \alpha_2$
4	Lower plastic	Δh_4	z_4	$w_4 = r$
5	Upper plastic	Δh_5	z_5	$w_5 = r$

It should be understood that not all five zones might be active at any given time. Un-active zones are characterized with $\Delta h_j = 0$, so that $h = \sum_{j=1}^{5} \Delta h_j$ always hold true.

With the above understanding, the effective axial stiffness for trial load step i+1 is given by,

$$EA^* = \int_A E_C dA = E_e A^* \qquad \text{Equation 2.2-3a}$$

where, $$A^* = (A_0/h)\sum_{j=1}^{5} w_j \Delta h_j \qquad \text{Equation 2.2-3b}$$

The current reference axis is given by,

$$y^* = (\int_A E_C y\, dA)/(\int_A E_C\, dA) \;=\; (\sum_{j=1}^{5} w_j z_j \Delta h_j)/A^* \qquad \text{Equation 2.2-4}$$

And finally, the effective bending stiffness is given by,

$$EI^* = \int_A E_C (y^*-y)^2 dA = E_e I^* \qquad \text{Equation 2.2-5a}$$

where, $$I^* = C_0\,(A_0/h)\sum_{j=1}^{5} w_j (\Delta h_j^{\,3}/12 \;+\; \Delta h_j (z_j - y^*)^2) \qquad \text{Equation 2.2-5b}$$

In CANDE-2007 the above computations are carried out in Subroutine EMOD wherein convergence is achieved when two successive trial solutions produce A*, y* and I* within 1% of the previous trial solution for all elements.

2.3 Reinforced Concrete

2.3.1 Overview of reinforced concrete pipe type

Wall sections for reinforced concrete culverts are defined by the concrete wall thickness with up to two rows of reinforcing steel, typically placed near the inner and outer surface with specified cover depths. In tension, concrete behavior is characterized by cracking when tension stress levels exceed the tensile strain limit. When this occurs the pre-existing tensile stresses are redistributed to the uncracked section, and the cracked location is assumed not to heal for any subsequent tensile loading. In compression, concrete is simulated with a tri-linear stress-strain curve. Initially, the concrete response is linear up to a specified strain level after which the concrete exhibits plastic-hardening behavior. When the compressive stress reaches the ultimate strength limit (fc'), the stress-strain response becomes perfectly plastic with no increase in stress as compressive strain increases. Reinforcing steel behavior is characterized by an elastic-plastic stress-strain model, which becomes perfectly plastic when the steel yield stress is reached in tension or compression.

2.3.2 Design criteria for reinforced concrete

Design criteria for reinforced concrete culverts include strength limits for yielding of steel reinforcement, crushing of concrete in compression, diagonal cracking due to shear failure, and radial cracking due to curved tension steel (also called bowstringing). Finally, a performance limit on the allowable flexure crack width, typically taken as 0.01 inches, completes the set of design criteria. It is believed that the proposed design criteria faithfully represent the intent and in some cases improve the clarity of the criteria as presented in the AASHTO LRFD specifications.

Table 2.3.2-1 Reinforced Concrete Design Criteria.

Design Criterion (Strength limits)	**Demand**	**Capacity**
(1) Steel yielding (psi)	f_{max} = max steel stress	f_y = yield strength
(2) Concrete crushing (psi)	σ_{max} = max compression	f'_c = compressive strength
(3) Shear failure (lb/in)	V_{max} = max shear force	V_{ult} = concrete shear capacity
(4) Radial tension failure (psi)	t_{max} = max radial stress	t_{ult} = ultimate radial strength
(Performance Limits) (at Service Load)		
(5) Allowable crack width* (in)	CW_{max} = max crack width	CW_{Allow} = allowable CW $(0.01\,\text{inch})$

The above design criteria are equally applicable to working stress or LRFD design methodologies. For the working stress approach, the demand and the capacity quantities are unfactored, and the design evaluation is given by safety factors defined as capacity divided by demand. Typically safety factors on the order of 2.0 are desirable for strength-related criteria. For the LRFD approach the demand and the capacity quantities are factored (see Chapter 6), and the design evaluation is given by ratios of demand-to-capacity. Demand-to-capacity ratios less than or equal to 1.0 are acceptably safe. Further discussion on the design criteria is provided below.

1. *Steel yielding*. The maximum steel-stress demand is computed directly from the nonlinear reinforced concrete model. On the capacity side, the steel yield strength is an input or default value, nominally 60,000 psi for deformed bars and 65,000 psi for smooth wire fabric.

2. *Concrete crushing.* On the demand side, the maximum outer-fiber concrete compressive stress is determined directly from the reinforced concrete model as a result of thrust and compression bending. The ultimate compressive strength or capacity is an input or default value typically in the range of 4000 to 6000 psi.

3. *Shear failure*. The maximum shear-force demand is computed directly from the beam-column internal forces. Shear-force capacity is the shear force causing diagonal tension failure at a given cross-section. AASHTO

LRFD specifications prescribe three different shear-force capacities depending on structural shape and burial depth.

- For concrete pipes and arches, the shear capacity is specified by V_{max} = Equations 12.10.4.2.5, which yield variable values for shear capacity dependent on the values for moment, thrust and shear around the culvert wall.
- For boxes and 3-sided structures with 2 or more feet of soil cover, the shear capacity is specified by V_{max} = Equations 5.14.5.3-1 wherein the value is dependent on moment and shear (not thrust).
- For boxes and 3-sided structures with less than 2 feet of soil cover, the shear capacity is specified by equations in Section 5.8.3.3 that, in some cases, depend on the nature of the traverse reinforcement (stirrups).

Clearly there is a need to unify the AASHTO shear-capacity equations because rational mechanics indicates that shear capacity should be a function of the cross-section properties and state of loading, not on the culvert shape or depth of burial. CANDE allows the user to select among the three choices for shear-force capacity, however, Equation 12.10.4.2.5 is considered the best predictor of shear-force capacity because of the large experimental data base (Reference 14). CANDE also provides the option to choose the classical shear-strength method where shear-strength = $\beta\sqrt{f'_c}$, where β is a specified factor, typically = 2.0.

4. *Radial tension failure*. On the demand side, the concrete radial tensile stress is caused by tensile forces in curved inner cage reinforcement steel as it tends to straighten out and exerts radial tensile stresses on the interior concrete cover thickness. The phenomenon is sometimes called bow stringing. CANDE predicts the radial tensile stress by dividing the interior cage steel force (maximum tensile force per unit length) by the radius of curvature of the steel cage, or letting As = steel area per unit length., we have;

$$t_{max} = A_s f_{max} / \text{Radius} \qquad \text{Equation 2.3-1}$$

The ultimate radial stress is related to the tension strength of concrete and the structure span. The radial tensile strength capacity is adapted from AASHTO LRFD Equation 12.10.4.2.4c-1. and restated in psi units as:

$$t_{ult} = 37.92\sqrt{f'_c/1000}\ F_{rt} \qquad \text{Equation 2.3-2}$$

where F_{rt} is a scale factor dependent on structure span, specified in the contents of Equation 12.10.4.2.4c-1.

5. *Allowable crack width*. The allowable crack width at service loading is generally taken as 0.01 inches in accordance with AASHTO LRFD specification 12.10.3. CANDE offers three empirical formulas to predict crack width; the traditional Gergely-Lutz formula (Reference 16), the recently developed Heger-McGrath formula (Reference 15), and a simple concrete strain-based formula proposed by the author.

The Gergely-Lutz and Heger-McGrath equations are similar in form and are driven by the computed tension steel stress when it exceeds f_0 , the threshold stress for initial cracking. Their crack width predictions are concisely stated in the equation below,

$$CW = S(f_s - f_0) > 0 \qquad \text{Equation 2.3-3}$$

where, CW = the crack width in inches,
f_s = computed tension steel stress in psi,
S and f_0 = model parameters specified in the table below.

Table 2.3.2-1 Crack width model parameters S and f_0

Gergely-Lutz (Reference 16)	Heger-McGrath (Reference 15)
$S = (0.122 \times 10^{-6})(2t_b^2 s_l)^{1/3}$ where, t_b = concrete cover thickness (inches) s_l = spacing between rows of steel reinforcement (inches)	$S = (0.333 \times 10^{-6})(t_b s_l / 2n)^{1/3}$ where, t_b = concrete cover thickness (inches) s_l = spacing between rows of steel reinforcement (inches) n = number of steel reinforcement layers in the tension zone (1 or 2)
$f_0 = 5{,}000$.	$f_0 = 31.6 C_1 (h/d)^2 \sqrt{f_c'} / \rho$ where, C_1 = 1.0 for smooth wire, 1.5 for welded wire fabric, and 1.9 for deformed wire/bars. h/d = total concrete thickness –to- effective height (tension steel to other face) ρ = reinforcement area ratio (A_s/h).

The Heger-McGrath prediction is well calibrated for predicting crack widths near 0.01 inches, however it tends to underestimate the prediction of smaller crack widths. The Gergely-Lutz formula is more accurate in predicting smaller crack widths.

The concrete strain-based crack width prediction is given by,

$$CW = L_S(\varepsilon_{tension} - \varepsilon_{crack}) \qquad \text{Equation 2.3-4}$$

where, $\varepsilon_{tension}$ = computed tensile strain in outer fiber of concrete.

ε_{crack} = tensile strain at initial concrete cracking, a concrete model property.

L_S = characteristic length for crack spacing, nominally about 10 inches.

This crack width prediction is useful for fiber-reinforced and plain concrete or when there is no tension steel to drive the Heger-McGrath or Gergely-Lutz crack width predictions.

2.3.3 Nonlinear model for reinforced concrete

Concrete model. The concrete constitutive model was originally developed in References 3 and 17. As shown in Figure 2.3.3-1, the model for plain concrete is a tri-linear curve in compression and an abrupt tension rupture at initial tension cracking.

Figure 2.3.3-1 Concrete stress-strain model and parameters.

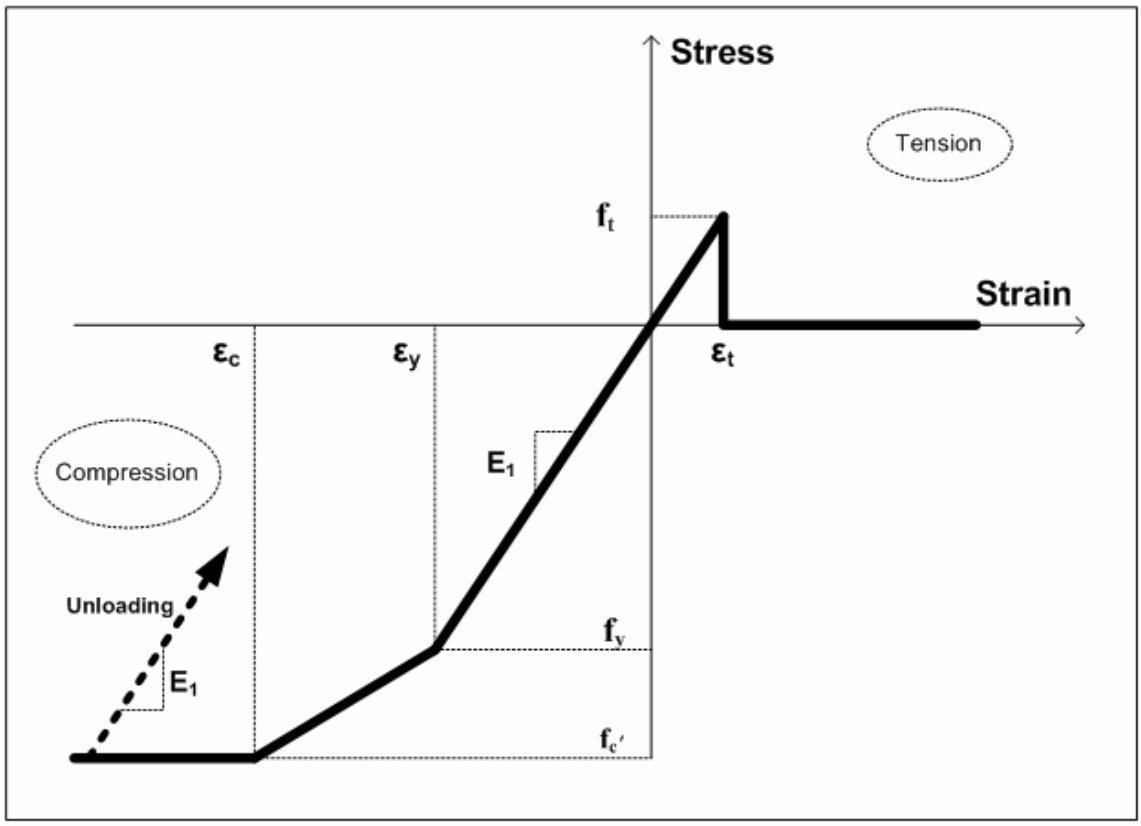

Primary model input parameters are defined below along with typical values shown in parenthesis

ε_t = concrete strain at initial tensile cracking (0.0001 in/in)

ε_y = concrete strain at initial elastic limit in compression (0.0006 in/in)

ε_c = concrete strain at onset of unconfined compressive strength (0.002 in/in)

f_c' = unconfined compressive strength of concrete (4,000 psi)

E_1 = Young's modulus of concrete in linear zone (3,800,000 psi)

Using the above input variables, three additional parameters are derived as follows:

$E_2 = (f_c' - E_1 \varepsilon_y) / (\varepsilon_c' - \varepsilon_y)$ = Young's modulus in compression yielding zone

$f_{yc} = E_1 \varepsilon_y$ = compressive stress at initial yielding (2,000 psi)

$f_t = E_1 \varepsilon_t$ = tensile strength at initial cracking and rupture (380 psi)

The following material constants are used for plane strain conditions:

$E_e = E_1/(1-\nu_c^2)$ = effective plane strain modulus of concrete in elastic zone

ν_c = Poisson ratio for concrete

$r = E_2/E_1$ = ratio of compression yielding modulus to initial modulus

$r E_e$ = effective plane strain modulus for compression yielding zone.

The above model has the following behavior characteristics. In tension, the concrete is linear until the initial tensile strain exceeds the cracking strain limit ε_t. When cracking occurs, the tensile stress becomes abruptly zero (redistributed to non-cracked portions of concrete). Once a point in the cross section is cracked, the crack is assumed not to heal so that there is no future tensile strength. Thus after initial cracking, the tensile strength parameter f_t is set to zero for all subsequent reloading in tension.

For initial compression loading, the concrete behaves linearly until the stress level reaches the initial yield strength f_{yc} after which plastic hardening begins to occur in the yield zone. Perfect plasticity occurs when the stress level reaches compressive strength f_c'. Unloading is elastic and with permanent plastic strain, and reloading is elastic until the stress reaches its previous maximum value after which it follows the original stress-strain curve.

Steel model. The assumed stress-strain behavior for reinforcing steel is shown in Figure 2.3.3-2.

Figure 2.3.3-2 Stress-strain model for reinforcing steel.

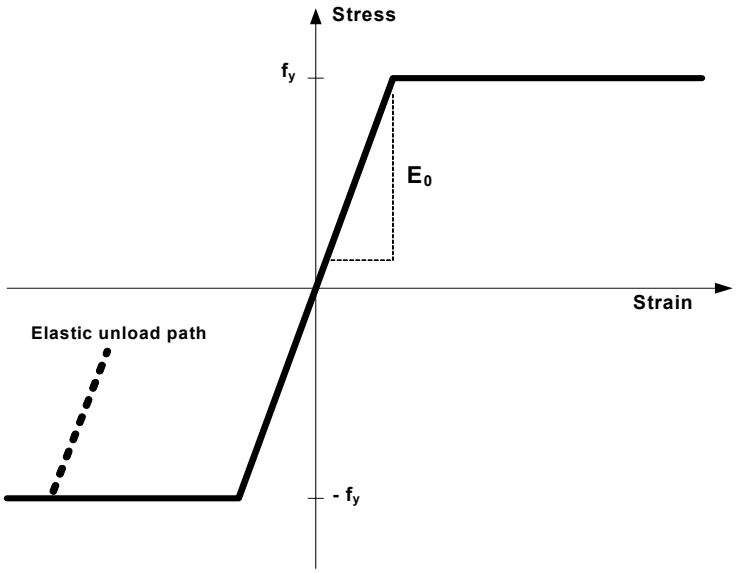

Steel behavior is assumed to be elastic-perfectly plastic defined by the input variables:

E_0 = Young's modulus for steel

f_y = steel yield strength

Behavior in compression and tension is identical so that material is elastic whenever the stress magnitude is less than the yield strength. Non-hardening plastic flow occurs when the stress attempts to exceed the yield strength. Unloading from the plastic range is elastic and results in permanent plastic strains.

For the purposes of a plane-strain formulation, the steel modulus is denoted as;

$E_s = E_0/(1-\upsilon_s^2)$ = effective plane-strain modulus of steel

υ_s = Poisson ratio for steel

Section geometry. Figure 2.3.3-3 shows a unit width of concrete wall with steel reinforcement located near the inner face (bottom) and the outer face (top).

Figure 2.3.3-3 Section geometry of reinforced concrete wall

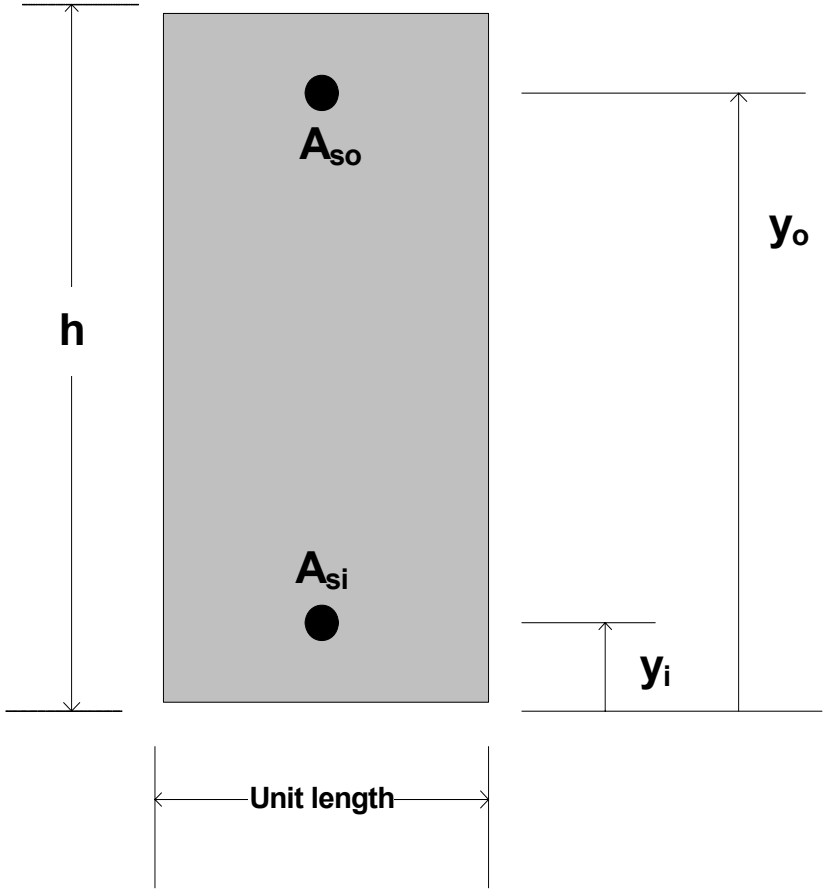

Geometric measures of the reinforced concrete section are defined below:

h = concrete wall thickness

A_{si} = area of steel for inner cage per unit length of wall

A_{so} = area of steel for outer cage per unit length of wall

y_i = distance to centroid of A_{si} from bottom face

y_o = distance to centroid of A_{so} from bottom face

The uncracked, transformed, elastic section properties are computed as,

$$EA^* = E_e(h + (n-1)(A_{si}+A_{so})) \quad \text{Equation 2.3.3-1}$$

$$y^* = (h^2/2 + (n-1)(y_i A_{si} + y_o A_{so}))/A^* \quad \text{Equation 2.3.3-2}$$

$$EI^* = E_e[h^3/12 + h(h/2-y^*)^2 + (n-1)(A_{si}(y_i-y^*)^2 + A_{so}(y_o-y^*)^2)] \quad \text{Equation 2.3.3-3}$$

where, $n = E_s/E_e$ = ratio of steel modulus to concrete modulus (transform method).

The uncracked, transformed elastic section properties are used for the first iteration of the first load step to obtain a trial solution. If the loading does not cause cracking, concrete yielding or steel yielding, then the section properties as currently computed are correct, and the next load step is considered. More generally however, nonlinear responses are observed and iteration within the load step is required to obtain the solution as described next.

Nonlinear Strategy. We assume we have a converged solution at load step i and we seek an incremental solution for load step i +1. Using the values of EA*, y* and EI* from the previous load step, a trial solution is obtained for the first iteration thereby providing new estimates of the strain distribution at each reinforced concrete cross-section. To compute the next estimate for EA*, y* and EI*, numerical integration is used over the concrete wall section to cope with nonlinear chord modulus as illustrated in the figure below.

Figure 2.3.3-4 Strain profile from step i to i+1 and 11-point Simpson integration

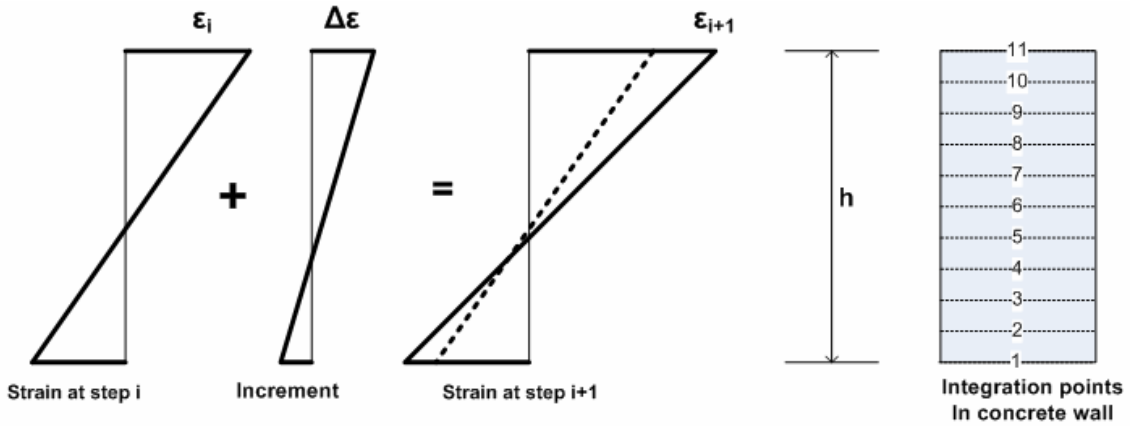

Concrete chord modulus. The effective chord modulus, E', from the known stress-strain state (σ_i, ε_i) to the estimated stress-strain state (σ_{i+1} , ε_{i+1}) is computed at each integration point using the concrete stress-strain curve as indicated in Figure 2.3.3-5 and quantified in Table 2.3.3-1.

Figure 2.3.3-5 Illustration of concrete chord moduli from σ_i, ε_i to σ_{i+1} , ε_{i+1}

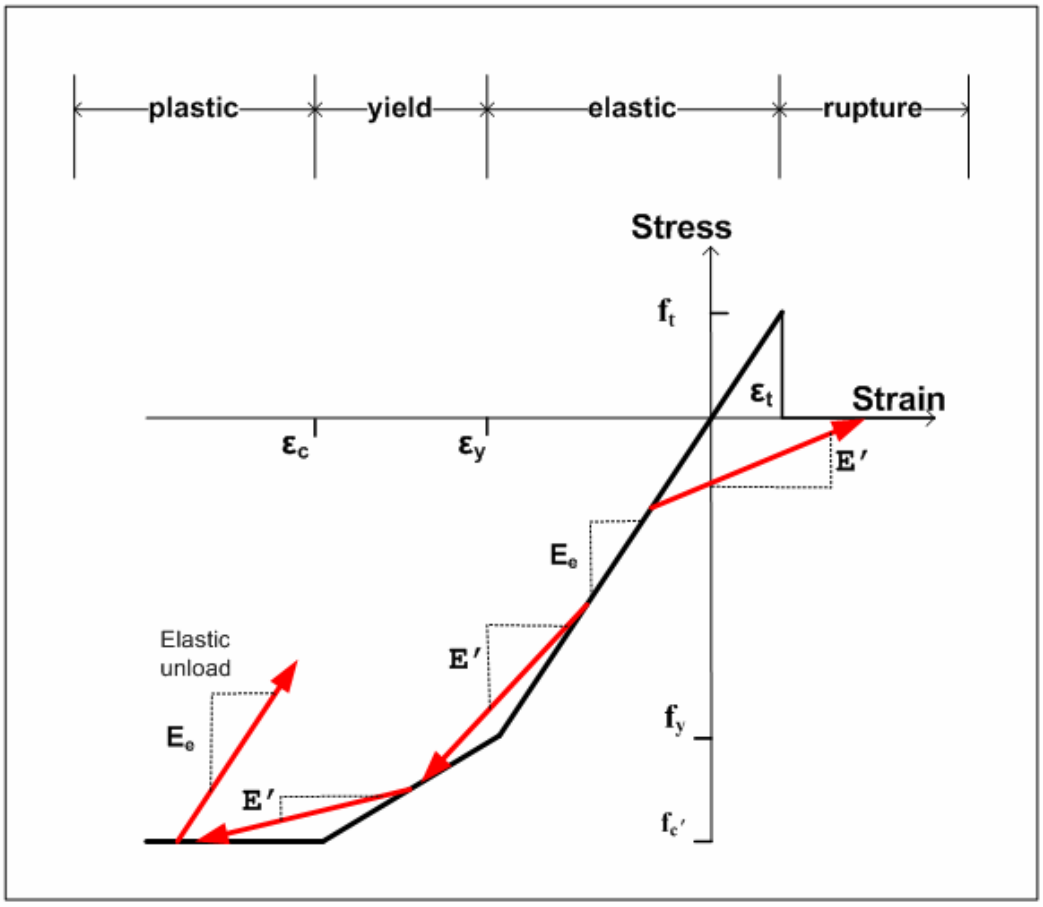

The above figure implies the chord modulus, E', connects the known starting point (σ_i ε_i,) to the estimated end point (σ_{i+1}, ε_{i+1}) where ε_{i+1} is obtained from the trial solution and σ_{i+1} is the corresponding stress determined from the stress-strain relationship as quantified in the table below.

Table 2.3.3-1. Concrete chord modulus and modulus ratio for specified starting and ending zones.

Starting Zone ε_i	Ending Zone ε_{i+1}	Corresponding Stress σ_{i+1}	Chord modulus E'	Modulus ratio $F'(y) = E'/ E_e$
elastic	elastic	$\sigma_i + E_e\Delta\varepsilon$	E_e	1.0
elastic	yield	$\sigma_i + rE_e(\varepsilon_{i+1} - \varepsilon_y)$	$rE_e(\varepsilon_{i+1} - \varepsilon_y)/ \Delta\varepsilon$	< 1.0
elastic	plastic	f_c'	$(f_c' - \sigma_i)/ \Delta\varepsilon$	< 1.0
yield	yield	$\sigma_i + rE_e\Delta\varepsilon$	rE_e	r
yield	plastic	f_c'	$(f_c' - \sigma_i)/ \Delta\varepsilon$	< 1.0
plastic	plastic	f_c'	0.0	0.0
any compress zone	unloading	$\sigma_i + E_e\Delta\varepsilon$	E_e	1.0
elastic	rupture	0.0	$- \sigma_i/ \Delta\varepsilon$	< 1.0
rupture	rupture	0.0	0.0	0.0

In the above table, the concrete-modulus ratio is defined as the chord modulus divided by the initial elastic modulus, $F'(y) = E'/ E_e$. Thus, F' varies through the cross-section in the range, $0 \le F'(y) \le 1$.

Elastic unloading occurs from any compression zone whenever $|\varepsilon_{i+1}| < |\varepsilon_i|$ with the provision that neither strain is in the rupture zone.

For the case when the starting strain is tensile but not yet at initial crack strength, $0 < \varepsilon_i < \varepsilon_t$, and the ending strain is in the rupture zone causing initial concrete cracking, we set E' = 0 (instead of a negative softening modulus) and the pre-existing tensile stress is distributed to the uncracked portion of the cross section by adjusting the thrust and moment increment to compensate for the loss of stress at the cracked location. Once a point in the cross section is cracked the tensile strength is set to zero for all future loading conditions implying the crack does not heal. Crack depth is directly predicted from the concrete model.

The above algorithm requires maintaining data records at each integration point to keep track of the cracking history as well as the maximum compressive stress encountered during the loading schedule to properly simulate unloading and reloading.

Steel chord modulus. Reinforcing steel is lumped at the inner and outer cage locations, measured by y_i and y_o. The chord modulus for steel at either location is easily deduced from the elastic-plastic relationship as shown in the following table.

Table 2.3.3-2. Steel chord modulus and modulus ratio for specified starting and ending zones.

Starting Zone ε_i	Ending Zone ε_{i+1}	Corresponding Stress σ_{i+1}	Chord modulus E_s'	Modulus ratio $W' = E_s'/E_s$
elastic	elastic	$\sigma_i + E_s\Delta\varepsilon$	E_s	1.0
elastic	plastic	f_y	$(f_y - \sigma_i)/\Delta\varepsilon$	< 1.0
plastic	plastic	f_y	0.0	0.0
unloading	elastic	$\sigma_i + E_s\Delta\varepsilon$	E_e	1.0

In the above table, the steel-modulus ratio is defined as the chord modulus divided by the initial elastic steel modulus, $W' = E_s'/E_s$, where the ratio is in the range, $0 \le W' \le 1$.

To summarize, the relationships for chord moduli of concrete and steel are listed below:

$$E'(y) = E_e F'(y) \quad \text{= concrete chord modulus at location y in cross section} \qquad \text{Equation 2.3.3-4}$$

$$E'_{si} = E_s W'_i \quad \text{= steel chord modulus at inner cage location, } y_i. \qquad \text{Equation 2.3.3-5}$$

$$E'_{so} = E_s W'_o \quad \text{= steel chord modulus at outer cage location, } y_o. \qquad \text{Equation 2.3.3-6}$$

Re-expressing the steel chord moduli with concrete-transform parameters, we have

$$E'_{si} = n_i E_e W'_i \qquad \text{Equation 2.3.3-7}$$

$$E'_{so} = n_o E_e W'_o \qquad \text{Equation 2.3.3-8}$$

where, $n_i,\ n_o = E_s/E_e - 1,$ if concrete is not cracked around the steel

$n_i,\ n_o = E_s/E_e,$ if concrete is cracked around the steel

The transform method expresses the elastic steel modulus as a multiple "n" of the concrete elastic modulus with the understanding that the uncracked concrete area needs to be reduced by the steel area. On the other hand, if the concrete is already cracked then further reduction of concrete area by the steel area is not required.

Key section properties. The equations for the key section properties are expressed in transformed parameters as:

$$EA^* = E_e\left(\int_0^h F'(y)dy + n_i W_i A_{si} + n_o W_o A_{so}\right) \quad \text{Equation 2.3.3-9}$$

$$y^* = \left(\int_0^h F'(y)ydy + n_i W_i A_{si} y_i + n_o W_o A_{so} y_o\right)/A^* \quad \text{Equation 2.3.3-10}$$

$$EI^* = E_e\left(\int_0^h F'(y)(y-y^*)^2 dy + n_i W_i A_{si}(y_i - y^*)^2 + n_o W_o A_{so}(y_0 - y^*)^2\right) \quad \text{Equation 2.3.3-11}$$

The integrals over the concrete wall thickness is achieved with 11-point Simpson integration to evaluate the following three sums where $F'(y_i)$ is the concrete modulus ratio at integration point i.

$$S_1 = \int_0^h F'(y)dy = h/30[F'(y_1)+4F'(y_2)+2F'(y_3)+...+F'(y_{11})] \quad \text{Equation 2.3.3-12}$$

$$S_2 = \int_0^h F'(y)ydy = h/30[F'(y_1)y_1+4F'(y_2)y_2+2F'(y_3)y_3+...+F'(y_{11})y_{11}] \quad \text{Equation 2.3.3-13}$$

$$S_3 = \int_0^h F'(y)y^2dy = h/30[F'(y_1)y_1^2+4F'(y_2)y_2^2+2F'(y_3)y_3^2+...+F'(y_{11})y_{11}^2] \quad \text{Equation 2.3.3-14}$$

Using the above integration results, the final results for the key section properties are expressed as,

$$EA^* = E_e(S_1 + n_i W_i A_{si} + n_o W_o A_{so}) \quad \text{Equation 2.3.3-15}$$

$$y^* = (S_2 + n_i W_i A_{si} y_i + n_o W_o A_{so} y_o)/A^* \quad \text{Equation 2.3.3-16}$$

$$EI^* = E_e(y^{*2}S_1 - 2y^*S_2 + S_3 + n_i W_i A_{si}(y_i - y^*)^2 + n_o W_o A_{so}(y_0 - y^*)^2) \quad \text{Equation 2.3.3-17}$$

Iterations with in the load step continue until successive calculations for EA*, y* and EI* are within 1% relative error for all cross section..

2.4 Thermoplastic Pipe

2.4.1 Overview of thermoplastic pipe type

Thermoplastic materials include high-density polyethylene (HDPE), polyvinyl chloride (PVC) and polypropylene (PP). CANDE-2007 provides three options to characterize the wall sections for thermoplastic pipe: smooth, general or profile. Smooth refers to a uniform wall (gun barrel) whose cross-section properties are completely defined by the wall thickness. General refers to an arbitrary properties described generically by the wall's area and moment of inertia per unit length. Profile refers to the majority of manufactured plastic pipe whose wall section properties are characterized by the geometry of profile elements including web, valley, crest, liner, and link elements.

Material properties are assumed linear elastic with default values provided for high-density polyethylene, polyvinyl chloride and polypropylene for both short-term and long-term loading conditions. Short-term properties are generally used when vehicular loading is dominant and long-term properties are used when earth loading is dominant. A nonlinear local buckling algorithm is provided for the profile option wherein the profile's section properties are reduced in proportion to the amount of compressive strain computed in the sub elements due to local buckling.

2.4.2 Design criteria for thermoplastic pipe

Design criteria for thermoplastic pipes include strength limits for thrust stress against material failure in hoop compression and global buckling. Another strength state is a limit on the maximum outer fiber combined strain (hoop plus bending strain). Performance limit states include allowable vertical deflection and maximum allowable tensile strain, dependent on type of plastic. The design criteria are summarized in the following table.

Table 2.4.2-1 Thermoplastic Design Criteria.

Design Criterion (Strength limits)	**Demand**	**Capacity**
(1) Thrust stress (psi)	$\sigma_{max} = N_{max}/A$	f_u = ultimate strength
(2) Global Buckling (psi)	$\sigma_{max} = N_{max}/A$	f_b = buckling capacity
(3) Combined strain (in/in)	ε_{max} = bending + thrust	ε_{ult} = ultimate strain
(Performance Limits) (at Service Load)		
(4) Allowable tensile strain	$\varepsilon_{t\text{-}max}$ =max tensile strain	$\varepsilon_{t\text{-}allow}$ = allowable tensile strain
(5) Allowable deflection *(%)	Δ_{max} = computed deflect %	Allowable = 5% (recommended)

The above design criteria are equally applicable to working stress or LRFD design methodologies. For the working stress approach, the demand and the capacity quantities are unfactored, and the design evaluation is given by safety factors defined as capacity divided by demand. Typically safety factors on the order of 2.0 are desirable for strength-related criteria. For the LRFD approach the demand and the capacity quantities are factored (see Chapter 6), and the design evaluation is given by ratios of factored demand-to-factored capacity. Ratios less than or equal to 1.0 are acceptably safe. Further discussion on the design criteria is provided below.

1. *Thrust stress*. Thrust-stress demand is computed by the dividing the maximum thrust force in the culvert by the cross-sectional area. The ultimate strength for thrust stress is dependent on the type plastic and the load duration. Nominal values, taken from the ASSHTO LRFD specifications and elsewhere, are shown in the table below.

Table 2.4.2-2 Recommended plastic properties for short and long-term loading

Type of plastic	Effective Young's Modulus (PE)		Ultimate strength (PU)	
	Short-term (ksi)	Long-term (ksi)	Short-term (ksi)	Long-term (ksi)
HDPE –	110.0	22.0	3.00	0.90
PVC –	400.0	140.0	6.00	2.60
PP –	135.0	27.0	3.10	1.00

2. *Global buckling*. The thrust stress level that causes global buckling may be conservatively approximated from the simplified AASHTO LRFD equations 12.7.2.4-1-2. A more accurate alternative is to utilize the new large deformation formulation with buckling capacity prediction available in CANDE-2007 (see Chapter 5).

3. *Combined strain*. Combined strain means the maximum outer-fiber strain from thrust and bending and the demand is the largest combined strain anywhere in the culvert. The combined strain limit value (or capacity) as recommended by AASHTO LRFD specifications is equal to 1.5 times the long-term strength divided by the long-term modulus. Accordingly, HDPE = 0.06 in/in, PVC = 0.028 in/in. and PP = 0.045 in/in.

4. *Allowable tensile strain*. This criterion is intended to preclude cracking and crazing under service load due the maximum outer-fiber tensile strain. The allowable tensile strain as recommended by AASHTO LRFD specifications is 0.05 in/in for HDPE and 0.035 or 0.05 in/in for PVC depending on cell class.

5. *Allowable deflection*. Computed deflection is the relative vertical movement between the top and bottom of the culvert structure, and the percent deflection is relative the vertical distance. The service load value for allowable deflection is generally taken as 5% of the diameter for all plastic pipes; however, the deflection limit is not directly specified in the AASHTO LRFD design specifications.

Local Buckling. Local buckling is not a direct design criterion for plastic pipe, but it does influence the demands and capacities of the design criteria listed above. Similar to corrugated metal pipe wherein some amount of outer fiber yielding is permitted, some amount of local buckling is permitted in plastic profile pipe. The nonlinear model to account for local buckling in profile plastic pipe is presented next.

2.4.3 Nonlinear model for local buckling in profile plastic pipe

Although the stress-strain models for all thermoplastic pipe materials are assumed linear and characterized by the elastic moduli in the above table, local buckling is a nonlinear phenomenon. Local buckling is caused by compressive strains that induce the elements of profile wall pipe to deform out-of-plane in a wrinkled pattern. Section 12.12.3.5.3 of AASHTO LRFD specifications provides a methodology to simulate the effect of local buckling by reducing the effective area of the profile elements dependent upon the average level of compressive strain in each element. This AASHTO methodology is incorporated into CANDE-2007 as described below.

The geometry of the profile wall is defined with two web elements and up to four horizontal elements (valley, liner, crest and link) as shown in the figure below.

Figure 2.4.3-1 Profile wall geometry and sub elements

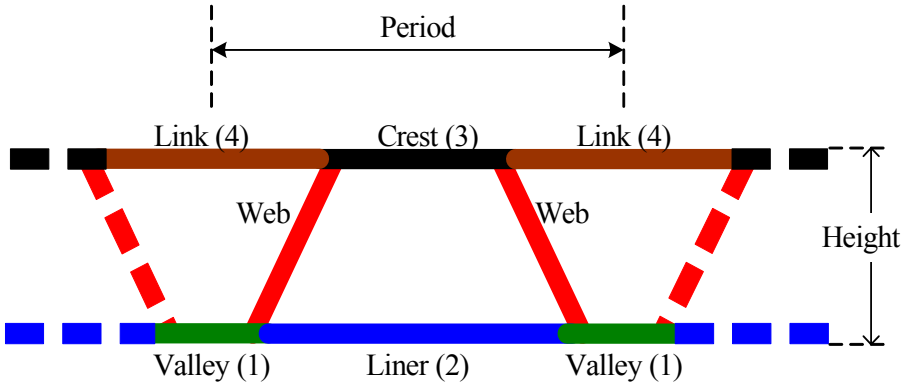

The web element lengths, which form a mirror symmetric pair within each period, are defined to span the distance between the valley and crest element so that the web elements offer support to the ends of the crest and valley elements. Hence, the defined length of the crest element is the unsupported span between the web supports plus the length of the web supports, taken as twice the web thickness. Similarly, the defined length of the valley element is twice the web thickness plus the unsupported valley span between the web supports. The defined length of the liner element is the horizontal distance between two valley elements so that the liner's defined length and unsupported length are identical. Similarly, the defined length of the link element is the horizontal distance between two crest elements so that the crest's defined length and unsupported length are identical.

Given the defined lengths and thicknesses of all elements, the angle of the web elements, and the overall height of the profile wall, it is a straightforward matter to calculate the initial section properties of the profile wall. The area per unit length, A*, is equal to the sum of all element areas (lengths multiplied by thickness) divided by the period length. The wall centroid, y*, is the first area moment taken about the bottom fiber divided by the area. And finally, the moment inertia per unit length , I*, is the second area moment taken about y* divided by the period length. Thus in the absence of local buckling, the beam-column section properties are initially known for the first iteration of the first load step to provide the first trial solution.

The AASHTO LRFD methodology, which accounts for local buckling by reducing the effective length of the elements due to compressive strain, is achieved by using the following two equations.

$$\lambda = (w/t)\sqrt{(\varepsilon/k)} \;>\; 0.673 \qquad \text{Equation 2.4-1}$$

where, λ = measure of propensity to buckle, called slenderness ratio
w = unsupported length of element
t = thickness of element
ε = average compressive strain in element
k = edge support coefficient (typically taken as 4.0 for fix-ended elements)

$$\rho = (1/\lambda)(1 - 0.22/\lambda) \;<\; 1.0 \qquad \text{Equation 2.4-2}$$

where, ρ = reduction factor applied to w
ρw = remaining unsupported length of element

Each profile element (web, valley, liner, crest and link) is evaluated with above equations. Equation 2.4-1 is evaluated to compute λ using the predicted compressive strain at each element's centroid as determined from the trial solution. If

$\lambda < 0.673$, then the compressive strain is not large enough to trigger local buckling for the element under consideration so that ρ remains = 1. Otherwise if $\lambda > 0.673$, we evaluate Equation 2.4.2 producing a value for ρ less than 1.0 wherein ρ is the fraction of the element's unsupported length that remains effective in the cross section. Note that the total effective length for the crest and valley elements also includes the web support thicknesses. The element length measures are clarified in the table below:

Table 2.4.3-1 Local buckling profile dimensions

Element length measures	**Symbol**	**Derivation**	**Description**
Defined length	L	Defined by user (input)	The actual length of the element
Unsupported length	w	$w = L$, (for web, liner and link) $w = L - 2t_{web}$, (for crest & valley)	The free distance between supports where buckling can occur
Effective length	L_{eff}	$L_{eff} = \rho L$, (for web, liner and link) $L_{eff} = \rho w + 2t_{web}$, (for crest & valley)	The effective remaining length of element after local buckling

Since the central portion of each element is the most prone to local buckling damage, we assume the original element length has effective gap length equal to $L - L_{eff}$ located in the central portion of the element. This assumption is needed to compute the effective moment of inertia.

Once the effective lengths of the elements have been determined and the location of the gaps understood, it is, once again, a straightforward matter to calculate the new section properties for the next trial solution as;
A* = Sum of all effective element areas (effective lengths times thicknesses)
y* = Centroid of A* measured from bottom fiber
I* = Sum of all effective element moment of inertias about y*

The above process dovetails with the general nonlinear solution strategy described in Section 2.19 by forming EA* and EI* where E is the appropriate linear elastic modulus (Table 2.4.2-2). When two successive trial solutions produce the same compressive stain values within a 0.1% tolerance level for all elements at all nodes, the load step is said to converge and we proceed to the next load step.

2.5 Basic Pipe Type

The so-called basic pipe-type is not associated with any particular pipe material. Therefore, it is restricted to linear material behavior, and it is not associated with any design criteria for evaluating its safety or performance. The material model is defined by an elastic Young's modulus and Poisson's ratio, and the cross-sectional properties are defined an area and moment of inertia.

If desired, each element in the basic pipe-type group may be assigned different elastic and cross-sectional properties, and the element group has the option to include large deformation theory and buckling capacity predictions. In addition to academic studies, the basic pipe-type groups are useful for modeling struts and braces and discrete reinforcement in the soil mass.

Lastly, if it is desired to use only continuum elements without beam-column elements in particular problem in the CANDE-2007 program, the basic pipe type is declared in the input with zero elements assigned to the group.

(This page intentionally left blank)

3 SOIL MODELS

Soil models, or constitutive forms, define a relationship between stress and strain based on phenomenological observations of material behavior at the macroscopic level. The term soil model and constitutive form are used interchangeably throughout this chapter. CANDE-2007 offers the following suite of soil models; isotropic elastic, orthotropic elastic, overburden dependent, Duncan and Duncan/Selig, and extended Hardin. The common feature of these models, which have proven effective in simulating the soil layers in culvert installations, is that the models are based on elastic-like or variable modulus constitutive forms as opposed to plasticity based constitutive forms.

Each of the soil models is discussed in subsequent sections. However in order to properly set the stage, we first discuss the basic formulation of the continuum elements in which the soil models are contained.

3.1 Continuum Elements

Plane-strain continuum elements are used to represent the soil zones in the soil-structure system. Two continuum element shapes are available in CANDE, triangular and quadrilateral. Both element shapes utilize identical interpolation functions and are classified as non-conforming elements. These elements, developed by Herrmann in Reference 11, have superior qualities in all basic deformation modes and out perform the well-known linear strain triangle and eight-node isoperimetric quadrilateral, respectively. For example, one row of CANDE's quadrilateral elements is capable of properly replicating beam-bending behavior.

3.1.1 Triangle elements

The triangular element, shown below, employs area coordinates (the natural coordinate system for triangles) to define interpolation functions for the x-displacement function u(x,y) based on 3-external nodal degrees of freedom at the triangle vertices and 3-internal element degrees of freedom. Similarly, the y-displacement function v(x,y) is based on 3-external and 3-internal degrees of freedom.

Figure 3.1.1-1. Characteristics of triangular continuum element

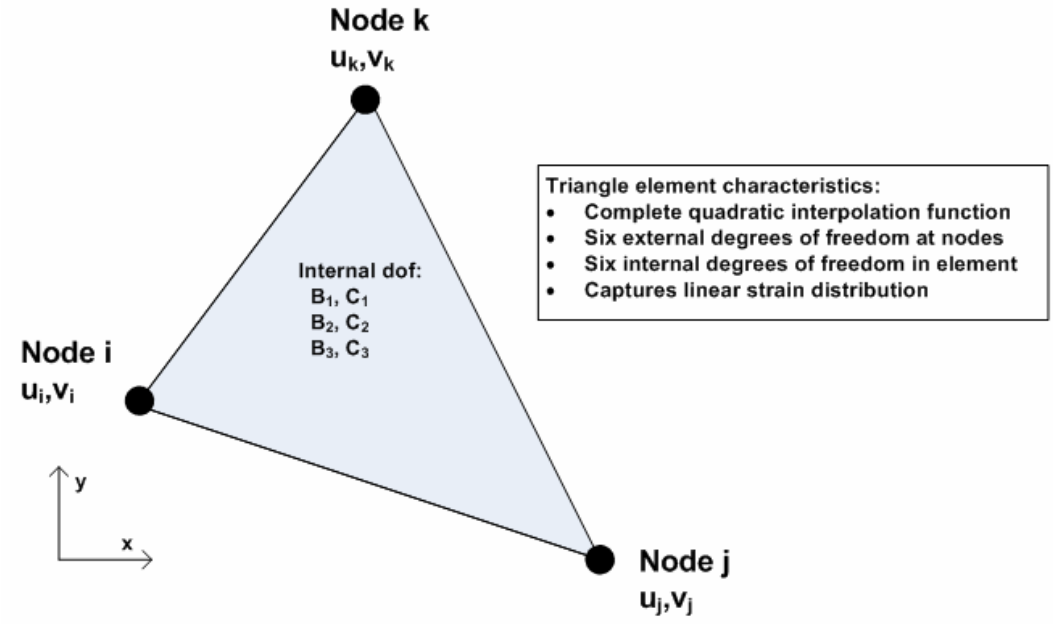

Linear interpolation functions are used for the external nodal degrees of freedom, which by themselves are equivalent to a constant strain triangle. Superimposed on the linear displacement functions are complete quadratic interpolation

functions associated with internal degrees of freedom within the element. Constraint equations are applied to the internal degrees of freedom so that the element is convergent when the element size approaches zero and passes the patch test. The internal degrees of freedom are statically condensed at the element level resulting in a 6x6 element stiffness matrix and a 6x1 body-load vector associated with the external degrees of freedom, and ready for global assembly.

3.1.2 Quadrilateral elements

As shown in the figure below, the quadrilateral element is composed of two triangles wherein the x-displacement function u(x,y) is based on 4-external nodal degrees of freedom at the vertices and 6-internal degrees of freedom within the element. Similarly, the y-displacement function v(x,y) is based on 4-external and 6-internal degrees of freedom.

Figure 3.1.2-1. Characteristics of quadrilateral continuum element

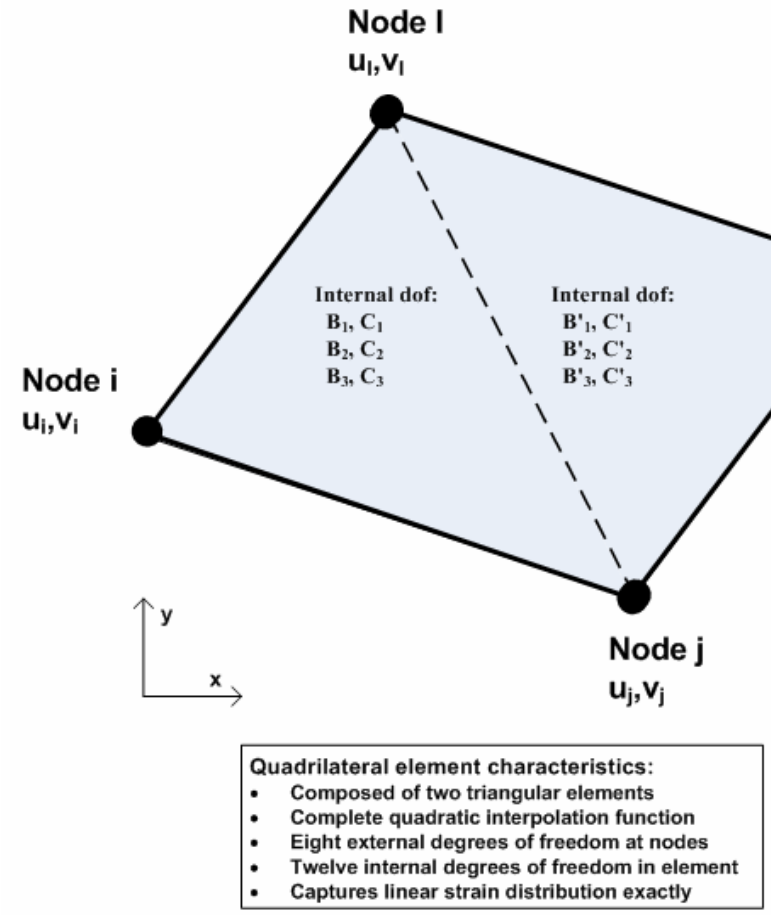

To insure that the quadrilateral element is convergent and passes the patch test, the influence of the internal degrees of freedom must approach zero as the element becomes vanishingly small. This requirement places three constraints on the twelve internal degrees of freedom, resulting in nine internal degrees of freedom. The nine internal degrees of freedom are statically condensed at the element level resulting in an 8x8 element stiffness matrix and an 8x1 body-load vector associated with the external degrees of freedom, and ready for global assembly.

3.1.3 Finite element development

Interpolation functional forms. The interpolation functions used for triangle and quadrilateral elements may be generically expressed using the notation presented in Chapter 1 as,

$$\Delta u_e = N\Delta\hat{u}_e \qquad \text{Equation 3.1-1}$$

$$\Delta v_e = N\Delta\hat{v}_e \qquad \text{Equation 3.1-2}$$

where, Δu_e, Δv_e = displacement functions for x- and y-directions in triangle or quadrilateral element.

$\Delta\hat{u}_e$, $\Delta\hat{v}_e$ = column-vector of degrees-of-freedom for x and y displacement functions in element.

N = row-vector of interpolation functions in area coordinates, also expressible in x and y variables.

Of course, the length of the interpolation row-vector is larger for the quadrilateral element than for the triangle element, as are also the lengths of the degree-of-freedom column-vector.

Strain-displacement relationship. Small strain and small deformation theory are used for all continuum elements. Accordingly, the strain components for plane strain are given by the partial derivatives of the displacement functions as expressed in the matrix relationship below,

$$\begin{pmatrix} \Delta\varepsilon_x \\ \Delta\varepsilon_y \\ \Delta\gamma \end{pmatrix} = \begin{pmatrix} N,x & 0 \\ 0 & N,y \\ N,y & N,x \end{pmatrix} \begin{pmatrix} \Delta\hat{u}_e \\ \Delta\hat{v}_e \end{pmatrix} \qquad \text{Equation 3.1-3}$$

where, $\Delta\varepsilon_x$, $\Delta\varepsilon_y$, $\Delta\gamma$ = strain increments for x-direction, y-direction and shear components, respectively.

N,x & N,y = partial derivatives of interpolation functions in the row vector with respect to x and y.

Stress-strain relationship. All soil models conform to a general constitutive form relating increments of stress to increments of strain via a matrix of variable coefficients dependent on the stress-stain state at step i and step i+1 as indicated below,

$$\begin{pmatrix} \Delta\sigma_x \\ \Delta\sigma_y \\ \Delta\tau \end{pmatrix} = \begin{pmatrix} C_{11} & C_{12} & C_{13} \\ C_{21} & C_{22} & C_{23} \\ C_{31} & C_{32} & C_{33} \end{pmatrix} \begin{pmatrix} \Delta\varepsilon_x \\ \Delta\varepsilon_y \\ \Delta\gamma \end{pmatrix} \qquad \text{Equation 3.1-4}$$

where, $\Delta\sigma_x$, $\Delta\sigma_y$, $\Delta\tau$ = stress increments for x-direction, y-direction and shear components, respectively.

C_{ij} = variable coefficients generally dependent on current stress and strain state.

Components of the constitutive matrix are symmetric ($C_{ij} = C_{ji}$) and are explicitly defined for each soil model in subsequent sections.

Element stiffness matrix. Using the above relationships, the element stiffness for the triangle or quadrilateral is obtained by integrating the following matrix products,

$$\underline{k}_e = \int_A \begin{pmatrix} N,x & 0 \\ 0 & N,y \\ N,y & N,x \end{pmatrix}^T \begin{pmatrix} C_{11} & C_{12} & C_{13} \\ C_{21} & C_{22} & C_{23} \\ C_{31} & C_{32} & C_{33} \end{pmatrix} \begin{pmatrix} N,x & 0 \\ 0 & N,y \\ N,y & N,x \end{pmatrix} dA \qquad \text{Equation 3.1-5}$$

Integration of the interpolation functions is performed exactly using area coordinates whereas the components of the constitutive matrix are taken as constant within the element based on the stress-strain state at the center of the element. After the internal degrees of freedom are statically condensated from the element, the element stiffness for the triangle element is a 6x6 matrix associated with the 6-external degrees of freedom, two per node. The quadrilateral element stiffness is an 8x8 matrix, associated with the 8-external degrees of freedom, two per node.

3.2 Isotropic Linear Elastic

The linear elastic soil model in isotropic form is the simplest soil model. Linear elastic implies the soil stiffness remains constant irrespective of the stress state, and isotropic implies the soil stiffness is uniform in all spatial directions. The model is useful for characterizing stiff in-situ soils and pre-consolidated soils such as the soil remaining after excavation. Moreover when the exact character of the soil is not well known, the linear-elastic isotropic soil model is useful for parametric studies and/or to conservatively represent soil stiffness with modest moduli values.

The isotropic form of the elastic constitutive matrix is expressed by the following incremental stress-strain relationship,

$$\begin{pmatrix} \Delta\sigma_x \\ \Delta\sigma_y \\ \Delta\tau \end{pmatrix} = \begin{pmatrix} C_{11} & C_{12} & 0 \\ C_{12} & C_{11} & 0 \\ 0 & 0 & C_{33} \end{pmatrix} \begin{pmatrix} \Delta\varepsilon_x \\ \Delta\varepsilon_y \\ \Delta\gamma \end{pmatrix} \qquad \text{Equation 3.2-1}$$

where, C_{11}, C_{12} and C_{33} are material constants defined by two elastic parameters. In the above matrix, the C_{22} coefficient is identified as C_{11} to emphasize they are identical in value for the isotropic case.

In CANDE, the elastic parameters used to characterize C_{11}, C_{12} and C_{33} are Young's modulus and Poisson ratio as shown in the second column of Table 3.2-1. The exact equivalent using other pairs of elastic parameters are shown in the third column for the confined modulus and lateral coefficient, and in the fourth columns for the bulk modulus and shear modulus.

Table 3.2-1 Components for constitutive matrix defined by elastic parameters

Components of Constitutive matrix	Elastic parameter equivalent pairs		
	E = Young's modulus ν = Poisson ratio (E, ν)	**M_s = confined modulus K_0 = lateral coefficient (M_s, K_0)**	**B = bulk modulus G = shear modulus (B, G)**
C_{11} =	$E(1-\nu) / (1+\nu)(1-2\nu)$	M_s	$B + (4/3)G$
C_{12} =	$E\nu / (1+\nu)(1-2\nu)$	$M_s K_0$	$B - (2/3)G$
C_{33} =	$E / 2(1+\nu)$	$M_s (1-K_0)/2$	G

The inference in the above table is that if any two elastic pairs are known, they may be equivalently expressed with any other elastic pairs using the above relationships.

Depending on the soil quality and compaction, representative ranges of Young's modulus and Poisson ratio are shown in Table 3.2-2 for three broad classes of soil.

Table 3.2-3 Representative ranges of Young's modulus and Poisson ratio

Soil type	Elastic parameters, nominal range	
	Young's modulus, E psi	**Poisson ratio, ν (-)**
Granular	600 to 2000	0.30 to 0.35
Mixed	400 to 1400	0.30 to 0.40
Cohesive	200 to 400	0.33 to 0.40

Well-compacted soils are characterized by the high-range values of Young's modulus, whereas poorly compacted soils are characterized by the low-range values.

3.3 Orthotropic Linear Elastic

Like the isotropic model above, the linear-elastic designation means the stiffness of the orthotropic model remains constant irrespective of the stress state. However unlike the uniform isotropic model, the stiffness of the orthotropic model may be different in one direction, say x', than it is an orthogonal direction say, y'. Some stratified sedimentary soil deposits exhibit orthotropic properties, but this is rather rare in culvert installations. A more common occurrence of orthotropic stiffness is due to man-made inclusions in soils such as reinforced earth and geo-textile fabrics.

The orthotropic form of the elastic constitutive matrix is expressed by the following incremental stress-strain relationship wherein the x-y coordinate system is assumed to be aligned with the principal material axis.

$$\begin{pmatrix} \Delta\sigma_x \\ \Delta\sigma_y \\ \Delta\tau \end{pmatrix} = \begin{pmatrix} C_{11} & C_{12} & 0 \\ C_{12} & C_{22} & 0 \\ 0 & 0 & C_{33} \end{pmatrix} \begin{pmatrix} \Delta\varepsilon_x \\ \Delta\varepsilon_y \\ \Delta\gamma \end{pmatrix} \qquad \text{Equation 3.3-1}$$

C_{11}, C_{22}, C_{12} and C_{33} are four independent material constants, however their values are constrained by the requirement the constitutive matrix must be positive definite. If the x-y coordinate system is not coincident with the principal material directions, then the angle between the two coordinate systems is used to transform the constitutive matrix to the x-y system.

3.3.1 Orthotropic properties from testing specimens

Direct measurements to characterize C_{11}, C_{22}, C_{12} and C_{33} in naturally occuring orthotropic soils can be achieved with a tri-axial testing machine by performing K_0-tests wherein the axial load is applied and the confining pressure is adjusted so that there is no net lateral strain, also called a confined compression test, or uni-axial strain test. For the case when the material x-axis is aligned with specimen's vertical axis, the results of the K_0-test may be used to determined the following three coefficients,

$$C_{11} = \sigma_{axial} / \varepsilon_{axial} \qquad \text{Equation 3.3-2}$$

$$C_{12} = \sigma_0 / \varepsilon_{axial} \qquad \text{Equation 3.3-3}$$

$$C_{33} = (\sigma_{axial} - \sigma_0) / 2\varepsilon_{axial} \qquad \text{Equation 3.3-4}$$

where, σ_{axial} = net axial stress including confining pressure,

ε_{axial} = net axial strain including confining strain,

σ_0 = confining pressure.

In a similar manner, the K_0-test may be repeated with the test specimen rotated 90 degrees such that the material y-axis is aligned with the vertical direction in order to determine the last coefficient C_{22} as,

$$C_{22} = \sigma_{axial} / \varepsilon_{axial} \qquad \text{Equation 3.3-5}$$

This second set of test results may also be used to confirm the previously computed results for C_{12} and C_{33}.

3.3.2 Orthotropic properties for reinforced soil

Placing strips of metal or geo-textile fabrics into soil has proven to be very effective in improving the directional stiffness of soils in embankments and pavement systems. Directional soil reinforcement has also been studied for use in long-span culvert installations in Reference 18. As developed Reference 18 and outlined below, the orthotropic model is useful for simulating the directional stiffness obtained from reinforced soil. This is based on the unit cell concept.

The upper portion of Figure 3.3.2-1 illustrates a unit cell of soil with a single reinforcing strip at the center of the cell extending in the x-direction. The y-z face of the cell measures d inches by b inches with the inference that the

reinforcement strips repeat themselves every d inches in the y-direction and every b inches in the z-direction to form a uniform grid in some large zone of soil.

Figure 3.3.2-1 Unit cell concept for modeling reinforced earth

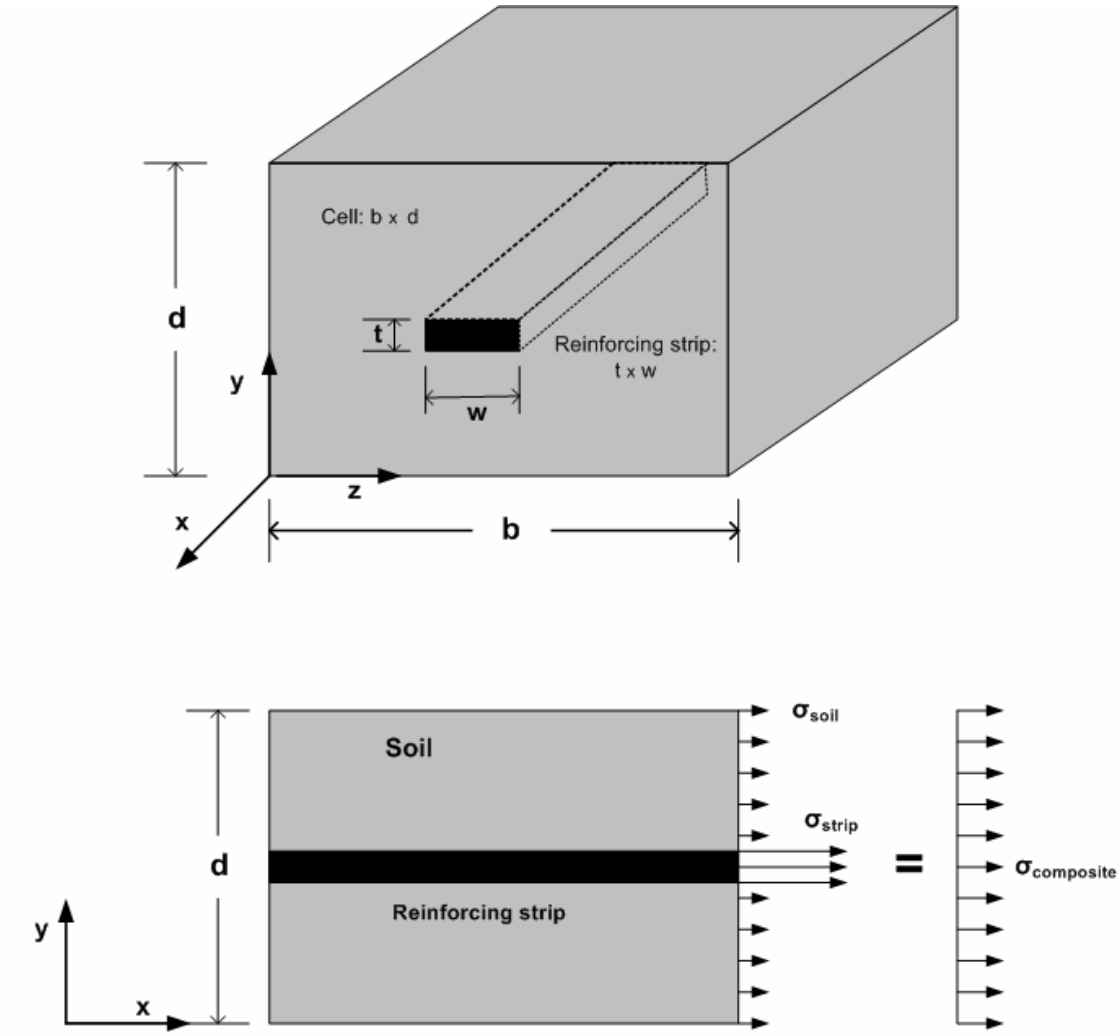

Assuming the reinforcing strips act as one-dimensional elements and remain bonded to the soil, the composite stiffness in the x-direction is determined by applying a uniform strain ε_x while holding all other strains in the soil cell to zero. As illustrated in the bottom of Figure 3.3.2-1, the uniaxial straining produces stresses in the soil and the reinforcing strip as expressed below.

$$\sigma_{soil} = M_s \varepsilon_x \qquad \text{Equation 3.3-6}$$

$$\sigma_{rs} = E_{rs} \varepsilon_x \qquad \text{Equation 3.3-7}$$

where, σ_{soil}, σ_{rs} = stress in x-direction for soil and reinforcing strip, respectively.
M_s = confined modulus of isotropic soil
E_{rs} = Young's modulus of reinforcing strip

To determine the composite stress-strain modulus in the x direction, we evoke force equilibrium such that the net force from the composite stress over the cell face is equal to force contributions from the soil and reinforcement,

$$A_{cell}\sigma_x = A_{soil}\sigma_{soil} + A_{rs}\sigma_{rs} \qquad \text{Equation 3.3-8}$$

where, A_{cell} = bd = area of unit cell face

A_{soil} = bd -wt = soil area per unit cell

A_{rs} = wt = reinforcing strip area per unit cell

Replacing σ_{soil}, σ_{rs} in the above equilibrium equation with their strain equivalents, we have the key stress-strain expression for the x-direction as,

$$\sigma_x = (M_s + \alpha(E_{rs} - M_s))\varepsilon_x \qquad \text{Equation 3.3-9}$$

where, α = wt/bd = ratio of reinforcement area to unit cell area.

To simplify and summarize, let the second term in the above expression be written as, $R = \alpha (E_{rs} - M_s)$, which is the contribution of reinforcing strip to the C_{11}component of the constitutive matrix for a unit cell area of soil. Thus, the final form of the orthotropic constitutive matrix may be written as,

$$\begin{pmatrix} \Delta\sigma_x \\ \Delta\sigma_y \\ \Delta\tau \end{pmatrix} = \begin{pmatrix} M_s+R & M_sK_0 & 0 \\ M_sK_0 & M_s & 0 \\ 0 & 0 & G \end{pmatrix} \begin{pmatrix} \Delta\varepsilon_x \\ \Delta\varepsilon_y \\ \Delta\gamma \end{pmatrix} \qquad \text{Equation 3.3-10}$$

where, $R = \alpha(E_{rs} - M_s)$ = additional soil modulus stiffness in x-direction due to reinforcing strips

α = wt/bd = ratio of reinforcement area to area of unit cell

E_{rs} = Young's modulus of reinforcing strips

M_s = confined modulus of isotropic soil = $E(1-\nu)/(1+\nu)(1-2\nu)$

K_0 = lateral coefficient of isotropic soil = $\nu/(1-\nu)$

G = shear modulus of isotropic soil = $E/2(1+\nu)$

To apply the above in the CANDE program, input $C(1,1) = M_s + R$, $C(1,2) = M_sK_0$, $C(2,2) = M_s$, and $C(3,3) = G$.

3.4 Overburden Dependent Soil Model

The overburden-dependent model is the application of the isotropic elastic model in a series of steps. Each step represents an increment of soil fill or overburden pressure so that the elastic moduli are modified at each step to account for an increased stiffness due to increased confining pressure.

Implicit in the model is the assumption that soil stiffness increases with overburden pressure. This assumption holds true when the soil is in a state of confined compression (one-dimensional straining), wherein increased overburden pressure further increases the lateral confining pressure and the soil tends to stiffen. On the other hand if the soil is unconfined, then increased overburden pressure will not stiffen the soil but, on the contrary, stiffness will be reduced due to shear straining as observed in standard tri-axial tests.

The significant point is that overburden-dependent models are only valid insofar as the soil is predominantly in a state of confined compression. Generally, gravity loading of the soil promotes states of confined compression; however, in regions of strong interaction, such as certain areas in the vicinity of the pipe or around other inclusions, the assumption of confined compression is questionable.

3.4.1 Input data for overburden dependent model

The overburden-dependent model is characterized using the stress-strain data obtained from a confined compression test as illustrated in Figure 3.4.1-1. In this test, increasing levels of axial stress are applied to the top surface of the soil specimen and the corresponding axial strains are measured for each stress level, all other normal strains are zero due to the confining chamber.

Figure 3.4.1-1 Illustration of confined compression test data and secant confined moduli

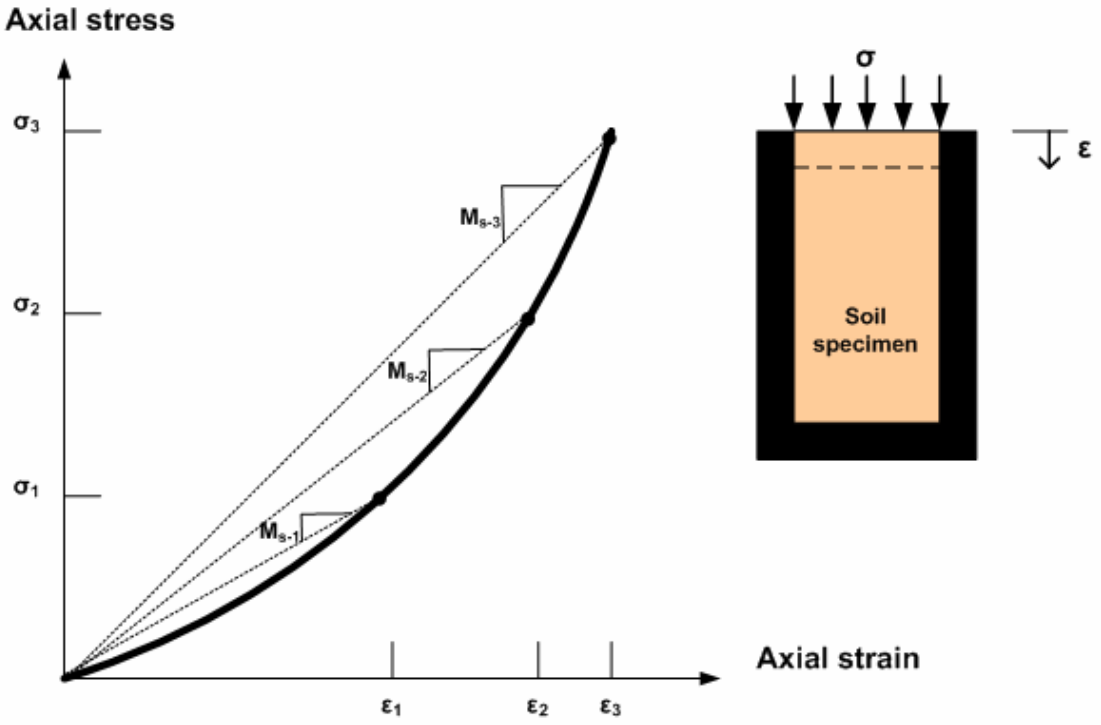

As illustrated in the figure, the secant confined modulus is defined as, $M_{si} = \sigma_i / \varepsilon_i$, and generally increases as overburden pressure increases. The word secant is used to denote that M_{si} is the slope of total stress to total strain, not an incremental relationship. Experimental results from confined compression test are used to compute and list secant moduli values as function of overburden pressure as depicted in the table below for n data points.

Table 3.4.1-1 Data table of secant moduli versus overburden pressure.

Overburden Pressure (vertical stress)	Secant confined Modulus $M_{si} = \sigma_i/\varepsilon_i$	Secant Young's modulus $E_{si} = M_{si}(1+\nu)(1-2\nu)/(1-\nu)$
σ_1	M_{s1}	E_{s1}
σ_2	M_{s2}	E_{s2}
σ_3	M_{s3}	E_{s3}
*	*	*
*	*	*
*	*	*
σ_n	M_{sn}	E_{sn}

For most soils the lateral soil pressure exerted on the sides of the chamber typically increases in direct proportion to the overburden pressure. Thus the lateral coefficient K_0, which is the ratio of lateral pressure to vertical stress, remains practically constant for all levels of vertical stress. Since Poisson ratio $\nu = K_0/(1+K_0)$, a constant value of Poisson ratio is used to provide the second elastic parameter for the overburden dependent model. Accordingly as shown in the last column of the above table, secant values for Young's moduli are easily computed by multiplying secant confined

moduli by a constant factor $\beta = (1+\nu)(1-2\nu)/(1-\nu)$, which is derived from elasticity parameter equivalent relationships (see Table 3.2.1-1).

To briefly recap, Table 3.4.1-1 is representative of the data needed to exercise the overburden model in a typical soil-structure problem. CANDE-2007 has "canned tables" of secant Young's moduli corresponding to increasing values for overburden pressure for typical soils that may be used in lieu of actual test data.

3.4.2 Overburden model development

To incorporate the overburden pressure data into the incremental stress-strain relationship, it is necessary to convert the secant moduli data into chord moduli relating increments of vertical stress to increments of vertical strain in going from load step i to step i +1as illustrated in the figure below.

Figure 3.4.2-1 Incremental stress-strain relationship and chord modulus

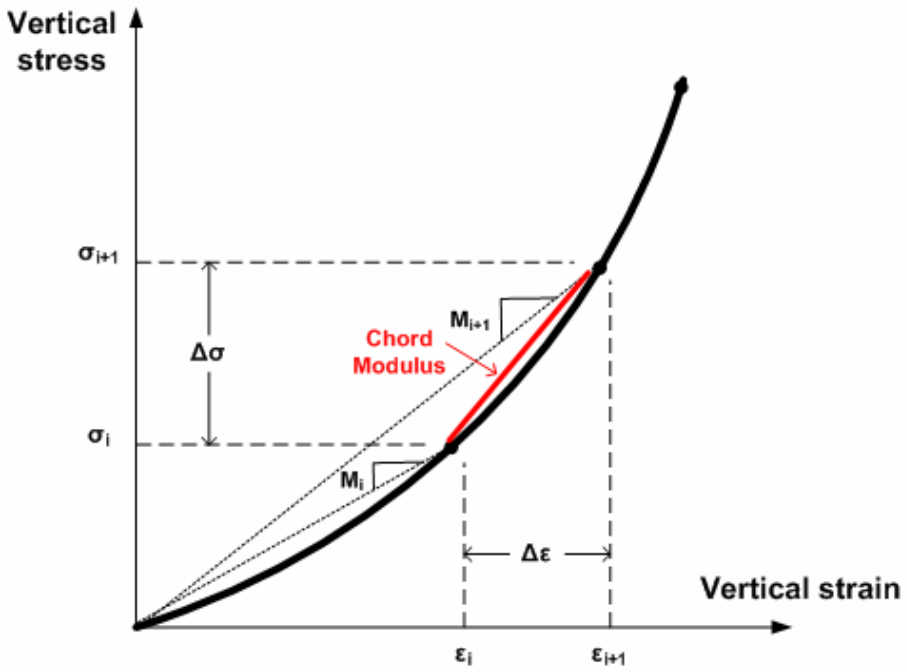

Specifically for each plane-strain element in the soil system, the incremental constitutive matrix has the form,

$$\begin{pmatrix} \Delta\sigma_x \\ \Delta\sigma_y \\ \Delta\tau \end{pmatrix} = \begin{pmatrix} C_{11} & C_{12} & 0 \\ C_{12} & C_{11} & 0 \\ 0 & 0 & C_{33} \end{pmatrix} \begin{pmatrix} \Delta\varepsilon_x \\ \Delta\varepsilon_y \\ \Delta\gamma \end{pmatrix} \qquad \text{Equation 3.4-1}$$

where C_{11}, C_{12}, and C_{13} are chord moduli dependent on the stress state at load step i and step i+1.

Letting σ_i and ε_i represent the known vertical stress and strain at load step i in element #n, the increment of vertical stress in element #n is estimated by determining the vertical pressure contributions of all elements above element #n that enter the soil system in load step i+1. Tersely, this is stated as,

$\Delta\sigma \approx$ increment of overburden pressure from added soil elements above element #n

The algorithm that computes the estimate for $\Delta\sigma$ utilizes the finite element mesh topology and element material property data to determines which elements entering the system during load step i+1 are above element #n along with their contributing pressures. The algorithm is laborious but straightforward.

Once the estimate for $\Delta\sigma$ is obtained, the chord moduli (see above figure) may be determined as,

$$C_{11} = \frac{\Delta\sigma}{(\sigma_i + \Delta\sigma)/M_{i+1} - \varepsilon_i}$$ Equation 3.4-2

$$C_{12} = K_0 C_{11}$$ Equation 3.4-3

$$C_{33} = \frac{1}{2}(1-K_0)C_{11}$$ Equation 3.4-4

where, σ_i , ε_i = known stress and strain values in element #n at load step i.

M_{i+1} = secant confined modulus interpolated from data table at pressure $\sigma_i + \Delta\sigma$.

K_0 = $\nu/(1-\nu)$ = constant lateral coefficient (ν = Poisson ratio)

Herein lies the advantage of an overburden-dependent model over the nonlinear models to be described next. That is, to advance the solution from step i to i+1, the overburden-dependent chord moduli are determined based on the soil layering within the finite element mesh, not on a trial solution. Thus, there are no iterations within the load step and convergence is not an issue with the overburden dependent soil model.

3.4.3 Overburden dependent secant moduli data tables in CANDE

For reference, reasonable ranges of Young's secant moduli are provided in Table 3.4.3-1 along with suggested values for Poisson ratio. The table offers three broad categories of soil; granular, mixed and cohesive for two compaction levels, fair and good.

Table 3.4.3-1 – Secant Young's modulus versus overburden pressure

Soil Class→	Granular		Mixed		Cohesive	
Compaction→	Good	Fair	Good	Fair	Good	Fair
MATNAM→	GGOOD	GFAIR	MGOOD	MFAIR	CGOOD	CFAIR
Overburden Pressure psi	Young's Modulus psi	Young's Modulus psi	Young's Modulus psi	Young's Modulus psi	Young's Modulus psi	Young's Modulus psi
5	1,100	550	600	400	250	150
10	1,300	750	850	550	325	200
15	1,500	850	1,000	600	375	225
20	1,650	1,000	1,100	700	375	250
25	1,800	1,100	1,200	750	400	250
30	1,900	1,150	1,250	800	400	250
40	2,100	1,300	1,350	900	400	250
50	2,250	1,400	1,450	900	400	250
Poisson ratio (pressure independent)	0.30 to 0.35		0.30 to 0.40		0.33 to 0.40	

The above values are a composite of seven different references as well as experimental data from the original CANDE investigation (Reference 1). As a whole the data values are conservative (low side) and are suitable for design if actual soil data is not available.

3.5 Duncan and Duncan/Selig Soil Models

The Duncan and Duncan/Selig soil models are variable-modulus elasticity formulations using stress-dependent equations for Young's modulus and bulk modulus. The Duncan form and Duncan/Selig form are very similar, differing slightly in the expression for the bulk modulus function. Both forms of the soil models are considered to be very representative of actual soil behavior particularly for representing the stress-dependent behavior of backfill soil in culvert installations. Basically, the models exhibit stiffening of constitutive moduli when confining stress increases and softening when shear stress increases.

Duncan's original work for the Young's modulus formulation, which is based on a hyperbolic stress-strain relationship, dates back to 1970 (Reference 19) and remains today as originally developed. In 1978 (Reference 20), Duncan and his colleagues introduced a variable bulk modulus to serve as the second constitutive parameter, replacing the previous assumption of a constant Poisson ratio. The bulk modulus function is based on a power law function of confining pressure. Today, Duncan's original Young's modulus formulation together with the power-law bulk modulus function is referred to as the Duncan soil model.

Selig proposed an alternative form of the bulk modulus function in 1988 (Reference 21). Selig's bulk modulus function is based on an observed hyperbolic relationship between volumetric strain and hydrostatic pressure from soil specimens in hydrostatic compression. Thus, the so-called Duncan/Selig soil model is based on Duncan's original Young's modulus formulation and Selig's hyperbolic bulk modulus formulation. Selig also performed independent tests to characterize the parameters of the Duncan/Selig model.

3.5.1 Plane-strain constitutive matrix

From an overall perspective, the Duncan and the Duncan/Selig soil models are used to define the nonlinear components of an isotropic, elasticity-based constitutive matrix for plane-strain conditions as expressed below.

$$\begin{pmatrix} \Delta\sigma_x \\ \Delta\sigma_y \\ \Delta\tau \end{pmatrix} = \begin{pmatrix} C_{11} & C_{12} & 0 \\ C_{12} & C_{11} & 0 \\ 0 & 0 & C_{33} \end{pmatrix} \begin{pmatrix} \Delta\varepsilon_x \\ \Delta\varepsilon_y \\ \Delta\gamma \end{pmatrix} \qquad \text{Equation 3.5-1}$$

where, $\Delta\sigma_x, \Delta\sigma_y, \Delta\tau$ = stress increments for x-direction, y-direction and shear components, respectively

$\Delta\varepsilon_x, \Delta\varepsilon_y, \Delta\gamma$ = strain increments for x-direction, y-direction and shear components, respectively

C_{11}, C_{12}, C_{33} = nonlinear coefficients dependent on Young's modulus and bulk modulus functions.

The table below shows the relationship between the constitutive matrix components and the elastic functions.

Table 3.5.1-1 Components for constitutive matrix relationship to moduli functions

Components of Constitutive matrix	E = Young's modulus B = bulk modulus (E, B)	E = Young's modulus ν = Poisson ratio (E, ν)
C_{11} =	$\frac{3B(3B + E)}{9B - E}$	$\frac{E(1- \nu)}{(1+ \nu)(1-2\nu)}$
C_{12} =	$\frac{3B(3B - E)}{9B - E}$	$\frac{E\nu}{(1+ \nu)(1-2\nu)}$
C_{33} =	$\frac{3BE}{9B - E}$	$\frac{E}{2(1+ \nu)}$

The middle column in the above table defines the matrix coefficients C_{11}, C_{12} and C_{13} in terms of Young's modulus and bulk modulus, which are the elastic parameter functions developed in the current Duncan and Duncan Selig models. The third column defines the matrix coefficients in terms of Young's modulus and Poisson ratio, which was the 1970 form of the Duncan model. We will return to the implications of the constitutive matrix after the functional forms of Young's modulus and bulk modulus are presented.

3.5.2 Duncan Young's modulus development

Duncan's formulation is based on experimental observations of soil behavior from standard tri-axial tests. A standard tri-axial test is conducted by placing a cylindrical soil specimen in a pressure chamber and initially subjecting the specimen to a uniform hydrostatic pressure, called σ_3. Next a steadily increasing axial load is applied to the specimen producing a net axial stress, called σ_1, which includes the hydrostatic pressure. Note that σ_3 and σ_1 are principal stresses in the lateral and axial directions, respectively. The difference in principal stresses $\sigma_1 - \sigma_3$ is called the deviator stress and is equal to twice the maximum shear stress occuring on 45-degree plane.

As the axial stress increases, axial strain is computed by measuring the axial shortening of the specimen divided by the specimen length. Note the measured axial strain does not include the initial hydrostatic strain.

The dashed curve in Figure 3.5.2-1 is a plot of deviator stress versus axial strain for a typical tri-axial test. Here, $(\sigma_1 - \sigma_3)_f$ is the measured maximum deviator stress at failure, and E_i is the initial slope representing Young's modulus at zero deviator stress. As discussed subsequently, $(\sigma_1 - \sigma_3)_f$ and E_i are dependent on the hydrostatic stress level.

Figure 3.5.2-1 Deviator stress versus axial strain for tri-axial test and hyperbolic approximation

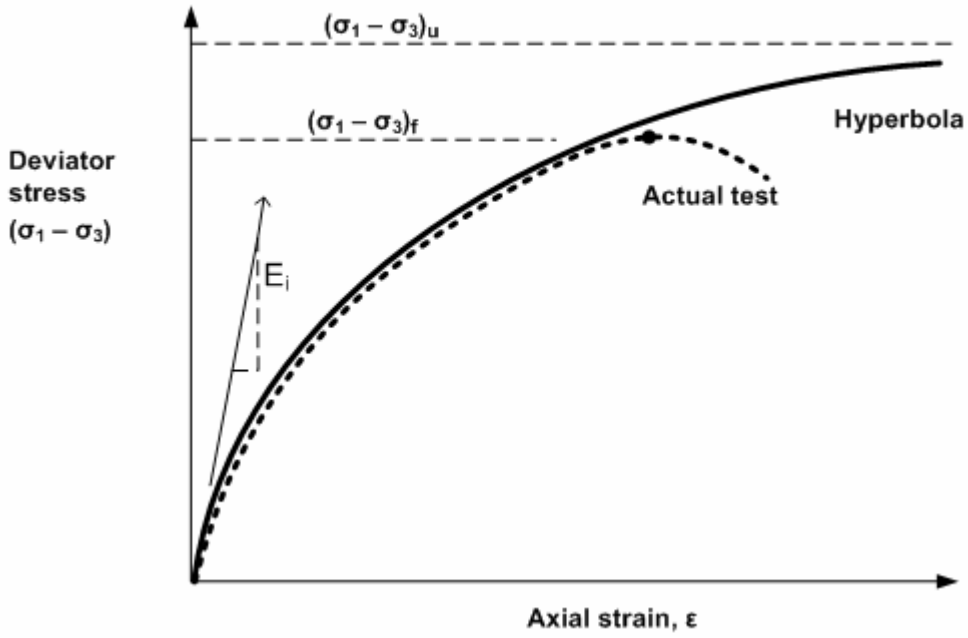

Duncan hyperbolic function. Duncan's fundamental insight is that the experimental curve is fairly well approximated by equating the deviator stress to a hyperbolic function of axial strain as follows,

$$\sigma_1 - \sigma_3 = \frac{\varepsilon}{\frac{1}{E_i} + \frac{\varepsilon}{(\sigma_1 - \sigma_3)_u}} \qquad \text{Equation 3.5-2}$$

where, E_i = initial slope for Young's modulus (dependent on minimum principal stress)

$(\sigma_1 - \sigma_3)_u$ = ultimate deviator stress from hyperbolic model (dependent on minimum principal stress)

ε = axial strain, not including initial hydrostatic strain

As illustrated in by the solid curve in the above figure, the hyperbolic function provides a good representation of the actual test data up to the point of actual failure, $(\sigma_1 - \sigma_3)_f$. Thereafter the hyperbolic function tends to overshoot the actual softening behavior as the hyperbolic function asymptotically approaches the limit, $(\sigma_1 - \sigma_3)_u$. In order to preserve the good curve fit from zero to actual failure, it should be evident that $(\sigma_1 - \sigma_3)_u$ cannot, in general, be set equal to the actual failure deviator stress, $(\sigma_1 - \sigma_3)_f$. Rather, the Duncan model introduces a model parameter called the failure ratio defined as,

$$R_f = \frac{(\sigma_1 - \sigma_3)_f}{(\sigma_1 - \sigma_3)_u} \leq 1.0 \qquad \text{Equation 3.5-3}$$

Given that $(\sigma_1 - \sigma_3)_f$ is characterized from actual experimental data, then Equation 3.5-3 may be used to define $(\sigma_1 - \sigma_3)_u$ for the hyperbolic function.

To complete the hyperbolic model, functional forms for $(\sigma_1 - \sigma_3)_f$ and E_i must be defined based on a sequence of tri-axial tests. Figure 3.5-2 illustrates the typical behavior of a specific soil specimen subjected to a series of tri-axial tests with increasing confining pressure.

Figure 3.5.2-2 Typical behavior of a soil specimen in a sequence of tri-axial tests.

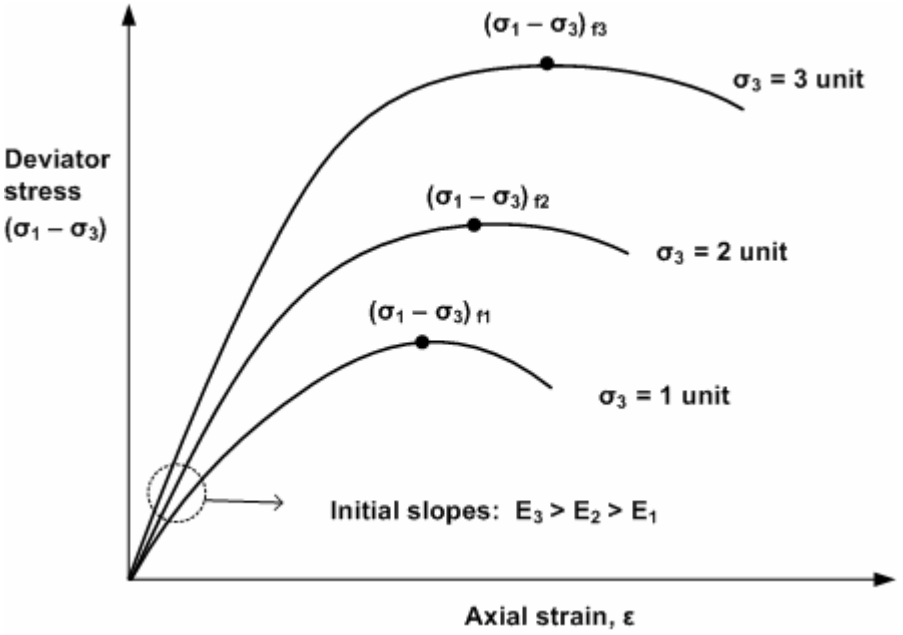

Initial Young's modulus. Based on a wide variety of soil tests as typified by the above figure, the initial modulus is observed to increase with confining pressure according to the following power law,

$$E_i = KP_a(\sigma_3/P_a)^n \qquad \text{Equation 3.5-4}$$

where, E_i = initial Young's modulus when deviator stress = 0

K = dimensionless magnitude of initial Young's modulus

P_a = atmospheric pressure used to nondimensionalize parameters K and n

n = power-law coefficient usually less than 1.0

σ_3 = confining pressure or minimum magnitude of principle stress

Mohr-Coulomb failure envelope. As portrayed in the Figure 3.5-2, the deviator stress at failure increases with confining pressure. Based on the well-known Mohr-Coulomb failure theory, the $(\sigma_1 - \sigma_3)_{f\,i}$ data points define a failure envelope in terms of normal stress and shear stress as depicted in the figure below.

Figure 3.5.2-3 Failure envelope in normal and shear stress space

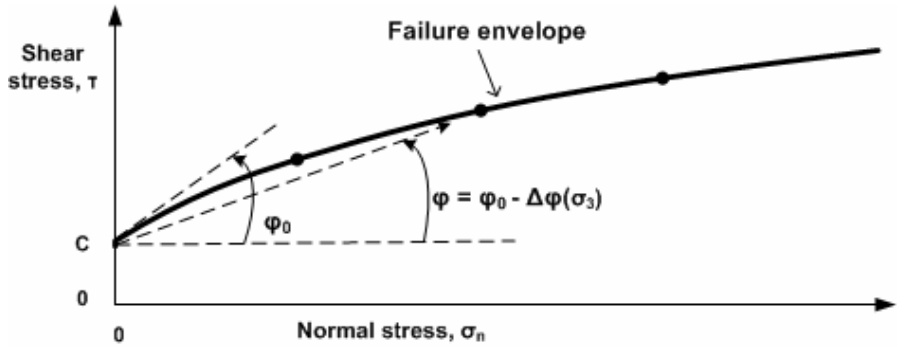

Typically, the Mohr-Coulomb failure surface is a straight line defined by two constants, C and φ_0, representing the cohesion intercept and a constant soil friction angle, respectively. As illustrated in the above figure, a more general form of the Mohr-Coulomb failure surface is used in this development wherein the soil friction angle is a decreasing function of the confining pressure. Often, this is a better representation of actual soil behavior.

Based on the generalized Mohr-Coulomb theory, the tri-axial deviator stress at failure is characterized as follows,

$$(\sigma_1 - \sigma_3)_f = \frac{2C\cos\varphi + 2\sigma_3 \sin\varphi}{1 - \sin\varphi} \qquad \text{Equation 3.5-5}$$

where, $\varphi = \varphi_0 - \Delta\varphi \log_{10}(\sigma_3/P_a)$ = variable soil friction angle Equation 3.5-6

C = cohesion intercept, units of stress

φ_0 = initial soil friction angle

$\Delta\varphi$ = reduction of soil friction angle for 10-fold increase in σ_3

Tangent Young's modulus. Tangent Young's modulus is equal to the derivative of axial stress to axial strain under the conditions of tri-axial testing wherein the confining stress is constant. Since all the terms are now identified in Equation 3.5-2, we can compute tangent Young's modulus by forming the derivative $d\sigma_1/d\varepsilon$ and replacing strain values with equivalent stresses via Equation 3.5-2 to arrive at,

$$E_t = E_i\left[1 - \frac{R_f(1-\sin\varphi)(\sigma_1 - \sigma_3)}{2(C\cos\varphi + \sigma_3\sin\varphi)}\right]^2 \qquad \text{Equation 3.5-7}$$

where, E_t = tangent Young's modulus dependent on stress state

σ_1 = maximum compressive principal stress

σ_3 = minimum compressive principal stress

Equation 3.5.7 is fundamental for both the Duncan soil model and the Duncan/Selig soil model.

3.5.3 Bulk modulus formulations

By definition, the tangent bulk modulus is the change in mean stress divided by the change in volumetric strain, which is expressed as

$$B_t = \frac{d\sigma_m}{d\varepsilon_{vol}} \qquad \text{Equation 3.5-8}$$

where, B_t = tangent bulk modulus, usually stress dependent for soils.

$\sigma_m = (\sigma_{11} + \sigma_{22} + \sigma_{33})/3$ = mean average stress, also called hydrostatic stress

$\varepsilon_{vol} = dV/V_0 = \varepsilon_{11} + \varepsilon_{22} + \varepsilon_{33}$ = volumetric strain

Duncan bulk modulus function. Duncan used tri-axial test data including measurements of volumetric strain to obtain experimental values for the tangent bulk modulus computed as,

$$B_{measured} = \frac{1}{3}\Delta\sigma_{axial}/\Delta\varepsilon_{vol} \qquad \text{Equation 3.5-9}$$

For a given confining pressure, the change in axial stress and corresponding change in volumetric strain are measured when the axial stress reaches 70% of the failure stress or the volumetric strain peaks in contraction, whichever occurs first.

Based on a series of tri-axial tests with increasing confining pressure, Duncan proposed a power-law function (very similar to the initial Young's modulus function) to describe the tangent bulk modulus as,

$$B_t = K_b P_a (\sigma_3 / P_a)^m \qquad \text{Equation 3.5-10}$$

where, K_b = dimensionless magnitude of tangent bulk modulus

P_a = atmospheric pressure used to nondimensionalize parameters K_b and m

m = power-law coefficient usually less than 1.0

σ_3 = confining pressure or minimum magnitude of principle stress

Selig bulk modulus function. Selig developed an alternate form of the tangent bulk modulus function based on hydrostatic tests. In the hydrostatic test the soil specimen is compressed under increasing confining pressure applied equally in all directions and the change of volume is measured as function of confining pressure as depicted in the figure below.

Figure 3.5.3-1 Hydrostatic test and Selig's hyperbolic model

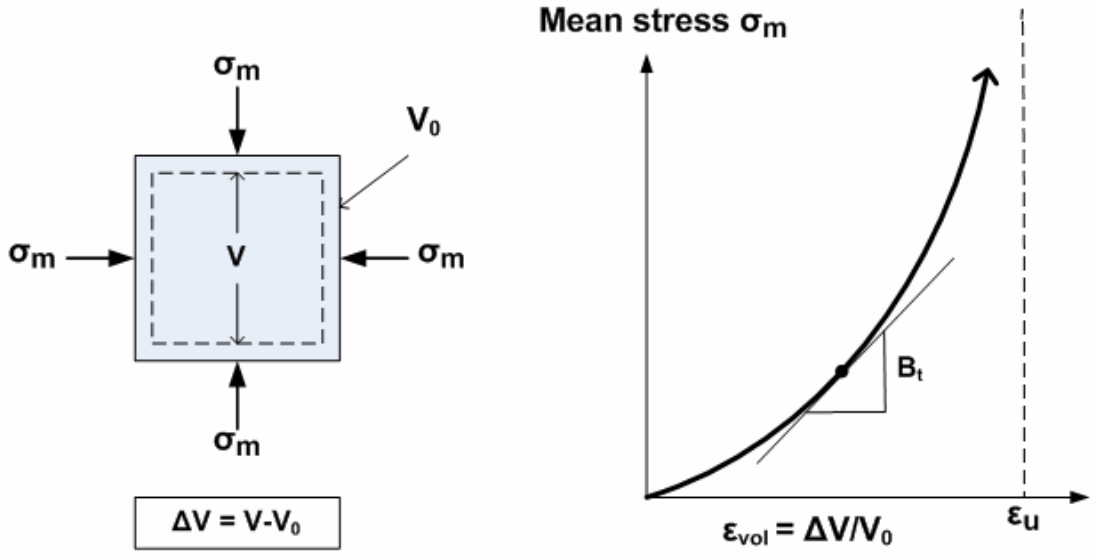

Selig observed that the experimental curves relating mean stress to volumetric strain is reasonably described by a hyperbolic equation in the form,

$$\sigma_m = \left(\frac{B_i}{1 - \varepsilon_{vol}/\varepsilon_u}\right)\varepsilon_{vol} \qquad \text{Equation 3.5-11}$$

where, B_i = initial tangent bulk modulus when volumetric strain = 0.

ε_u = ultimate volumetric strain at large hydrostatic stress.

As illustrated in Figure 3.5.3-1, the tangent bulk modulus is determined by forming the derivative $d\sigma_m/d\varepsilon_{vol}$ and again using Equation 3.5-11 to replace volumetric strain with hydrostatic stress to get the final result,

$$B_t = B_i[1+ \sigma_m/(B_i/\varepsilon_u)]^2 \qquad \text{Equation 3.5-12}$$

where, B_t = Selig form of tangent bulk modulus dependent on mean hydrostatic stress.

3.5.4 Summary of Duncan and Duncan/Selig soil models.

Both Duncan and Duncan/Selig employ tangent Young's modulus given by,

$$E_t = E_i \left[1 - \frac{R_f(1-\sin\varphi)(\sigma_1-\sigma_3)}{2(C\cos\varphi + \sigma_3\sin\varphi)}\right]^2 \qquad \text{Equation 3.5-13}$$

$$E_i = KP_a\left(\frac{\sigma_3}{P_a}\right)^n \qquad \text{Equation 3.5-14}$$

$$\varphi = \varphi_0 - \Delta\varphi \log_{10}(\sigma_3/P_a) \qquad \text{Equation 3.5-15}$$

where, E_t = tangent Young's modulus dependent on complete stress state,

E_i = initial tangent dependent on minimum compressive stress,

φ = angle of internal friction dependent on minimum compressive stress,

σ_1 = maximum compressive principal stress,

σ_3 = minimum compressive principal stress,

P_a = atmospheric pressure, a constant for units of stress.

Material properties required for the tangent young's modulus functions are,

K = dimensionless magnitude of initial Young's modulus,

n = power-law coefficient for initial modulus usually less than 1.0,

C = cohesion intercept for failure, units of stress,

φ_0 = initial soil friction angle of failure surface,

$\Delta\varphi$ = reduction of soil friction angle for 10-fold increase in σ_3,

R_f = failure ratio of actual to model failure stress usually les than 1.0.

For the second elasticity function, the choice is between Duncan's tangent bulk modulus power law or Selig's tangent bulk modulus derived from a hyperbolic relationship between hydrostatic pressure and volumetric strain.

Duncan's tangent bulk modulus power-law function is given by,

$$B_t = K_b P_a(\sigma_3/P_a)^m \qquad \text{Equation 3.5-16}$$

where, σ_3 = minimum magnitude of compressive principle stress,

P_a = atmospheric pressure, a constant for units of stress.

Material properties required for Duncan's tangent bulk modulus power law are,

K_b = dimensionless magnitude of tangent bulk modulus,

m = power-law coefficient usually less than 1.0.

Selig's tangent bulk modulus function is given by,

$$B_t = B_i[1+ \sigma_m/(B_i/\varepsilon_u)]^2 \qquad \text{Equation 3.5-17}$$

where, σ_m = mean hydrostatic stress.

Material properties required for Selig's tangent bulk modulus function are,

B_i = initial tangent bulk modulus when hydrostatic stress is zero,

ε_u = ultimate volumetric strain at large hydrostatic stress.

3.5.5 Behavioral characteristics and special considerations

The behavioral characteristics and limitations of the Duncan and the Duncan/Selig soil model are nearly identical and are enumerated below along with discussions on special treatments for limiting cases. Recall that maximum shear stress is equal to half the difference in principal stresses, $(\sigma_1 - \sigma_3)/2$.

- If confining pressure increases while shear stress is held constant, E_t and B_t become stiffer. However if maximum shear increases with constant confining pressure, E_t becomes softer while B_t remains constant.

- Shear failure is said to occur when E_t approaches zero as shear stress increases to the failure limit. To avoid numerical problems, the bracketed term in Equation 3.5-13, which varies from 1.0 to 0.0 as shear stress increases, is limited to the minimum value 0.05 so that $E_t = 0.0025E_i$ is the minimum tangent Young's modulus, which is effectively a near-zero stiffness.

- Tension failure is said to occur when the minimum compressive stress σ_3 becomes tensile wherein most soils breakdown and lose all stiffness. This is simulated in the soil models by assigning a small limiting value to the minimum compressive stress, $\sigma_3/Pa = 0.1$, so that E_t and B_t are near-zero stiffness values whenever the minimum principal stress approaches tension.

- Although E_t and B_t are developed as two independent functions, energy considerations require constraints between the functions (e.g. see Table 3.5-1). The soil models programmed in CANDE satisfy the energy constraints by enforcing,

  $$E_t > 0, \text{ and } E_t/3 < B_t < 8E_t.$$

  Lower and upper limits on B_t are equivalent to maintaining Poisson ratio in the range, $0 < \nu < 0.48$. The programmed soil models also have the option to use a constant Poisson ratio instead of the tangent bulk modulus functions.

- Lastly, it is emphasized the Duncan and Duncan/Selig soil models are nonlinear elastic and behave the same in loading or unloading. There is not a special unloading algorithm with different material characteristics. For the record, it is noted that some investigators have incorporated ad hoc unloading algorithms into the Duncan soil model. However such algorithms, which are not based on plasticity concepts, violate the continuity principal of load path. Two load paths that are arbitrarily close to one another should not result in dramatically different stress-strain response. Suffice to say, that a theoretically correct unloading model for the Duncan soil model is yet to be developed.

3.5.6 Implementation of soil models and nonlinear solution strategy

Recall that Equation 3.5-1 is the fundamental plane-strain constitutive matrix relating stress increments to strain increments from a known stress-strain state at load step i to the unknown stress-strain state at load step i +1. Accordingly, the matrix coefficients, C_{11}, C_{12} and C_{13} are chord moduli as notionally illustrated on the stress-strain curve in the figure below along with the tangent moduli at the beginning and end of the load step.

Figure 3.5.6-1 Chord and tangent moduli on a notional stress-strain curve.

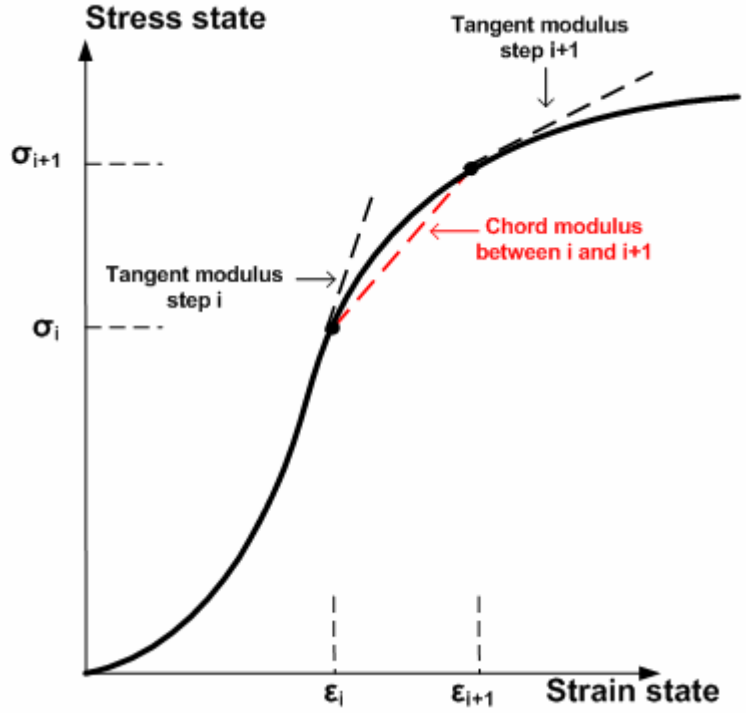

Chord moduli representation. To convert the Duncan and Selig tangent Young's modulus and tangent Bulk modulus to chord moduli suitable for defining C_{11}, C_{12} and C_{13}, the following averaging technique is used,

$$E_c = (1 - r)E_{t_i} + rE_{t_{i+1}} \qquad \text{Equation 3.5-18}$$

$$B_c = (1 - r)B_{t_i} + rB_{t_{i+1}} \qquad \text{Equation 3.5-19}$$

where E_c, B_c = chord moduli for Young's modulus and bulk modulus, respectively

E_{t_i}, $E_{t_{i+1}}$ = tangent Young's moduli at load step i and i+1, respectively

B_{t_i}, $B_{t_{i+1}}$ = tangent bulk moduli at load step i and i+1, respectively

r = averaging ratio usually taken as ½.

The justification for averaging the tangent moduli to obtain the chord moduli follows from the mean-value-theorem of differential calculus, which implies that the process becomes exact as the size of the load step decreases. Generally the averaging ratio is taken as r = ½. However as explained in the next paragraph, it is reasonable to set r =1when in situ soil elements enter the structural system for the first time. For this reason, the averaging ratio is treated as a material input parameter.

Entering soil elements. Soil elements enter the structural system in one of two categories. The first category applies to pre-existing or in-situ soil elements in which an initial state of stress exists but is generally not known prior to the solution. Elements entering in this category are typically part of the initial configuration and are assigned to the first construction increment.

The second category applies to fill soi1 elements, i.e., soil layers added to the system in a predefined construction schedule. Here, the initial stress state is non-existent prior to entry into the system. Both categories present special starting problems for the iteration scheme because the initial stress state is unknown in the first category or nonexistent in the second category.

For the first category, the initial stress state can be determined iteratively by assuming the pre-existing soil zone is a construction increment loaded with its own body weight (and, if desired, a consolidation pressure). In this case the averaging ratio should be set to 1.0, so that, E_c and B_c are equal to the tangent values at the end of the load step because this corresponds to the existing stress state. When r = 1, the tangent moduli at the beginning of the load step have no influence on the averaging process. After the first construction increment is complete, the algorithm automatically changes r = 1/2 so that all subsequent moduli calculations represent chord values in going from a known stress state to an unknown stress state.

For the second category, soil layers entering the system for the first time have zero initial stress and zero initial stiffness at the beginning of the load step but gain stiffness at the end of the load step from self-weight and/or compaction load. In this case, using r = 1/2 implies the effective chord moduli during the load step is equal to one-half the tangent moduli at the end of the load step, which is considered to be a reasonable assumption. For all load steps following the initial load step, there is no longer any ambiguity and we set r =1/2 because we know the stress state at the start of each subsequent load step.

To start the iteration process for entering elements of either category, some initial guess must be made for the end-of-load-step tangent moduli because the start-of-load step moduli are zero. Thus in order to construct the first trial stiffness matrix, "dummy" principle stresses are used to get the first trial moduli value. The dummy principle stresses have no effect on the final converged solution, but they do influence the number of iterations required to achieve convergence. After an element has entered the system, the initial guess for end-of-load-step tangent moduli for all subsequent load steps are equated to the last calculated values and the use of dummy principal stresses is not required.

Nonlinear solution summary. Based on the forgoing discussion, a summary on the nonlinear solution strategy is provided in the flowchart shown in Figure 3.5.6-2. The flow chart depicts the iteration cycle to determine the constitutive matrix of a soil element wherein the principal stresses from the last iteration are used make closer and closer estimates of the chord moduli until convergence occurs. Convergence of the algorithm occurs when the chord moduli obtained from two successive iterations differ by no more than 1% for all elements.

Two additional features of the algorithm not shown in the flow chart are listed below.

1. An under-relaxation scheme to improve the rate of convergence for the tangent moduli comes into play after the second iteration wherein each estimate of the end-of-load-step tangent moduli is a weighted average of the current estimate and the previous iteration estimate. This feature takes advantage of the observation that convergence occurs in an oscillatory manner.

2. A constant Poisson ratio option may be chosen by the user that replaces the tangent bulk modulus formulation. When the constant Poisson ratio option is exercised, the bulk modulus formulations are bypassed. Otherwise, the algorithm is essentially the same.

Figure 3.5.6-2 Duncan and Duncan/Selig flow chart for computing constitutive matrix.

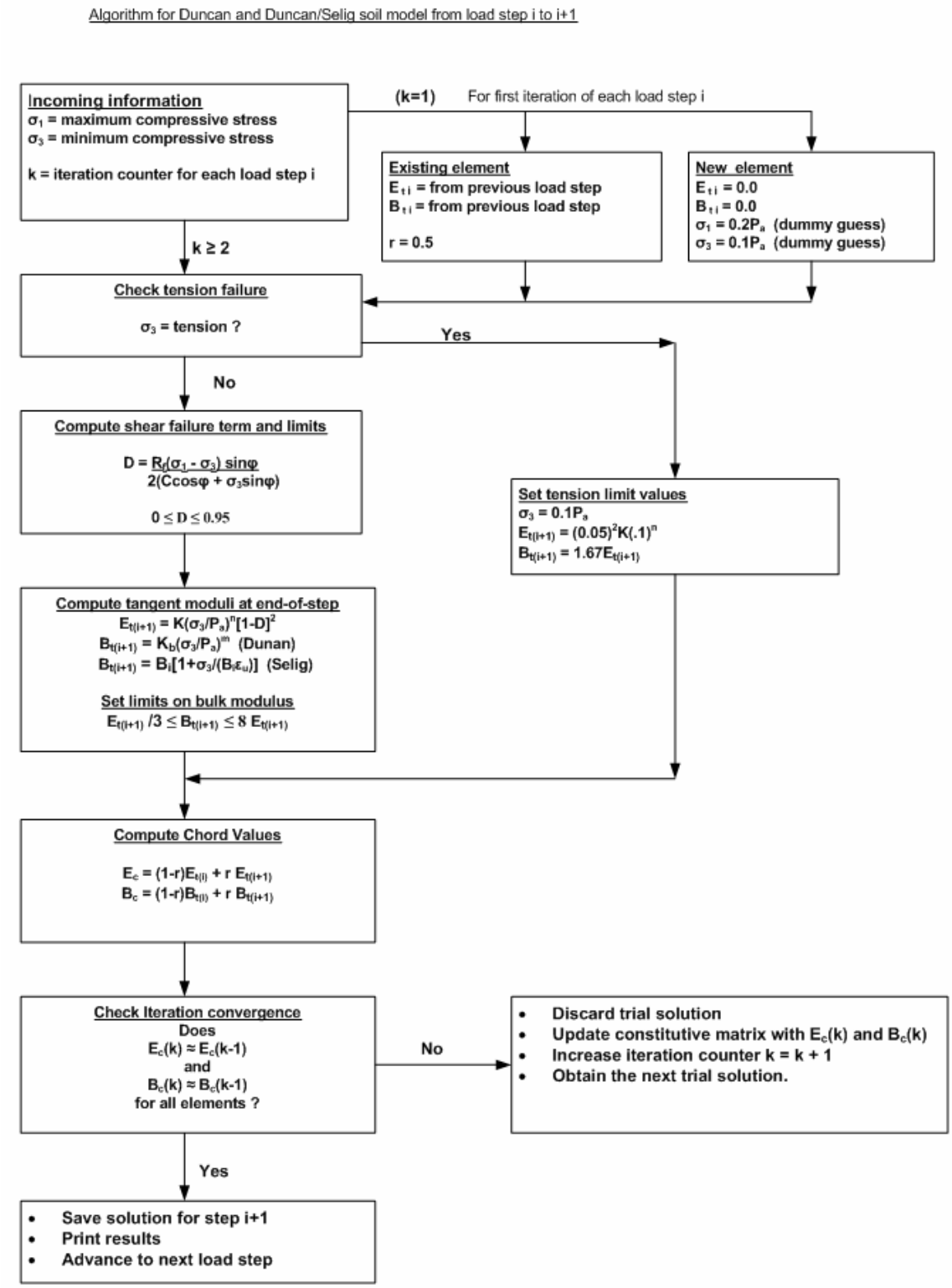

3.5.7 Recommended Duncan and Duncan/Selig parameters for standard soils

Whenever possible, the Duncan and/or Duncan Selig soil model parameters should be determined directly from tri-axial test equipment using established curve-fitting procedures. In many instances, however, tri-axial data may be unavailable, and so, it is convenient to establish standard parameter values for various types of soil and degrees of compaction.

Table 3.5.7-1 provides parameter values for the Duncan soil model for four soil classifications, each with three levels of compaction. These standard values, extracted from References 19 and 20, are conservative in the sense that they are the lower bounds of strength and moduli values observed from numerous tri-axial tests for each soil type. An independent study at the University of Notre Dame utilizing the same database verified that the table parameters give a good but conservative representation of the experimental data.

Table 3.5.7-1 Duncan soil model parameters (from Duncan Reference

Soil type and compaction	Young's Tangent Modulus Parameters						Bulk Parameters		Density reference (lb/ft^3)
	K	n	C	φ_0	$\Delta\varphi$	R_f	K_b	m	
	(--)	(--)	(psi)	(deg)	(deg)	(--)	(--)	(--)	
CA105	600	0.40	0.0	42	9	0.7	175	0.2	150
CA95	300	0.40	0.0	36	5	0.7	75	0.2	140
CA90	200	0.40	0.0	33	3	0.7	50	0.2	135
SM100	600	0.25	0.0	36	8	0.7	450	0.0	135
SM90	300	0.25	0.0	32	4	0.7	250	0.0	125
SM85	150	0.25	0.0	30	2	0.7	150	0.0	120
SC100	400	0.60	0.5	33	0	0.7	200	0.5	135
SC90	150	0.60	0.3	33	0	0.7	75	0.5	125
SC85	100	0.60	0.2	33	0	0.7	50	0.5	120
CL100	150	0.45	0.4	30	0	0.7	140	0.2	135
CL90	90	0.45	0.2	30	0	0.7	80	0.2	125
CL85	60	0.45	0.1	30	0	0.7	50	0.2	120

In the above table the soil type is defined as follows: CA = Course Aggregates, SM = Silty Sand, SC = Silty-Clayey Sand and CL = Silty Clay. The compaction number is percent relative compaction, per AASHTO T-99. As an example, SM100 means silty sand compacted to 100% relative density per T-99.

In a similar manner Table 3.5.7-2 provides parameter values for the Duncan/Selig soil model for three soil classifications, each with five levels of compaction. These values were computed by Selig in Reference 21 and are generally conservative. The bulk modulus parameters were determined from hydrostatic tests which, according to Selig, tend to be more conservative than those determined from standard tri-axial tests.

Table 3.5.7-2 Duncan/Selig soil model parameters (from Selig Reference)

Soil type and compaction	Young's Tangent Modulus Parameters						Bulk Parameters		Density reference (lb/ft^3)
	K	n	C	φ_0	$\Delta\varphi$	R_f	B_i/P_a	ε_u	
	(--)	(--)	(psi)	(deg)	(deg)	(--)	(--)	(--)	
SW100	1300	0.90	0.0	54	15	0.65	108.8	0.01	148
SW95	950	0.60	0.0	48	8.0	0.70	74.8	0.02	145
SW90	640	0.43	0.0	42	4.0	0.75	40.8	0.05	140
SW85	450	0.35	0.0	38	2.0	0.80	12.7	0.08	130
SW80	320	0.35	0.0	36	1.0	0.90	6.1	0.11	120
ML95	440	0.40	4.0	34	0.0	0.95	48.3	0.06	135
ML90	200	0.26	3.5	32	0.0	0.89	18.4	0.10	130
ML85	110	0.25	3.0	30	0.0	0.85	9.5	0.14	122
ML80	75	0.25	2.5	28	0.0	0.80	5.1	0.19	115
ML50	16	0.95	0.0	23	0.0	0.55	1.3	0.43	66
CL95	120	0.45	9.0	15	4.0	1.00	21.2	0.13	130
CL90	75	0.54	7.0	17	7.0	0.94	10.2	0.17	125
CL85	50	0.60	6.0	18	8.0	0.90	5.2	0.21	120
CL80	35	0.66	5.0	19	8.5	0.87	3.5	0.25	112

In the above table the soil type is defined as follows: SW = Gravelly sand, ML = Sandy silt, and CL = Silty Clay. The compaction number is percent relative compaction, per AASHTO T-99. As an example, SW95 means gravelly sand compacted to 95% relative density per T-99.

In the old CANDE-1989 documentation, Selig presented less conservative values for the tangent bulk modulus parameters by uniformly increasing the parameter B_i/P_a by a factor of 2.5 and uniformly decreasing ε_u by the factor 0.71. However, in recent years most researchers prefer the original hydrostatic data given in the above table.

3.6 Extended Hardin Soil Model

The extended Hardin soil model is a variable-modulus elasticity formulation using stress/strain-dependent functions for the shear modulus and Poisson ratio. Basically, the model exhibits stiffening of constitutive moduli when confining stress increases and softening when shear strain increases.

Hardin's original work for the variable shear modulus formulation, which is based on a hyperbolic relationship between shear stress and shear strain, is summarized in a 1973 Air Force technical report (Reference 22). In 1974 a variable Poisson ratio function was developed to be the companion elasticity function so that together the two elasticity functions, shear modulus and Poisson ratio, are referred to as the extended Hardin soil model. Reference 1 documents the development of the variable Poisson function as well as validation of the shear modulus function against an independent set of experimental data.

In many ways the extended Hardin model is similar in behavior to the Duncan and Duncan/Selig models, although the later models are more popular and are supported by a larger database of soil parameters dependent on soil quality and compaction. However, a unique feature of the extended Hardin model is that the soil parameters for the shear modulus function are characterized in terms fundamental soil properties including void ratio, plasticity index and percent saturation of the soil.

3.6.1 Plane-strain constitutive matrix

From an overall perspective, the extended Hardin soil model functions are used to define the nonlinear components of an isotropic, elasticity-based constitutive matrix for plane-strain conditions as expressed below.

$$\begin{pmatrix} \Delta\sigma_x \\ \Delta\sigma_y \\ \Delta\tau \end{pmatrix} = \begin{pmatrix} C_{11} & C_{12} & 0 \\ C_{12} & C_{11} & 0 \\ 0 & 0 & C_{33} \end{pmatrix} \begin{pmatrix} \Delta\varepsilon_x \\ \Delta\varepsilon_y \\ \Delta\gamma \end{pmatrix} \qquad \text{Equation 3.6-1}$$

where, $\Delta\sigma_x, \Delta\sigma_y, \Delta\tau$ = stress increments for x-direction, y-direction and shear components, respectively

$\Delta\varepsilon_x, \Delta\varepsilon_y, \Delta\gamma$ = strain increments for x-direction, y-direction and shear components, respectively

C_{11}, C_{12}, C_{33} = nonlinear coefficients dependent on shear modulus and Poisson ratio functions.

The table below shows the relationship between the constitutive matrix components and the shear modulus and Poisson ratio functions that define the extended Hardin model.

Table 3.6.1-1 Components for constitutive matrix relationship to moduli functions

Components of Constitutive matrix	**G = shear modulus ν = Poisson ratio (G, ν)**	**G = shear modulus B = bulk modulus (G, B)**
C_{11} =	$\frac{2G(1-\nu)}{1-2\nu}$	$B + \frac{4}{3}G$
C_{12} =	$\frac{2G\nu}{1-2\nu}$	$B - \frac{2}{3}G$
C_{33} =	G	G

The middle column in the above table defines the matrix coefficients C_{11}, C_{12} and C_{13} in terms of shear modulus and Poisson ratio, which are the elastic parameter functions directly developed for the extended Hardin soil model. The third column defines the matrix coefficients in terms of shear modulus and bulk modulus, which is a more natural pair of elasticity functions and often easier to implement. The equivalence between column 2 and 3 is given by the elasticity relationship,

$$B = G\frac{2(1+\nu)}{3(1-2\nu)} \qquad \text{Equation 3.6-2}$$

The motivation for choosing Poisson ratio as second elasticity function is because it easy to develop a smooth function that insures Poisson ratio remains within the admissible bounds, $0 \le \upsilon \le ½$. In contrast, the constraints on an independent bulk modulus function requires that $B > 2/3\ G$, which is more difficult to achieve with a smooth function.

3.6.2 Hardin shear modulus development

Hardin's formulation is based on experimental observations of soil behavior from standard tri-axial tests. A standard tri-axial test is conducted by placing a cylindrical soil specimen in a pressure chamber and initially subjecting the specimen to a uniform hydrostatic pressure, called σ_3. Next a steadily increasing axial load is applied to the specimen producing a net axial stress, called σ_1, which includes the hydrostatic pressure. Note that σ_3 and σ_1 are principal stresses in the lateral and axial directions, respectively. The difference in principal stresses $\sigma_1 - \sigma_3$ is equal to twice the maximum shear stress occuring on 45-degree plane.

As the axial stress increases, axial strain ε_1 is computed by measuring the axial shortening of the specimen divided by the specimen length. Similarly, the lateral strain ε_3 is measured at each load step so that the maximum shear stain is equal to $\varepsilon_1 - \varepsilon_3$. Note that ε_1 and ε_3 do not include the initial hydrostatic strain and the algebraic signs must be strictly observed in computing differences. The above concepts are summarized below.

$$\tau = \frac{1}{2}(\sigma_1 - \sigma_3) \qquad \text{Equation 3.6-3}$$

$$\gamma = \varepsilon_1 - \varepsilon_3 \qquad \text{Equation 3.6-4}$$

$$\tau = G_s\gamma \quad \text{(implied nonlinear relationship)} \qquad \text{Equation 3.6-5}$$

where, τ = accumulated shear stress from tri-axial test
γ = accumulated shear strain from tri-axial test
G_s = secant shear modulus, a function of stress and strain

The curve in Figure 3.6.2-1 is an idealized plot of shear stress versus shear strain for a typical tri-axial test. Here, G_{max} is the initial slope at zero shear strain and τ_{max} is the maximum shear strain at failure. As discussed subsequently, G_{max} and τ_{max} are dependent on the hydrostatic stress level.

Figure 3.6.2-1 Idealized shear stress-strain curve for tri-axial test

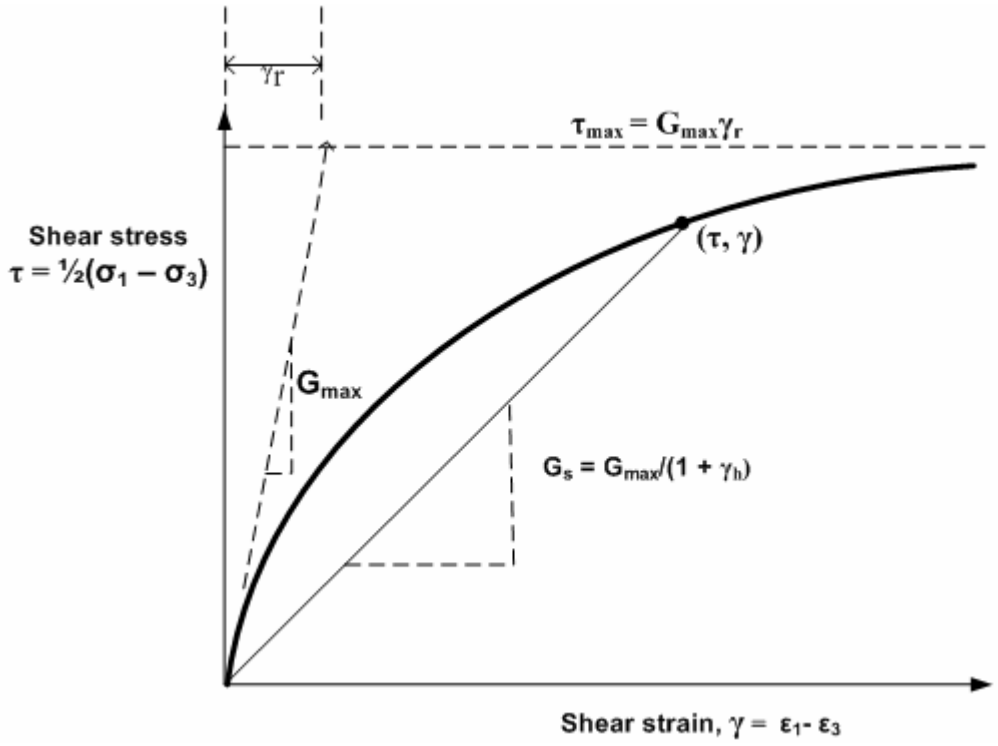

Hardin hyperbolic function. Hardin's fundamental insight is that for any tri-axial test, the shear stress-strain curve is fairly well approximated by equating the shear stress to a hyperbolic function of shear strain as follows,

$$\tau = \frac{G_{max}}{1+\gamma_h}\,\gamma \qquad \text{Equation 3.6-6}$$

$$\gamma_h = \frac{\gamma}{\gamma_r}\left(1 + \frac{\alpha}{\exp\left(\frac{\gamma}{\gamma_r}\right)^{0.4}}\right) \qquad \text{Equation 3.6-7}$$

$$\gamma_r = G_{max}/C_1 \qquad \text{Equation 3.6-8}$$

where, G_{max} = initial slope for shear modulus (dependent on hydrostatic stress)

γ_h = hyperbolic strain function

γ_r = reference shear stain

α = dimensionless soil parameter, related to soil type and percent saturation.

C_1 = soil parameter with units of stress, related to void ratio, percent saturation, and plasticity index.

As shear strain increases to infinity, the shear stress in Equation 3.6-6 approaches an asymptotic limit representing the maximum shear stress (or shear failure stress) given by,

$$\tau_{max} = G_{max}\gamma_r \qquad \text{Equation 3.6-9}$$

Initial shear modulus. Based on a wide variety of soil tests as typified by the above figure, Hardin discovered that the initial shear modulus increased in proportion with the square root of the initial tri-axial confining pressure as expressed below.

$$G_{max} = S_1\sqrt{\sigma_m} \qquad \text{Equation 3.6-10}$$

where, G_{max} = initial shear modulus when shear strain = 0

S_1 = soil parameter related to void ratio (units in $\sqrt{psi}$)

$\sigma_m = 1/3(\sigma_{11} + \sigma_{22} + \sigma_{33})$ = hydrostatic stress (units psi)

Equations 3.6-6 through 3.6-10 form the complete mathematical description of the Hardin secant shear modulus function, which is characterized by three soil model parameters, C_1 , S_1 and α. The direct method of determining the soil model parameters is to conduct a series of tri-axial tests on the particular soil being investigated. Alternatively, Hardin has developed an indirect method for determining soil parameters based on fundamental soil properties. Both the direct and indirect methods are presented below.

Direct method of soil parameter identification. Clearly the most accurate way to determine the shear modulus parameters, C_1 , S_1 and α, is to perform a series of tri-axial tests on the soil under investigation. For each confining pressure σ_3, it is required to plot an experimental stress-strain curves similar to Figure 3.6.2-1 and then follow the steps below.

1. Construct the initial tangent at zero shear stain and denote its value as G_{max}. Based in Equation 3.6-10, the parameter S_1 may be computed as follows.

   $$S_1 = G_{max}/\sqrt{\sigma_3} \qquad \text{Equation 3.6-11}$$

   Ideally each confining pressure would produce the same value for S_1. However since the model is not perfect, the final value for S_1 should be the average value determined from all initial confining pressures.

2. Using the measured value of G_{max} from step 1 along with the experimentally observed max shear stress τ_{max} , the parameter C_1 may be computed by combining Equations 3.6-8 and 3.6-9 as follows.

   $$C_1 = G_{max}^{\ 2}/\tau_{max} \qquad \text{Equation 3.6-12}$$

   In an ideal world, the computed value of C1 should be the same for all confining pressures. However since the model is not perfect, the final value for C_1 should be the average value determined from all initial confining pressures.

3. The third and last soil parameter α controls the shape (concavity)of the shear stress-strain curve in Figure 3.6.2-1. Since all parameters of the secant shear modulus model are known except α, Equation 3.6-6 may be applied at a single experimental data point (τ^*, γ^*) to provide an algebraic equation to solve for α. A natural data point to select is midway in the stress range, $\tau^* = \frac{1}{2}\tau_{max}$ along with the corresponding experimentally measured shear strain γ^*.

Indirect method of soil parameter identification. A particularly useful result of Hardin's work is that he developed an indirect method for determining soil parameters based on fundamental soil properties. This was accomplished by correlating the results of many tri-axial tests for many types soil with basic soil properties including void ratio, percent saturation, and plasticity index.

Listed below are the expressions he developed to quantify the soil parameters C_1 , S_1 and α for three broad classes of soil, granular, mixed and cohesive.

$$C_1 = \frac{F^2 R^2}{0.6 - 0.25(PI)^{0.6}} \quad \text{(units psi)} \qquad \text{Equation 3.6-13}$$

$$S_1 = 1230\ F \qquad \text{(units } \sqrt{\text{psi}}\text{)} \qquad \text{Equation 3.6-14}$$

$$\alpha = \begin{bmatrix} 3.2 & \text{for granular soil} \\ 2.54(1+0.02S) & \text{for mixed soil} \\ 1.12(1+0.02S) & \text{for cohesive soil} \end{bmatrix} \quad \text{(dimensionless)} \qquad \text{Equation 3.6-15}$$

where, $F = \dfrac{(2.973 - e)^2}{1 + e}$ for all soil types

$$R = \begin{bmatrix} 1100 & \text{for granular soil} \\ 1100 - 6.0\ S & \text{for mixed and cohesive soil} \end{bmatrix}$$

and, e = void ratio $(0 \le e \le 1)$
S = percent saturation $(0 \le S \le 100)$
PI = plasticity index $(0 \le PI \le 1)$

Thus knowing the type of soil, void ratio, percent saturation, and plasticity index, Hardin's secant shear modulus function is completely characterized without the need of a tri-axial test.

3.6.3 Poisson ratio development

Poisson ratio may be back calculated from tri-axial test data providing that principal stresses and principal strains are measured during the test. Reference 1 presents a study showing back-calculated values of Poisson ratio for a sequence of tri-axial tests with increasing confining pressure. Two significant findings from this study are summarized below.

1. For each individual tri-axial test with a specified confining pressure, the measured Poisson ratio increases as shear strain increases. Starting at a low value of approximately 0.01, the measured Poisson ratio asymptotically approaches an upper limit, nominally equal to 0.49, as the shear strain approaches the shear failure limit.

2. When confining pressure is increased, the starting and ending values of Poisson ratio remain the same as noted above, however the rate of increase of Poisson ratio with shear strain increases as confining pressure increases. Said another way, the measured value of Poisson ratio at a given level of shear strain is inversely related to the confining pressure. The above two observations are illustrated in Figure 3.6.3-1.

Figure 3.6.3-1 Illustration of measured Poisson ratio from tri-axial tests.

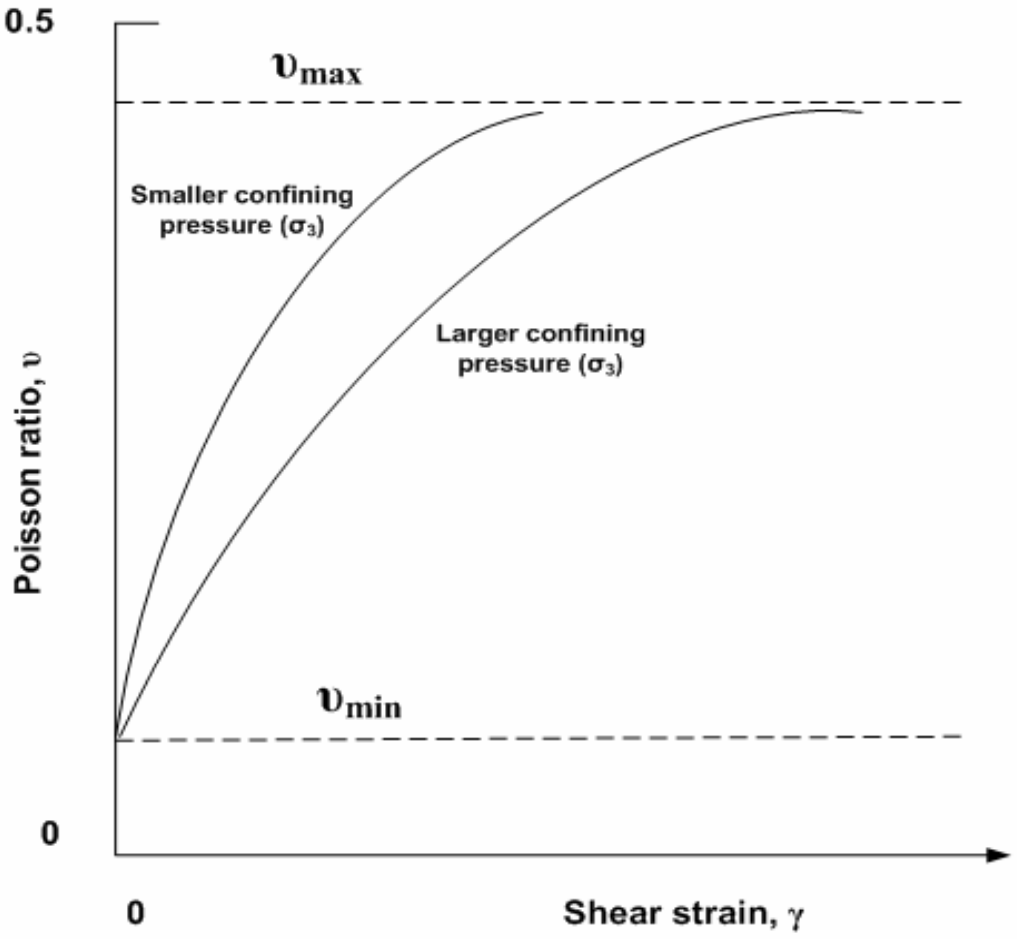

Poisson ratio function. A Poisson ratio function that simulates the above two observations is shown below, wherein γ_p is a scaled measure of shear stain.

$$\nu = \frac{\nu_{min} + \gamma_p \nu_{max}}{1 + \gamma_p} \qquad \text{Equation 3.6-16}$$

$$\gamma_p = \frac{q}{\gamma_r}\,\gamma \qquad \text{Equation 3.6-17}$$

where, ν = Poisson ratio function.

γ_p = scaled shear strain measure.

γ_r = Hardin reference shear strain (= G_{max}/C_1 from Equation 3.6-8)

and, ν_{min} = Poisson function parameter denoting minimum value (dimensionless constant)

ν_{max} = Poisson function parameter denoting maximum value (dimensionless constant)

q = Poisson function parameter controlling curve shape (dimensionless constant)

Upon inspecting the Poisson ratio function, it is clear that when shear strain is zero, $\nu = \nu_{min}$, and when shear strain becomes very large, $\nu = \nu_{max}$. Thus, the Poisson ratio function satisfies the first observation noted above. The second observation is achieved by defining γ_p with Hardin reference strain γ_r in the denominator as shown in Equation 3.16-7. Since γ_r is proportional to G_{max} and G_{max} is an increasing function of confining pressure, γ_p is reduced for tests with higher confining pressures so that the Poisson ratio function behaves as illustrated in the above.

It is important to realize that the predicted and observed variation in Poisson ratio as portrayed in Figure 3.6.3-1 is only for the case of a standard tri-axial loading environment. When Equation 3.6-16 is used to predict the behavior of Poisson ratio in a uniaxial-strain loading environment (K_0-test), the Poisson ratio prediction remains nearly constant as axial strain (or shear strain) increases. This is because the steadily increasing confining pressure increases the value of G_{max} at nearly the same rate as the increase in strain so that γ_p remains nearly constant in accordance with observed behavior.

Parameter identification. The Poisson ratio function requires identifying values for three model parameters, ν_{min}, ν_{max} and q. The study presented in Reference 1 measured Poisson ratio values from five tri-axial tests with confining pressures ranging from 25 psi to 250 psi. The soil specimens were dry, dense sand, and the model parameters identified as,

$$\nu_{min} = 0.10$$

$$\nu_{max} = 0.49$$

$$q = 0.26$$

Choosing values for ν_{min} and ν_{max} are straightforward observations from the experimental data, and the selection of the shape parameter q is determined by standard curve fitting techniques. The study concludes that the Poisson ratio function with the above parameter values is in excellent agreement with the measured Poisson ratio data points for all five tri-axial tests.

Of course, it is always best to conduct tri-axial tests on new soils to identify the parameters of the Poisson ratio function. However, experience has shown that ν_{min}, ν_{max} and q are not overly sensitive to the type of soil and soil properties, thus if no other data is available the above parametric values are fairly reasonable for all soil types.

3.6.4 Summary of extended Hardin soil model functions

The extended Hardin soil model is composed of the secant shear modulus function and the Poisson ratio function both of which are functions of maximum shear strain and hydrostatic pressure.

The secant shear modulus function is given by the following function and sub functions.

$$G_s = \frac{G_{max}}{1+\gamma_h} \quad \text{= shear modulus function} \qquad \text{Equation 3.6-18}$$

$$\gamma_h = \frac{\gamma}{\gamma_r}\left(1 + \frac{\alpha}{\exp\left(\frac{\gamma}{\gamma_r}\right)^{0.4}}\right) \quad \text{= hyperbolic strain function} \qquad \text{Equation 3.6-19}$$

$$\gamma_r = G_{max}/C_1 \text{ = reference shear stain} \qquad \text{Equation 3.6-20}$$

$$G_{max} = S_1\sqrt{\sigma_m} \text{ = initial shear modulus when shear strain = 0} \qquad \text{Equation 3.6-21}$$

where, γ = maximum shear strain

$\sigma_m = 1/3(\sigma_{11} + \sigma_{22} + \sigma_{33})$ = hydrostatic stress (units psi)

and, S_1 = soil parameter related to void ratio (units in $\sqrt{\text{psi}}$)

α = soil parameter, related to soil type and percent saturation (dimensionless)

C_1 = soil parameter related to void ratio, percent saturation, and plasticity index (units psi)

Parameter identification for C_1 , S_1 and α may be accomplished directly with tri-axial tests as outlined in the discussion associated with Equations 3.6-11 and 3.6-12. Alternatively the parameters may be quantified by the indirect method outlined with the discussion associated with Equations 3.6-13, -14, and –15.

The Poisson ratio function is given by the following function and sub functions.

$$\nu = \frac{\nu_{min} + \gamma_p \nu_{max}}{1 + \gamma_p} \quad = \text{Poisson ratio function} \qquad \text{Equation 3.6-22}$$

$$\gamma_p = \frac{q}{\gamma_r}\,\gamma \quad = \text{scaled shear strain measure} \qquad \text{Equation 3.6-23}$$

where, γ_r = Hardin reference shear strain (= G_{max}/C_1 from Equation 3.6-20)

and, ν_{min} = Poisson function parameter denoting minimum value (dimensionless constant)

ν_{max} = Poisson function parameter denoting maximum value (dimensionless constant)

q = Poisson function parameter controlling curve shape (dimensionless constant)

Parameter identification for ν_{min}, ν_{max} and q may be accomplished with tri-axial tests as outlined in the discussion in Section 3.6.3. If no independent test data is available, the default values, ν_{min}, = 0.1, ν_{max} = 0.49, and q = 0.26 are reasonable for all soil types.

The overall behavior of the extended Hardin soil model mimics the actual behavior of soil. The model exhibits a stiffening behavior when confining pressure dominates shear strain, and conversely a softening behavior when shear strain dominates confining pressure.

Lastly, it is emphasized the extended Hardin soil model is a nonlinear elasticity model and behaves the same in loading or unloading. Like the Duncan and Duncan/Selig soil models, additional research needs to be done in order to incorporate plasticity-like concepts into the model so that unloading behavior can be simulated without violating energy theorems and continuity principles.

3.6.5 Implementation of soil models and nonlinear solution strategy

To implement the extended Hardin model into the plane-strain constitutive matrix given by Equation 3.6-1, it is more convenient to use the bulk modulus function with the shear modulus function (G, B) rather than the Poisson ratio function (G ,ν) as was indicated in Table 3.6.1-1. The bulk modulus function is related to the extended Hardin functions by elasticity identity relationships as,

$$B_s = G_s \frac{2(1+\nu)}{3(1-2\nu)} \qquad \text{Equation 3.6-24}$$

where, B_s = secant bulk modulus function

G_s = secant shear modulus function (Equation 3.6-18)

ν = Poisson ratio function (Equation 3.6-22)

Letting σ_1, σ_2, σ_3 be the total principal stresses and ε_1, ε_2 and ε_3 the corresponding total principal stains, then, the secant moduli (G_s, B_s) relate total stress quantities to total strain quantities as follows.

$$\tau = G_s \gamma \qquad \text{Equation 3.6-25}$$

$$\sigma_m = B_s \varphi \qquad \text{Equation 3.6-26}$$

where, $\tau = (\sigma_1 - \sigma_3)/2$ = maximum shear stress

$\gamma = \varepsilon_1 - \varepsilon_3$ = maximum shear strain

$\sigma_m = (\sigma_1 + \sigma_2 + \sigma_3)/3$ = mean stress or hydrostatic stress

$\varphi = \varepsilon_1 + \varepsilon_2 + \varepsilon_3$ = volumetric strain

Chord moduli representation. To progress from load step i to load step i+1, the moduli must be expressed as incremental chord moduli, which are related to secant moduli as illustrated in the figures below.

Figure 3.6.5-1 Chord modulus relationship to secant modulus for shear modulus.

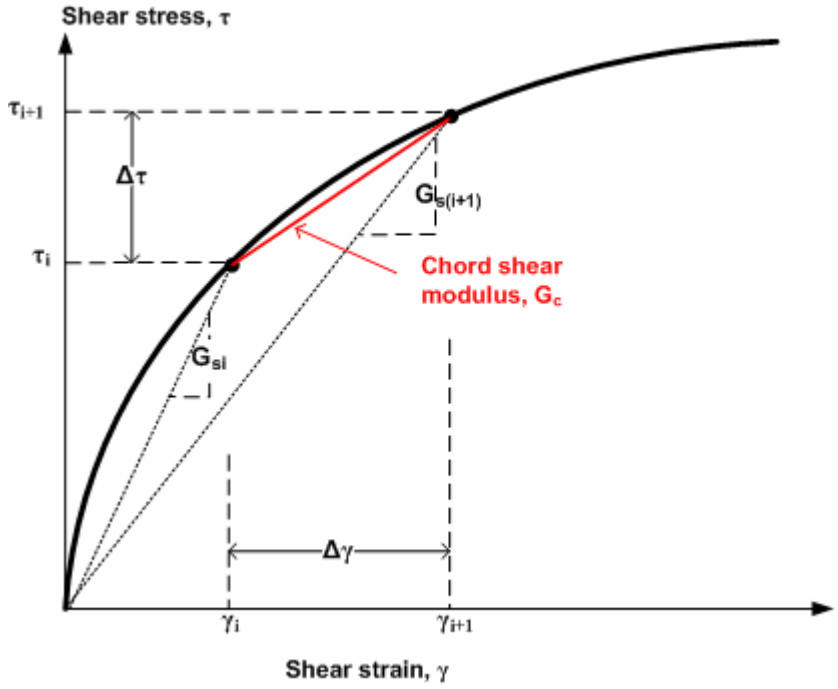

Figure 3.6.5-2 Chord modulus relationship to secant modulus for bulk modulus.

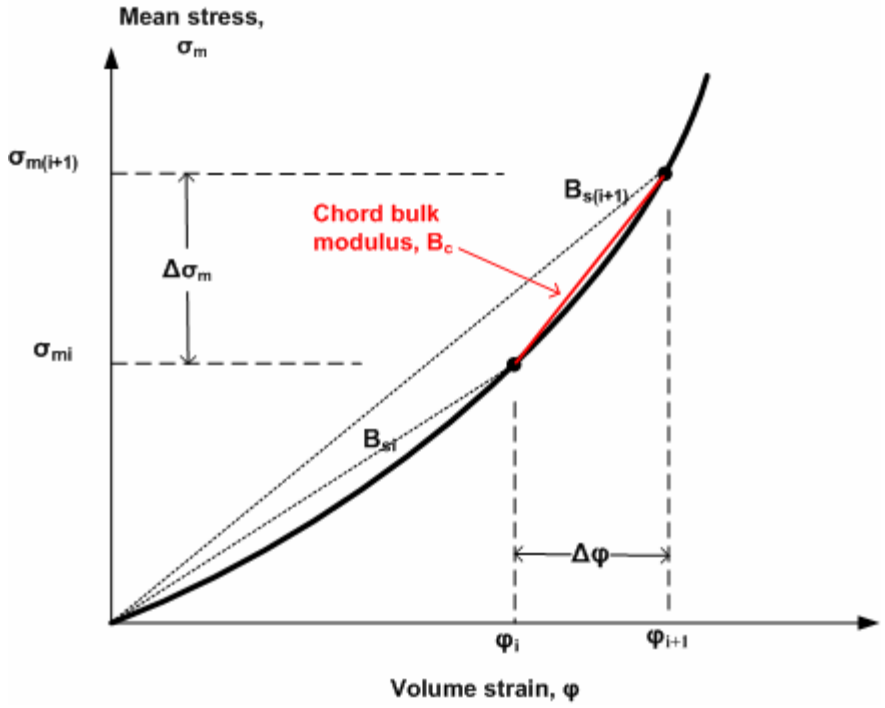

The incremental relationships between load step i and i+1 as portrayed in the above figures are defined below.

$$\Delta\tau = G_c \Delta\gamma \qquad \text{Equation 3.6-27}$$

$$\Delta\sigma_m = B_c \Delta\varphi \qquad \text{Equation 3.6-28}$$

$$G_c = \frac{G_{s(i+1)}\gamma_{i+1} - \tau_i}{\gamma_{i+1} - \gamma_i} \qquad \text{Equation 3.6-29}$$

$$B_c = \frac{B_{s(i+1)}\varphi_{i+1} - \sigma_{m(i)}}{\varphi_{i+1} - \varphi_i} \qquad \text{Equation 3.6-30}$$

where, G_c = chord shear modulus from load step i to i+1

B_c = chord bulk modulus from load step i to i+1

$\Delta\tau = \tau_{i+1} - \tau_i$ = shear stress increment

$\Delta\gamma = \gamma_{i+1} - \gamma_i$ = shear strain increment

$\Delta\sigma_m = \sigma_{m(i+1)} - \sigma_{mi}$ = mean stress increment

$\Delta\varphi = \varphi_{i+1} - \varphi_i$ = volumetric strain increment.

Nonlinear solution strategy. The solution strategy is based on a direct iterative approach, also called trial and error.

We begin with the understanding that we have a converged solution at load step i so that we know the total stress and total strain state, $\underline{\sigma}_i$ and $\underline{\varepsilon}_i$, respectively. Our objective is to advance the solution to load step i+1 following the steps below.

1. To obtain the first trial solution, assume the values for G_c and B_c remain the same as they were for load step i for each individual element.

2. Construct the element stiffness matrix using G_c and B_c to define the current constitutive matrix for each element (Equation 3.6-1)

3. Assemble the global stiffness matrix and load increment vector for step i+1. Solve the system for a trial solution and recover current estimates for increments of stress and strain vectors. Update trial vectors for total stress and strain as indicated below.

   $\Delta\underline{\varepsilon}$ = incremental strain vector determined from strain-displacement relationship.

   $\Delta\underline{\sigma}$ = incremental stress vector determined from current constitutive matrix

   $$\underline{\varepsilon}_{i+1} = \underline{\varepsilon}_i + \Delta\underline{\varepsilon}$$
   $$\underline{\sigma}_{i+1} = \underline{\sigma}_i + \Delta\underline{\sigma}$$

4. Based on the known stress-strain state at step i and the estimated stress-strain state at step i+1, compute new estimates for G_c and B_c .

   $$G_c = \frac{G_{s(i+1)}\gamma_{i+1} - \tau_i}{\gamma_{i+1} - \gamma_i}$$ (see Equation 3.6-18)

   $$B_c = \frac{B_{s(i+1)}\varphi_{i+1} - \sigma_{m(i)}}{\varphi_{i+1} - \varphi_i}$$ (see Equations 3.6-18,-22,-24)

5. If G_c and B_c computed in step 4 are sufficiently close to the previous estimates, say within 1% difference, then the load step has converged, the solution is saved, and control shifts back to step 1 to advance to the next load step. Otherwise, the iterative process continues wherein the incremental solution is discarded and control shifts back to step 2 to repeat the load increment using the new values for G_c and B_c to get a new trial solution.

Typically the above algorithm converges for all elements in three to ten iterations for each load step, depending on the scope of the problem. Convergence means that static equilibrium and the constitutive matrix are simultaneously satisfied.

4 INTERFACE ELEMENT

This chapter presents the development of a simple friction-contact interface element that simulates frictional slippage, separation, and re-bonding of two bodies initially mating at a common interface and subsequently deforming under an arbitrary static loading schedule. Constraint equations between initially mating pairs of nodes and the general principle of virtual work are used to formulate the interface element for a finite element solution methodology. The practical application of the interface elements is to mimic the behavior of the interface between a culvert and backfill soil by simulating frictional slippage of the soil over the pipe wall during the backfilling operations. Similarly, the model is useful for simulating the slippage of backfill soil along trench walls for steep walled trench installations. The model is also useful for enforcing a pinned connection between pipe element groups.

4.1 Introduction

CANDE's interface element dates back to its original development in 1976, which is documented in Reference 1 and published in the open literature in Reference 24. Today, the interface element remains as originally developed with a few minor modifications to enhance convergence. Engineering literature contains a variety of interface element formulations; however, they can generally be classified as either a stiffness approach (e.g. directionally stiff elements) or a constraint approach typically formulated with the use of Lagrange multipliers. The constraint approach is used in this development, however rather than using Lagrange multipliers, the development is based on a novel extension of virtual work, which in itself became a contribution to FEM technology. Motivations for adopting the constraint approach include, avoidance of numerical round-off problems inherent in the stiffness approach, direct control of interface forces and relative movements, accuracy, and ease of FEM implementation.

The interface element is capable of responding to a general step-by-step loading history, such that tensile separation, frictional sliding, or complete bonding (or re-bonding) is possible during any load step. Two nodes, one on either side of an interface, defined by the interface angle, are used to establish the interface element along with a third "dummy node" to represent interface forces. By selectively applying constraint equations to the interface nodes in an incremental-iterative solution procedure, the behavior of a contact-friction interface is simulated.

Two computational advantages are inherent in the interface element. First, unlike the traditional Lagrange-multiplier method that requires a minimization principle, the virtual work formulation is not restricted to conservative systems. Secondly, the formulation results in an element 'constraint matrix' and element 'load vector' analogous to a typical element stiffness matrix and load vector. Thus, the interface element can be assembled into the global equations by standard techniques.

4.2 Virtual Work and Constraint Equations

In Chapter 1, the traditional virtual work formulation is presented without constraints resulting in the classical, stiffness-based finite equations expressed in a scalar virtual work statement as,

$$\delta\hat{u}^T(\underline{K}\Delta\hat{u} - \Delta P) = 0 \qquad \text{Equation 4.2-1}$$

where, $\Delta\hat{u}$ = incremental unknown nodal displacements
$\underline{K}$ = current global stiffness matrix (generally nonlinear)
ΔP = incremental load vector.

Since δu^T is an arbitrary virtual displacement, the satisfaction of Equation 4.2-1 requires that $\underline{K}\Delta u = \Delta P$, usually solved iteratively to find displacements.

If Equation 4.2-1 represented a finite element model of two separate bodies initially in contact at node pairs as suggested in Figure 4.2-1, then the bodies can deform independently resulting in overlapping and/or separation along the interface. At the other extreme, if the node pairs at the interface are constrained to move together, a completely bonded response is obtained. Between these two extremes, a slipping response can be obtained by constraining only the displacements normal to the interface at each node pair.

Figure 4.2-1 Idealization of two bodies with initially mating node pairs along interface

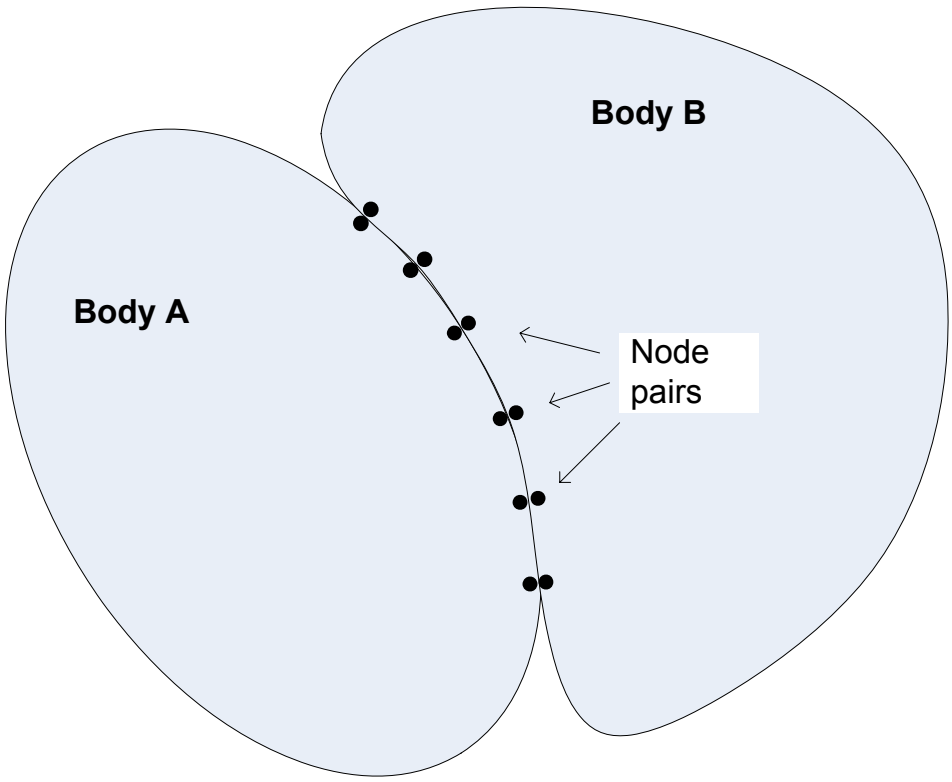

4.2.1 Constraint equations general form

To achieve the above, the immediate objective is to incorporate an arbitrary set of constraint equations into a global virtual work statement. Formally, any set of algebraic nodal point constraint equations can be expressed as:

$$\underline{C}\Delta\hat{u} - \Delta\hat{a} = \hat{0} \qquad \text{Equation 4.2-2}$$

where, $\underline{C}$ = constraint coefficient matrix

$\Delta\hat{u}$ = subset of nodal degrees of freedom being constrained

$\Delta\hat{a}$ = vector of specified constants (for example, displacement gaps)

$\hat{0}$ = vector of zeroes, one zero for each constraint equation.

To fix ideas by means of a simple example, suppose it is desired to constrain one node in body A to be glued (fixed) to the partner node in body B with no displacement gap between the node pair. In this case, Equation 4.2-2 would be written in expanded notation as,

$$\begin{pmatrix} -1 & 0 & 1 & 0 \\ 0 & -1 & 0 & 1 \end{pmatrix} \begin{pmatrix} u_{Ax} \\ u_{Ay} \\ u_{Bx} \\ u_{By} \end{pmatrix} - \begin{pmatrix} 0 \\ 0 \end{pmatrix} = \begin{pmatrix} 0 \\ 0 \end{pmatrix}$$

In the above example we are simply imposing the two constraint equations, $u_{Ax} = u_{Bx}$ and $u_{Ay} = u_{By}$, which forces the x and y displacement component of the node in body A to be equal to those of the paired node in body B.

Associated with each constraint equation, there exists an unknown internal constraint force λ enforcing the constraint. For convenience, Equation 4.4-2 can be expressed in a scalar (work) form as:

$$\delta\hat{\lambda}^T(\underline{C}\Delta\hat{u} - \Delta\hat{a}) = 0 \qquad \text{Equation 4.2-3}$$

where, $\hat{\lambda}$ = vector of interface constraint forces, one force component for each constraint equation.

Since $\delta\hat{\lambda}$ is an arbitrary variation of the constraint force vector, Equation 4.2-3 is satisfied if and only if the constraint equations are satisfied.

As yet the virtual work of constraint forces has not been established or defined. To this end, we argue that the internal constraint forces produce internal virtual work when the constraint is given a small virtual movement (variation) as follows.

$$VW_{constraint} = \delta(\underline{C}\Delta\hat{u} - \Delta\hat{a})^T\Delta\hat{\lambda} = \delta\hat{u}^T\underline{C}^T\Delta\hat{\lambda} \qquad \text{Equation 4.2-4}$$

In the above definition for the incremental virtual work of constraints, we assume the system is equilibrium at load step i and moves to a new equilibrium position at load step i+1 consistent with the incremental constraint equations, which in turn generate incremental constraint forces, $\Delta\lambda$. When the constraints are given a small virtual disturbance (variation), the constraint forces perform virtual work as they move with the virtual disturbance. Physically, this is analogous to imposing constraints with stiff springs between node pairs wherein the internal spring force corresponds to the constraint force. However, in this case the constraint forces are primary unknowns.

4.2.2 Global virtual work statement with constraints

With the above understandings, we complete the formulation by adding the internal virtual work of constraints (Equation 4.2-4) to the standard virtual work statement in Equation 4.2-1 and append the constraint requirement in Equation 4.2-3 to get the general virtual work statement including constraints.

$$\begin{pmatrix} \delta\hat{u} \\ \delta\hat{\lambda} \end{pmatrix}^T \left(\begin{pmatrix} \underline{K} & \underline{C}^T \\ \underline{C} & \underline{0} \end{pmatrix} \begin{pmatrix} \Delta\hat{u} \\ \Delta\hat{\lambda} \end{pmatrix} - \begin{pmatrix} \Delta P \\ \Delta\hat{a} \end{pmatrix} \right) = 0 \qquad \text{Equation 4.2-5}$$

Since the virtual displacements and virtual constraint forces are arbitrary, the virtual work statement leads to the following global system of equations.

$$\begin{pmatrix} \underline{K} & \underline{C}^T \\ \underline{C} & \underline{0} \end{pmatrix} \begin{pmatrix} \Delta\hat{u} \\ \Delta\hat{\lambda} \end{pmatrix} = \begin{pmatrix} \Delta P \\ \Delta\hat{a} \end{pmatrix} \qquad \text{Equation 4.2-6}$$

The coupled set of global matrix equations is to be solved for nodal displacements and constraint forces. Note that the separate partitioning of the global system into Δu and $\Delta\lambda$ is a mere formality and not required in actual global assembly.

4.2.3 General element constraint matrix and load vector

Recalling that the global stiffness equations are formed from the summation element stiffness matrices and load vectors based on the element's contributions to total virtual work, we can in the same manner construct an element constraint matrix and load vector based on the constraint element's contribution to the virtual work as shown below.

$$\delta V_{\substack{\text{contstraint} \\ \text{element}}} = \begin{pmatrix} \delta\hat{u}_e \\ \delta\hat{\lambda}_e \end{pmatrix}^T \left(\begin{pmatrix} \underline{0} & \underline{C}_e^T \\ \underline{C}_e & \underline{0} \end{pmatrix} \begin{pmatrix} \Delta\hat{u}_e \\ \Delta\hat{\lambda}_e \end{pmatrix} - \begin{pmatrix} \hat{0} \\ \Delta\hat{a}_e \end{pmatrix} \right) \qquad \text{Equation 4.2-7}$$

Since the above expression represents the contribution of a general constraint element to the global virtual work statement given by Equation 4.2-5, the element-level constraint matrix and load vector are established as follows.

$$\underline{C}^* = \begin{pmatrix} \underline{0} & \underline{C}_e^T \\ \underline{C}_e & \underline{0} \end{pmatrix} \qquad \text{Equation 4.2-8}$$

$$\hat{f} = \begin{pmatrix} \hat{0} \\ \Delta\hat{a}_e \end{pmatrix} \qquad \text{Equation 4.2-9}$$

where, C^* = symmetric element constraint matrix, dimension (n+m) x (n+m)
$\underline{C}_e$ = constraint coefficient matrix for element, dimension m x n
$\hat{f}$ = incremental load vector of zeros and displacement gaps, dimension n+m
$\Delta\hat{a}$ = specified incremental displacement gaps, dimension m
m = number of constraint equations associated with element (m = 2 for interface element)
n = number of constrained degrees of freedom within element (n= 4 for interface element)

Just as the global stiffness matrix is assembled by a summation of element stiffness matrices $\underline{k}^*$, the global constraint matrix is assembled by a summation of element constraint matrices $\underline{C}^*$. Similarly, the global constraint load vector is assembled by a summation of element load vectors $\hat{f}$.

4.3 Interface Element Matrix and Load Vector

To specialize the foregoing to friction-contact interfaces, we assume that any interface can be modeled as a sequence of node pairs (Figure 4.2-1), so that attention can be focused on a single node pair that forms an interface element.

4.3.1 Definition of interface element

The interface element is composed two nodes on either side of a common interface plus an interior node (a stand alone node K) that represents interface forces. Figure 4.3.1-1 shows an exploded view of the interface element.

Figure 4.3.1-1 Interface element exploded view defining normal and tangential directions

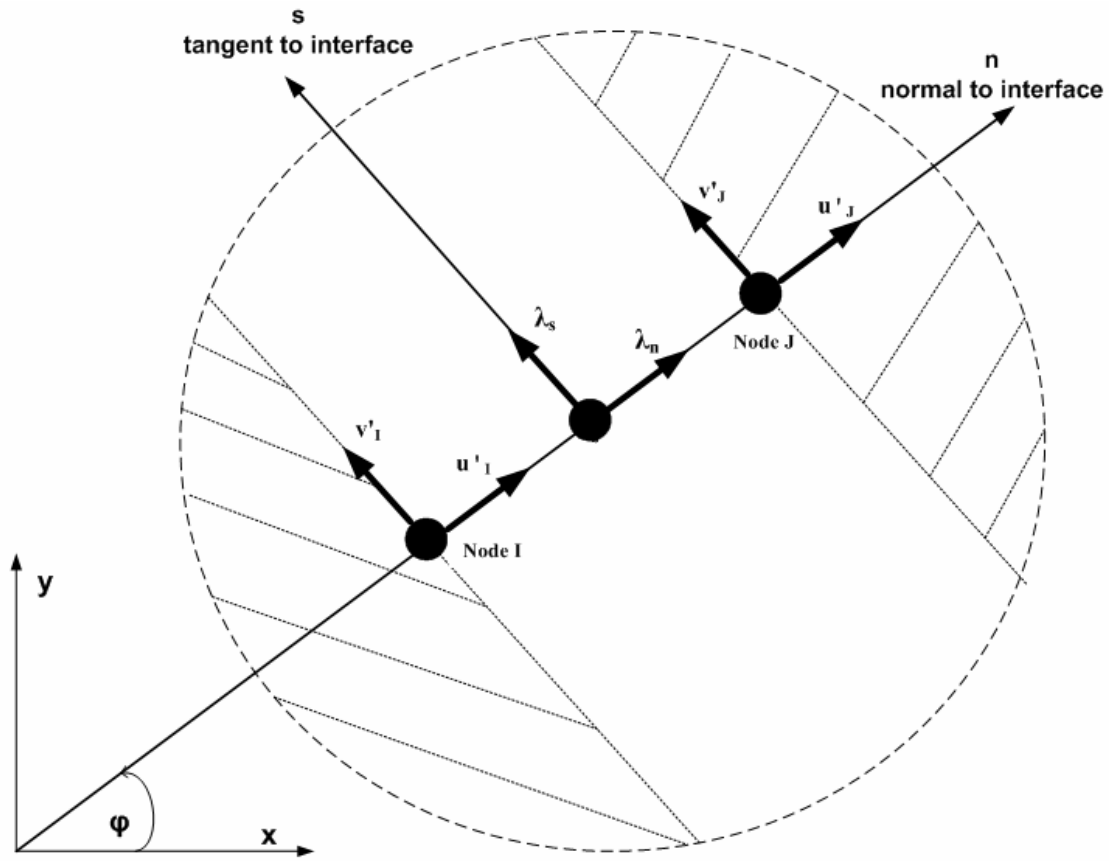

Here, the interface element is defined in the local n, s coordinates, rotated φ degrees from the global x, y coordinate system. Node I belongs to the body on one side of the interface and Node J belongs to the body on the other side of the interface. Node I and J are initially assigned to the same x, y coordinate location prior to loading. The positive normal direction is in the direction of travel from node I to node J. Nodal displacement components in the n-s system are marked with a prime to distinguish them from the unprimed components in the x-y system.

Physical properties assigned to the interface element are listed below.

μ = coefficient of friction (Coulomb type)

β = tensile rupture force (typically = 0)

φ = angle of the interface normal with respect to x-axis

The coefficient of friction and tensile rupture force are discussed subsequently, however it should be evident that if these properties are assigned very large numbers the interface will remain bonded (fixed) regardless of the interface angle and internal forces.

4.3.2 Incremental and total responses (notation)

As with all developments in this manual, the interface element is an incremental relationship from load step i to load step i+1. Letting the symbol q represent any interface response, we adopt the following notation for incremental relationships.

$$q^{i+1} = q^{i} + \Delta q \qquad \text{Equation 4.3-1}$$

where, q^{i+1} = total response at load step i+1

q^{i} = total response at load step i

Δq = incremental response from step i to i+1

The following list defines interface response notation represented by the symbol q

u'_I = displacement of node I in the normal direction.

u'_J = displacement of node J in the normal direction

v'_I = displacement of node I in the tangent direction.

v'_J = displacement of node J in the tangent direction.

λ_n = normal force between node I and J

λ_s = tangent force between node I and J

u_I = displacement of node I in the global x direction.

u_J = displacement of node J in the global x direction

v_I = displacement of node I in the global y direction.

v_J = displacement of node J in the global y direction.

d_n = interface gap distance in normal direction

d_s = interface gap distance in tangent direction

Interface gap distances are illustrated in the figure below for load step i wherein the two bodies have separated at nodes I and J producing normal and tangential gaps between the nodes.

Figure 4.3.1-1 Interface element in separated state at load step i.

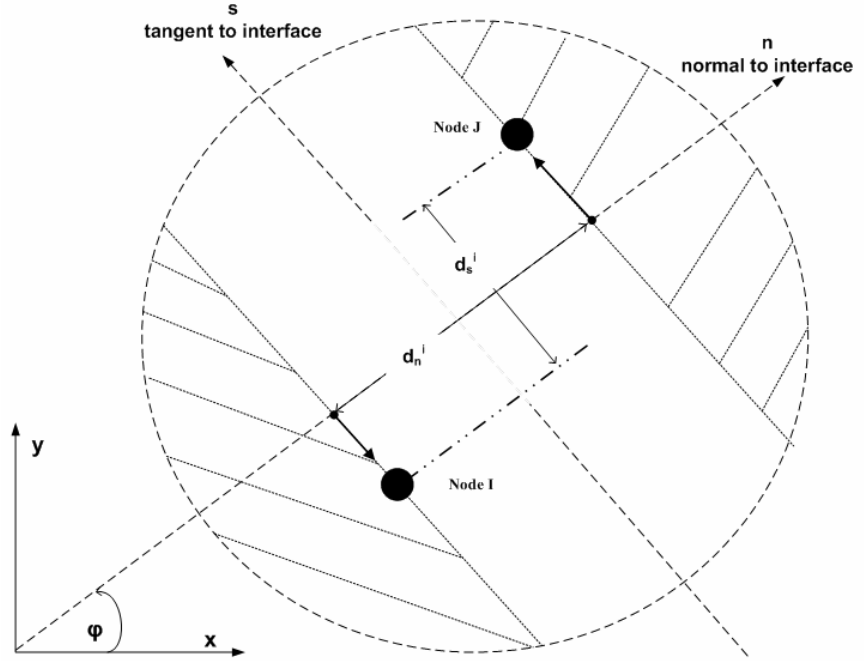

The total normal gap and the total tangential gap at load step i are determined by the difference of nodal displacement components in the n-s coordinates as given below.

$$d_n^{\,i} = u'^{i}_J - u'^{i}_I \qquad \text{Equation 4.3-2a}$$

$$d_s^{\,i} = v'^{i}_J - v'^{i}_I \qquad \text{Equation 4.3-2b}$$

4.3.3 Element constraint matrices and load vectors for three interface states.

We now identify three 'interface states' that may be imposed during a load step depending on the current responses of the interface element. The three states are called fixed, slip, and free. In each case we will define the element constraint matrix and load vector.

Fixed State. The fixed state means that nodes I and J are constrained to move during the load step such that specified incremental gaps will occur in the normal and tangent direction (usually the incremental gaps are specified to be zero). In the local n-s coordinates system the fixed state is expressed with the following two constrain equations.

$$-\Delta u'_I + \Delta u'_J = \Delta a \qquad \text{Equation 4.3-3}$$

$$-\Delta v'_I + \Delta v'_J = \Delta b \qquad \text{Equation 4.3-4}$$

where, Δa = specified normal gap increment (often zero)
Δb = specified tangential gap increment (often zero)

Since the global equations require that displacement components be expressed in x-y coordinates, the primed displacement components are transformed to x-y displacement components by standard coordinate transformation techniques so that the above constraint equations become,

$$\begin{pmatrix} -\cos\varphi & -\sin\varphi & \cos\varphi & \sin\varphi \\ \sin\varphi & -\cos\varphi & -\sin\varphi & \cos\varphi \end{pmatrix} \begin{pmatrix} \Delta u_I \\ \Delta v_I \\ \Delta u_J \\ \Delta v_J \end{pmatrix} = \begin{pmatrix} \Delta a \\ \Delta b \end{pmatrix} \qquad \text{Equation 4.3-5}$$

Here the 2x4 matrix is the constraint coefficient matrix $\underline{C}_e$ that is imbedded in the symmetric element constraint matrix $\underline{C}^*$ defined by Equation 4.2-8. The right hand side is the specified incremental gap vector for the element load vector defined in Equation 4.2-9. If Δa and Δb are both specified zero, then the normal gap and tangential gap do not change during the load step, i.e. both nodes experience identical displacement increments. If, on the other hand, we wish to return the nodes to their initial position (no gaps), we specify Δa and Δb equal to the total displacement gaps defined in Equations 4-3-2a,b.

The fixed state is summarized in the top portion of Table 4.3.3-1, which explicitly defines the element constraint matrix $\underline{C}^*$ and the element load vector. These may be assembled in the global system just like element stiffness matrix.

Table 4.3.3-1 Element constraint matrix $\underline{C}^*$ (6x6) and load vector $\hat{f}$ (6x1) for three interface states.

State	Δu_I	Δv_I	Δu_J	Δv_J	$\Delta\lambda_n$	$\Delta\lambda_s$	$\hat{f}$ (load)
Fixed	**0**	**0**	**0**	**0**	**-c**	**s**	**0**
	0	**0**	**0**	**0**	**-s**	**-c**	**0**
	0	**0**	**0**	**0**	**c**	**-s**	**0**
	0	**0**	**0**	**0**	**s**	**c**	0
	-c	**-s**	**c**	**s**	**0**	**0**	**Δa**
	s	**-c**	**-s**	**c**	**0**	**0**	**Δb**
Slip	**0**	**0**	**0**	**0**	**-c**	**0**	**-sΔT**
	0	**0**	**0**	**0**	**-s**	**0**	**cΔT**
	0	**0**	**0**	**0**	**c**	**0**	**sΔT**
	0	**0**	**0**	**0**	**s**	**0**	**-cΔT**
	-c	**-s**	**c**	**s**	**0**	**0**	**Δa**
	0	**0**	**0**	**0**	**0**	**1**	**ΔT**
Free	**0**	**0**	**0**	**0**	**0**	**0**	**cΔN - sΔT**
	0	**0**	**0**	**0**	**0**	**0**	**sΔN + cΔT**
	0	**0**	**0**	**0**	**0**	**0**	**-cΔN + sΔT**
	0	**0**	**0**	**0**	**0**	**0**	**-sΔN - cΔT**
	0	**0**	**0**	**0**	**1**	**0**	**ΔN**
	0	**0**	**0**	**0**	**0**	**1**	**ΔT**

$c = \cos\varphi$, and $s = \sin\varphi$

Slip State. The slipping state is defined by constraining the normal displacement increments of nodes I and J such that a specified incremental gap will occur in the normal direction during the load increment. The tangential displacement constraint is suppressed and replaced with a specification for the incremental interface force in the tangent direction. Specifically, the slip state is expressed with the following constraint equation and force equation in the n-s system.

$$-\Delta u'_I + \Delta u'_J = \Delta a \qquad \text{Equation 4.3-6}$$

$$\Delta\lambda_s = \Delta T \qquad \text{Equation 4.3-7}$$

where, Δa = specified normal gap increment (often zero)
ΔT = specified increment of tangential force between nodes I and J

Since other types of elements share nodes I and J, the n-s displacement components must be transformed to the common x-y system for global assembly and solution. Thus the above constraint equation is transformed to x-y system as shown below.

$$\begin{pmatrix} -\cos\varphi & -\sin\varphi & \cos\varphi & \sin\varphi \end{pmatrix}^T \begin{pmatrix} \Delta u_I \\ \Delta v_I \\ \Delta u_J \\ \Delta v_J \end{pmatrix} = \Delta a \qquad \text{Equation 4.3-8}$$

With regard to the force equation (Equation 4.3-7), it may be retained in the n-s coordinate system because the dummy node K containing the interface forces is not shared with any other element.
Whenever we suppress a constraint and specify $\Delta\lambda_s = \Delta T$, we must also assign a positive ΔT force to node I and a negative ΔT force to node J thereby effecting the interface force on the nodes. Also we must transform these forces to x-y system for proper assembly in the global load vector as shown in the load vector column in Table 4.3.3-1.

The slipped state is summarized in the central portion of Table 4.3.3-1. Here the $\underline{C}^*$ matrix contains one constraint equation and force equation ($\lambda_s = T$), wherein the matrix size remains 6 x 6 for computational convenience. As discussed above, the load vector includes force components at nodes I and J from the specified interface force, ΔT.

To simulate a friction-contact interface, Coulomb-type friction is assumed so that the maximum possible interface tangent force in advancing from load step i to i+1 is a function of the normal compressive force and given by,

$$F^{i+1} = \mu \left|\lambda_n{}^{i+1}\right| \mathrm{sgn}(\lambda_s{}^{i+1}) \qquad \text{Equation 4.3-9}$$

where, F^{i+1} = maximum Coulomb frictional force at step i+1 (signed)
μ = coefficient of friction

$$\mathrm{sgn}(\lambda_s{}^{i+1}) = \begin{cases} +1, \text{ for } \lambda_s{}^{i+1} > 0 \\ -1, \text{ for } \lambda_s{}^{i+1} < 0 \end{cases}$$

With the above understanding, a frictional slipping interface requires that the specified incremental tangent force from load step i to i+1 satisfy the equilibrium condition as written below.

$$\Delta T = F^{i+1} - \lambda_s{}^i \qquad \text{Equation 4.3-10}$$

where, $\lambda_s{}^i$ = known tangential interface force at load step i.

Of course, ΔT is recomputed by iterating within the load step until two successive values of F^{i+1} are acceptably close, say within 1%.

Free State. The free state is defined by suppressing both constraint equations and specifying the normal and tangent interface force increments as shown below.

$$\Delta\lambda_n = \Delta N \qquad \text{Equation 4.3-11}$$

$$\Delta\lambda_s = \Delta T \qquad \text{Equation 4.3-12}$$

where, ΔN = specified increment of normal force between nodes I and J
ΔT = specified increment of tangential force between nodes I and J

Again, the above force equations may be expressed in the n-s coordinate system because the dummy node K containing the interface forces is not shared with any other element. In addition, the specified interface forces ΔN and ΔT must be assigned to nodes I and J, positive for node I and negative for node J. Also these forces must be transformed to x-y system for proper assembly in the global load vector.

The free state is summarized in the bottom portion of Table 4.3.3-1. Here the $\underline{C}^*$ matrix is all zeros except $\underline{C}^*$ (5,5) = $\underline{C}^*$ (6,6) = 1 that enforces the equations $\Delta\lambda_n = \Delta N$ and $\Delta\lambda_s = \Delta T$. Again, the matrix size remains 6 x 6 for computational convenience. Lastly, the load vector includes x-y force components at nodes I and J from the specified interface forces.

4.4 Nonlinear Solution Strategy for Interface

The problem is posed as follows. We assume we know the interface solution at end of load step i, which includes converged solutions for the following accumulated interface responses.

$\lambda_n^{\,i}$, $\lambda_s^{\,i}$ = total interface normal and tangent interface forces at end of load step i.

$d_n^{\,i}$, $d_s^{\,i}$ = total interface normal and tangent displacement gaps at end of load step i.

We seek to determine an incremental solution ($\Delta\lambda_n$, $\Delta\lambda s$, Δd_n, Δd_s) to achieve a valid solution for the total interface responses at the end of load step i+1 computed as follows.

$$\lambda_n^{\,i+1} = \lambda_n^{\,i} + \Delta\lambda_n \qquad \text{Equation 4.4-1}$$

$$\lambda_s^{\,i+1} = \lambda_s^{\,i} + \Delta\lambda_s \qquad \text{Equation 4.4-2}$$

$$d_n^{\,i+1} = d_n^{\,i} + \Delta d_n \qquad \text{Equation 4.4-3}$$

$$d_s^{\,i+1} = d_s^{\,i} + \Delta d_s \qquad \text{Equation 4.4-4}$$

By a valid solution we mean the physical compatibility and equilibrium conditions of the contact-friction interface are satisfied. In general the valid solution must be determined iteratively wherein a particular state (fixed, slip, or free) is assumed and solved to obtain a trial solution. The trial solution is used to determine if the assumed state is correct, and if not, what state is more likely to be correct. At the same time, the trial solution is used to estimate new parameters for the trial load vector associated with trial interface state as listed below.

- Fixed state load parameters = Δa, Δb
- Slip state load parameters = Δa, ΔT
- Free state load parameters = ΔN, ΔT

Recall that Δa and Δb are specified incremental displacement gaps in normal and tangential directions, respectively, and ΔN and ΔT are specified incremental interface forces in normal and tangential directions, respectively.

4.4.1 Selecting a new trial interface state

Table II offers an exhaustive set of physical criteria to test the validity of an assumed state. The table may be viewed as a 3 x 3 decision matrix wherein the previously assumed state forms rows and the new candidate states form columns.

Table 4.4.1-1 Decision matrix for selecting new trial interface state during iteration cycle from load step i to i+1

New trial state → / **Previous trial state ↓**		**Fix** ↑	**Slip** ↑	**Free** ↑
(1)	**Fix →**	$\lambda_n^{\,i+1} < \beta$ and $\lambda_s^{\,i+1} < F^{i+1}$	$\lambda_n^{\,i+1} < \beta$ and $\lambda_s^{\,i+1} > F^{i+1}$	$\lambda_n^{\,i+1} > \beta$
(2)	**Slip →**	$\lambda_n^{\,i+1} < \beta$ and $\Delta d_s F^{i+1} < 0$	$\lambda_n^{\,i+1} < \beta$ and $\Delta d_s F^{i+1} > 0$	$\lambda_n^{\,i+1} > \beta$
(3)	**Free →**	$d_n^{\,i+1} < 0$	--	$d_n^{\,i+1} > 0$

To illustrate the decision matrix, if the previously assumed state was fixed, then row 1of the decision matrix is entered from the left. The fist query determines if the fixed state is correct by checking if the current normal interface force is compressive (or less than the tensile rupture force β) and the magnitude of the tangential force is less than the current frictional resistance calculated from Equation 4.3-9. If both of these inequalities are satisfied than the fixed state is correct, and the fixed state is assumed for the next iteration. Otherwise, we proceed to query the slip conditions to see if the tangential force exceeds the frictional resistance while the interface normal force is compressive. If both of these conditions are satisfied, then we select the slip sate for the next iteration. The only remaining possibility is that the normal force exceeds the tensile resistance, implying the interface is prone to separate so that we choose the free state for the next iteration.

If the previous state was slip, we enter row 2 of the decision matrix to determine the most likely state for the next iteration. The first query determines whether or not we should shift to a fixed state based on the conditions that the normal force remains compressive, but there is a change in the direction of relative slip determined by the sign of the product of the slip increment, Δd_s, and the signed value of frictional resistance from Equation 4.3-9. This somewhat subtle argument is based on the observation that relative slip movement cannot reverse its direction until the passive frictional force totally reverses its direction. Therefore, a fixed state for the next iteration is assumed. On the other hand, if the product of the slip increment and the frictional resistance is positive (that is, the have the same sign), then we assume the slip state remains correct for the next iteration. The only remaining possibility is that the normal force exceeds the tensile resistance implying the interface is prone to separate so that we choose the free state for the next iteration.

Lastly if the previous state was free, we enter row 3 to determine whether or not to remain in the free state or shift to a fixed state for the next iteration. We shift to a fixed state if the current normal gap is less than zero meaning that the two bodies have incorrectly penetrated each other at this point. Otherwise, we remain in the free state for the next iteration. Note that row 3 does not provide a direct path from a free state to a slip state. This does not mean a slip state cannot be reached from a free state; it simply means a slip state must be reached by the iterative path, free to fix to slip.

Recapping, the decision matrix provides the choice for the next assumed state, thereby dictating the form of the element constraint matrix $\underline{C}^*$ defined in Table 4.3.3-1. Before we can obtain the next trial solution, we must determine the constraint load parameters as discussed next.

4.4.2 Computing load vector parameters for next iteration

Given that we know the interface state (fixed, slip or free) from the converged solution at load step i and the new trial interface state from the above decision matrix, then the trial parameters for the new load vector may be determined by referring to Table 4.4.2-1. That is, go directly to the unique row/column position in the table where row = known state at step i, and column = current trial state for step i+1.

Table 4.4.2-1 Specified incremental parameter values for trial constraint load vector

New trial state for load step i+1 → **Load step i ↓**	**Fix (a,b)**	**Slip (a,T)**	**Free (N,T)**
Fix	$\Delta a = 0$ $\Delta b = 0$	$\Delta a = 0$ $\Delta T = F^{i+1} - \lambda_s^{\,i}$	$\Delta N = -\lambda_n^{\,i}$ $\Delta T = -\lambda_s^{\,i}$
Slip	$\Delta a = 0$ $\Delta b = 0$	$\Delta a = 0$ $\Delta T = F^{i+1} - \lambda_s^{\,i}$	$\Delta N = -\lambda_n^{\,i}$ $\Delta T = -\lambda_s^{\,i}$
Free	$\Delta a = -d_n^{\,i}$ $\Delta b = \Delta d_s \left\lvert d_n^{\,i} / \Delta d_n \right\rvert$	$\Delta a = -d_n^{\,i}$ $\Delta T = F^{i+1}$	$\Delta N = 0$ $\Delta T = 0$

For example, if a slip state existed at the end of load step i and the next iteration for step i+1 is to be assumed free, then we locate slip/free table position and set ΔN and ΔT equal to the negative value of the interface forces existing at the end of load step i. As a consequence, the trial solution will result in net zero values for the interface forces, which must be the case for a free interface state.

Recall that the specification for ΔT under the slip column has already been addressed in the development of Equation 4.3-10. The remaining entries in Table 4.4.2-1 are generally self-explanatory except, perhaps, for the free/fix table position. Here the implication is that the node pair began in a free state at the end load step i, however interface penetration is observed in the decision matrix so that we are assuming a fixed state (re-bonding) for the next iteration. To this end, the normal gap is closed by specifying Δa equal to the negative of existing normal gap, which is physically correct, resulting in zero normal gap at the end of load step i+1. With regard to specifying the slip gap increment, we observe that the ratio existing-gap/incremental gap must be less than 1, otherwise penetration would not have been observed. Thus, it is reasonable to assume that the slip gap increment can be specified by reducing the incremental slip gap in the same proportion, which explains the logic for the Δb specification.

4.4.3 Algorithm summary and convergence

The following step-by-step algorithm summarizes the solution strategy and convergence criteria. As always it is assumed that a valid solution exists for a load step i ,and we seek an incremental solution to advance the solution to load step i+1.

1. At the beginning of each new load step assume each interface element remains in the same state (fixed, slip or free) as determined by the converged solution of the previous load step. Therefore, the element constraint matrix is initially known (Table4.3.3-1) and the constraint element load vector is set to zero for the first iteration. (For the very first load step, all constraints elements are initially assumed to be in the fixed state)

2. Assemble the global system matrix (see Equation 4.2-6) and solve the system for incremental displacements and incremental interface forces. Form a temporary trial solution for load step i+1by summing the interface responses as shown in Equations 4.4-1 to 4.4-4.

3. Using the decision matrix in Table 4.4.1-1 evaluate each constraint element to see if it changed state with respect to the previous iteration. Assign new constraint matrices to all elements that changed state and keep a record of how elements changed state.

4. Using Table 4.4.2-1 compute a new load vector for each element. For each constraint element currently in a slipping state, compare the current value of frictional resistance (F^{i+1} in Equation 4.3-9) with the value determined in the previous iteration and record the number of elements that have relative differences higher than 1%.

5. Check for convergence.

    - Convergence is achieved if all constraint elements remain in the same state for two successive iterations, and the frictional resistance of all slipping elements is within 1 % tolerance on successive iterations. When this occurs the load step is converged and we proceed to step 6.

    - Otherwise if convergence is not achieved, we through away the trial solution, and return to step 2 for another iteration.

6. Update the solution by permanently adding the incremental solution to the previous converged solution and return to step 1 to solve for the next load step until all load steps have been processed.

In closing this chapter, the reader is referred References 1 and 24 for practical applications of the using constraint elements to successful predict the performance real-world culvert installations.

(This page intentionally left blank)

5 LARGE DEFORMATIONS AND BUCKLING

This chapter presents the development of beam theory with large deformations that includes beam bending, column deformation, material nonlinearity, and incremental loading. The development is an extension on the small-deformation beam theory presented in Section 2.1 but removes the limitations of small deformation theory.

5.1 Updated Lagrange Formulation

The major assumptions and limitations are listed below:

1. Two-dimensional framework in a plane strain formulation.
2. Bernoulli-Euler beam kinematics without shear deformation.
3. Material nonlinearity is a function of normal stress and strain.
4. Incremental virtual work formulation with incremental stress-strain relationships and loading.
5. Updated Lagrange strain-displacement relationship appropriate for large rotations and small stretch.

5.1.1 Coordinates and incremental relationships.

Consider a beam element originally in an undeformed state that has experienced a sequence of load steps (1, 2, 3, …i) and is in equilibrium after load step i. Let the nodes at either end of the element be labeled "a" and "b", and let their current location in the global X-Y coordinate system be denoted as (X_{ai}, Y_{ai}) and (X_{bi}, Ybi), respectively.

Next, construct a local x-y coordinate system with the origin at node a. The x-axis extends from node a to node b along the base of the beam, and the y-axis is orthogonal to the x-axis with y = 0 at the bottom of the beam cross section. From this reference position we apply load step i + 1 and seek to determine the incremental structural responses. The local displacement increments in displacing from load step i to step i + 1 will be denoted as Δu in the x direction and Δv in the y direction.

Equilibrium of all the forces and moments acting on the element at load step i + 1 will be in reference to the x-y coordinate system of the previous load step i, not the element's original position as assumed in small deformation theory.

5.1.2 Bernoulli-Euler beam kinematics.

Based on the assumption that cross-sectional planes remain plane in bending and axial deformation, the well-known Bernoulli-Euler assumption for displacement increments Δu and Δv at any station x along the beam length and at any point y in the beam's cross section may be expressed as:

$$\Delta u(x, y) = \Delta a(x) + (y^*-y)\Delta v' \qquad \text{Equation 5-1}$$

$$\Delta v(x) = \Delta v(x) \rightarrow \text{a function of x only} \qquad \text{Equation 5-2}$$

where, Δu(x,y) = displacement in x direction from column and bending deformation
Δa(x) = uniform displacement in x direction from column, independent of y
Δv(x) = displacement in y direction as function of x, independent of y
Δv' = d(Δv)/dx, derivative of Δv with respect to x (local deformation slope)
y* = a reference plane in the beam cross section at y = y*, yet to be specified
( )' = d( )/dx, prime symbol denotes derivative of any quantity with respect to x

5.1.3 Total Lagrangian strain for large rotations.

The total normal strain (x direction) at load step i at any station x along the beam length and at any point y in the beam's cross section may be described by a truncated form of total Lagrangian strain given by,

$$E_i(x,y) = u_i' + \tfrac{1}{2}(v_i')^2 \qquad \text{Equation 5-3a}$$

All quantities are in reference to the original undeformed position, i = 0. It is evident that u_i' is the standard definition of small strain in the x direction. The nonlinear term, $\tfrac{1}{2}(v_i')^2$, is a second order correction term that adds a uniform stretching strain to the axial strain as a result of beam rotation. The correction term may be visualized as the stretch that is induced in the leg of a right triangle as it is rotated into the position of the hypotenuse through an angle approximated by v_i'. The larger the value of v_i' the more inaccurate is the approximation of the angle.

If we express an increment of the total Lagrangian strain from step i to i+1 we obtain:

$$\Delta E(x,y) = E_{i+1}(x,y) - E_i(x,y) = \Delta u' + \tfrac{1}{2}(\Delta v')^2 + v_i'\Delta v' \qquad \text{Equation 5-3b}$$

The last term in Equation 5-3b contains v_i', which is not an incremental term but rather the approximated angle at step i in reference to the undeformed position at i = 0. Thus the incremental form of total Lagrangian strain, $\Delta E(x,y)$, produces the same error as Equation 5-3a when dealing with large rotations. Note that when determining the strain increment for the first load increment starting from i = 0, we have $v_i' = v_0' = 0$, because the reference configuration has no displacements or rotations.

5.1.4 Updated Lagrangian strain increments.

The so-called updated Lagrange formulation provides improved accuracy for calculating strains by updating the x and y coordinates of the beam element's position to step i prior to solving for step i + 1. In other words the beam element's position at step i is taken as the reference position for equilibrium and for measuring additional displacements resulting from the loads that are imposed at step i + 1, which means $v_i' = 0$ for each load step from i to i + 1.

With the above understanding, we can rewrite Equation B-3 in the updated Lagrangian description as:

$$\Delta\varepsilon(x,y) = \Delta u' + \tfrac{1}{2}(\Delta v')^2 \qquad \text{Equation 5-4a}$$

where the symbol $\Delta\varepsilon$ is used to represent updated Lagrangian strain increments in order to distinguish it from increments of total Lagrangian strain, ΔE.

Inserting the Bernoulli-Euler kinematical equations for Δu into the updated Lagrangian strain increment equation, we arrive at the incremental strain-displacement relationships for beams under large rotations, given as,

$$\Delta\varepsilon(x,y) = \Delta a' + (y^*-y)\,\Delta v'' + \tfrac{1}{2}(\Delta v')^2 \qquad \text{Equation 5-4b}$$

Equation 5-4b is the new equation for this development. That is, the remainder of the basic equations for the nonlinear stress-strain model, internal force resultants, and virtual work remain valid as expressed in the small-deformation formulation. However, the interaction of these basic equations with Equation 5-4b results in new nonlinear governing equations for beam deformations.

5.1.5 Incremental stress-strain model.

The nonlinear stress-strain laws used in CANDE are specific to each pipe material such as corrugated metal and reinforced concrete, which are detailed in previous chapters. However, all these stress-strain models conform to the same generic form that may be expressed as

$$\Delta\sigma = E_c\,\Delta\varepsilon \qquad \text{Equation 5-5}$$

where, $\Delta\sigma$ = increment of axial stress from load step i to i + 1, ($\Delta\sigma = \Delta\sigma(x,y)$)
$\Delta\varepsilon$ = increment of axial strain from load step i to i + 1, ($\Delta\varepsilon$ = Equation 5-4b)
E_c = chord modulus of total stress-strain curve from load step i to i + 1

The chord modulus is dependent on the pipe material and the history of stress and strain throughout all loading steps. It is determined iteratively during each load step by repeating the solution process until the value of E_c converges for each element to a small tolerance of error.

Replacing $\Delta\varepsilon$ in Equation 5-5 with Equation 5-4b, the fundamental stress-displacement relationship may be expressed as,

$$\Delta\sigma = E_c(\Delta a' + (y^*-y)\,\Delta v'' + \tfrac{1}{2}(\Delta v')^2) \qquad \text{Equation 5-6}$$

Next, we will use Equation 5-6 to define the internal thrust and internal moment acting on the cross section at any station x.

5.1.6 Internal thrust and moment increments.

As is customary, we define the thrust increment as the integral of $\Delta\sigma$ over the cross section area A, and the moment increment as the integral of $\Delta\sigma$ (y*-y) over the cross section area A. Specifically,

$$\Delta N = \int_A \Delta\sigma\, dA = \int_A E_c(\Delta a' + (y^*-y)\,\Delta v'' + \tfrac{1}{2}(\Delta v')^2)\, dA \qquad \text{Equation 5-7a}$$

$$\Delta M = \int_A \Delta\sigma\,(y^*-y)\, dA = \int_A E_c(\Delta a' + (y^*-y)\,\Delta v'' + \tfrac{1}{2}(\Delta v')^2)\,(y^*-y)\, dA \qquad \text{Equation 5-7b}$$

where, ΔN = thrust increment from load step i to i + 1, ($\Delta N = \Delta N(x)$)
ΔM = moment increment from load step i to i + 1, ($\Delta M = \Delta M(x)$)
$dA = b(y)dy$, a differential area of cross section where b(y) is the width with y measured from bottom.

The arbitrary reference position y* is now chosen so that $\int_A E_c\,(y^*-y)\, dA = 0$, which simplifies Equations 5-7a,b, and gives the location of y* measured from the bottom as,

$$y^* = \left(\int_A E_c\, y\, dA\right) / \left(\int_A E_c\, dA\right) \qquad \text{Equation 5-8}$$

The remaining area integrals in Equation 5-7a,b relate to effective axial stiffness and effective bending stiffness and are defined as,

$$EA^* = \int_A E_c\, dA = \text{Effective axial stiffness of beam element} \qquad \text{Equation 5-9}$$

$$EI^* = \int_A E_c\,(y^*-y)^2 dA = \text{Effective bending stiffness of beam element} \qquad \text{Equation 5-10}$$

All of the integrals in Equations 5-8, 5-9, and 5-10 are computed numerically for every iteration within each load step until convergence is achieved.

With the above definitions for y*, EA* and EI*, the thrust and moment increments (Equations 5-7a,b) simplify to the following equations,

$$\Delta N = EA^*(\Delta a' + \tfrac{1}{2}(\Delta v')^2) \qquad \text{Equation 5-11}$$

$$\Delta M = EI^*\,\Delta v'' \qquad \text{Equation 5-12}$$

Note that the moment-increment expression is the familiar bending stiffness-curvature relationship used in small deformation theory. However, the thrust-increment expression, in addition to the familiar column stiffness-deformation relationship, also contains a nonlinear stiffness term related to rotation, $\tfrac{1}{2}(\Delta v')^2$.

5.1.7 Virtual work for beam-column element.

The general concept of virtual work is fully developed in Chapters 1 and 2. Here the attention is focused on the internal virtual of beam-column elements.

The internal virtual work for the beam-column element under consideration may be expressed as the following volume integration at any load step i + 1:

$$\delta U_{i+1} = \int_V \delta\varepsilon_{i+1}\sigma_{i+1}\, dV \qquad \text{Equation 5-13}$$

where, $\delta\varepsilon_{i+1}$ = virtual strain field arising from the imposed virtual displacements
σ_{i+1} = stress field existing in beam element at load step i +1
$\int_V (\ldots) dV$ = volume integration over the beam element

The virtual symbol δ means a small variation of the strain field. Similar to variational calculus, δ operates on the displacement variables like a total derivative. Thus operating on the updated Lagrangian strain, the virtual strain field is determined as:

$$\delta\varepsilon_{i+1} = \delta[a' + (y^*-y)\, v'' + \tfrac{1}{2}(v')^2]_{i+1} = \delta a' + (y^*-y)\delta v'' + v'_{i+1}\delta v' \qquad \text{Equation 5-14}$$

The displacement variables prefaced with the symbol δ are arbitrary motions and need not be associated with the values at load step i+1. However, the term v'_{i+1} is associated with load step i+1 and is equivalent to, $v'_{i+1} = \Delta v'$, since $v'_i = 0$ by virtue of the updated Lagrange formulation.

The incremental form of the element internal virtual work is defined by;

$$\delta\Delta U_e = \delta U_{i+1} - \delta U_i = \int_V (\delta\varepsilon_{i+1}\sigma_{i+1} - \delta\varepsilon_i\sigma_i)dV \qquad \text{Equation 5-15}$$

Observing that $\delta\varepsilon_{i+1} = \delta\varepsilon_i + \Delta v'\delta v'$, the above becomes;

$$\delta\Delta U_e = \int_V \{(\delta a'+(y^*-y)\delta v'')\Delta\sigma + \Delta v'\delta v'\sigma_{i+1}\}dV \qquad \text{Equation 5-16}$$

Separating the volume integral into area and length integrals, dV = dAdx, we arrive at,

$$\delta\Delta U_e = \int_x \{\delta a' \int_A \Delta\sigma\, dA + \delta v'\Delta v' \int_A \sigma_{i+1}\, dA + \delta v'' \int_A \Delta\sigma\,(y^*-y)dA\}\, dx \qquad \text{Equation 5-17}$$

Here it is observed that the two area integrals involving Δσ have already been identified as ΔN and ΔM in Equations 5-7a,b. The area integral involving σ_{i+1} will now be designated as N_{i+1}, which is the total thrust at step i+1 referred to the beam element's coordinate system at step i. Thus Equation 5-17 is written as;

$$\delta\Delta U_e = \int_x \{\, \delta a'\Delta N + \delta v'\, \Delta v'\, N_{i+1} + \delta v''\Delta M\,\}\, dx \qquad \text{Equation 5-18}$$

Since we have already established expressions for ΔN and ΔM in terms of displacements in Equations 5-11 and 5-12, we replace the unknown force increments ΔN and ΔM in Equation 5-18 with the equivalent unknown displacements. However with regard to N_{i+1}, which is nonlinear because it is coupled with Δv', we choose to leave N_{i+1} as expressed to facilitate the nonlinear solution strategy. With the above replacements, Equation 5-18 becomes,

$$\delta\Delta U_e = \int_x \{\delta a'EA^*\Delta a' + \delta a'EA^*\, \tfrac{1}{2}(\Delta v')^2 + \delta v'\Delta v'N_{i+1} + \delta v''EI^*\Delta v''\}\, dx \qquad \text{Equation 5-19}$$

For the sake of clarity, we will express Equation 5-19 as the sum of four terms,

$$\delta\Delta U_e = \delta\Delta U_a + \delta\Delta U_r + \delta\Delta U_g + \delta\Delta U_b \qquad \text{Equation 5-20}$$

where,

$$\delta\Delta U_a = \int_x \{\delta a'EA^*\Delta a'\}\, dx \qquad \text{Equation 5-20a}$$

$$\delta\Delta U_r = \int_x \{\delta a' EA^* \tfrac{1}{2}(\Delta v')^2\} dx \qquad \text{Equation 5-20b}$$

$$\delta\Delta U_g = \int_x \{\delta v' \Delta v' N_{i+1}\} dx \qquad \text{Equation 5-20c}$$

$$\delta\Delta U_b = \int_x \{\delta v'' EI^* \Delta v''\} dx \qquad \text{Equation 5-20d}$$

Of the four terms in Equation 5- 20, the first term is the familiar column stiffness term and the fourth term is familiar bending stiffness term identical to small deformation theory. The middle two terms are nonlinear and are associated with large deformations. As we shall see in the subsequent FEM development, the second term will be treated as a load vector and the third term will lead to the so-called geometric stiffness matrix.

5.2 Finite Element Development

5.2.1 Finite element interpolation functions.

Equation 5-20 is the incremental internal virtual work of a beam column element with large deformation without numerical approximations. To express this in a FEM formulation we introduce interpolation functions for the displacements that become exact as the element lengths become small. The interpolation functions are expressed in terms of unknown nodal variables shown in the sketch below.

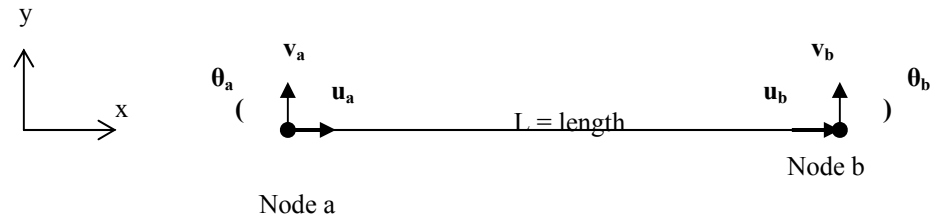

where, Δu_a, Δu_b = incremental nodal displacements in x direction at nodes a and b
Δv_a, Δv_b = incremental nodal displacements in y direction at nodes a and b
$\Delta\theta_a$, $\Delta\theta_b$ = incremental nodal rotations in counter-clockwise direction at nodes a and b

The incremental axial displacement function is approximated with a linear interpolation function expressed in vector notation as;

$$\Delta a(x) = < \varphi_1 \; \varphi_2 > < \Delta u_a \;\; \Delta u_b >^T \qquad \text{Equation 5-21}$$

where, $\varphi_1(x) = 1 - x/L$
$\varphi_2(x) = x/L$
L = element length

The incremental vertical displacement function is approximated by a cubic polynomial, known as a Hermetian interpolation function, and is expressed in vector notation by,

$$\Delta v(x) = < \gamma_1 \; \gamma_2 \; \gamma_3 \; \gamma_4 > < \Delta v_a \; \Delta\theta_a \; \Delta v_b \; \Delta\theta_b >^T \qquad \text{Equation 5-22}$$

where, $\gamma_1(x) = 1 - 3\,(x/L)^2 + 2\,(x/L)^3$
$\gamma_2(x) = L\,(1 - x/L)^2\,x/L$
$\gamma_3(x) = 3\,(x/L)^2 - 2\,(x/L)^3$
$\gamma_4(x) = L\,(1 - x/L)\,(x/L)^2$

5.2.2 Element matrices and vectors

Taking the necessary derivatives of the approximating functions for $\Delta a(x)$ and $\Delta v(x)$, inserting them into the four internal virtual work terms of Equation 5-20, and integrating with respect to x over the element length L, we arrive at the following evaluations.

For the internal virtual work of the axial stiffness term we have,

$$\delta\Delta U_a = < \delta\Delta u_a \;\; \delta\Delta u_b > \underline{\mathbf{K_a}} < \Delta u_a \;\; \Delta u_b >^T$$

where the axial stiffness matrix is defined as,

$$\underline{K}_a = (EA^*) \int_x [< \varphi'_1 \; \varphi'_2 >^T < \varphi'_1 \; \varphi'_2 >] dx \qquad \text{Equation 5-23a}$$

and upon evaluating the integral, the axial stiffness matrix is determined as,

$$\underline{K}_a = (EA^*/L) \begin{vmatrix} 1 & -1 \\ -1 & 1 \end{vmatrix} \qquad \text{Equation 5-23b}$$

For the internal virtual work of the bending stiffness term we have,

$$\delta\Delta U_b = < \delta\Delta v_a \; \delta\Delta\theta_a \; \delta\Delta v_b \; \delta\Delta\theta_b > \underline{K_b} < \Delta v_a \; \Delta\theta_a \; \Delta v_b \; \Delta\theta_b >^T$$

where the standard bending stiffness matrix is defined as,

$$\underline{K}_b = (EI^*) \int_x [< \gamma''_1 \; \gamma''_2 \; \gamma''_3 \; \gamma''_4 >^T < \gamma''_1 \; \gamma''_2 \; \gamma''_3 \; \gamma''_4 >] dx \qquad \text{Equation 5-24a}$$

and upon evaluating the integral, the standard bending stiffness matrix is determined as,

$$\underline{K}_b = (EI^*/L) \begin{vmatrix} 12/L^2 & 6/L & -12/L^2 & 6/L \\ 6/L & 4 & -6/L & 2 \\ -12/L^2 & -6/L & 12/L^2 & -6/L \\ 6/L & 2 & -6/L & 4 \end{vmatrix} \qquad \text{Equation 5-24b}$$

For the internal virtual work of the geometric stiffness term we have,

$$\delta\Delta U_g = < \delta\Delta v_a \; \delta\Delta\theta_a \; \delta\Delta v_b \; \delta\Delta\theta_b > \underline{K}_g < \Delta v_a \; \Delta\theta_a \; \Delta v_b \; \Delta\theta_b >^T$$

where the geometric stiffness matrix is defined as,

$$\underline{K}_g = (N_{i+1}) \int_x [< \gamma'_1 \; \gamma'_2 \; \gamma'_3 \; \gamma'_4 >^T < \gamma'_1 \; \gamma'_2 \; \gamma'_3 \; \gamma'_4 >] dx \qquad \text{Equation 5-25a}$$

and upon evaluating the integral, the geometric stiffness matrix, which is dependent on the current thrust scalar is determined as,

$$\underline{K}_g = (N_{i+1}) \begin{vmatrix} 6/5L & 1/10 & -6/5L & 1/10 \\ 1/10 & 2L/15 & -1/10 & -L/30 \\ -6/5L & -1/10 & 6/5L & -1/10 \\ 1/10 & -L/30 & -1/10 & 2L/15 \end{vmatrix} \qquad \text{Equation 5-25b}$$

For the remaining internal virtual work term (rotational stretch vector), we have

$$\delta\Delta U_r = < \delta\Delta u_a \;\; \delta\Delta u_b > \underline{r}_e$$

wherein the rotational stretch vector is expressed as,

$$\underline{r}_e = \rho \, (EA^*/2L) <-1 \;\; 1>^T \qquad \text{Equation 5-26a}$$

where, $\rho = \int_x (\Delta v')^2 dx = < \Delta v_a \; \Delta\theta_a \; \Delta v_b \; \Delta\theta_b > \underline{K}_g^* < \Delta v_a \; \Delta\theta_a \; \Delta v_b \; \Delta\theta_b >^T$

$\underline{K}_g^* = \underline{K}_g$ without the multiplier (N_{i+1})

Thus, the rotational stretch vector, which is dependent on the nonlinear scalar ρ, is determined as,

$$\underline{r}_e = \begin{vmatrix} r_a \\ r_b \end{vmatrix} = \rho \, (EA^*/2L) \begin{vmatrix} -1 \\ 1 \end{vmatrix} \qquad \text{Equation 5-26b}$$

The above four terms of the element's internal virtual work, $\delta\Delta U_e$, may be brought together into a single 6 x 6 matrix along with 6-component vectors where the six nodal unknowns are listed in the following order $< \Delta u_a \ \Delta v_a \ \Delta\theta_a \ \Delta u_b \ \Delta v_b \ \Delta\theta_b >$. Thus the finite element equivalent of Equation 5-20 is expressed as,

$$\delta\Delta U_e = < \delta\Delta u_a \ \delta\Delta v_a \ \delta\Delta\theta_a \ \delta\Delta u_b \ \delta\Delta v_b \ \delta\Delta\theta_b > (\underline{K_e} < \Delta u_a \ \Delta v_a \ \Delta\theta_a \ \Delta u_b \ \Delta v_b \ \Delta\theta_b >^T + \underline{r_e})$$

where, $\underline{K_e}$ = total effective element stiffness matrix (6 x 6) Equation 5-27

$$\underline{r_e} = < r_a \ 0 \ 0 \ \ r_b \ 0 \ 0 >^T = \text{rotational stretch vector (1 x 6)} \qquad \text{Equation 5-28}$$

Of course, it is understood that the components of $\underline{K_a}$, $\underline{K_b}$, and $\underline{K_g}$ are added into the proper locations of the $\underline{K_e}$ matrix corresponding to the ordering of nodal variables.

5.2.3 Transformation and global assembly.

The last step before adding the element's contribution of $\delta\Delta U_e$ into the entire system is to transform the nodal variables from local coordinates to global coordinates.

Let β = angle from global X-axis to local x-axis, then the local nodal variables may be expressed as global nodal variables by,

$$\Delta\underline{u_e} = \underline{T} \ \Delta\underline{u_E} \qquad \text{Equation 5-29}$$

where, $\Delta\underline{u_e} = < \Delta u_a \ \Delta v_a \ \Delta\theta_a \ \Delta u_b \ \Delta v_b \ \Delta\theta_b >^T$ local nodal variables for element

$\Delta\underline{u_E} = < \Delta u_A \ \Delta v_A \ \Delta\theta_A \ \Delta u_B \ \Delta v_B \ \Delta\theta_B >^T$ global nodal variables for element

$$\underline{T} = \begin{vmatrix} C & S & 0 & 0 & 0 & 0 \\ -S & C & 0 & 0 & 0 & 0 \\ 0 & 0 & 1 & 0 & 0 & 0 \\ 0 & 0 & 0 & C & S & 0 \\ 0 & 0 & 0 & -S & C & 0 \\ 0 & 0 & 0 & 0 & 0 & 1 \end{vmatrix}$$

and, $C = \cos(\beta)$ and $S = \sin(\beta)$

With the above transformation matrix, the element stiffness matrix and rotational stretch vector may be expressed in global coordinates as,

$$\underline{K_E} = \underline{T}^T \underline{K_e} \ \underline{T} \qquad \text{Equation 5-30}$$

$$\underline{r_E} = \underline{T}^T \underline{r_e} \qquad \text{Equation 5-31}$$

It should be clear that lower-case subscripts are used for element quantities that are in expressed in local coordinates, whereas upper-case subscripts are used for element quantities that are in expressed in global coordinates.

The effevtive element stiffness matrix $\underline{K_E}$ and the rotational stretch vector $\underline{r_E}$ are in the proper form for global assembly wherein $\underline{K_E}$ is added to the global effective stiffness matrix and $\underline{r_E}$ is brought to the right-hand-side of the equations to be subtracted from the load vector.

5.3 Solution Strategy

The overall solution process is a direct iterative method as outlined below. The viewpoint is that we have a converged solution at load step i, and we seek a solution for load step i+1.

5.3.1 Iterative methodology

In obtaining a solution from load step i to i+1, we begin by assuming $N_{i+1} = N_i$ and $\rho = 0$ so that element matrices and vectors may be computed for each element. After global assembly, the current set of equations may be expressed for iteration k as

$$\underline{K}_{Gk}\,\Delta u_{Gk} = \Delta P_{Gk} \qquad \text{Equation 5-32}$$

where, $\underline{K}_{G\boldsymbol{k}}$ = global stiffness matrix for iteration *k*, i.e., collection of elements $\sum \underline{K}_{E\boldsymbol{k}}$

$\Delta u_{G\boldsymbol{k}}$ = global vector of all unkown nodal variiable increments for iteration *k*

$\Delta P_{G\boldsymbol{k}}$ = global vector of load increments for iteration *k,* including negative rotational-stretch vector.

k = iteration counter; 1, 2, 3, …

The set of linear alebraic equations represented by Equation 5-32 is solved by Gauss Elimination for the dispacement increments Δu_{Gk}. This trial solution is used to form a new and better estimates for N_{i+1} and ρ, which leads to revised values for $\underline{K}_{G\boldsymbol{k}}$ and $\Delta P_{G\boldsymbol{k}}$ for the next iteration. When two successive iterations produce the same results within an acceptable tolerance, the solution has coverged for load step i + 1, and all quantities are updateded as,

$$q_{i+1} = q_i + \Delta q \qquad \text{Equation 5-33}$$

where q stands for all structural responses such as displacements, stresses, strains, moments, thrusts, and so on. In addition, the updated Lagrange formulation implies that the global coordinate locations of each node are updated so that q also repesents each (X,Y) nodal coordinate that are updated by the corresponding displacement increments.

5.3.2 Recovery of element forces

When load step i+1 converges to a solution, we want to recover the incremental internal forces at the ends of the element, that is, increments of thrust, shear and moment at the element's nodes. We can obtain these force increments in reference to "configuration i coordinates" by making use of virtual work.

Let, ΔT_a, ΔT_b = Thrust force increments (x_i direction) at nodes a and b

ΔQ_a, ΔQ_b = Shear force increments (y_i direction) at nodes a and b

ΔM_a, ΔM_b = Moment increments at nodes a and b (invariant to x-y coordinates)

The incremental virtual external work of these end forces is given by;

$$\delta\Delta W_e = <\delta\Delta u_a\ \delta\Delta v_a\ \delta\Delta\theta_a\ \delta\Delta u_b\ \delta\Delta v_b\ \delta\Delta\theta_b> < \Delta T_a\ \Delta Q_a\ \Delta M_a\ \Delta T_b\ \Delta Q_b\ \Delta M_b>^T$$

With the element's incremental end loads defined, we can now express the net incremental virtual work of any element to be equal to zero; i.e.,

$$\delta\Delta V_e = \delta\Delta U_e - \delta\Delta W_e = 0$$

Using equation Equations 5-27 and 5-28 to express $\delta\Delta U_e$, we arrive at the following equations to determine the incremental end forces and moments:

$$\begin{pmatrix} \Delta T_a \\ \Delta Q_a \\ \Delta M_a \\ \Delta T_b \\ \Delta Q_b \\ \Delta M_b \end{pmatrix} = \left(\underline{\underline{K}}_a + \underline{\underline{K}}_b + \underline{\underline{K}}_g \right) \begin{pmatrix} \Delta u_a \\ \Delta v_a \\ \Delta \theta_a \\ \Delta u_b \\ \Delta v_b \\ \Delta \theta_b \end{pmatrix} + \begin{pmatrix} r_a \\ 0 \\ 0 \\ r_b \\ 0 \\ 0 \end{pmatrix} \qquad \text{Equation 5-34}$$

Thus the end forces can be recovered by multiplying the complete element stiffness matrix times the incremental displacements. For the end thrust forces we also add on the rotational stretch forces r_a and r_b . All of the above operations are carried out in reference to local the coordinate axis at step i.

5.3.3 Update coordinates

Before proceeding to the next load step, it is neccessary to update all quatities to the new starting configuation. In particular we need to update the thrust associated with the geometric stiffness matrix. Let N* represent the accumulation of all past thrust increments which is expressed in the x-direction of the previous step (i,e., $N^* = N_{i+1}$). Similary let Q* represent the accumulation of all past shear increments which is expressed in the y-direction of the previous step The goal is to express in N* in the x-direction and Q* in the y-direction of the current position. The increment of rotation, say α, that the element experienced in moving from the previous step to the current step may be computed as:

$$L_{new} = (L_{old} + \Delta u_b - \Delta u_a)^2 + (v_b - v_a)^2)^{1/2} \quad \text{(new length of element)} \qquad \text{Equation 5-35a}$$

$$\sin\alpha = (v_b - v_a)/ L_{new} \qquad \text{Equation 5-35b}$$

$$\cos\alpha = (L_{old} + \Delta u_b - \Delta u_a)/ L_{new} \qquad \text{Equation 5-35c}$$

Thus we can rotate the thrust and shear to the current configuration as

$$N^*_\alpha = \cos\alpha\, N^* + \sin\alpha\, Q^* \qquad \text{Equation 5-36a}$$

$$Q^*_\alpha = -\sin\alpha\, N^* + \cos\alpha\, Q^* \qquad \text{Equation 5-36b}$$

For the iteration process during the next load step, we use the following estimate for thrust in the geometric stiffness matrix;

$$N_{i+1} = N^*_\alpha + \Delta N \qquad \text{Equation 5-37}$$

where N^*_α is a fixed value and ΔN is determined iteratively. For the first iteration we assume ΔN = 0. In the absence of material nonlinearity, this process always converges in three load steps.

After all load steps are complete, the problem is finished and the load-deformation path of the structural system may be visualized. Note that this method of analysis by itself does not directly provide a critical buckling load like a linearized buckling (Euler) analysis. Rather, the actual buckling load is observed by noting the peak load (e.g., soil height) when the system fails due to unbounded displacements. In order to predict the buckling capacity at the end of each load increment, we augment the large-deformation analysis with a linearized buckling solution as discussed next.

5.4 Buckling Capacity

At the end of each converged load step, we have stored in memory the current components for the standard stiffness matrix and the geometric stiffness matrix, which, when taken together, form the global stiffness matrix that is expressed in Equation 5-32. Thus after convergence of load step i+1, we may write the global stiffness matrix in two parts as,

$$\underline{K}_G = \underline{K}_S + \underline{K}_{Geo}(N_{i+1}) \qquad \text{Equation 5-38}$$

where, $\underline{K}_S$ = global standard stiffness matrix (small deformations)

$\underline{K}_{Geo}(\underline{N}_{i+1})$ = global geometric stiffnes matrix written as a function of element thrust values

The known values for thrust $\underline{N}_{i+1}$ as expressed in the above geometric stiffness matrix, have been determined iteratively during the solution for step i + 1. Thus, $\underline{N}_{i+1}$ represents the current set of thrust values in the various beam-column elements at load step i+1.

If we temporarily assumed the matrices in Equation 5-38 remain constant except the geometric stiffness is scaled by a load parameter "c", then we can determine what magnitude increase in the set of thrust values $\underline{N}_{i+1}$ that would cause unlimited deformations, i.e., critical buckling. This will occur when the combined standard and geometric stiffness becomes singular (determinant = 0), which is dependent on the value of c.

To this end, let the global stiffness matrix be written as,

$$\underline{K}_G(c) = \underline{K}_S + c\,\underline{K}_{Geo}(\underline{N}_{i+1}) \qquad \text{Equation 5-39}$$

and pose the problem as, find the value(s) c such that,

$$\text{Det}\ \underline{K}_G(c) = 0 \qquad \text{Equation 5-40}$$

This, of course, is the classic eigenvalue problem for buckling bifurcation wherein the lowest eigenvalue "c" is a direct measure of the current buckling capacity. If, for example, the value of c is found to be 2.50, then the current set of thrust values $\underline{N}_{i+1}$ could be increased by any factor up to 2.5 before buckling would occur. Thus we can say that the value of "c" is the predicted buckling capacity or equivalently the safety factor against buckling.

In CANDE-2007, a determinant search process finds the value of "c". Starting with the guess c = 1, the determinant expressed in Equation 5-40 is evaluated. If the determinant is positive, meaning the matrix is structurally stable, then the value of c is steadily increased until the determinant is found to be negative, meaning the matrix structurally unstable. Knowing the correct value c lies in an interval bounded by the last two estimates, a binary-chop method is used to keep refining the estimate for "c" until it is accurate to two decimal places.

In summary, this chapter presents a complete derivation of a beam theory with large deformations that includes beam bending, column deformation, material nonlinearity, and incremental loading. The large deformation responses (forces, displacements, stresses and strain) are output at the end of each load step along with a prediction of the buckling capacity.

5.5 Illustration – Simply Supported Beam

This illustration compares the updated Lagrange CANDE-2007 solution and buckling prediction with a closed-form solution for an axially load, simply supported beam with initial constant end moment. The closed-form solution is theoretically equivalent to a one-step updated Lagrange solution (i.e., total Lagrange method) so that a direct comparison may be made if we limit the CANDE solutions to a single load step. Subsequently, we will obtain CANDE solutions with multiple load-steps to demonstrate a more realistic load-deformation behavior in contrast with the single-step solutions.

Thus, the specific objectives are:

1. Develop a closed form solution for a simply supported beam with an initial end moment and an increasing axial load based on total Lagrange formulation. Note a closed form Updated Lagrange solution is not tractable.

2. Compare CANDE load-deformation path and buckling prediction with the closed-form solution wherein the CANDE solution is obtained with a series of single load steps with increasing axial load (i.e., a series of total Lagrange solutions).

3. Show realistic load-deformation paths from CANDE solutions based on multiple steps to successively increase the axial load while updating the coordinates at the end of each load step (i.e., an updated Lagrange solution).

5.5.1 Development of closed-form solution

The idealized beam, shown in the figure below, is a flexible in bending with bending stiffness EI and inextensible in axial elongation. The right end is pinned supported, and the left end is on a roller with a constant moment M_o and an axially increasing thrust force, P_i .

Figure 5.5.1-1 Simply supported beam with increasing axial load and fixed end moment.

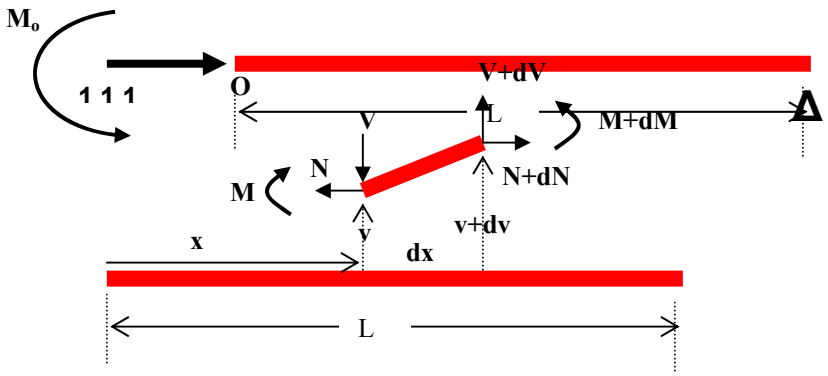

A differential segment of the test beam is shown above for formulating the governing differential equation,
where, M, dM = moment and differential
V, dV = shear and differential
N, dN = thrust and differential
v, dv = vertical displacement and differential
x = horizontal coordinate
(.)' = d(.)/dx denotes derivative with respect to x

Horizontal and vertical equilibrium of the differential segment requires:

$$dN \equiv N'dx = 0 \quad \text{(Thrust is constant)} \qquad \text{Equation 5-41}$$

$$dV \equiv V'dx = 0 \quad \text{(Shear is constant)} \qquad \text{Equation 5-42}$$

Moment equilibrium of the differential segment is approximated by letting v' represent the tangent of the total rotation so that the differential equation remains linear as expressed below:

$$M' + Nv' + V = 0 \qquad \text{Equation 5-43}$$

The Bernoulli-Euler moment-curvature relationship, wherein EI is the beam bending stiffness, is given by;

$$M = -EI\, v'' \qquad \text{Equation 5-44}$$

Taking the first derivative of Equation 3 and the second derivative of Equation 4 and combining the results we arrive at (recalling that N' = 0 and V' = 0):

$$-EI\, v'''' + N\, v'' = 0 \qquad \text{Equation 5-45}$$

Since N is constant, the boundary condition in Figure 1 dictates that N = - P, where P is the applied axial force, positive in compression, and we define the positive quantity q as,

$$q^2 = P/EI \qquad \text{Equation 5-46}$$

Using the above in Equation 5-45, we arrive at the governing ordinary differential equation written as,

$$v'''' + q^2 v'' = 0 \qquad \text{Equation 5-47}$$

The general solution to Equation 5-47 is given by,

$$v(x) = C_1 + C_2 x + C_3 \cos qx + C_4 \sin qx \qquad \text{Equation 5-48}$$

Where C_1, C2, C_3, and C_4 are constants determined from the four boundary conditions and written as,

$$v(0) = 0 \qquad \text{Equation 5-49a}$$
$$v''(0) = -M_0/EI \qquad \text{Equation 5-49b}$$
$$v(L) = 0 \qquad \text{Equation 5-49c}$$
$$v"(L) = 0 \qquad \text{Equation 5-49d}$$

After determining the constants, the final closed-form solution may be expressed as,

$$v(x) = (M_0/P)\{ -1.0 + x/L + \cos qx - (\cos qL/\sin qL)\sin qx\} \qquad \text{Equation 5-50}$$

Upon inspecting the last term in Equation 5-50, it is evident that the predicted vertical displacement becomes infinite when the devisor sinqL = 0. This occurs when the load P reaches the first critical value, $P_{critical}$, such that $qL = \pi$. Or, making use of Equation 5-46, we arrive at the well-known critical buckling load for a simply supported beam,

$$P_{critical} = EI(\pi/L)^2 \qquad \text{Equation 5-51}$$

The major approximation in the above derivation occurs in Equation 5-43 wherein the tangent of the rotation angle formed by the differential element with respect to the undeformed position is approximated by the derivative of the vertical displacement. This approximation is exactly equivalent to the total Lagrangian approach (truncated from) presented earlier in this chapter. Of course, this approximation becomes less and less accurate as the angle increases.

5.5.2 Example test problem for closed-form solution

To numerically illustrate the load-deformation behavior of Equation 5-50 as well as the critical buckling load given by Equation 5-51, hypothetical beam parameters are defined in the table below.

Table 5.5.2-1 Numerical values for test problem.

Beam Parameter	Parameter value
Total Length, L	12 inches
Bending Stiffness, EI	1000 lbs-in^2
Initial end moment, M_0	1 in-lb
Axial load, P (variable)	0 to $P_{critical}$
$P_{critical}$ (Eq 5-51)	68.539 lbs

The following figure shows a plot of the applied load P versus mid-span deflection where the applied load is presented as percentage of the critical load (68.54 lbs)

Figure 5.5.2-1 Load-deformation curve from closed-form solution of test problem.

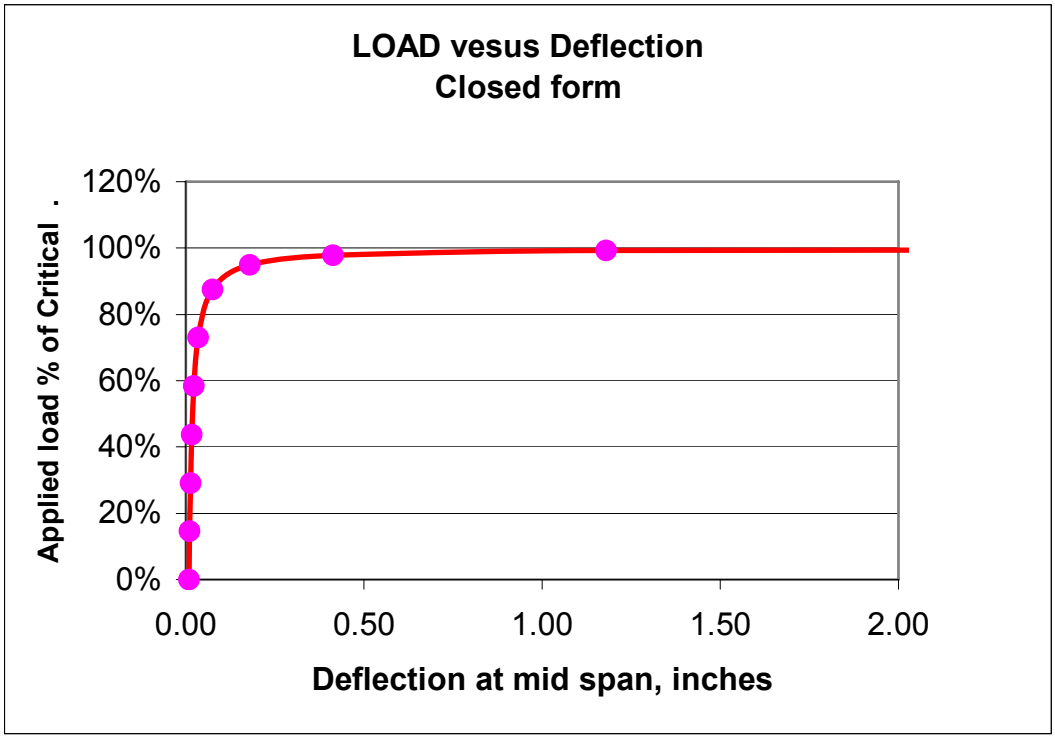

Deflections are observed to remain small until the applied load is near 80% of the critical load. After the 80% load level, the simple-theory solution predicts rapidly increasing displacements that become infinite as the load reaches 100% critical. The numerical values of displacements are less and less accurate as the displacements (and hence the rotations) increase in magnitude. The totally false prediction of an infinite displacement as the load approaches 100% of critical is a characteristic inaccuracy of this total Lagrangian formulation, which is limited to small rotations on the order of 5%. Another characteristic inaccuracy of total Lagrange is that for loads greater then 100% of critical is that predicted displacements are opposite in sign, which of course, is also obliviously unrealistic.

Although the total Lagrange formulation does not give realistic predictions for the displacement values for loads near the critical load, the prediction of the critical load level where rapid changes in displacement occur is quite accurate. This finding, which is demonstrated in the next section, is significant because it gives credence to the buckling load prediction method used in CANDE for load schedules that are significantly below the critical load.

5.5.3 CANDE model of test problem

The corresponding CANDE model is shown in the figure below with parameters defined in the following table. Twelve beam-column elements are used to simulate the test problem. The same beam properties previously defined for the

closed-form solution are assigned to the CANDE model except the CANDE model also includes axial deformation, which is not included in the closed-form formulation. In order to minimize the effect of axial deformation, the cross-sectional area is assigned a value two orders of magnitude larger than the moment of inertia so that bending deformation will dominate.

Figure 5.5.3-1 Twelve element CANDE model of test problem.

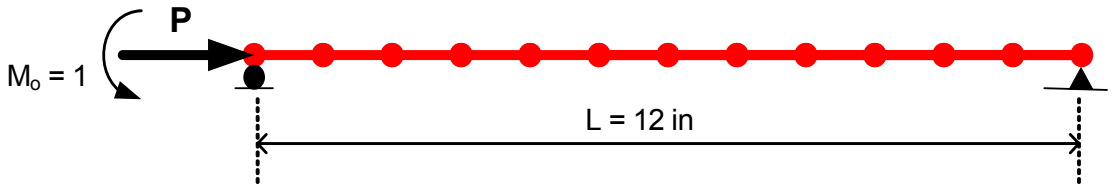

Table 5.5.3-1 Numerical values for CANDE model.

Beam Parameter	Parameter value
Total Length, L	12 inches
Young's modulus, E	1000 psi
Moment of inertia, I	1.0 in^4
Cross-section area, A	100.0 in^2
Initial end moment, M_0	1 in-lb
Axial load, P (variable)	0 to $P_{critical}$
$P_{critical}$ (Eq 5-51)	68.539 lbs

5.5.4 CANDE simulating total Lagrange approach.

Although CANDE is developed for an updated Lagrange methodology, it is easy to simulate a total Lagrange solution by specifying only one load step so that the original configuration remains the reference configuration and coordinates are not updated. By solving a series of problems (each with one load step) the axial load P can be successively increased from zero to $P_{critical}$, while the initial end moment is held constant for each problem.

As shown in the table below, the predicted deflections from this series of CANDE solutions are found to be nearly identical to the closed form solution with agreement to three significant digits. The lower part of the table shows CANDE's prediction for the critical buckling load at each axial load level.

Table 5.5.4-1a. Mid-span Deflections (inches) for increasing axial load % Critical Load

Axial load as percent of Critical	0%	29.18%	58.36%	87.54%	94.84%	99.21%	99.94%
Closed-form Deflections	0.0090	0.0128	0.0220	0.0742	0.1796	1.1803	16.357
CANDE (single-step) Deflections	0.0090	0.0128	0.0220	0.0742	0.1795	1.1800	16.170

Table 5.5.4-1b. CANDE prediction of Buckling load (lbs) at each axial load level

Predicted Buckling Load	N/A	68.6	68.4	68.4	68.3	68.8	69.2

The rather remarkable agreement of deflection predictions and buckling load predictions suggests that the CANDE formulation for the geometric stiffness matrix, the rotational stretch vector and the nonlinear solution strategy is

working properly. Typically CANDE underwent three solution iterations per load level to achieve convergence. Buckling predictions typically required 8 determinant searches per problem to find the buckling load factor. The error tolerance on the determinant search algorithm is set at 2%.

5.5.5 CANDE Solution for updated Lagrange approach.

In this more accurate approach, the CANDE solution is obtained by running a single problem wherein the axial load is increased on each load step with P starting at 0.0 and steadily increasing in value up to and well beyond $P_{critical}$.

The only difference between the previous total Lagrange methodology and the updated Lagrange methodology is that the beam's reference position is updated to the deformed position of the previous load step and the existing internal forces (thrust and shear) are transformed to be aligned with the deformed position.

Figure 5.5.5-1 shows load-deformation curves for mid-span deflection for the total and updated Lagrange methods. Recall that the total Lagrange solution as predicted by closed-form solution or by CANDE give nearly identical results.

Figure 5.5.5-1. Comparison of load-deformation curves from updated and total Lagrange.

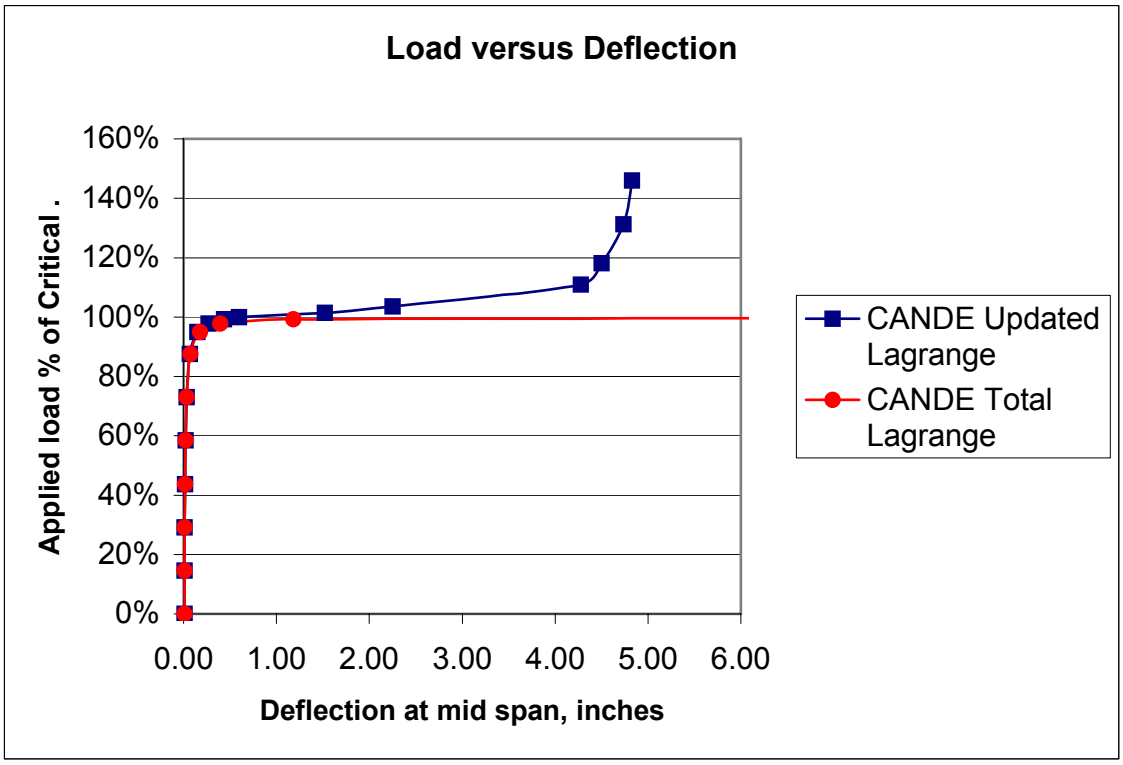

Some pertinent observations from the above figure are noted below:

1. The size of the load increments for the updated Lagrange solution are indicated by the points shown in the figure. Smaller steps are required in the vicinity of the critical load where large displacements occur.
2. For axial loads below 80% of the $P_{critical}$, the deflections as predicted by total Lagrange are close but not identical to Updated Lagrange, differing at most by 4% at the 80% load level
3. When the axial load approaches $P_{critical}$, both the updated and total Lagrange solutions exhibit buckling-like behavior by showing rapid increases in displacement for small increases load.
4. The large displacements predicted by the total Lagrange solution are not realistic for loads close to $P_{critical}$ and incorrectly infers that there is no stable equilibrium position as the deflections become infinite. In contrast the updated Lagrange solution predicts realistic displacement and finds a stable position at about 110% of $P_{critical}$..

5. Although not shown, the buckling load predictions for updated and total Lagrange methods are very close for all load levels below $P_{critical.}$. The updated Lagrange prediction for the buckling load when the axial load is very near $P_{critical}$ is about 2% higher than that predicted from the total Lagrange solution.

In summary for the simply supported beam example, the CANDE solution matches the closed form solution when restricted to one-step and loading. Under multi-step loading CANDE solutions are physically meaningful at load levels near and above the critical buckling load whereas the closed-form solution is not. In all cases, the prediction of buckling capacity is accurate.

5.6 Illustration -- Soil-Structure Interaction

This illustration examines the effects of large deformations and buckling capacity in the presence of other nonlinearities for a corrugated steel culvert installation. The primary purpose is to compare and contrast small deformation solutions versus large deformation solutions in the presence of linear versus nonlinear corrugated metal behavior, linear versus nonlinear soil model behavior, and bonded versus frictionless soil-structure interface behavior.

Specifically, three separate studies are investigated for a corrugated steel pipe under progressively deep soil fill for the modeling conditions identified in the table below.

Study #	Deformation theory		Corrugated Metal		Soil Model		Interface	
	Small	Large	Linear	Elast-plastic	Linear	Duncan/Selig	Bonded	Frictionless
1	✓		✓		✓		✓	
	✓			✓	✓		✓	
		✓	✓		✓		✓	
		✓		✓	✓		✓	
2	✓		✓			✓	✓	
	✓			✓		✓	✓	
		✓	✓			✓	✓	
		✓		✓		✓	✓	
3	✓		✓		✓			✓
	✓			✓	✓			✓
		✓	✓		✓			✓
		✓		✓	✓			✓

Each study contains four cases comparing small deformation solutions and large deformation solutions for linear and nonlinear corrugated metal models. Study #1 investigates the four cases under the assumption of a linear soil model and bonded interface. Study # 2 investigates the four cases under the assumption of a Duncan/Selig soil model and bonded interface. Study # 3 investigates the four cases under the assumption of a linear soil model and a frictionless interface.

5.6.1 CANDE soil-structure model and parameters

All the CANDE simulations are represented by finite element mesh shown in Figure 5.6.1-1 and have the following common features:

- Pipe is 60-inch corrugated steel, 3x1-inch corrugation, 0.109-inch thickness
- Soil is homogenous without bedding and weighs 120 pcf.
- Maximum soil height is 160 feet above the crown
- Truncated mesh height is 10 feet above crown (LEVEL 2 PIPE)
- Soil loading in excess of 10 feet is placed as equivalent increments of overburden pressure, where each increment represents 10 feet of soil.
- The first load increment includes the entire soil mass with 10 feet of fill followed by 15 increments of overburden pressure.

Figure 5.6.1-1. CANDE mesh of corrugated steel pipe (symmetric half)

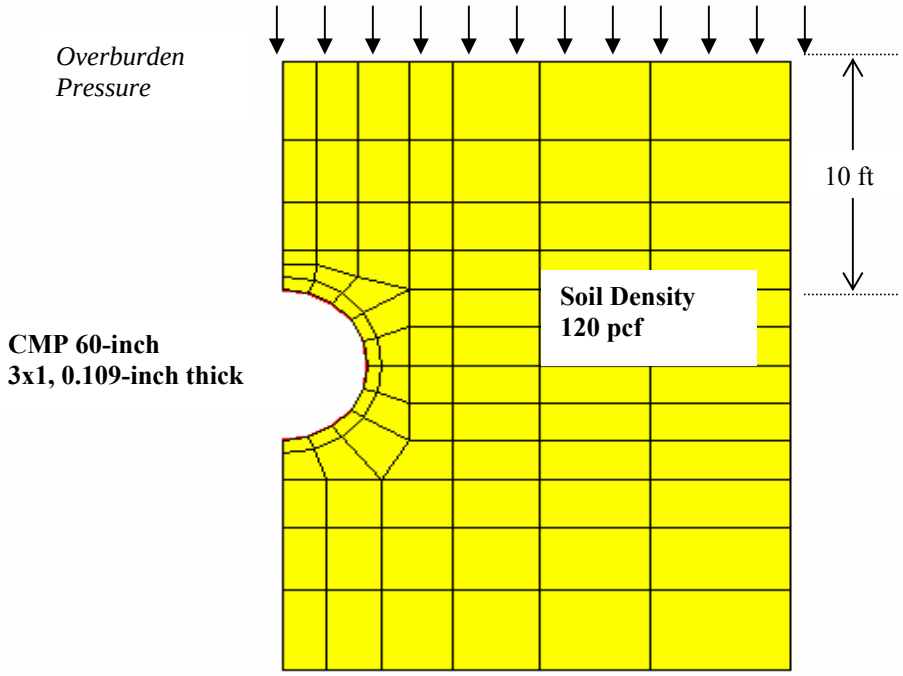

Parameter values for the linear and nonlinear cases are identified in the table below.

Table 5.6.1-1. Linear versus nonlinear modeling assumptions.

System Component	Linear form	Non-linear form
Deformation theory	Small deformation theory (Standard engineering)	Large deformation theory (Updated Lagrange)
Corrugated metal stress-strain relationship:	Linear Elastic: Young's mod = 29,000,000 psi	Elastic-Plastic: Modulus = 29,000,000 psi Yield stress = 33,000 psi
Soil stress-strain relationship:	Linear Elastic: Young's mod = 1000 psi Poisson ratio = 0.3	Duncan/Selig Hyperbolic model for ML90
Soil-culvert interface assumption:	Fully Bonded	Frictionless slippage with tension separation allowed

In each study, comparison of the four cases are presented as vertical deflection versus fill height, maximum thrust stress versus fill height, and buckling safety factor versus fill height. These quantities along with plastic penetration constitute the design criteria for corrugated metal pipe.

5.6.2 Study # 1 -- Linear soil and bonded interface

The first study assumes the culvert installation is defined by a linear elastic soil and a bonded soil-structure interface with the following four modeling cases:

(1) linear steel material and small deformation theory
(2) linear steel material and large deformation theory
(3) nonlinear steel material and small deformation theory
(4) nonlinear steel material and large deformation theory

Deflection. The following figure shows the vertical deflection of the corrugated steel pipe for four modeling cases.

Figure 5.6.2-1 Load-deflection plot – vertical deflection as percent of diameter (Study #1)

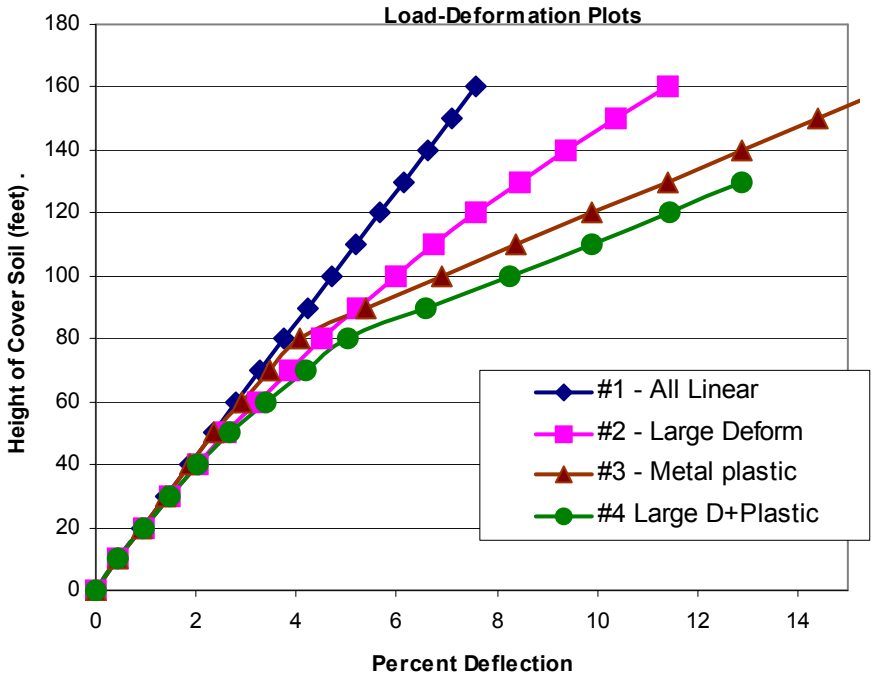

As expected, large deformation theory (case 2) produces deflections that progressively increase compared to the linear model (case 1). Although not shown, the large-deformation deflection curve becomes nearly flat at 300 feet of fill.

Case 3 shows that material nonlinearity by itself produces deflections that exceed case 2 after about 90 feet of fill. The dogleg bend in the deflection curve is caused by complete plastic hinging at crown, springline, and invert occurring at 80 feet of fill. Outer fiber compressive yielding first begins at the springline at 30 feet of fill, becomes a complete plastic hinge at 70 feet of fill, and finally forms a collapse mechanism at 80 feet of fill. After 80 feet fill the soil provides the elastic stiffness to resist complete collapse.

Case 4, which includes both material nonlinearity and large deformations, is presumably the most realistic case for applying the design criteria for deflection. Assuming 5% deflection is the allowable design limit, then 80 feet of fill is the maximum safe burial depth.

Thrust stress. The figure below shows the load-thrust plots for the same four cases wherein the maximum thrust occurs at the springline.

Figure 5.6.2-2 Load-Thrust stress plots of corrugated metal pipe (Study #1)

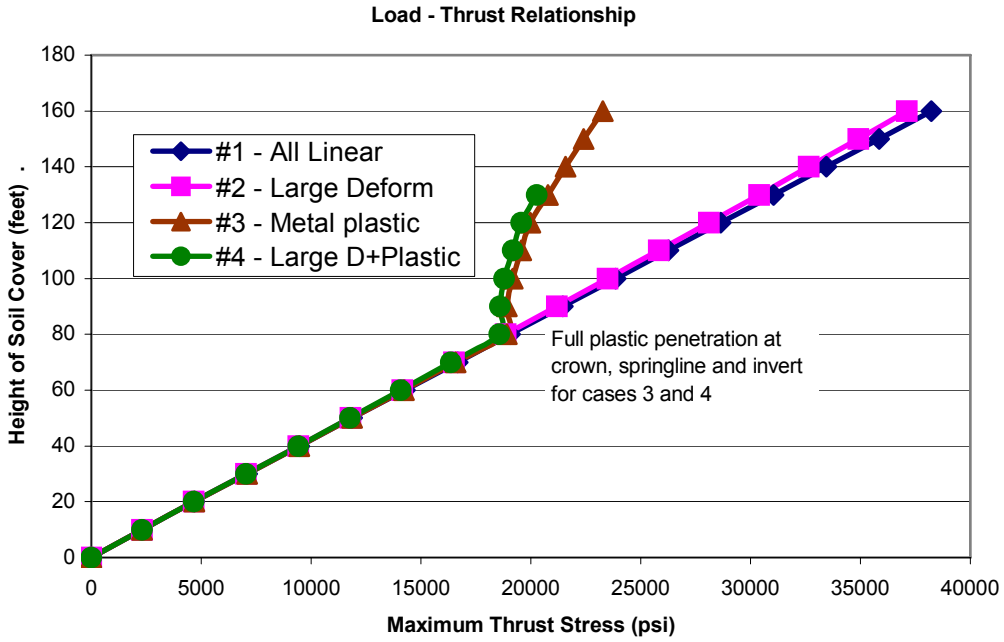

Comparing plots for cases 1 and 2, we observe that the large-deformation solutions are only slightly less than small deformation solutions. The same finding applies to comparing cases 3 and 4 so that it may be concluded that the thrust response is fairly insensitive to the large deformations.

In contrast to the above, when we compare cases 1 and 3 (or cases 2 and 4) we see that the thrust stress response is very sensitive to complete plastic penetration of the corrugated cross-section, causing an abrupt change of behavior. The abrupt change of thrust behavior in cases 3 and 4 is characterized by significantly smaller increases in thrust stress as increments of overburden pressure are applied. This behavior is to be expected because the combination of thrust and moment has produced complete plastic penetration of the corrugated cross-section at the crown, springline and invert so that the pipe now has minimal hoop stiffness (like slotted joints) which forces the soil to carry the bulk of the additional overburden pressure.

For the reasons described above, cases 3 and 4 do not produce a maximum thrust stress that approaches the yield stress value of 33,000 psi even at 160 feet of fill. This result reinforces the notion that the design criteria for corrugated metal should include a limit on the allowable plastic penetration because thrust stress alone can be misleading as evidenced in the above figure.

Buckling Stress and Safety Factor. The last comparison for Study # 1 is the buckling load and associated safety factor. Table 5.6.2-1 lists CANDE's prediction for the thrust stress level that will produce a singular system matrix for each load increment. The buckling capacity is the maximum thrust stress value multiplied by the computed buckling factor "c". Of course, the CANDE predictions, which are based on large deformation theory, only apply to cases 2 and 4.

For reference Table 5.6.2-1 also shows the simplified AASHTO prediction for buckling stress (LRFD specifications 12.7.2.4). The AASHTO equation for buckling stress is only dependent on the pipe diameter, modulus and cross-section geometry, it is not dependent on soil stiffness (assumed the same for all installations), nor is it dependent on metal yield stress. Thus, the predicted AASHTO buckling stress is the same for cases studied herein and is computed to be 42,867 psi, which is 30% greater than yield stress. Another reference value is the often-used Chelapatti-Allgood prediction, which predicts the buckling thrust equal to 54,275 psi. This prediction is based on the buckling of an elastic ring embedded in elastic springs (soil) and subjected to hydrostatic pressure.

Table 5.6.2-1 Buckling stress predictions

Fill Height (feet)	Predicted Thrust Stress Level For Buckling-like Response (psi)			
	CANDE – (Case 2) Linear steel	CANDE – (Case 4) Nonlinear steel	ASSHTO Prediction	Chelapatti-Allgood
10	100,385	100,385	42,867	54,257
20	100,195	100,195	42,867	54,257
30	103,025	101,980	42,867	54,257
40	100,648	97,322	42,867	54,257
50	100,025	80,563	42,867	54,257
60	103,398	58,011	42,867	54,257
70	101,341	42,049	42,867	54,257
80	101,104	15,989	42,867	54,257
90	102,561	0	42,867	54,257
100	102,238	0	42,867	54,257
160	102,057	0	42,867	54,257

For the case of linear steel, CANDE's prediction for buckling stress remains nearly constant and is roughly twice the value of the AASHTO or Chelapati-Algood approximations. However for the case of nonlinear steel, the CANDE predictions for buckling capacity begin to steadily decrease as the steel begins to yield at about 30 feet of fill. When the complete collapse mechanism has formed at 80+ feet of fill, the buckling capacity approaches zero. Recall that CANDE's prediction of buckling stress is based on the current system stiffness matrix that becomes less and less robust as steel yielding increases with each load step.

Figure 5.6.2-3 shows the buckling safety factors as a function of fill height. Safety factors are defined as the buckling stress capacity listed in Table 2 divided by the corresponding thrust stress shown in Figure 5.6.2-2. Note that the loading axis in the figure has been switched to the horizontal in order to illustrate the decrease in safety as fill height increases.

For the case of linear steel, it is evident that the AASHTO buckling safety factor is more conservative than CANDE prediction for all stages of fill height. However when comparison is made for cases including nonlinear steel, the AASHTO safety factor predictions become less conservative after 80 feet of fill. That is the AASHTO safety factor tends to stay constant beyond 80 feet of fill due to the nearly constant thrust stress from the nonlinear steel solution.

In contrast the CANDE safety factor rapidly decreases due to the rapid loss of buckling capacity such that, after 70 feet of fill, CANDE provides a more conservative (and accurate) prediction of buckling safety than does the AASHTO prediction,

From the above study it is concluded that the AASHTO prediction for global is buckling is not always conservative.

Figure 5.6.2-3 Buckling safety factor versus fill height for corrugated steel pipe (Study # 1)

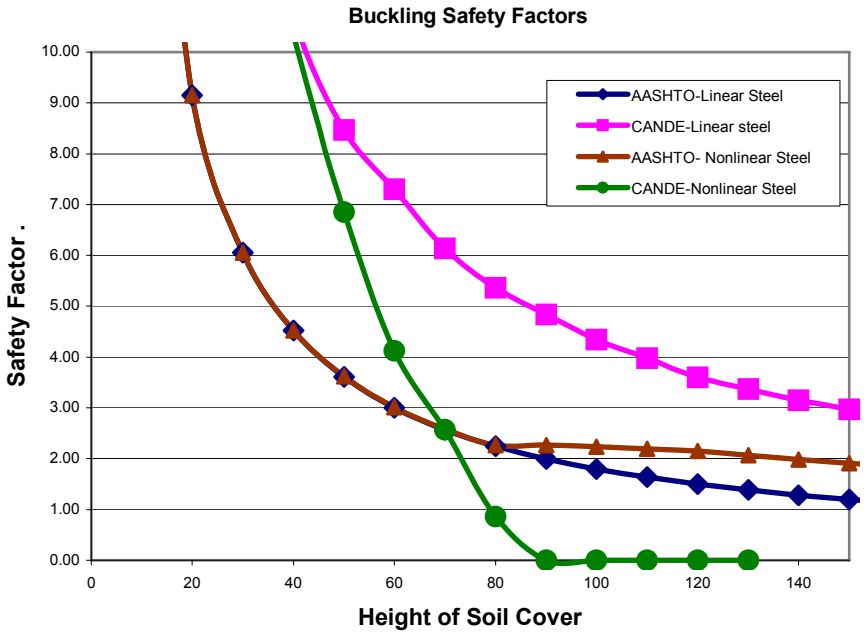

5.6.3 Study # 2 -- Nonlinear soil and bonded interface

This study assumes a nonlinear soil model while retaining the bonded soil-structure interface to define the test problem. Specifically the nonlinear soil is called the Duncan/Selig hyperbolic formulation and represents silty sand compacted to 90% relative density (CANDE reference ML90).

Deflection. Figure 5.6.3-1 shows the vertical deflection of the corrugated metal pipe for four modeling cases composed small and large deformation theory and linear and nonlinear model for the corrugated steel. In this study the plot for case # 1 is not a linear response as it was in the previous study. Rather the curve exhibits a decreasing defection as fill height increases. This, of course, is the influence of the soil model, which becomes stiffer under as confining pressure increases. Note, the soil model becomes less stiff under increasing shear strain, however the overall effect in this case is a stiffening of the soil mass.

Comparative observations between the deflection plots for four cases in are similar to Study #1. Specifically, large deformation theory (case 2) produces deflections that progressively increase as compared to the small deformation model (case 1). The dogleg bends in the deflection curves of cases 3 and 4 are caused by complete plastic hinging at crown, springline, and invert occurring at 80 feet of fill. Outer fiber compressive yielding first begins at the springline at 30 feet of fill, becomes a complete plastic hinge at 70 feet of fill, and finally forms a collapse mechanism at 80 feet of fill. After 80 feet of fill the ever-stiffening soil provides the stiffness to resist complete collapse.

Case 4, which includes both material nonlinearity and large deformations, is presumably the most realistic case for applying the design criteria for deflection. Assuming 5% deflection is the allowable design limit, then 90 feet of fill is the maximum safe burial depth.

Figure 5.6.3-1 Load-Deflection plots of corrugated metal pipe (Study # 2)

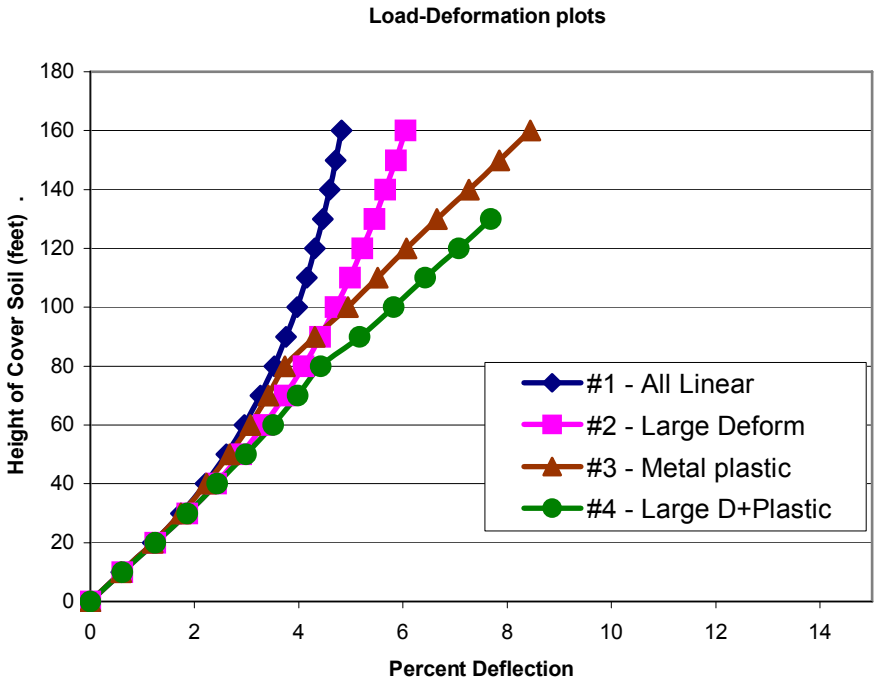

Thrust stress. Figure 5.6.3-2 shows the load-thrust plots for the same four cases. In all cases the maximum thrust stress occurs at the springline. The thrust stress responses in this figure are very similar to Study #1. Overall, the effect of the nonlinear soil model is to reduce thrust stress values by about 5%, otherwise the shape of the curves and behavior is the same. Again we conclude that the thrust response is fairly insensitive to large deformations.

As discussed in the previous study, the abrupt change of thrust behavior in cases 3 and 4 is to be expected because the combination of thrusts and moments has produced complete plastic penetration of the corrugated cross-section at the crown, springline and invert so that the pipe now has minimal hoop stiffness (like slotted joints) which forces the soil to carry the bulk of the additional overburden pressure.

As mentioned before, cases 3 and 4 do not produce a maximum thrust stress that approaches the yield stress value of 33,000 psi even at 160 feet of fill. This result reinforces the notion that the design criteria for corrugated metal should include a limit on the allowable plastic penetration because thrust stress alone can be misleading.

Figure 5.6.3-2 Load-Thrust stress plots of corrugated steel pipe (Study # 2).

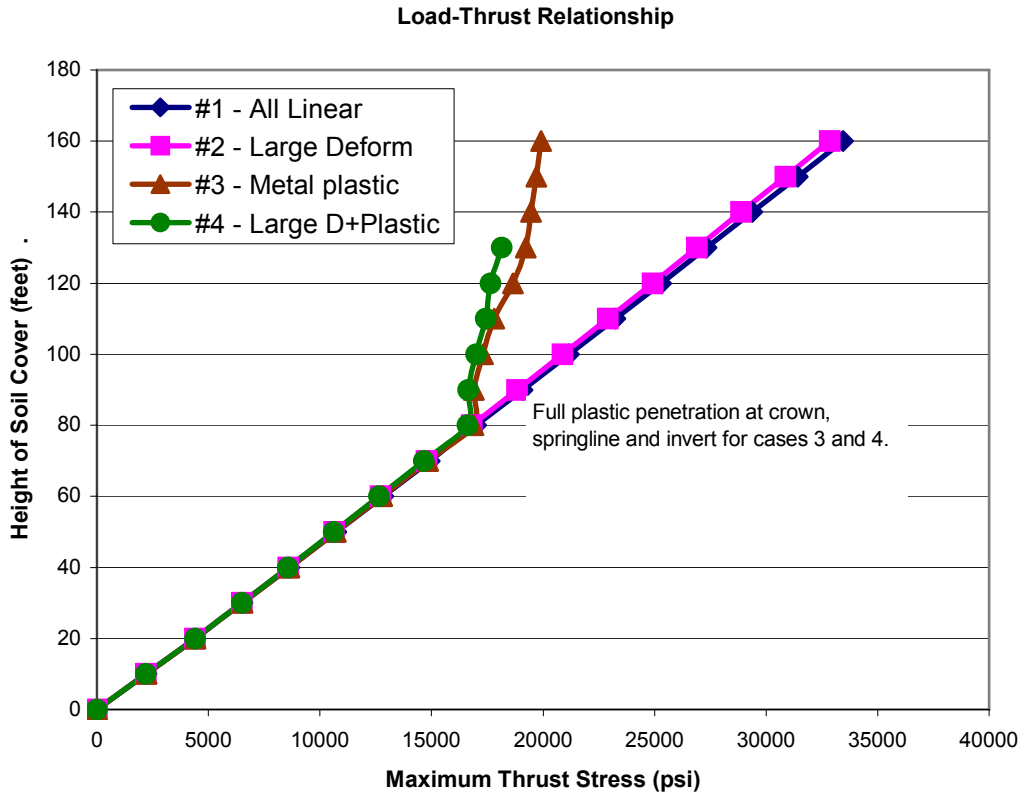

Buckling Stress and Safety Factor. The last comparison for Study # 2 is the buckling load and associated safety factor. Table 5.6.3-1 lists CANDE's prediction for the thrust stress level that will produce a singular system matrix for each load increment. Of course, the CANDE predictions, which are based on large deformation theory, only apply to cases 2 and 4.

As explained in Study # 1, the table also contains the simplified AASHTO prediction for ASSHTO buckling stress and the Chelapatti-Allgood prediction.

Table 5.6.3-1. Buckling stress predictions for Study # 2

Fill Height (feet)	*Predicted Thrust Stress Level For Buckling-like Response (psi)*			
	CANDE – (#2) Linear steel	**CANDE – (#4) Nonlinear steel**	**ASSHTO Prediction**	**Chelapatti-Allgood**
10	107174	107174	42,867	54,257
20	105029	105029	42,867	54,257
30	106067	109260	42,867	54,257
40	111191	102047	42,867	54,257
50	116490	98317	42,867	54,257
60	123310	88218	42,867	54,257
70	131538	67710	42,867	54,257
80	136658	37562	42,867	54,257
90	142060	0	42,867	54,257
100	150731	0	42,867	54,257
160	175659	0	42,867	54,257

For the case of linear steel, CANDE's prediction for buckling capacity increases steadily at each load step because the soil stiffness is increasing without a loss in structural stiffness. However for the case of nonlinear steel, the CANDE predictions for buckling stress begin to steadily decrease as the steel begins to yield at about 40 feet of fill. When the complete collapse mechanism has formed at 80+ feet of fill, the buckling capacity approaches zero. Recall that CANDE's prediction of buckling stress is based on the current system stiffness matrix that becomes less and less robust as steel yielding increases with each load step.

The following figure shows the buckling safety factors as a function of fill height. Safety factors are defined as the buckling stress capacity listed in the above table divided by the corresponding thrust stress shown in Figure 5.6.3-2. Note that the loading axis in the figure has been switched to the horizontal in order to illustrate the decrease in safety as fill height increases.

Figure 5.6.3-3. Buckling safety factor versus fill height for corrugated steel pipe (Study #2)

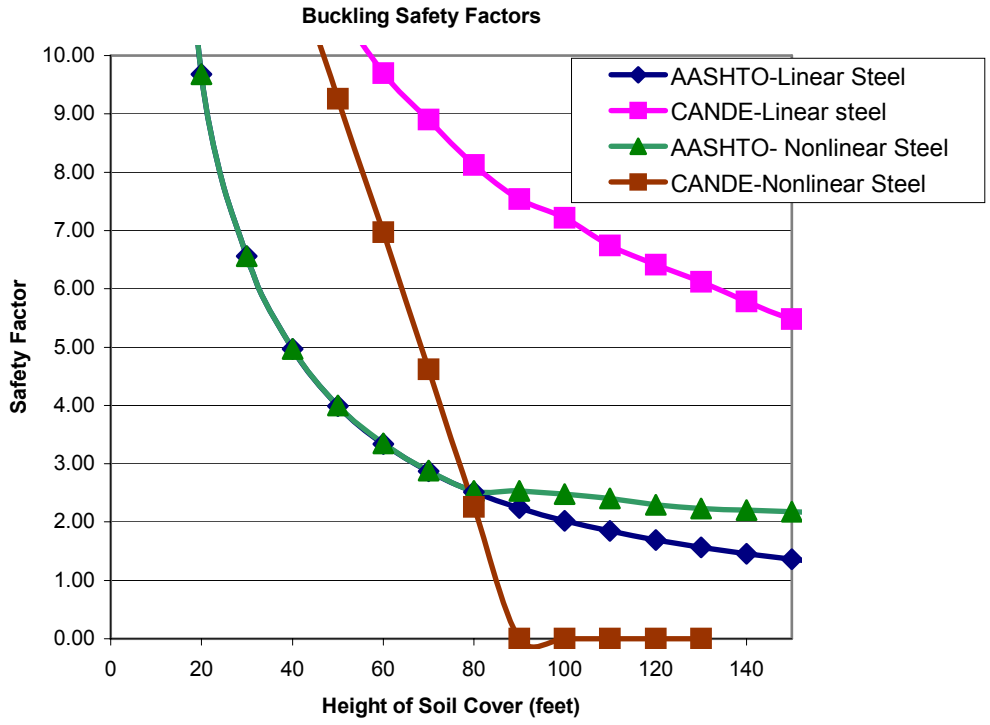

In the above figure we can make the same observations as we did in Study # 1. Namely for the case of linear steel, the AASHTO buckling safety factor is more conservative than CANDE prediction for all stages of fill height. However when comparison is made for cases including yielding steel, the AASHTO safety factor predictions become less conservative after 80 feet of fill. That is the AASHTO safety factor stays relatively constant due to the nearly constant thrust stress from the nonlinear steel solution.

In contrast to AASHTO, the CANDE safety factor rapidly decreases due to the rapid loss of buckling capacity such that, after 80 feet of fill, CANDE provides a more conservative (and accurate) prediction of buckling safety than does the AASHTO prediction. Again, it is concluded that the AASHTO prediction for global is buckling is not always conservative.

5.6.4 Study # 3 -- Linear soil and frictionless interface

Like the first study, Study # 3 uses a linear soil model, however the soil-structure interface is now assumed to be frictionless. The frictionless interface also infers that the culvert will separate from the soil if tension forces should occur.

Deflection. Figure 8 shows the vertical deflection of the corrugated metal pipe for three modeling cases: (the case of steel yielding with small deformations is no longer of interest)

(1) linear steel material and small deformation theory
(2) linear steel material and large deformation theory
(3) yielding steel material and large deformation theory

Figure 5.6.4-1 Load-Deflection plots of corrugated steel pipe (Study # 3)

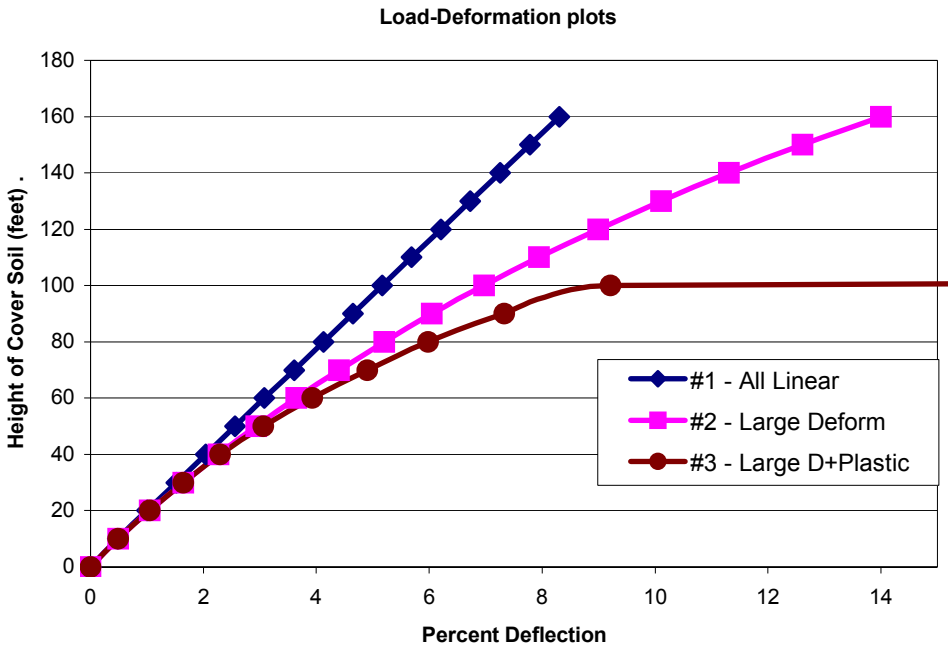

The load-deflection curves for Study 3 are similar to the corresponding curves in Study 1except that all displacements in the above figure are somewhat larger. In the case of combined large deformations and steel yielding, the deflections become excessive at 100 feet fill. This is because at 90 feet of fill the steel at the crown and the invert begin to buckle inward and separates from the soil due to tension break in the interface model. This causes the large displacement observed at 100 feet of fill in the above figure.

Thrust stress. Figure 5.6.4-2 shows the load-thrust plots for the same three cases. In all cases the maximum thrust stress occurs at the springline. Again, the thrust-load plots are similar to the corresponding plots in Study # 1 except that all thrusts are somewhat lower than the completely bonded case. This result is ascribed to loss of shear traction in the frictionless case. For case # 3, the combination of thrust and moment form a collapse mechanism at about 80 feet of fill so that further increase in thrust stress is retarded

Figure 5.6.4-2. Load-Thrust stress plots of corrugated metal pipe (Study # 3).

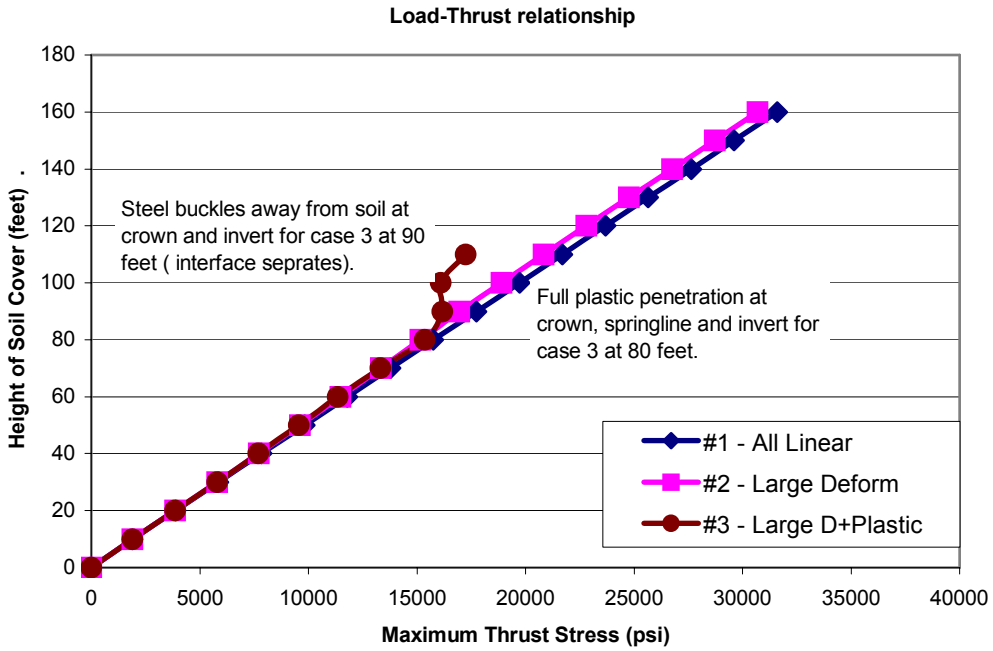

Buckling Stress and Safety Factor. The last comparison for Study # 3 is the buckling capacity and associated safety factor. Table 5.6.4-1 lists CANDE's prediction for the thrust stress level that will produce a singular system matrix for each load increment. The table also contains the simplified AASHTO prediction for ASSHTO buckling stress and the Chelapatti-Allgood prediction.

Table 5.6.4-1 Buckling stress predictions for Study #3

Fill Height (feet)	Predicted Thrust Stress Level For Buckling-like Response (psi)			
	CANDE – (#2) Linear steel	CANDE – (#3) Nonlinear steel	ASSHTO Prediction	Chelapatti-Allgood
10	84219	84219	42,867	54,257
20	84318	84318	42,867	54,257
30	83282	83663	42,867	54,257
40	82244	77324	42,867	54,257
50	83348	64154	42,867	54,257
60	83256	43962	42,867	54,257
70	81915	27274	42,867	54,257
80	81140	4196	42,867	54,257
90	83076	0	42,867	54,257
100	82295	0	42,867	54,257
160	83145	0	42,867	54,257

For the case of linear steel, the predicted buckling stress remains relatively constant at a nominal value of 83,000 psi, which is about 20% less than the corresponding predictions in Study # 1. The 20% reduction is attributed to the observation that the frictionless interface does not generate the same amount of shear stiffness in the soil as does the fully bonded condition. Note that the Chelapati-Algood model is completely devoid of shear stiffness, which is one reason that their buckling predictions are on the low side.

As observed in the previous studies, the CANDE predictions for buckling stress in the presence of yielding steel begin to steadily decrease as the steel begins to yield between 30 and 40 feet of fill. When the complete collapse mechanism has formed at 80+ feet of fill, the buckling capacity approaches zero.

Figure 5.6.4-3 shows the buckling safety factors as a function of fill height. Safety factors are defined as the buckling stress capacity listed in the above table divided by the corresponding thrust stress shown in Figure 5.6.4-2. Again it is observed that in the case of yielding steel, the CANDE safety factor rapidly decreases due to the rapid loss of buckling capacity. After 60 feet of fill, CANDE provides a more conservative (and accurate) prediction of buckling safety than does the AASHTO prediction.

Figure 5.6.4-3 Buckling safety factor versus fill height for corrugated metal pipe (Study #3)

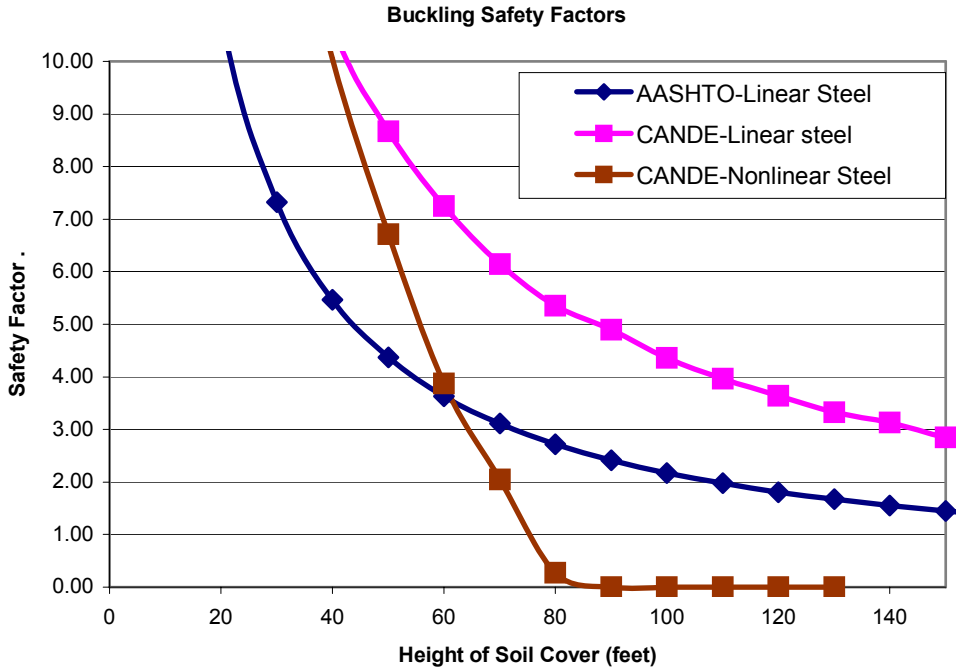

5.6.5 Comparing Studies #1, #2 and #3 with design criteria

We conclude this chapter by comparing the maximum allowable fill heights for the three studies based on working-stress design criteria for corrugated steel pipe. Restricting the comparison to the cases of large deformation with steel yielding, which are presumably the most realistic CANDE solutions, the three studies are differentiated as follows:

- Study #1 = linear soil with bonded interface,
- Study #2 = nonlinear soil with bonded interface
- Study #3 = linear soil with frictionless interface

The design criteria and safety factors are given in the table below,

Table 5.6.5-1 Working stress design criteria for corrugated metal pipe

Design Criterion	Safety Factor	Allowable limit
Thrust yielding	2.0	Thrust stress = ½(yield stress)
Global buckling	2.0	Thrust stress = ½(buckling prediction)
Plastic penetration	1.5	Amount of wall yielding = 2/3 of depth
Vertical deflection	1.0	Deflection = 5% of diameter

Using the above allowable limits and referring to the previous plots for the cases of large deformation with steel yielding, the maximum fill height may determined for each design criterion. The results for each study are recorded in the table below.

Table 5.6.5-2. Allowable fill heights for each design criterion (feet)

Study #	Thrust Yielding	Global Buckling	Plastic Penetration	Vertical Deflection
1	73.0 ft	73.3 ft	55.2 ft	79.5 ft
2	79.4 ft	81.1 ft	49.7 ft	87.7 ft
3	88.9 ft	70.3 ft	53.9 ft	70.9 ft

Plastic penetration is the controlling design criterion for each study, which limits the maximum burial depth on the order of 50 feet. It is interesting to note that all three studies (installation conditions) have both strengths and weaknesses with regard to the design criteria.

As a final comment, the CANDE program performed in a robust manner to obtain converged solutions with several nonlinear models being exercised simultaneousl

6 DESIGN CRITERIA AND LRFD DESIGN METHODOLGY

6.1 Introduction

The probabilistic-based design philosophy known as load and resistance factor design (LRFD) has been adopted into the AASHTO LRFD Bridge Design Specifications (Reference 6) wherein the specifications for buried structures are primarily contained in Section 12. One of the tasks in the NCHRP CANDE Upgrade project was to incorporate LRFD methodology for all culvert materials into CANDE-2007 in addition to the traditional working stress design (WSD) methodology.

This chapter provides a succinct interpretation of the AASHTO LRFD specifications for buried structures with regard to defining factored loads and establishing design criteria. Tabularized values are summarized in this chapter for load factors and load modifiers to quantify dead loads, earth loads, and live loads, which are required for a LRFD analysis to produce the factored demands. The contents of this chapter are published in the Transportation Research Record No. 2028, Reference 23.

Also presented are tabularized descriptions of the design criteria and the corresponding factored capacities, which are defined and quantified herein for corrugated metal, reinforced concrete, and plastic pipe materials. In some cases, the design criteria have been generalized to provide mechanistically meaningful statements that are compatible with comprehensive analysis methods like CANDE.

Although this chapter is focused on LRFD design methodology, the fundamental design criteria presented herein are also used for CANDE's WSD methodology. The WSD approach uses service loads and unfactored capacities to compute safety factors defined as capacity divided by service-load demand. The LRFD approach uses factored loads and factored capacities to compute ratios of factored demand divided by factored capacity for strength related design criteria, and service-load demand divided by performance limits for service related design criteria.

6.2 Objective and Scope

The objectives of this chapter are as follows:

- Summarize the loading definitions and load factors for LRFD methodology that are applicable to the comprehensive solution approach embodied in the CANDE-2007 program.
- Provide a clear and concise set of design criteria for buried structures for corrugated metal, reinforced concrete and plastic pipe that are mechanistically consistent with AASHTO LRFD specifications, but are not dependent on simplified design equations.
- Identify areas where improvements in the current AASHTO specifications are desirable and offer suggestions for a more generalized statement of the design criteria.

LRFD methodology for buried structures includes both service limit states and strength limit states. One consequence of the two limit states when using a comprehensive solution method is that two separate solutions may need to be obtained, one with service loading and one with factored loading. The definitions of service loading and factored loading are provided in the following discussion along with tables summarizing the specified load factors. To augment this discussion, guidance is provided on applying these factored loads in the context of a comprehensive finite element solution methodology.

6.3 Service Loads

A common example of a design criterion that is associated with service loading is the allowable deflection of flexible culverts. In the case of rigid culverts, a common example is the allowable concrete crack width. Later, the exact form of these and other design criteria will be discussed and quantified. For present purposes it is only necessary to understand that a solution at the service load level is required in order to evaluate the service limit design criteria. For a culvert system to successfully pass the service load design criteria, the predicted response such as the percent deflection must be less than or equal to the allowable limit.

The service load level is the actual design load experienced by the culvert system as if one were performing a working stress analysis. Service loads include the following conditions:

1. Dead load of structure
2. Earth load on the soil
3. Live load pressure on the structure transmitted through soil
4. Live load multiplier due to vehicle impact
5. Live load multiplier due to multiple lane presence
6. Other design load considerations such as hydrostatic or thermal loading

In terms of finite element modeling, the structure dead load (body weight of the culvert) is typically applied in the first load step after consideration of in situ soils, followed by a sequence of load steps composed of soil element layers, which are placed around and above the culvert up to the design cover height. Each soil layer is loaded with its own body weight according to the soil density associated with the region. Live loads are typically applied in the last load step(s) on the soil surface as a pressure boundary condition, representing the tire footprint pressures from the design-truck. AASHTO specifications also require that service-load tire pressures be increased by multipliers to account for dynamic impact and the effects of multiple lane presence, which are prescribed as follows:

- Impact multiplier = $1 + 0.33(1.0 – H/8.0) \geq 1.0$ Equation 6-1
  where, H is height of soil cover above the crown in feet.

- Multiple-lane-presence multiplier = 1.2 Equation 6-2

The multiple lane presence factor is 1.2 for a single loaded lane and considers that a single truck has a high likelihood of being overloaded. While LRFD allows reduced values of the multiple presence factor when more than one lane is loaded, calculations for culverts under live load show that the single loaded land condition virtually always controls the design.

As a side comment, it is noted that the prescription of the basic live load tire pressure presents a special problem for two-dimensional, plane strain finite element programs because the tire foot print area extends to infinity in the out-of-plane direction, thereby overestimating the actual loading on the culvert from as compared to the actual footprint width of finite dimensions. One way to correct for this problem is to reduce the surface pressure using the procedure described in Reference 12 and Reference 13. Other methods are currently being invested under NCHRP Project 15-29.

6.4 LRFD Loads for Strength-limit States

For strength limit states such as the yield strength, ultimate strain, or global buckling capacity of the soil-structure system, the LRFD methodology assigns net multiplying factors to the service loads. The resulting structural responses, which are at higher levels of stress than the service load responses, are called the factored demands. Concurrently, resistance factors, whose values are typically 1.0 or less, are multiplied by the strength values and the resulting products are called factored capacities. The test of a successful culvert design using the LRFD methodology is that the factored capacities are greater or equal to the corresponding factored demands for all the strength-state design criteria. In a simplistic sense, the ratio of the effective load factor to the resistance factor is comparable to the safety factor concept used in working stress design methodology. However, it is generally accepted that LRFD methodology offers a more logical design assessment than WSD methodology.

The net multiplying factor applied to service loads is product of two terms called the load factor and the net load modifier. Stated explicitly, the net factored load at any load step may be written as:

$$\text{Factored load} = \boldsymbol{\gamma}\,\boldsymbol{\eta}\,(\text{Service load}) \qquad \text{Equation 6-3}$$

where, $\boldsymbol{\gamma}$ is the specified load factor, and $\boldsymbol{\eta}$ is the net load multiplier.

6.4.1 Load Factors.

The load factor term, symbolically denoted as γ, is currently specified in AASHTO LRFD specifications as shown in the table below. A general observation that should fit well with reader's intuition is that $\boldsymbol{\gamma_{max}}$ (on average) increases in value from the dead load case to the earth load case to the live load case. This increase in load factor value roughly corresponds with our lack-of-confidence in knowing the actual load value in these three cases.

TABLE 6.4.1-1 Load factors and load modifiers for buried structures

Culvert Type	Dead Load Culvert (DC)			Earth fill Loading (EB)			Live Load (LL)	
	γ_{max}	γ_{min}	η_{DC}	γ_{max}	γ_{min}	η_{EB}	γ_{max}	η_{LL}
Reinforced Concrete pipe	1.25	0.9	1.05	1.3	0.9	1.05	1.75	1.00
Reinforced Concrete box	1.25	0.9	1.05	1.3	0.9	1.05	1.75	1.00
Reinforced Concrete arch	1.25	0.9	1.05	1.3	0.9	1.05	1.75	1.00
Corrugated metal pipe or arch	1.25	0.9	1.05	1.95	0.9	1.05	1.75	1.00
Corrugated metal box	1.25	0.9	1.05	1.50	0.9	1.05	1.75	1.00
Plastic pipe (HDPE or PVC)	1.25	0.9	1.05	1.95	0.9	1.05	1.75	1.05

Symbols:
$\boldsymbol{\gamma_{max}}$ = maximum load factor dependent on load case and culvert type**.**
$\boldsymbol{\gamma_{min}}$ = minimum load factor dependent on load case and culvert type.
$\boldsymbol{\eta_{DC}}$ = net load modifier for DC load case = {(ductility)(redundancy)(importance)}
$\boldsymbol{\eta_{EB}}$ = net load modifier for EB load case = {(ductility)(redundancy)(importance)}
$\boldsymbol{\eta_{LL}}$ = net load modifier for LL load case = {(ductility)(redundancy)(importance)}

Two observations about the load factors in Table 1 that require further explanation are; (1) there are two values, γ_{max} and $\gamma_{min,}$ listed for each load case, and (2) the load factors are dependent on the type of culvert material and shape.

With regard to the first observation, the maximum load factor, γ_{max}, is generally the value used in an analysis to produce the worst-case structural response. However during the sequence of load steps in a comprehensive solution

method, it is conceivable that for some load steps the consistent application of γ_{max} may not produce a worst case scenario for a given design criteria. For example, if the earth-fill layers of soil are heavily compacted along the sides of the culvert so that lateral pressure causes an inward movement, the resulting change in moments in the culvert may become less than the initial moment caused by the dead load of culvert in step 1, and also counter to the sign of the moments that will be added into the culvert when subsequent earth-fill layers are placed on top of the culvert. Thus in the spirit of seeking the worst-case LFRD loading scenario, it may be reasonable to use $\boldsymbol{\gamma_{min}}$ for those load steps wherein earth-load layers are placed along the sides of the culvert.

The second observation, i.e., the load factor values are dependent on culvert type and shape, does not have a rational explanation except to say the AASHTO specifications represent work-in-progress. It is certainly reasonable to assign different resistance factors to different structural materials; however it is difficult to argue why the load factors, such as those for vertical earth load, should be different. Perhaps at sometime in the future, the load factors will be uniform for all buried structures. However until that time comes, Table 1 serves as the reference for load factors.

6.4.2 Load Modifiers.

The so-called net load modifier, symbolically denoted as $\boldsymbol{\eta}$, is a product of three sub-factors related to ductility, redundancy and operational importance that are described in AASHTO LRFD Specifications 1.3.2.1. For buried structures it is customary to assign the sub-factors associated with ductility and operational importance to be 1.0. However for the redundancy sub-factor the LRFD specification suggests that value should be 1.05 for buried structures under dead loads and earth loads, but not live loads.

Based on the above discussion, the values in Table 6.4.1-1 for η_{DC} and η_{EB} are recommended to be 1.05 when the maximum load factor $\boldsymbol{\gamma_{max}}$ is being used. On the other hand, if the minimum load factor $\boldsymbol{\gamma_{min}}$ is assigned to a particular load step, then the corresponding load modifier is the inverse value, e.g. load modifier = 1/1.05 = 0.95.

The load modifier for operational importance is a function of the specific structure being designed, thus, while often set to 1.0, other values may be appropriate.

The above loading conditions are not a recipe for all culvert problems because worst loading scenario depends on the structure type, installation, and the governing limit state. However, the beauty of comprehensive solution procedures like CANDE is that it easy to re-run the same problem with different load factors to find the worst loading condition.

6.4.3 LRFD load factors and nonlinear soil models.

A long standing issue with regard to LRFD analysis is whether or not nonlinear soil models should be driven by stresses and strains from factored loading or from service loading. Although there is no question that factored loads are required to produce the factored demands to evaluate the LRFD design criteria against the factored capacities, some engineers argue that the factored soil stresses and strains cause the nonlinear soil models to become overly stiff due to the increased confining pressure from factored loads, especially for the case of deep burial wherein nonlinear soil models like the Duncan/Selig hyperbolic soil models generally result in substantially increased soil stiffness due to "artificially" increased confining stress from the earth load factor. Others argue that the LRFD philosophy implies that factored loads have some "real" probability of occurring so that the increased soil stiffness is the proper analysis approach. Of course, this dilemma only applies to nonlinear soil models because linear soil models are insensitive to the level of stress.

Rather than adopting only one method or the other in the CANDE-2007 program, the Duncan/Selig soil model is programmed to operate by either method at the user's option. Specifically, the input variable called NON in the Duncan/Selig input instructions allows the user to choose whether "service stresses" (NON = 0) or "factored stresses" (NON =1) are used to compute the Duncan/Selig stiffness values for Young's modulus and Bulk modulus. Thus even though factored loads are input into CANDE and the solution output are actual factored structural responses, for the case NON = 0, the stiffness calculations performed within the Duncan/Selig subroutine are based on service stresses at each load step. This is achieved by dividing the factored stress and strain increments by the corresponding load factor for that load step and maintaining a running total of the service stresses and strains to drive the nonlinear soil model.

6.5 Design Criteria

In the following paragraphs, the AASHTO LRFD design criteria are regrouped into three material types called corrugated metal, reinforced concrete, and plastic pipe. The design criteria are summarized in tables followed by a discussion of each design criterion. The tables list the resistance factors, factored capacities and the corresponding reference to AASHTO LRFD Specification. We believe the tabularized design criteria accurately reflect the intentions of the AASHTO specifications; however in some cases, denoted with an asterisk, we have generalized the criterion to be mechanistically compatible with comprehensive solution methods like CANDE-2007.

6.5.1 Corrugated metal

Corrugated steel and corrugated aluminum have the same general AASHTO design criteria, differing only by the numerical value of design criterion limits such as the yield stress. Table 2 is applicable to both types of corrugated metal. The criterion for plastic penetration is a generalization of the AASHTO specifications and is discussed below.

Table 6.5.1-1 Corrugated Metal LRFD Design Criteria.

Design Criterion (Strength limits)	**Resistance Factor**	**Factored Capacity**	**Definition and AASHTO Reference**
(1) Thrust stress (psi)	$\varphi_1 = 1.0$	$\varphi_1 F1$	F1 = metal yield strength (Equation 12.7.2.3-1.)
(2) Global Buckling (psi)	$\varphi_2 = 1.0$	$\varphi_2 F2$	F2 = buckling thrust stress (Equations 12.7.2.4-1-2)
(3) Seam strength (psi)	$\varphi_3 = 0.67, 1.0$	$\varphi_3 F3$	F3 = seam strength (Section 12.7.2.5)
(4) Plastic Penetration *(%)	$\varphi_4 = 0.90$	$\varphi_4 F4$	F4 = fully plastic (100%) (Replaces 12.9.4.3.1)
Performance Limits (Service Load)			
(5) Allowable deflection *(%)	--	P5	P5 = 5%, (2% LS)

1. The thrust stress limit value, F1, is typically 33,000 psi for steel and 24,000 psi for aluminum. The thrust stress criterion is based on AASHTO LRFD equation 12.7.2.3-1.

2. The thrust stress level that causes global buckling, F2, may be conservatively approximated from the simplified AASHTO LRFD equations 12.7.2.4-1-2. A more accurate alternative is to utilize the new large deformation formulation with buckling capacity prediction available in CANDE-2007

3. If seams are not present, the factored seam strength value $\varphi_3 F3$ may be set equal to F1. If longitudinal seams are present, F3 should represent the measured seam capacity and $\varphi_3 = 0.67$

4. Failure from full plastic penetration occurs when the cross section becomes fully plastic due to plastic hinging, which occurs when the internal moment approaches the plastic moment capacity (F4 = 100%). The recommended LRFD resistance factors are 0.90 for steel and 0.85 for aluminum, respectively. This criterion is a generalization of the original AASHTO LRFD equation 12.9.4.3.1 for structural plate box culverts.

   AASHTO specifications are silent on limiting moments or plastic hinging for corrugated metal structures other than structural plate box structures. As implied in the above table, we believe plastic penetration design criterion should applicable to all corrugated metal structures including pipes, arches and long spans.

5. The service load limit for allowable deflection, P5, is generally taken as 5% for all corrugated metal structures except long spans, which are usually limited to 2% of the vertical rise. Although AASHTO Bridge

Specification does not currently specify deflection limits, experience has shown that deflections greater than 5% indicate that the backfill type and/or compaction are below standard.

6.5.2 Reinforced concrete

The AASHTO design criteria for reinforced concrete are the most challenging criteria to generalize because the criteria are masked in simplified solution methods and are differentiated for various culvert shapes. In Table 6.5.2-1 and the ensuing discussion, it is believed that the proposed design criteria faithfully represent the intent and in some cases improve the clarity of the criteria as presented in the AASHTO LRFD specifications.

Table 6.5.2-1 Reinforced Concrete LRFD Design Criteria

Design Criterion (Strength limits)	**Resistance Factor**	**Factored Capacity**	**Definition and AASHTO Reference**
(1) Steel yielding (psi)	$\varphi_1 = 0.90$	$\varphi_1 F1$	F1 = reinforcement strength (Alternative to 12.10.4.2.4a-1)
(2) Concrete crushing* (psi)	$\varphi_2 = 0.75$	$\varphi_2 F2$	F2 = concrete strength (New proposed criterion)
(3) Shear failure (lb/in)	$\varphi_3 = 0.90$	$\varphi_3 F3$	F3 = concrete shear strength (Multiple AASHTO equations)
(4) Radial tension failure (psi)	$\varphi_4 = 0.90$	$\varphi_4 F4$	F4 = radial tension strength (Adapted from 12.10.4.2.4c-1)
Performance Limits (Service Load)			
(5) Allowable crack width* (in)	--	P5	P5 = 0.01 inch (Recommendation)

1. The steel yielding stress limit value, F1, is nominally 60,000 psi for deformed bars and 65,000 psi for smooth wire fabric. This criterion is a generalization of AASHTO LRFD Equation 12.10.4.2.4a-1 and more fundamental then the AASHTO equation for steel area. Note that the AASHTO equation specifies the required steel area for the steel-yielding criterion based on a simplified solution method.

2. The outer-fiber concrete crushing stress limit value, F2, is the ultimate compressive strength f_c'. A concrete compression criterion is explicitly stated in the AASHTO LRFD specifications because it is assumed that reinforcing steel is designed to yield prior to the load level causing the concrete to begin crushing. Here it is proposed that concrete crushing should be retained as a direct design criterion and the specified resistance factor for concrete crushing be less than specified the resistance factor for steel yielding, with values of 0.75 and 0.90, respectively.

3. The shear capacity, F3, is the shear force causing diagonal tension failure at a given cross-section. If the shear demand exceeds the shear capacity, then transverse reinforcement (stirrups) is required. The value of F3 is specified differently by AASHTO depending on structural shape and burial depth.

    - For concrete pipes and arches, the shear strength is specified by Equations 12.10.4.2.5, which yield a variable value for F3 dependent on the values for moment, thrust and shear around the culvert wall.

    - For boxes and 3-sided structures with 2 or more feet of soil cover, the shear strength is specified by Equations 5.14.5.3-1 wherein the value for F3 is dependent on moment and shear (not thrust).

    - For boxes and 3-sided structures with less than 2 feet of soil cover, the shear strength is specified by equations in Section 5.8.3.3 that, in some cases, depend on the nature of the traverse reinforcement (stirrups).

Clearly there is a need for unifying the AASHTO LRFD specifications for the shear strength capacity because rational mechanics suggests that shear strength capacity should be a function of the cross-section properties

and state of loading, not on the culvert shape or depth of burial. Hopefully this remark may stimulate a future research study to develop a more fundamental criterion, which is the root cause of diagonal cracking. However until that time, we propose that AASHTO Equation 12.10.4.2.5 is the best predictor of shear strength capacity for culverts because of the large experimental data base upon which it was developed (Reference 14).

4. The radial tension failure stress, F4, is related to the tension strength of concrete and the structure span. The criterion is adapted from AASHTO LRFD equation 12.10.4.2.4c-1. It is restated here in psi units as:

$$F4 = 37.92(f_c'/1000)^{1/2} F_{rt} \qquad \text{Equation 6-4}$$

where F_{rt} is a scale factor dependent on structure span, which is specified in the paragraphs following Equation 12.10.4.2.4c-1.

The corresponding factored demand is the average radial tensile stress that the curved inner cage exerts on the inside concrete cover thickness. This is automatically determined in CANDE-2007 by dividing the interior cage steel force (maximum tensile force per unit length) by the radius of curvature of the steel cage.

5. The allowable crack width at service loading is generally taken as 0.01 inches in accordance with AASHTO LRFD specification 12.10.3. An empirical formula to predict crack width, developed by Heger and McGrath (Reference 15), has been adopted by AASHTO in the form of Equation 12.10.4.2.4d-1. For purposes of this paper, the authors reworked the equation in a more fundamental form, which linearly relates crack width to the tension stress in the reinforcing steel once it exceeds the surrounding concrete tensile strength. The revised equation is:

$$CW = (t_b s_l / 2n)^{1/3}\{f_s - 0.0316C_1(h/d)^2\sqrt{f_c'}/\rho\}/3000 \qquad \text{Equation 6-5}$$

where, CW is crack width in inches, ≥ 0
f_s is tension steel stress in ksi units
f_c' is concrete strength in ksi units
All other symbols are section properties defined in Section 12.10.4.2.4d

CANDE-2007 predicts the crack width at each point around the culvert by feeding the computed tension steel stress f_s into Equation 5.6 thereby producing a semi-empirical prediction.. This procedure has been well calibrated for crack widths of approximately 0.01 in. and becomes increasingly uncertain as the crack width varies from this value. As an alternative, CANDE 2007 provides the option to use the older Gergely-Lutz formula instead of Equation 6-5.

6.5.3 Plastic pipe

The design criteria for plastic pipe, summarized in Table 6.5.3-1, are straightforward interpretations of the AASHTO LRFD specifications. Said another way, the AASHTO fundamental design criteria are easily understood and not confounded with the simplified methods that are offered to predict the factored demands. The main difficulty in applying the plastic pipe design criteria is deciding whether to use the long-term or short-term material properties. Typically an engineer would select short-term material properties if live loads were the major concern. On the other hand, for a deep burial situation long-term properties are appropriate. In some cases, it may be prudent to solve the problem twice, once with short-term properties and once with long-term properties. This is a relatively easy task with CANDE-2007.

Table 6.5.3-1 Plastic Pipe LRFD Design Criteria.

Design Criterion (Strength limits)	**Resistance Factor**	**Factored Capacity**	**Definitions and AASHTO Reference**
(1) Thrust failure (psi)	$\varphi_1 = 1.0$	$\varphi_1 F1$	F1 = plastic yield strength (Equation 12.12.3.5.1)
(2) Global buckling (psi)	$\varphi_2 = 1.0$	$\varphi_2 F2$	F2 = thrust stress for buckling (Equation 12.12.3.5.2-1)
(3) Combined strain (in/in)	$\varphi_3 = 1.0$	$\varphi_3 F3$	F3 = fiber strain limit (Equation 12.12.3.5.4a-1)
Performance Limits (Service Load)			
(4) Allowable displacement (%)	--	P4	P4 = 5% (Recommendation)
(5) Allowable tensile strain (in/in)	--	P5	P5 = 0.05 (for HDPE) (Table 12.12.3.3-1)

1. The thrust stress limit or ultimate strength, F1, is dependent on the type plastic and the load duration. Types of plastic identified by AASHTO include high-density polyethylene (HDPE) and polyvinyl chloride (PVC) with characteristic material properties for short-term or long-term loading. Nominal values, taken from the ASSHTO LRFD specifications and elsewhere, are shown in Table 6.5.3-2. Thrust load capacity is also influenced by profile geometry, which can reduce section capacity due to susceptibility to local buckling as discussed below.

Table 6.6.3-2 Recommended plastic properties for short and long-term loading

Type of plastic	**Effective Young's Modulus (PE)**		**Ultimate strength (PU)**	
	Short-term (ksi)	**Long-term (ksi)**	**Short-term (ksi)**	**Long-term (ksi)**
HDPE –	110.0	22.0	3.00	0.90
PVC –	400.0	140.0	6.00	2.60
PP –	135.0	27.0	3.10	1.00

2. The thrust stress level that causes local global buckling, F2, may be conservatively approximated from the simplified AASHTO LRFD equations 12.7.2.4-1-2. A more accurate alternative is to utilize the new large deformation formulation with buckling capacity prediction available in CANDE-2007.

3. The combined strain limit value (combined thrust and bending), F3, is specified by AASHTO LRFD Equation 12.12.3.5.4a-1 and is equal to 1.5 times the long-term strength divided by the long-term modulus. Accordingly, HDPE ~ 0.06 in/in, PVC ~ 0.028 in/in. and PP ~ 0.045 in/in.

4. The service load value for allowable deflection, P4, is generally taken as 5% of the diameter for all plastic pipes; however, the deflection limit is not directly specified in the AASHTO LRFD Design Specifications.

5. The service load value for maximum allowable tensile strain, P5, is specified in AASHTO LRFD table 12.12.3.3-1 and is 0.05 in/in for HDPE and 0.035 or 0.05 in/in for PVC depending on cell class.

Local Buckling. Local buckling is not a direct design criterion for plastic pipe, but it does influence the demands and capacities of the design criteria listed above. Local buckling is a nonlinear phenomenon caused by compressive forces

that induce the sub elements of profile wall pipe to deform out-of-plane in a wrinkled pattern. Similar to corrugated metal pipe wherein some amount of outer fiber yielding is permitted, some amount of local buckling is permitted in plastic profile pipe. Chapter 2 provides a description of the CANDE's nonlinear model to account for local buckling based on Section 12.12.3.5.3 of AASHTO LRFD specifications. The procedure simulates the effect of local buckling by reducing the effective area of the sub elements dependent upon the average level of compressive strain in each sub element. Thus, local buckling increases the demand and/or decreases the capacity of design criteria listed above.

6.6 Illustration of LRFD Factors and Evaluation with CANDE

This example is for a concrete arch with straight legs installed in a trench-like installation with backfill soil placed in eight layers to a final cover height of 2 feet above the crown. A live load is placed over the arch centerline on the ninth and last load increment. To evaluate this problem under LRFD design methodology, CANDE's Level-2 arch mesh option is used to automatically construct a symmetric finite element mesh with nine construction increments with the load factors taken from Table 6.4.1-1 and computed as described in the following paragraphs.

6.6.1 Construction increment number 1.

As shown in Figure 6.6.1-1, the first construction increment includes the surrounding in situ soil (red), concrete footing (yellow), and reinforced concrete arch culvert (black). The in-situ soil and the footing are assigned appropriate stiffness values, but with zero body weight. That is, since the in-situ soil and footing are in place before the arch is constructed, the arch is only loaded with its own self-weight. Thus, the arch is assigned a body weight of 150 pcf, representing body weight of concrete. LRFD analysis requires the user to define the load factor for each construction increment. In this case, the first load step represents dead load ($\gamma = 1.25$ and $\eta = 1.05$) so that the net load factor $= 1.25*1.05 = 1.31$.

6.6.2 Construction increment numbers 2 through 8

Figure 6.6.2-1 shows construction increments 2 through 8, which are all associated with earth loading. The 2nd increment is shown as two rows of orange elements, the 3rd increment is shown in yellow, the 4th in green and so on up to the final cover height. Each of these layers of soil is assigned the actual body weight (120 pcf) of the fill soil. Also each increment is assigned the same load factor based on earth loading, computed as ($\gamma = 1.30$ and $\eta = 1.05$) = 1.37. CANDE applies the load factor to the earth loads in steps 2 through 8 so that the accumulated solution is the factored demand at the end of each step.

Figure 6.6.1-1 Concrete arch installation for first construction increment (net load factor =1.31)

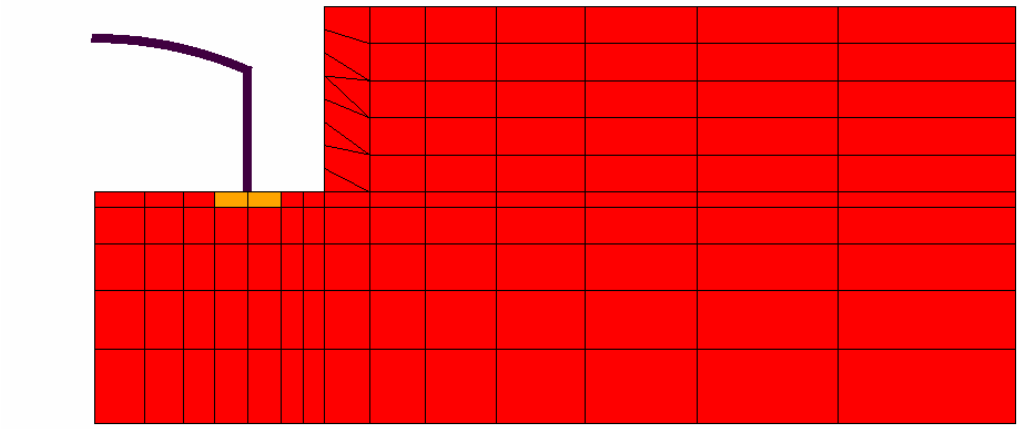

Figure 6.6.2-1 Concrete arch installation for construction increments 2-8 (net load factor =1.31)

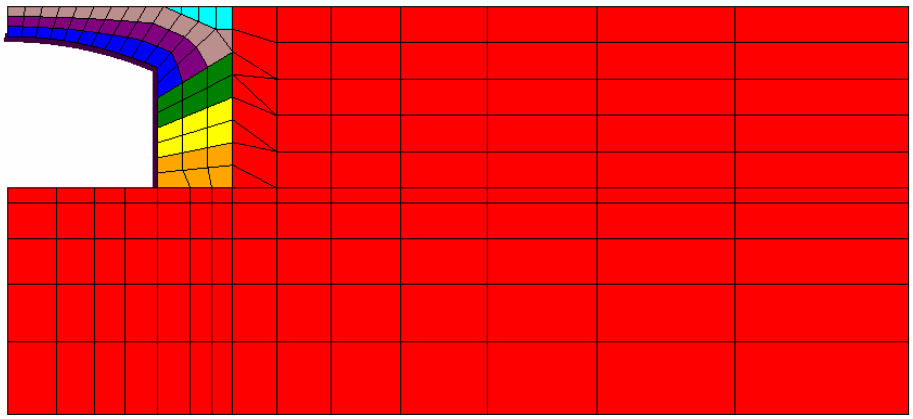

6.6.3 Construction increment number 9 (live load).

The last construction increment represents a live load as illustrated by the red circle in the figure below. The load is applied in the 9th step without additional soil loading as a downward force (boundary condition) representing the actual service load of a design truck, but reduced for plane-strain considerations. In this case the net load factor is computed as (γ = 1.75 and η = 1.05) = 1.84. CANDE applies this load factor to the service load as prescribed in the boundary condition. Thus CANDE's final accumulated solution at the end of load step 9 is the total factored demand.

Figure 6.6.3-1 Concrete arch installation for ninth construction increment (net load factor =1.84)

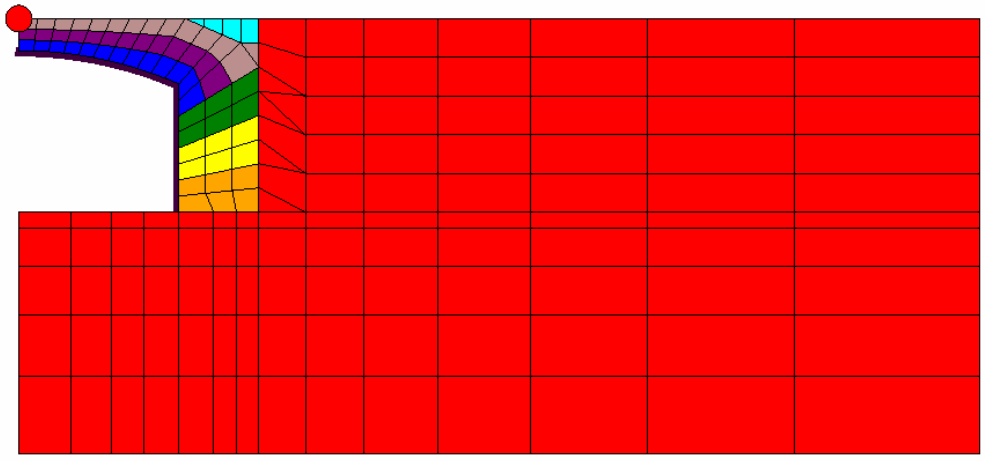

6.6.4 Final evaluation of LRFD design criteria

The final evaluation of the reinforced concrete arch is shown Figure 6.6.4-1in terms of the design criteria for reinforced concrete. CANDE prints out this evaluation at each load step but our interest is focused on the last load step because it represents the worst case. Here we observe that the concrete arch is safe for the proscribed loading conditions because all demand-to-capacity ratios are less than 1.0. In this example, the steel yielding design criterion is called the controlling design criterion because it has the highest ratio. The controlling node number in the evaluation summary identifies the location in the concrete arch where each design criterion has the maximum demand-to-capacity ratio. Although not shown here, the evaluation summary also includes a performance assessment including the predicted crack width under service load conditions.

Figure 6.6.4-1 LRFD evaluation summary for concrete arch after load step 9 (copy from CANDE)

LRFD SUMMARY EVALUATION FOR GROUP 1, LOAD STEP 9

DESIGN-CRITERION	CONTROL NODE	FACTORED DEMAND	FACTORED CAPACITY	RATIO VALUE
STEEL YIELDING (psi)	1	46450.1	54000.0	0.860
CONCRETE CRUSHING (psi)	12	1934.2	3000.0	0.645
SHEAR FAILURE (lbs/in)	11	460.5	782.7	0.588
RADIAL-TENSION FAIL (psi)	1	7.8	54.6	0.142

(Print out from CANDE-2007)

T(This page intentionally left blank)

7 BANDWIDTH MINIMIZATION

A bandwidth minimizer is installed in CANDE-2007 that reduces the maximum bandwidth of the system of equations characterizing the finite element mesh topology. Bandwidth minimization is achieved by strategically renumbering the node numbers that were originally input by the user. Node renumbering is accomplished heuristically by swapping node numbers, a pair at a time, starting with the node number with the highest bandwidth and exchanging it with another node number that optimally reduces the maximum bandwidth at the first location while not generating a bandwidth at the second location that is greater or equal to the original maximum bandwidth.

7.1 Background

For any given finite element problem solved by CANDE, the number rows in global stiffness matrix is dictated by the number of nodal unknowns, which defines the number of equations. In contrast, the number of rows in the global stiffness matrix is dependent on the maximum bandwidth, which depends on the nodal numbering pattern, not the number of equations. By judiciously numbering the nodal pattern, the maximum bandwidth can de reduced. The motivations for reducing the maximum bandwidth are, (1) to reduce storage space for the global stiffness matrix whose size is equal to the number of equations times the maximum bandwidth, and (2) to reduce the time required to solve the system of equations, which is proportional to the number of equations times the square of the bandwidth.

For Level 2 operations, which use "canned" finite element meshes, a bandwidth minimizer is not necessary because the nodal numbering pattern has been optimized once and for all time. On the other hand for Level 3 operations, which implies a user-defined mesh topology, a bandwidth minimizer can be useful. Although experienced users usually construct nodal numbering patterns that are reasonably close to an optimum pattern, there are situations in which the nodal numbering pattern may differ substantially from optimum. For example, when a pre-existing finite element mesh is altered to include more elements and nodes in a local area, the added nodes are likely to have node numbers that are numerically much larger than the existing nodes in this neighborhood, thereby resulting in an excessively large bandwidth.

The bandwidth minimization problem may be formally stated as follows. Given a sparse, n x n, matrix A with components $a_{ij,}$ find a permutation of rows and columns (node renumbering pattern) such that all the non-zero components of matrix A reside in a band that is close as possible to the main diagonal. Or expressed mathematically, Minimize$\{$ i-j for i, j = 1 to n: $a_{ij} \neq 0\}$.

Beginning in the 1950s, the bandwidth minimization problem received a lot of attention from mathematicians due to the emergence of the computer for solving large systems of equations representing a wide range of applications. The classical Cuthill-McKee algorithm, published in 1969, employs the breadth-first search method to construct a level structure in the context of graph theory. A similar but more efficient algorithm, known as Gibbs-Poole-Stockmeyer, was published in 1976, and remains very popular.

Although the above and many other general-purpose bandwidth minimization algorithms are available in the literature, the following development is unique and takes advantage of the finite element assembly methodology to systematically reduce the bandwidth. To the best of the author's knowledge the bandwidth minimization algorithm presented herein is novel.

7.2 Objective and Scope

Within the context of the CANDE finite element program and mesh topology, the objectives are;

1. Develop a robust algorithm to convert an arbitrary node-numbering input pattern into a new node-numbering pattern that minimizes the maximum bandwidth.

2. Display all printed and graphical output from the CANDE solutions in terms of the original node-numbering pattern so that the user does not need to learn the new node number scheme, i.e., transparent to user.

Like other finite element programs, CANDE's finite element methodology has three properties that are extremely useful for the bandwidth minimization algorithm:

- First, the global system matrix is symmetric so that bandwidth minimization is restricted to one side of the matrix diagonal.
- Second, each node number represents a group of nodal unknowns (e.g., x-displacement, y-displacement, and rotation) each with the same bandwidth. Thus bandwidth minimization is reduced to reordering the node-number pattern as opposed to the entire set of equations.
- Third, all the information required to minimize the bandwidth is contained in the so-called element connectivity matrix, which simply identifies the node numbers associated with each element.

The above advantages are exploited in the following development.

7.3 Bandwidth Minimization Methodology in CANDE

7.3.1 Element connectivity matrix

The element connectivity matrix contains the node numbers that are attached to each element and is symbolically denoted and dimensioned as NOD(NET,NDX), where NET is the total number of elements and NDX is the maximum number of nodal locations as required by the various element types. In the CANDE program, for example, NDX = 4 to accommodate the 4-noded quadrilateral elements, which has more nodes than the other types of elements as shown in the table below.

Element Type (connected nodes)	NOD(NE,1)	NOD(NE,2)	NOD(NE,3)	NOD(NE,4)
Beam-column (nodes=2)	Node-1	Node-2	0	0
Triangle (nodes=3)	Node-1	Node-2	Node-3	0
Interface (nodes=3)	Node-1	Node-2	Node-3	0
Quadrilateral (nodes=4)	Node-1	Node-2	Node-3	Node-4

Letting NE be a counter from 1 to NET, then the components of element connectivity matrix are identified as:

- NOD(NE,1) = node number assigned to location 1 of element NE
- NOD(NE,2) = node number assigned to location 2 of element NE
- NOD(NE,3) = node number assigned to location 3 of element NE (depending on element type)
- NOD(NE,4) = node number assigned to location 4 of element NE (depending on element type)

If, for example, element number 10 is a beam element with the two end-nodes numbered 33 and 43, then NOD(10,1) = 33 and NOD(10,2) = 43. The remainder of the nodal list for element 10 is equal to 0.

7.3.2 Algorithm Cycle.

With the above information as a starting point, bandwidth minimization is accomplished by swapping node numbers, a pair at a time, starting with a node number that has the highest bandwidth and exchanging it with another node number that optimally reduces the maximum bandwidth at the first node location while not generating a bandwidth at the second location that is greater or equal to the original maximum bandwidth.

The process is presented in the following four steps. These steps are repeated iteratively until no additional node pairs can be found to further reduce the bandwidth.

Step 1. Use the current NOD connectivity matrix to create a new matrix denoted and dimensioned as MT(NDT,3) where NDT is the total number of nodes in the mesh. Letting N represent each node number in turn, the three components of the MT matrix are defined as follows:

- MT(N,1) = Maximum node number among all nodes that are attached to any element that is also attached to node N. MT(N,1) is referred to as NDMAX.

- MT(N,2) = Minimum node number among all nodes that are attached to any element that is also attached to node N. MT(N,2) is referred to as NDMIN.

- MT(N,3) = Maximum of {ILEFT or IRITE}, where ILEFT = N - NDMIN, which is the bandwidth to the left of node N, and IRITE = NDMAX – N, which is the bandwidth to the right of node N. MT(N,3) is referred to as MAXB, which is the largest bandwidth associated with node N.

The computational key to establishing the MT matrix is to start with an outer do-loop for each node number (referred to as the pivot node). Insert an imbedded do-loop for the element numbering and use the NOD connectivity array. If any of the element's connectivity nodes match the pivot node, then record the maximum and minimum nodal values found in that element's connectivity array. Replace the maximum and/or minimum nodal values by node numbers from subsequent element connectivity arrays if the node values are more extreme than the previously recorded values. At completion of the element loop, the values of NDMAX, NDMIN and MAXB for the current pivot node are stored in the MT matrix.

Step 2. Search the MT(N,3) column to find the maximum bandwidth of all nodes. Denote and save this value as MAXALL, (i.e., MAXALL = Maximum of {MT(N,3), N=1 to total number of nodes}. It is often the case that several nodes share the same maximum bandwidth value, MAXALL. Accordingly, each of these node numbers is a candidate for the current nodal position to be called node-1. The primary goal is to optimally reduce the bandwidth at the node-1 position by interchanging the node-1 number with an as yet undetermined node number, called node-2. Of course, the insertion of the node-1 number into the node-2 position must also be considered as explained in the next step.

Step 3. The purpose of step 3 is to select an optimum pair of nodes, called node-1 and node-2, such that the interchange of their node numbers reduces the local bandwidth at node-1, while maintaining the bandwidth at node-2 to be less than MAXALL. A candidate number for node-1 is labeled N1 and a candidate number for node-2 is labeled N2. We begin with an outer do-loop for all nodes using the node counter N1, and we exclude all N1 node numbers such that MT(3,N1) ≠ MAXALL. Thus, the N1 nodes that are not excluded are candidates for node-1. For node-2 candidates, we use an inner do-loop wherein we restrict our search for N2 node numbers in the sequential range;

$$N2(start) = MT(1,N1) - MAXALL + 1$$

$$N2(end) = MT(2,N1) + MAXALL - 1$$

This restricted range of N2 contains the only node numbers that will reduce the bandwidth at the N1 position.

If the candidate node pair, N1 and N2, were interchanged such that number N2 is assigned to position 1 and number N1 is assigned is assigned to position 2, then the new bandwidths at these two positions can be respectively determined as;

MAXB1 = Maximum of {N2-MT(N1,2) or MT(N1,1)-N2}

MAXB2 = Maximum of {N1-MT(N2,2) or MT(N2,1)-N1}

The next step within the inner loop is to test whether or not the current candidate pair, N1 and N2, is a better choice than the best of the previous candidate pairs. This test is passed by satisfying two simultaneous requirements:

(1) MAXB1 is smaller than that produced by any previous candidate pairs, and

(2) MAXB2 is less than MAXALL

When all candidate node pairs have been tested, there are two possible outcomes, which dictate one of two possible courses of action:

(1) A final node pair, node-1 and node-2, has been identified that reduces the bandwidth. In this case we proceed to Step 4 to update matrices and vectors to perform the node swapping.

(2) No node pair could be found to reduce the current maximum bandwidth (MAXALL). In this case, we exit from the bandwidth minimization process because the job is done.

Step 4. Given a viable solution for node-1 and node-2, the purpose of this step is to update the element connectivity matrix with the current node swap. It is also useful to update a history vector that keeps track of all the nodal changes, called an "is-was" vector.

To update the connectivity matrix, we perform an outer loop search with element counter NE, and an inner loop search with node-location counter K. At any point during the update process, let node-x be the nodal value representing NOD(NE,K). The update is easily achieved by two successive if-then statements:

If node-x equals node-1, then set NOD(NE,K) = node-2

If node-x equals node-2, then set NOD(NE,K) = node-1

When the search loops are completed, the NOD connectivity matrix is completely updated and we may return to Step 1 to repeat the entire process with the new NOD matrix, which provides new starting conditions.

However before returning to Step 1, it is useful to update a history vector that relates the current node numbering to the original node numbering defined by the user. To this end, denote and dimension a nodal vector ISWAS(NPT) and initialize ISWAS(N) = N, for N progressing from 1 to NPT. This initialization infers that new node numbers N are identical to the old node numbers ISWAS(N).

To update for each node swap, let K1 = ISWAS(node-1) and K2 = ISWAS(node-2), where K1 and K2 are the original node numbers that are currently represented by node-1 and node-2, respectively. Then nodal swap is easily updated and saved as

ISWAS(node-1) = K2

ISWAS(node-2) = K1

When all cycles of node swapping is complete (job done), the ISWAS vector will contain the final correspondence between the new node number N and the old node number ISWAS(N). Said another way, ISWAS(N) is the original node number that identifies the same nodal location that is now identified as N. As discussed in the next section, the ISWAS vector is useful for updating other nodal vectors such as nodal coordinates that must be converted to the new nodal numbering pattern.

This marks the end of Step 4 and the algorithm requires that we return to Step 1 for another cycle. The termination of cycles is decided in Step 3.

7.3.3 Post algorithm-cycle updates.

When the algorithm cycle is exited at Step 3, the maximum bandwidth has been minimized, and the updated NOD connectivity matrix and the ISWAS vector are complete. However before the finite element solution process can begin, other nodal data that is defined in the original nodal numbering scheme must be converted to the new node numbering scheme such as nodal coordinate vectors and boundary condition vectors prescribing displacements and/or forces at nodes. The ISWAS vector is used to accomplish these conversions.

For vectors such as nodal coordinates, say X and Y, that implicitly reference the old nodal number by means of the vector index number N, it is necessary to first make the conversion to a temporary vector, say T, over a do loop N = 1 to NDT as shown below:

T(N) = X(ISWAS(N))

After this do-loop is completed, the X vector is converted to the new node numbers by a second do-loop over the same index range:

X(N) = T(N)

The two-step conversion is required so that information in X vector is not prematurely overwritten, which would occur in a one-step conversion.

For vectors that explicitly define old node numbers such as the list of nodes where boundary conditions are applied, say vector NB, the conversion can be made in one do-loop as,

NB(I) = NB(ISWAS(I))

where I = 1, to the number of boundary conditions.

After the last conversion of old node numbers to new numbers is completed, the ISWAS vector as previously defined is no longer useful. In preparation for the finite element solution phase, it is convenient to redefine the ISWAS vector to be the inverse of its original definition. That is, ISWAS (N) is the new node number corresponding to the old node number N. The inverse is accomplished in a two-step process using a temporary vector T, similar to the conversion of nodal coordinates. Specifically, for N = 1 to NDT:

T(ISWAS(N)) = N

Followed by a second do-loop to store inverse definition back into the ISWAS,

ISWAS(N) = T(N)

In summary, the entire process described above is easily executed in a single subroutine (called BMIZER in CANDE). The output from this subroutine includes the updated NOD matrix, the updated nodal vectors (X, Y, NB, etc.) and the ISWAS vector in its second definition, that is, ISWAS(N) is the new node number associated with old node number N. From this point on, the finite element assembly and solution routines will be working the new node numbering pattern.

7.4 Transparency of Node Numbers in Solution Output.

The second objective of this development is to list the solution output with reference to the original node numbers. A prime example is the tabular listing of displacements where, for example, the output displays values for N, U(N), V(N), where U(N) and V(N) are the x and y displacements at node N. Since U(N) and V(N) are in reference to the new node-numbering pattern, we must redefine the displacement indexes if N represents the sequential numbers of the old numbering pattern.

The proper indexes for the displacements are contained in the ISWAS vector (2nd definition). Therefore, to display the information by a write statement imbedded in a do-loop for N = 1 to NPT, the write statement would read as,

```
WRITE(*,*)  N,  U(ISWAS(N)), V(ISWAS(N))
```

Output of any other nodal data is handled in the same manner.

Fortunately, element output data such as stress and strain measures are referenced to element numbers, not node numbers. Thus element output data is the same for either the old or new nodal number pattern.

7.5 Illustration of Bandwidth Minimization

A simple finite element mesh layout, resembling a house on stilts, is shown in Figure 7.5-1 and is used to illustrate the bandwidth minimization algorithm. The mesh contains a total of eight elements composed of 4 beam elements, 2 quadrilateral elements, and 2 triangular elements. The initial node-numbering pattern, subsequently referred to as the old node numbers, is shown in the figure with red numbers. A quick inspection of Figure 1 reveals that the initial node-numbering pattern is far from optimum because of the intentional disparity between node number values surrounding each node point. Thus, there is room for improvement from the bandwidth minimization algorithm.

Figure 7.5-1. Mesh topology for house-on-stilts showing elements and original node pattern

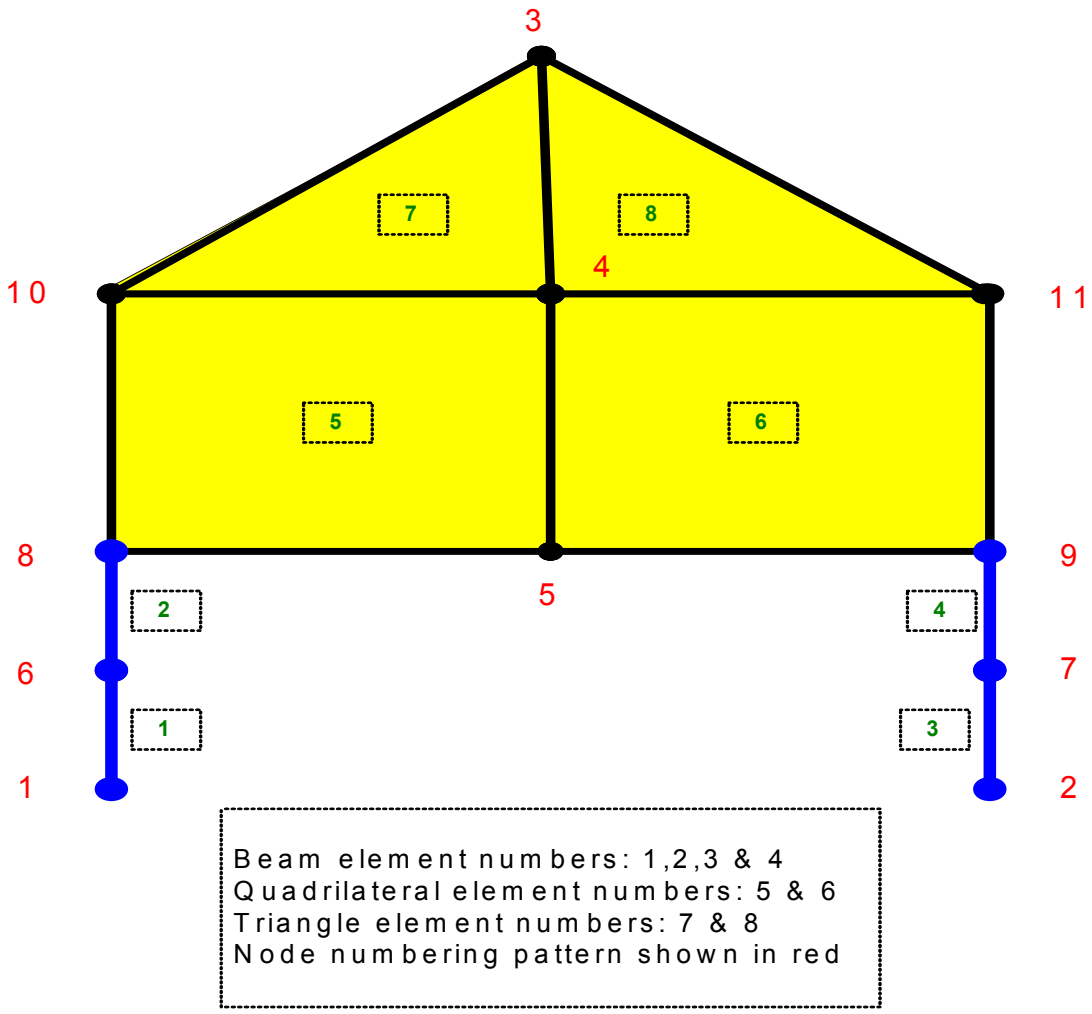

Table 7.5-1 shows the initial connectivity array for the eight elements that is easily deduced from the above figure. Also shown in the table is the initial MT Matrix that is constructed from the element connectivity array as described in Step 1 of the algorithm. For Step 2 it is observed from the last column in the MT matrix that the overall maximum bandwidth is eight (MAXALL = 8).

In Step 3, which is the heart of the algorithm, the MT matrix shows that both node #3 and node #11 are candidates for the primary swapping node because both have a maximum bandwidth equal to 8. For node #3, the candidate secondary node numbers are # 4 to #10, which is the node range that can reduce the bandwidth at node #3. Similarly for node #11, the candidate secondary node numbers are #4 to #10, which is the node range that reduces the bandwidth at node #11.

Of all the possible combinations of primary and secondary node pairs, the winning pair, passing the final test in Step 3, is shown at the bottom of Table 1 as primary node = #3 and secondary node = #7.

Table 7.5-1. NOD and MT Matrices for initial node numbering (Node swaps = 0)

NOD – Matrix (Element Connectivity)						MT-Matrix (Bandwidth Analysis)			
Element	**Node a**	**Node b**	**Node c**	**Node d**		**Pivot Node**	**NDMAX**	**NDMIN**	**MAXB**
1	6	1	0	0		1	6	1	5
2	8	6	0	0		2	7	2	5
3	7	2	0	0		3	11	3	8
4	9	7	0	0		4	11	3	7
5	10	8	5	4		5	11	4	6
6	4	5	9	11		6	8	1	5
7	10	4	3	0		7	9	2	5
8	4	11	3	0		8	10	4	4
						9	11	4	5
						10	10	3	7
						11	11	3	8
Results of Algorithm: Nodes to be swapped **Node-1 = 3** **Node-2 = 7**									

Step 4 updates the element connectivity matrix NOD with the node pair #3 and #7. After the update is complete the process starts again at Step 1 to build a new MT matrix.

Table 7.5-2, like the previous table, shows the current NOD and MT matrices after the first node swap.
The MT matrix shows that the bandwidth at node #3 was reduced from 8 to 6. However the largest bandwidth among all nodes is now reduced to seven (MAXALL = 7), occurring at nodes #4 and #11.

Table 7.5-2. NOD and MT Matrices after 1st node swap (Node swaps = 1)

NOD – Matrix (Element Connectivity)						MT-Matrix (Bandwidth Analysis)			
Element	**Node a**	**Node b**	**Node c**	**Node d**		**Pivot Node**	**NDMAX**	**NDMIN**	**MAXB**
1	6	1	0	0		1	6	1	5
2	8	6	0	0		2	3	2	1
3	3	2	0	0		3	9	2	6
4	9	3	0	0		4	11	4	7
5	10	8	5	4		5	11	4	6
6	4	5	9	11		6	8	1	5
7	10	4	7	0		7	11	4	4
8	4	11	7	0		8	10	4	4
						9	11	3	6
						10	10	4	6
						11	11	4	7
Results of Algorithm: Nodes to be swapped **Node-1 = 4** **Node-2 = 8**									

In like fashion Tables 7.5-3 to 7.5-7 show the algorithm results for five more successive node swaps.

Table 7.5-3. NOD and MT Matrices after 2nd node swap (Node swaps = 2)

NOD – Matrix (Element Connectivity)						MT-Matrix (Bandwidth Analysis)			
Element	**Node a**	**Node b**	**Node c**	**Node d**		**Pivot Node**	**NDMAX**	**NDMIN**	**MAXB**
1	6	1	0	0		1	6	1	5
2	4	6	0	0		2	3	2	1
3	3	2	0	0		3	9	2	6
4	9	3	0	0		4	10	4	6
5	10	4	5	8		5	11	4	6
6	8	5	9	11		6	6	1	5
7	10	8	7	0		7	11	7	4
8	8	11	7	0		8	11	4	4
						9	11	3	6
						10	10	4	6
						11	11	5	6

Results of Algorithm: Nodes to be swapped
Node-1 = 10
Node-2 = 7

Table 7.5-4. NOD and MT Matrices after 3rd node swap (Node swaps = 3)

NOD – Matrix (Element Connectivity)						MT-Matrix (Bandwidth Analysis)			
Element	**Node a**	**Node b**	**Node c**	**Node d**		**Pivot Node**	**NDMAX**	**NDMIN**	**MAXB**
1	6	1	0	0		1	6	1	5
2	4	6	0	0		2	3	2	1
3	3	2	0	0		3	9	2	6
4	9	3	0	0		4	8	4	4
5	7	4	5	8		5	11	4	6
6	8	5	9	11		6	6	1	5
7	7	8	10	0		7	10	4	3
8	8	11	10	0		8	11	4	4
						9	11	3	6
						10	11	7	3
						11	11	5	6

Results of Algorithm: Nodes to be swapped
Node-1 = 3
Node-2 = 6

Table 7.5-5. NOD and MT Matrices after 4th node swap (Node swaps = 4)

NOD – Matrix (Element Connectivity)				
Element	**Node a**	**Node b**	**Node c**	**Node d**
1	3	1	0	0
2	4	3	0	0
3	6	2	0	0
4	9	6	0	0
5	7	4	5	8
6	8	5	9	11
7	7	8	10	0
8	8	11	10	0

MT-Matrix (Bandwidth Analysis)			
Pivot Node	**NDMAX**	**NDMIN**	**MAXB**
1	3	1	2
2	6	2	4
3	4	1	2
4	8	3	4
5	11	4	6
6	9	2	4
7	10	4	3
8	11	4	4
9	11	5	4
10	11	7	3
11	11	5	6

Results of Algorithm: Nodes to be swapped
Node-1 = 5
Node-2 = 7

Table 7.5-6. NOD and MT Matrices after 5th node swap (Node swaps = 5)

NOD – Matrix (Element Connectivity)				
Element	**Node a**	**Node b**	**Node c**	**Node d**
1	3	1	0	0
2	4	3	0	0
3	6	2	0	0
4	9	6	0	0
5	5	4	7	8
6	8	7	9	11
7	5	8	10	0
8	8	11	10	0

MT-Matrix (Bandwidth Analysis)			
Pivot Node	**NDMAX**	**NDMIN**	**MAXB**
1	3	1	2
2	6	2	4
3	4	1	2
4	8	3	4
5	10	4	5
6	9	2	4
7	11	4	4
8	11	4	4
9	11	6	3
10	11	5	5
11	11	7	4

Results of Algorithm: Nodes to be swapped
Node-1 = 5
Node-2 = 6

Table 7.5-7. NOD and MT Matrices after 6th node swap (Node swaps = 6)

NOD – Matrix **(Element Connectivity)**

Element	Node a	Node b	Node c	Node d
1	3	1	0	0
2	4	3	0	0
3	5	2	0	0
4	9	5	0	0
5	6	4	7	8
6	8	7	9	11
7	6	8	10	0
8	8	11	10	0

MT-Matrix (Bandwidth Analysis)

Pivot Node	NDMAX	NDMIN	MAXB
1	3	1	2
2	5	2	3
3	4	1	2
4	8	3	4
5	9	2	4
6	10	4	4
7	11	4	4
8	11	4	4
9	11	5	4
10	11	6	4
11	11	7	4

Results of Algorithm: Nodes to be swapped
None (job done)
No further node swaps will reduce the maximum bandwidth less than 4

The algorithm exited after six node swaps, and Table 7.5-7 portrays the final element connectivity matrix and MT matrix. The final maximum bandwidth is 4, which is a 50% reduction of the original bandwidth.

It is reiterated here that the algorithm is intended to reduce the maximum bandwidth, not to minimize the skyline profile of all nodes, which in this example, includes eight different nodes sharing maximum the bandwidth. Indeed it is possible to construct a node pattern for this example in which only one node has a maximum bandwidth of 4 and all other nodes have a bandwidth of 3 or less.

Table 7.5-8 shows the final ISWAS vector for both definitions discussed in the algorithm. The second definition is used to reference finite element output back to the original nodal numbering system so that the user need not be concerned with the new numbering system that is only used internally in the solution routines.

Table 7.5-8. Final results of new and old node numbering

ISWAS Definition # 1		ISWAS Definition # 2	
New Nodes	Old Nodes	Old Nodes	New Nodes
1	1	1	1
2	2	2	2
3	6	3	10
4	8	4	8
5	7	5	7
6	10	6	3
7	5	7	5
8	4	8	4
9	9	9	9
10	3	10	6
11	11	11	11

As a closing comment, it is not claimed that the above method provides an absolute global minimum to the bandwidth problem. However all the results to date have produced node-numbering patterns that could not be further improved to reduce the maximum bandwidth. The method is robust and rapid, typically, achieving maximum bandwidth reduction with a minimal number of node swaps.

8 MODELING TECHNIQUES

When applying CANDE-2007 to analyze or design any culvert installation (or more generally any soil structure interaction problem), modeling questions always arise. Some common questions are; what extent of the insitu soil should be included in the finite element mesh, what soil models should be used for insitu and backfill soil, should interface elements be included between structure and soil, how many construction increments should be used, and is large deformation theory required. There is no clear-cut answer to these and similar modeling questions because each problem is unique and modeling assumptions that are appropriate for one case may not be appropriate for another.

The best advice is to try as many modeling approaches as can be practically undertaken for a particular problem. Sometimes it will be found that the differences in solutions from alternative modeling assumptions are inconsequential. At other times, a particular modeling assumption may substantially alter the structural behavior, impacting the safety of the design. In all cases, however, useful information is obtained that guides our insight into soil-structure interaction and permits a more intelligent assessment of the problem.

The remainder of this chapter provides suggested techniques for modeling live loads, pipe-group connections and combinations, and construction increments and soil compaction. However the "best advice" approach described above should always be kept in mind.

8.1 Live Loads

External loads (as opposed to element body weight loads) are defined by boundary-condition input data described in CANDE's user instructions. All external loads are applied at nodes as force components in the global x and y directions per unit length in the z direction. Alternatively, if desired, the force components can be defined in rotated x-y coordinates defined by the user.

Figure 8.1-1 illustrates F_x and F_y force components acting along a particular node strip along the z-direction. Also shown in the figure is a uniform surface-pressure strip load with a uniform pressure P_0.

Figure 8.1-1. Illustration of nodal strip load and surface-pressure strip load.

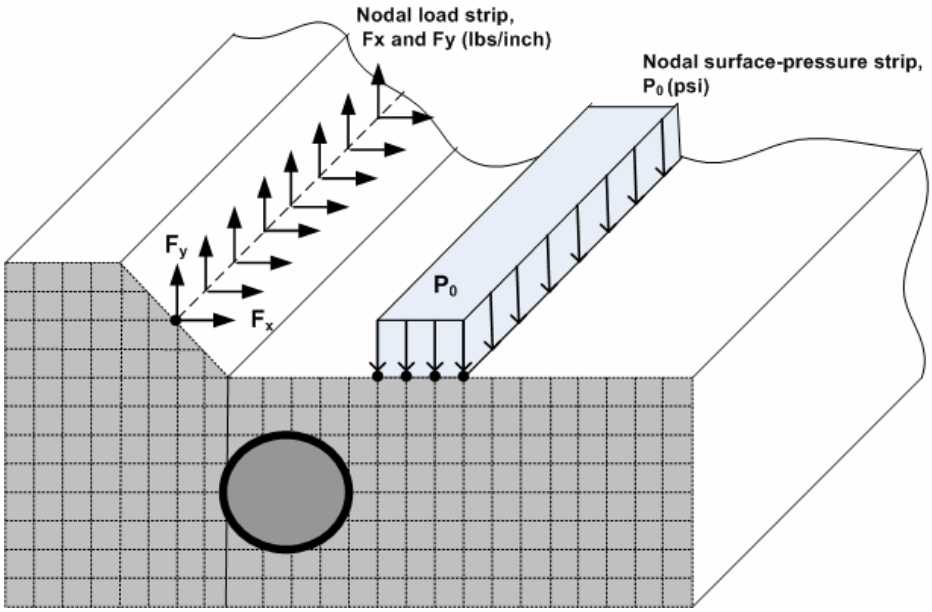

Pressure strip loadings are converted to equivalent nodal strip loads by distributing the pressure load acting on each element to the neighboring nodes and summing the results to determine the equivalent force strips, F_x and F_y. Figure

8.1-2 and the accompanying table shows an example of converting a pressure-strip load to nodal-strip loads in the negative y-direction.

Figure 8.1-2 Illustration of converting pressure strip to equivalent nodal forces

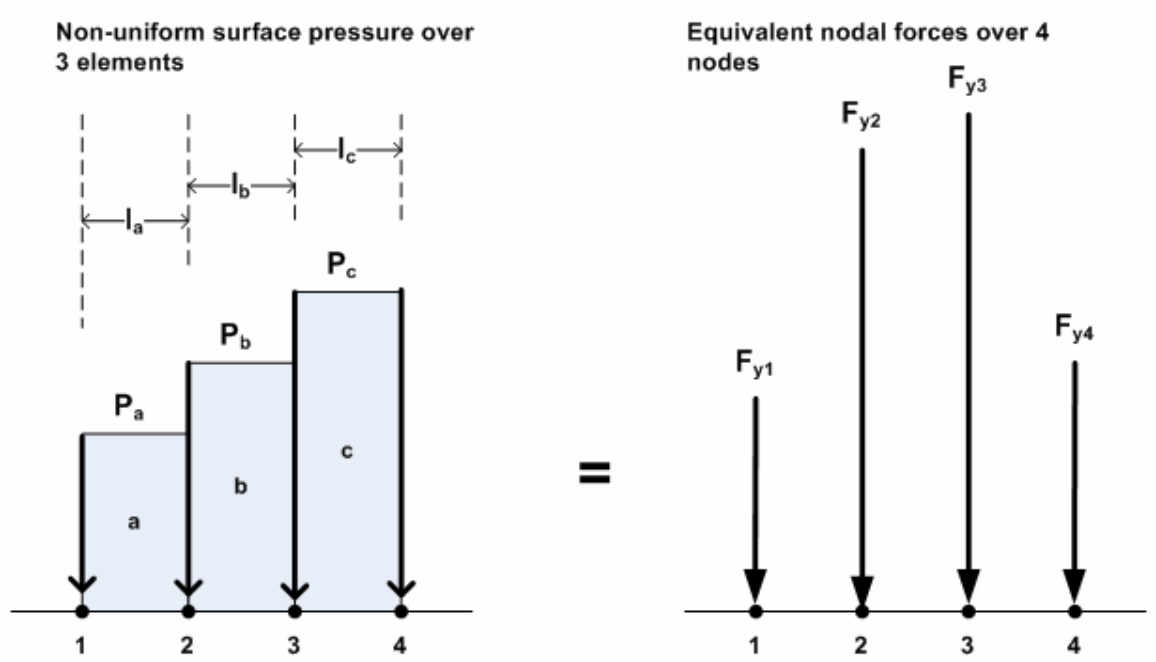

Table 8.1-1 Symbolic calculation of equivalent nodal forces

Contributing Element	Nodal force at nodes			
	Node 1 F_{y1}	**Node 2** F_{y2}	**Node 3** F_{y3}	**Node 4** F_{y4}
a	$P_a l_a/2$	$P_a l_a/2$	0	0
b	0	$P_b l_b/2$	$P_b l_b/2$	0
c	0	0	$P_c l_c/2$	$P_c l_c/2$
Totals	$\mathbf{P_a l_a/2}$	$\mathbf{P_a l_a/2 + P_b l_b/2}$	$\mathbf{P_b l_b/2 + P_c l_c/2}$	$\mathbf{P_c l_c/2}$

In the above, P_a, P_b and P_c are the average pressures on each element surface, and l_a, l_b and l_c are the surface lengths of each element, respectively. The total force recorded at the bottom of the table is the boundary-condition y-force value to be entered as input data (negative).

8.1.1 Live load modeling problem

If the live load is actually in the form of a very long surface-pressure strip, then there is no modeling problem, and the actual surface pressure is used to calculate the equivalent boundary-condition nodal forces for CANDE analysis. Usually, however, the surface pressure is not a very long strip, but rather a finite patch like a truck-tire footprint. In this case additional calculations are required to correct the surface-pressure for the CANDE analysis.

The live-load modeling problem is depicted in Figure 8.1.1-1, showing both an infinite surface-pressure strip and a finite pressure patch. When the pressure-patch load is transmitted through the soil, the load spreads outward in two planes, the x-y plane and y-z plane. In contrast, the surface pressure strip load only spreads outward in the x-y plane. Clearly, if the same surface pressure is assigned to the patch and to the strip, then the pressure strip load will cause greater soil pressure impinging on the culvert than will the pressure patch load.

Figure 8.1.1-1 Illustration of surface-pressure strip and patch-pressure footprint

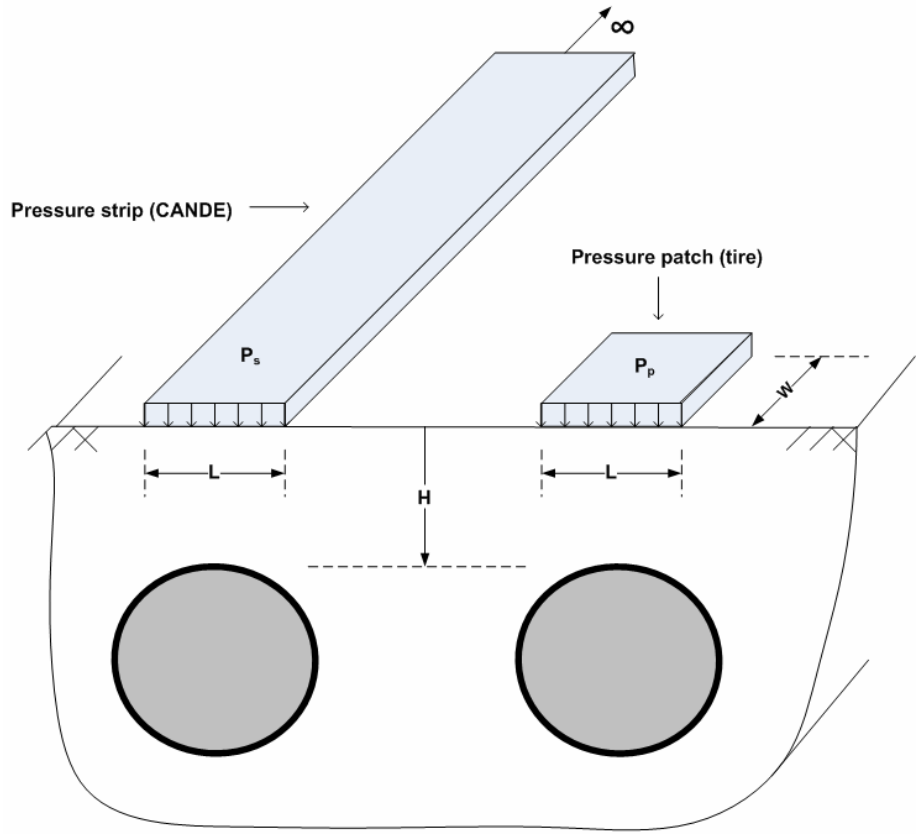

The live-load modeling problem is summarized as follows. If we use the actual patch pressure (say 80 psi representing an HS-20 truck tire) in a CANDE model or any two-dimensional model, we will over predict the loads on the culvert.

Although there is no exact cure for this problem (short of performing a three-dimensional analysis), reasonable CANDE solutions can be obtained by appropriately correcting the strip pressure magnitude. Two methods are presented to reduce the strip pressure, an elasticity-based method and the AASHTO-based load spreading method.

8.1.2 Elasticity-based correction for live-load strip pressure

The elasticity-based correction for strip pressure uses an exact solution for peak vertical stress in a homogenous elastic half space loaded by a pressure patch with footprint dimensions L x W and pressure Pt, as shown in above figure. As developed in Reference 25, the solution for peak vertical stress as a function of depth is given in the following expression.

$$\sigma_{y\text{-patch}} = 2\frac{P_p}{\pi}\left[\arctan\left(\frac{\alpha}{hR_3}\right) + \frac{\alpha h}{R_3}\left(\frac{1}{R_1^{\,2}} + \frac{1}{R_2^{\,2}}\right)\right] \qquad \text{Equation 8.1-1}$$

where, $\sigma_{y\text{-patch}}$ = peak vertical stress for any patch dimensions (L x W)

P_p = surface patch pressure

L = patch length (in x-y plane)

W = patch width (in y-z-plane)
H = depth of interest to compute peak vertical stress
$\alpha = W/L$ = ratio of patch width to length
$h = H/(L/2)$ = non-dimensional soil depth in half-tire lengths

$$R_1 = \sqrt{1+h^2}$$

$$R_2 = \sqrt{\alpha^2+h^2}$$

$$R_3 = \sqrt{1+\alpha^2+h^2}$$

To specialize the peak vertical stress equation to the case of pressure strip loading, we let the patch width approach infinity ($W \rightarrow \infty$) to get.

$$\sigma_{y\text{-strip}} = 2\frac{P_s}{\pi}\left[\arctan\left(\frac{1}{h}\right) + \frac{h}{R_1^2}\right] \qquad \text{Equation 8.1-2}$$

where, $\sigma_{y\text{-strip}}$ = vertical stress for strip pressure for any dimension L with $W = \infty$.
P_s = surface strip pressure

If we equate the vertical stress prediction for the patch load (Equation 8.1-1) to the vertical stress prediction from the strip load (Equation 8.1-2), we can determine the ratio of strip surface pressure to patch surface pressure that results in equal vertical stress at any depth of interest. Specifically, we find

$$r = \frac{P_s}{P_p} = \frac{\arctan\left(\frac{\alpha}{hR_3}\right) + \frac{\alpha h}{R_3}\left(\frac{1}{R_1^2}+\frac{1}{R_2^2}\right)}{\arctan\left(\frac{1}{h}\right) + \frac{h}{R_1^2}} \qquad \text{Equation 8.1-3}$$

The "r" ratio, is the reduction factor applied to P_p to get P_s , which is the key result of this development. For any specific pressure patch dimension (L and W) and for any specific depth H (usually culvert cover height), we can compute the reduced strip pressure that produces the same vertical stress on the culvert crown as the patch load for any depth H. Table 8.1.2- provides the solution to Equation 8.1-3 for most practical problems.

Table 8.1.2-1 Reduction factor "r" applied to strip load pressure

Non-dimensional depth h = H/(L/2)	Ratio of patch dimensions width-to-length (α = W/L)				
	(W/L) 0.8	(W/L) 1.2	(W/L) 1.6	(W/L) 2.0	(W/L) 2.4
1.2	0.717	0.862	0.931	0.963	0.979
1.8	0.558	0.730	0.837	0.900	0.937
2.4	0.449	0.615	0.737	0.820	0.877
3.0	0.372	0.524	0.647	0.740	0.809
3.6	0.317	0.454	0.571	0.666	0.742
4.2	0.275	0.399	0.508	0.601	0.679
4.8	0.243	0.354	0.456	0.546	0.623
5.4	0.217	0.319	0.413	0.498	0.573
6.0	0.196	0.289	0.376	0.457	0.530
6.6	0.179	0.265	0.346	0.421	0.491
7.2	0.164	0.244	0.319	0.391	0.457
7.8	0.152	0.226	0.297	0.364	0.427
8.4	0.141	0.210	0.277	0.340	0.401
9.0	0.132	0.197	0.259	0.320	0.377
9.6	0.124	0.185	0.244	0.301	0.356
10.2	0.117	0.174	0.230	0.285	0.337
10.8	0.110	0.165	0.218	0.270	0.320
11.4	0.105	0.156	0.207	0.256	0.304
12.0	0.100	0.149	0.197	0.244	0.290

To demonstrate the use of the above table, suppose we wish to analyze the effect of an HS-20 truck tire located 24 inches above the culvert crown. The tire footprint is L = 10 inches, W = 20 inches, and the surface pressure of 80 psi.

To find the equivalent strip pressure, we compute W/L = 2.0 and h = 24/(10/2) = 4.8, and enter the above table to find the reduction factor, r = 0.55. Thus the pressure assigned to the CANDE strip load is,

$$P_s = 0.546 P_p = 44 \text{ psi} \qquad \text{Equation 8.1-4}$$

Although the above procedure ignores the interaction of the culvert with the soil stress, the technique generally works well.

8.1.1 AASHTO-based method to compute live-load strip pressure

The AASHTO LRFD load spreading method is a simple concept that assumes the pressure patch load spreads uniformly with soil depth in the overall shape of a truncated pyramid. The top plane of the truncated pyramid has the patch pressure and area, L x W. The base-plane at any depth H is assumed to expand in the x-y plane and the y-z plane at a constant angle. The total force on any base-plane area remains constant so that the uniform pressure decreases in proportion the increase in base-plane area.

Single wheel correction. In order to adapt the AASHTO method to correct the strip pressure problem, we recognize that only the y-z plane needs to be corrected because the pressure distribution in the x-y plane is accurately determined by the plane-strain solution. Figure 8.1.3-1 shows the AASHTO approximation for load spreading in the y-z plane, which is along the length of the culvert.

Figure 8.1.3-1 AASHTO LRFD single wheel load distribution along axis of culvert.

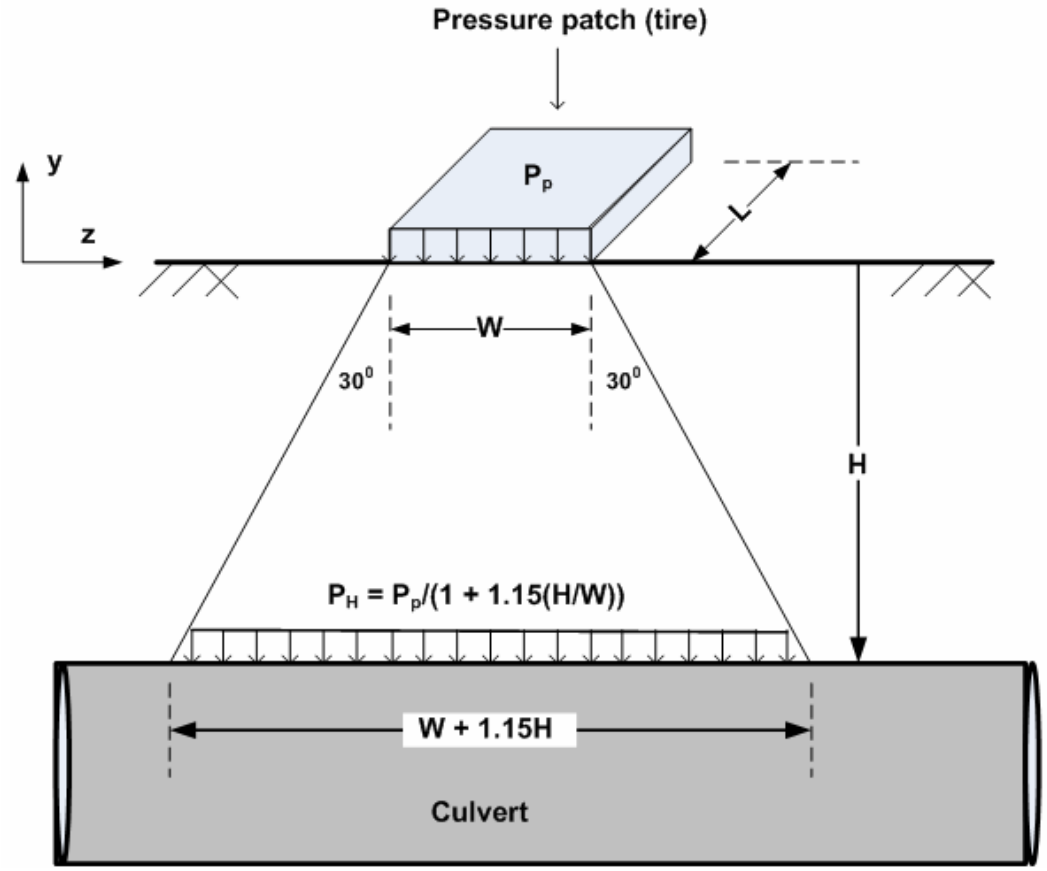

As illustrated in the above figure, the base-line pressure along the length of the culvert is given by,

$$P_H = P_p \frac{1}{(1 + 1.15\frac{H}{W})}$$ Equation 8.1-5

where, P_H = reduced pressure at depth H

P_p = surface pressure of patch, LxW.

H = depth to culvert crown

W = width of pressure patch along axis of culvert

Since the CANDE pressure strip does not account for the pressure reduction along the culvert axis, it follows that reduction factor is given as,

$$r = \frac{P_H}{P_p} = \frac{1}{(1 + 1.15\frac{H}{W})}$$ Equation 8.1-6

Again, the "r" ratio, is the reduction factor applied to P_p to get the corrected strip pressure P_s for CANDE analysis.

To demonstrate the use AASHTO method, we will repeat the previous example from the elasticity-based method. Again, we wish to analyze the effect of an HS-20 truck tire located 24 inches above the culvert crown. The tire

footprint is L = 10 inches, W = 20 inches with a surface pressure of 80 psi. Therefore, using H/W = 1.2, we evaluate Equation 8.1-6 to get the reduction factor, r = 0.42. Thus the pressure assigned to the CANDE strip load is,

$$P_s = 0.42P_p = 34 \text{ psi} \qquad \text{Equation 8.1-7}$$

In comparing the above AASHTO-based correction with the elasticity-based correction (Equation 8.1-4), we find the elasticity-based method is more conservative because it results in a higher CANDE loading pressure than the AASHTO-based method. This trend holds true for all practical patch dimensions and cover depths, however the percentage difference between the elasticity-based and AASHTO-based methods diminish with depth.

Two wheel correction. One useful feature of the AASHTO approach is that the interaction of two tires separated by a distance, S, can be accommodated by a simple extension of the one-wheel method. Typically the spacing distance S represents the truck axle length separating two tires.

The two-wheel approach should be used whenever the culvert cover depth is deeper than the so-called wheel interaction depth given by

$$H_{int} = \frac{S - W}{2\tan(30^0)} = \frac{S - W}{1.15} \qquad \text{Equation 8.1-8}$$

where, H_{int} = wheel interaction depth

S = spacing between wheels, center to center.

W = patch or tire width in y-z plane

When the culvert is buried deeper than H_{int} , the portion of the culvert between the wheels begins to experience soil pressure from both wheels. When pressure overlap begins to occur, the AASHTO load spreading method assumes the pressure remains uniform over the entire interaction zone. The total force from the two tires equilibrates the force from the pressure distribution along the culvert,. Figure 8.1.3-2 illustrates and summarizes the above concepts.

Figure 8.1.3-1 AASHTO LRFD two-wheel load distribution along axis of culvert.

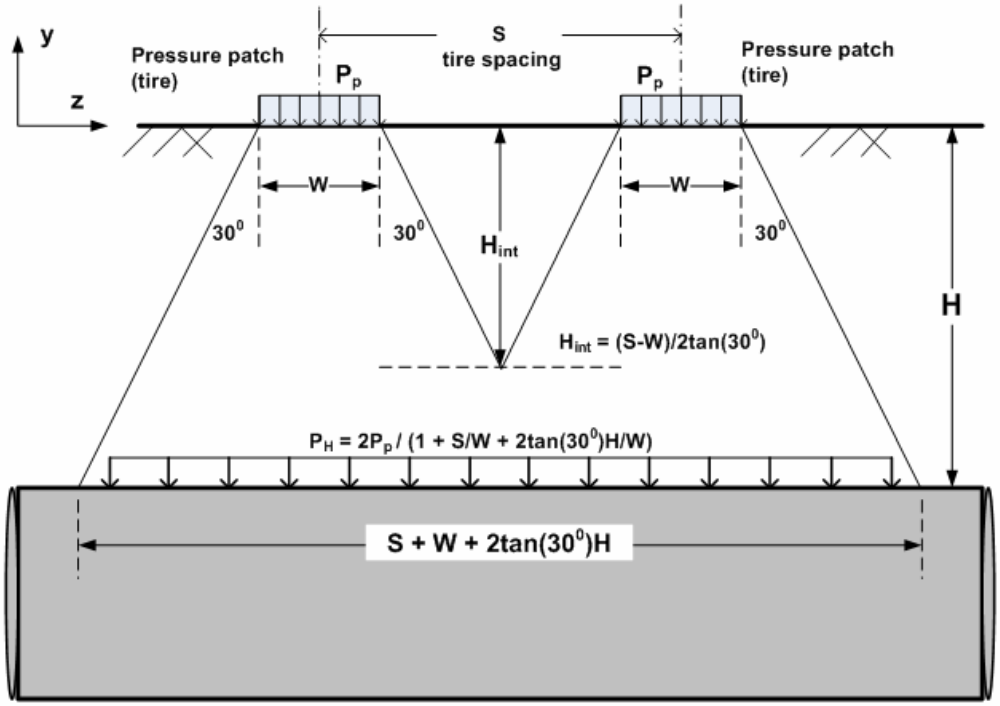

As illustrated in the above figure, the uniform pressure along the length of the culvert is given by,

$$P_H = 2P_p \frac{1}{(1 + \frac{S}{W} + 1.15\frac{H}{W})}$$ Equation 8.1-9

where, P_H = reduced pressure at depth H

P_p = surface pressure of tire 1and tire 2

H = depth to culvert, providing $H > H_{int}$

Following the same argument as presented for the single wheel correction, the two-wheel reduction factor is determined as,

$$r = \frac{P_H}{P_p} = \frac{2}{(1 + \frac{S}{W} + 1.15\frac{H}{W})}$$ Equation 8.1-10

As before, r is the reduction factor to compute strip pressure, $P_s = rP_p$ for CANDE analysis.

To demonstrate the two-wheel AASHTO method, the same parameters for the one-wheel example are used except we add a second wheel spaced 44 inches away. Thus the parameters are L = 10 inches, W = 20 inches, Pp = 80 psi, H = 24 inches, and S = 44 inches. We first calculate the interaction depth as H_{int} = 21 inches and observe that $H=24 > H_{int}=21$, therefore, the two-wheel solution is valid. Evaluating Equation 8.1-10 the reduction factor is found as r = 0.44 so that the pressure assigned to the CANDE strip load is,

$$P_s = 0.44P_p = 35 \text{ psi}$$ Equation 8.1-7

It is observed that the addition of the second wheel raised the equivalent strip pressure by 1 psi compared to the single wheel (Equation 8.1-7). The increase is small because the depth of burial is only slightly greater than the depth of in the interaction zone.

In closing this section on live loads, it is reiterated that there is no exact technique to simulate pressure-patch loads in a two-dimensional framework. The methods presented above provide a reasonable approximation for design and safety evaluations of buried culverts. However for point-by-point comparison with fully instrumented experimental tests, there are likely to be discrepancies that can be better predicted by three-dimensional analysis.

8.2 Pipe Group Connections and Combinations

Finite element models utilizing multiple pipe groups is a new feature in CANDE-2007 that offers many modeling capabilities that were not available in previous versions of CANDE. Discussed below are several techniques for combing pipe groups with each other and soil elements to achieve various desired objectives. Topics include connection modeling (fixed, pinned, and roller), long-span stiffeners, culvert rehabilitation with liners, and other pipe group combinations.

8.2.1 Connections among element types

A pipe group is a connected sequence of beam-column elements joined head-to-toe at common nodes and tracing an arbitrary curvilinear path in x-y space. Each beam-column node has three degrees of freedom, x-displacement, y-displacement and a rotation. Continuum elements (triangle or quadrilateral) only have two degrees of freedom per node, x-displacement and y-displacement.

When two or more pipe groups are connected to a common node the connection is called fixed, meaning moment continuity is preserved at the junction node. On the other hand, when a pipe group is attached to a continuum element the connection is called pinned, meaning the moment at the junction node is zero. These fundamental connections, representing the default conditions, are illustrated in the figure below.

Figure 8.2.1-1 Connections made by sharing common node at junction.

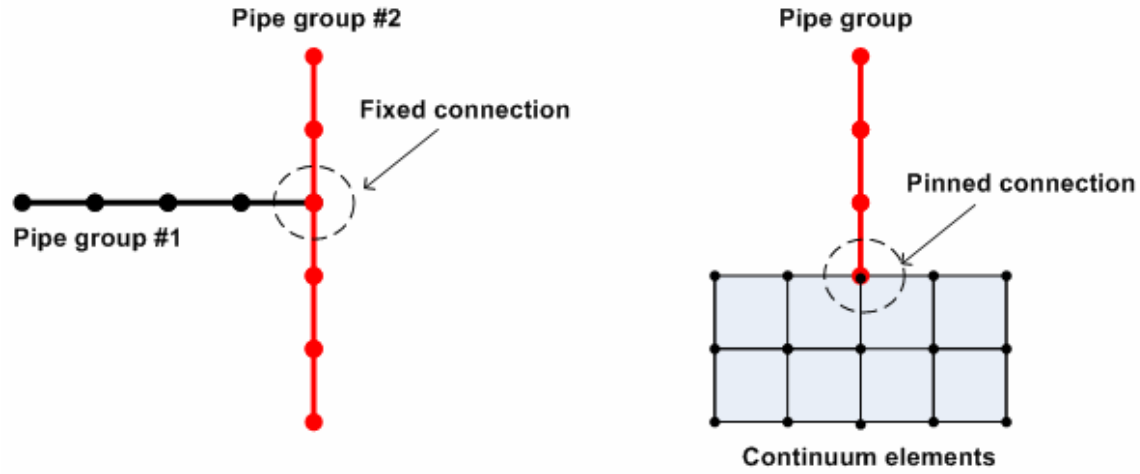

If it is desired to simulate a pinned or roller connection between two pipe groups such as pipe group #1 and pipe group # 2 in the above figure, then an interface element must be inserted at the junction of the two the two pipe groups. An interface element joins two independent nodes, initially assigned to the same x-y coordinate location, as a pinned connection, friction connection or roller connection depending on the properties assigned to the interface element. Figure 8.2.1-2 illustrates an interface element joining pipe group # 1to pipe group # 2 including the third interface node whose degrees of freedom are the interface forces required to enforce the desired connection.

Figure 8.2.1-2 Techniques to change connection conditions.

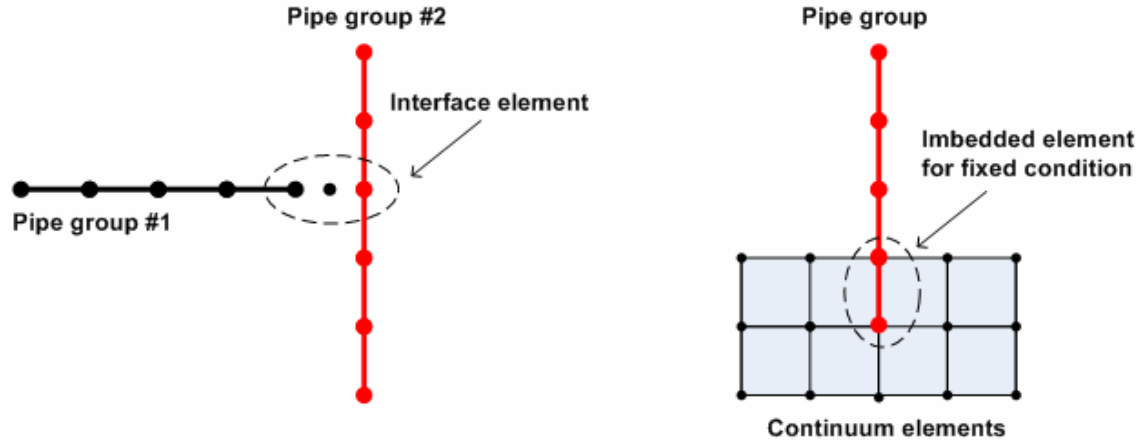

The assigned interface properties required to achieve various connection conditions are listed in the table below wherein the value 10^6 means a very large number such that frictional slippage or tensile rupture cannot occur.

Table 8.2.1-1 Interface property values to simulate various connection conditions

Desired Connection Type	Interface properties	
	Friction coefficient (μ)	Tensile breaking force (lbs/inch)
Pinned	10^6	10^6
Friction (no tensile separation)	0.3 (typical)	10^6
Friction (tensile separation)	0.3 (typical)	0.0
Roller (no tensile separation)	0.0	10^6
Roller (tensile separation)	0.0	0.0

Shown on the right side of Figure 8.2.1-2 is a modeling technique to simulate a fixed connection between a pipe group and a concrete footing (continuum elements). Here a beam-column element is added to the pipe group and imbedded in the concrete, mimicking reality.

8.2.2 Stiffeners and culvert rehabilitation with parallel pipe groups

When two pipe groups share the same set of nodes, referred to as parallel pipe groups, it is evident that both groups experience identical deformations (displacements and rotations) because both pipe groups are attached to the same nodes. The combined stiffness is additive, exactly like two parallel springs with individual stiffnesses k_1 and k_2 have a combined stiffness equal to $k_1 + k_2$. Even though parallel pipe groups experience identical deformations, the resulting internal forces (moment, thrust and shear) and stresses in one group may differ substantially from the other group, depending on individual stiffness properties of each group.

Many types of culvert stiffeners can be modeled with parallel pipe groups with one pipe-group modeling the culvert and the second pipe-group modeling the stiffener. As noted above, a stiffener that is modeled as a parallel pipe group provides an additive stiffness to the culvert without additional increase in bending stiffness from composite action. To achieve composite action the stiffener must be integrally attached to the culvert including complete shear bonding like a continuously welded built-up cross sections. Culvert sections that are truly stiffened in a composite manner can be

modeled with a single pipe group using composite section properties. Otherwise it is best to model stiffeners with the more conservative parallel-pipe-group method as illustrated below.

Long-span stiffener. Long-span corrugated metal culverts are often reinforced with discrete ring-beam stiffeners periodically spaced along the top arch. Typically the ring beams are lightly bolted to the corrugated metal so that the assumption of additive stiffness instead of composite stiffness is quite reasonable, erring slightly on the conservative side. Figure 8.2.2-1 illustrates how to model ring-beam stiffeners with parallel pipe groups.

Figure 8.2.2-1 Modeling technique for long-span culvert with ring beam stiffeners

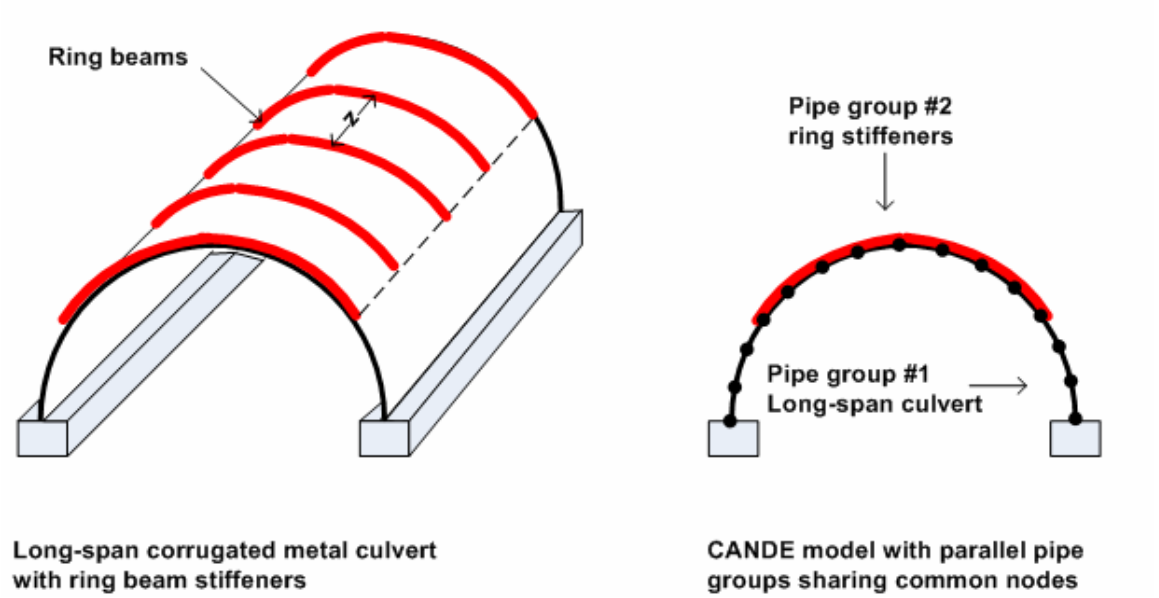

As shown in the table below input for the CANDE ring beam properties for pipe group #2 are smeared values based on a ring-beam spacing of z inches on center.

Section Properties of Ring Beam	Individual ring values	CANDE input values
Area	A (in^2)	A/z (in^2/inch)
Moment of Inertia	I (in^4)	I/z (in^4/inch)
Section Modulus	S (in^3)	S/z (in^3/inch)

Another advantage of the parallel-pipe-group method is due the fact that CANDE provides an individual assessment of each group so that the structural integrity of stiffener is evaluated in addition to the culvert.

Culvert rehabilitation stiffener. One method to rehabilitee structurally distressed culverts is to insert a pipe liner inside the old culvert to stiffen the old soil-culvert system. Typically, the liner is smooth wall plastic pipe inserted into a host culvert such as corrugated metal or reinforced concrete pipe. If the plastic-pipe liner is inserted into the host pipe with a snug fit, it is reasonable to assume the combined stiffness of the host pipe and liner is properly simulated by parallel pipe groups. The rationale is that the interface between the host pipe and liner does not have a sufficient shear bond for the two pipes to act in a composite manner. The left side of Figure 8.2.2-2 shows the recommended parallel pipe-group method for modeling a snug fit liner wherein both pipe groups share the same nodes.

Figure 8.2.2-2 Modeling techniques for culvert rehabilitation with liners

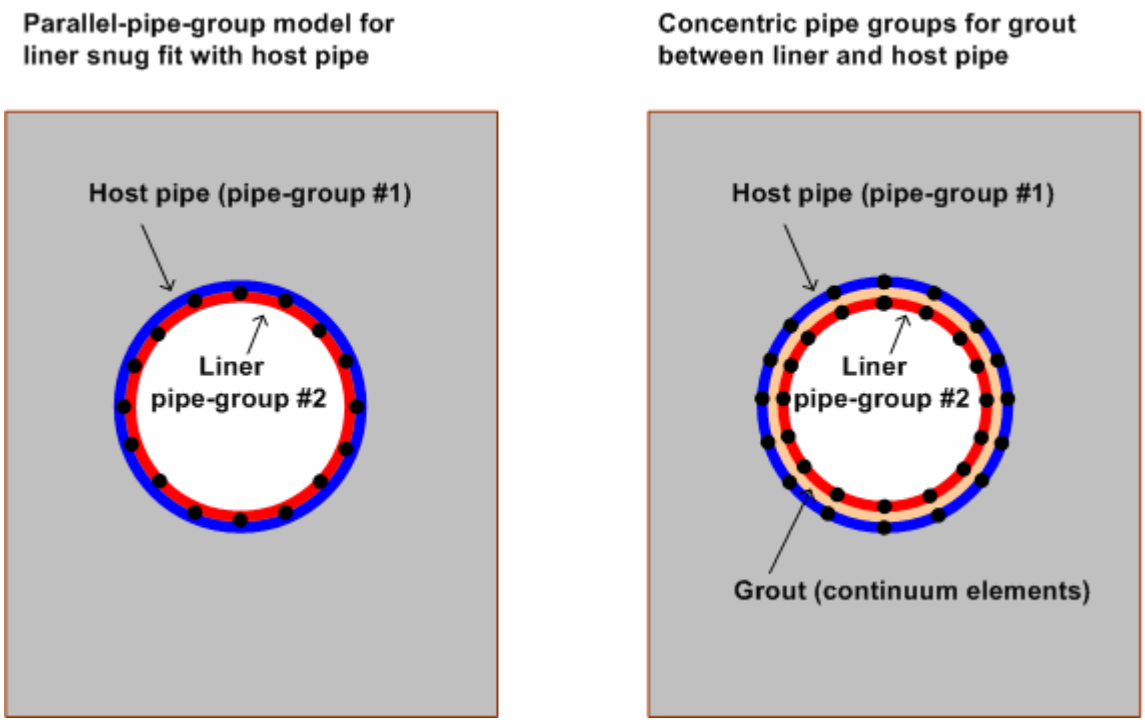

The right side of the above figure shows an alternative rehabilitation method in which the outside diameter of the liner is several inches smaller than the inside diameter of the host pipe thereby creating an annular space that is filled with grout. In this case the combined stiffness of liner, host pipe and grout is significantly greater than the snug fit condition using parallel pipe groups. As illustrated in the figure, an accurate simulation is achieved by assigning the liner an independent set of nodes tracing its smaller diameter and modeling the grout with continuum elements.

If the grout elements are assigned common nodes with the liner pipe and with the host pipe, the net effect is a composite bending stiffness that may be overly optimistic if the grout is not securely bonded both pipes. Therefore, a more conservative approach would be to assign independent node numbers to the grout elements and use frictional interface elements to connect the grout nodes to the pipe nodes, allowing relative slip along the pipe-grout boundaries.

8.2.3 Illustrations of pipe group combinations

In addition to the pipe group connections and combinations discussed above, additional pipe-group applications are illustrated in the Figure 8.2.2-3.

Figure 8.2.3-1 Illustrations of multiple pipe group applications

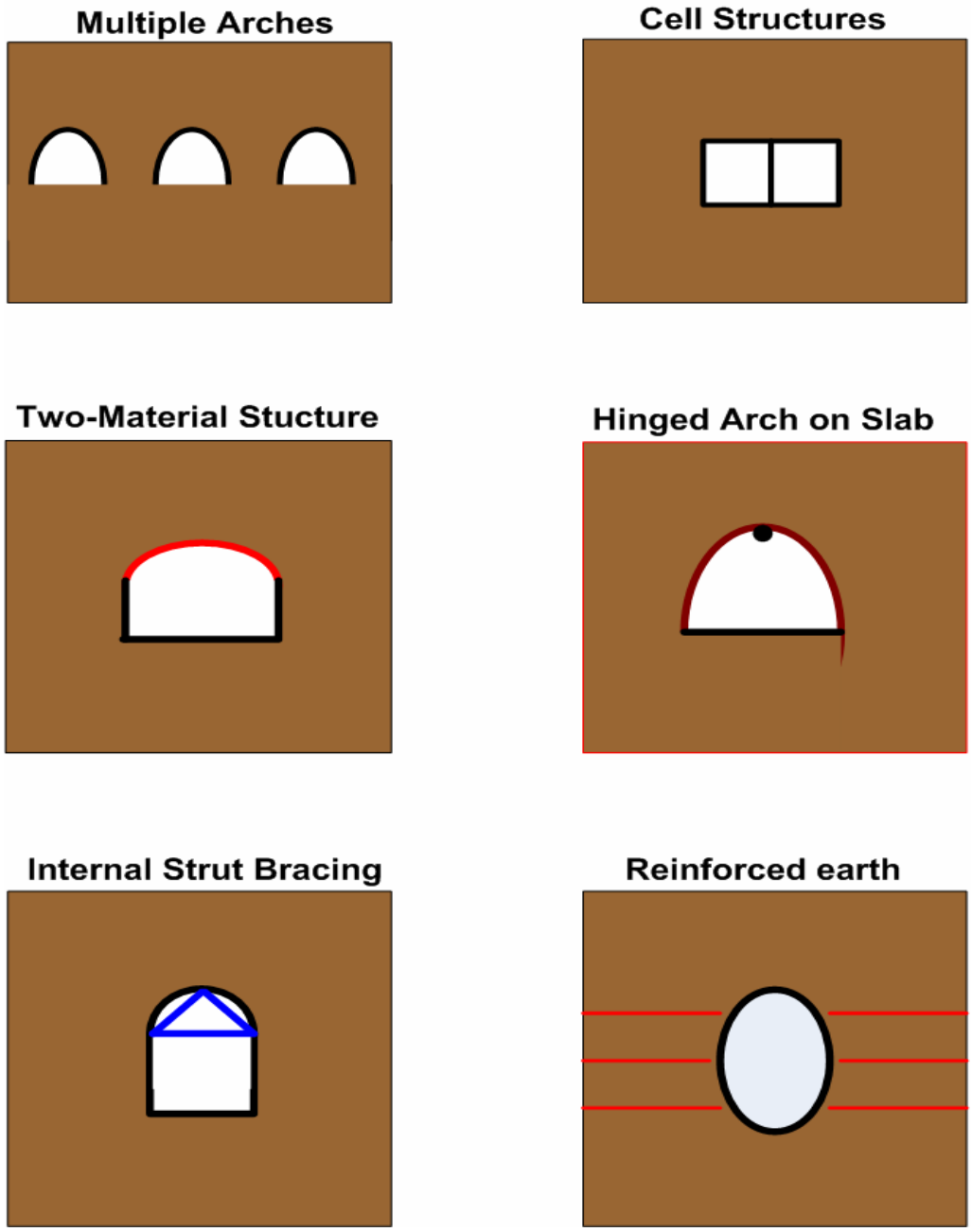

The above illustrations are intended to demonstrate the wide variety of modeling options that are possible with CANDE's multiple pipe-type capability. For example, the reinforced earth application (last figure) implies that pipe groups can be used to simulate soil reinforcement strips. If interface elements are inserted along these pipe groups, the model is capable of determining the ultimate pullout strength of the soil reinforcement.

8.3 Construction Increments

Incremental construction is the physical process of placing and compacting soil layers, one lift at a time, below, along side and above the culvert as the installation is constructed. Analytically this is achieved by adding incremental solutions from successive finite element configurations, where each new configuration contains additional soil elements (and/or structural elements) that mimics the real-world buildup of the soil-structure system, one load step at a time.

The terms "load step" and "construction increment" are closely related terms and are often used interchangeably, however they have slightly different meanings. Load step is an all-encompassing term referring to any incremental solution, which may or may not include a construction increment. For example a load step may only include boundary-condition loads without additional elements added to the system. A construction increment is a special kind of load step wherein additional elements are added to the global stiffness matrix usually representing an additional layer of soil. The body weight of added elements form the load increment associated with the load step along with any boundary loads such as soil compaction pressures, discussed subsequently.

8.3.1 Rules and insights for construction increments

With the above understanding, construction increments are subject to the following rules. Each element is assigned a construction increment number, which corresponds to the load step number that the element stiffness matrix and load vector is assembled into the global system. Once an element stiffness enters the system it remains active for all subsequent load steps (there is no element death). Of course, the element body-load vector is only applied during the load step corresponding to the element construction increment number; it is not reapplied on subsequent load steps. Similarly, surface pressure and/or point loads (i.e., force boundary conditions) are also assigned a particular construction increment number and are only applied during the corresponding load step. Likewise, displacement boundary conditions are applied during the load step they are specified and remain fixed for all subsequent load steps. In short, the rules simulate reality.

Although the rules seem simple, it is easy to be fooled. For example, novices generally think that if all construction increments are linear elastic and no other nonlinearities are involved, then a structure built in several steps behaves no differently then a structure built as a monolith (all in one step). A simple example demonstrating this is not true is shown in the figure below.

Figure 8.3.1-1 Illustration of two construction increments versus a single monolith

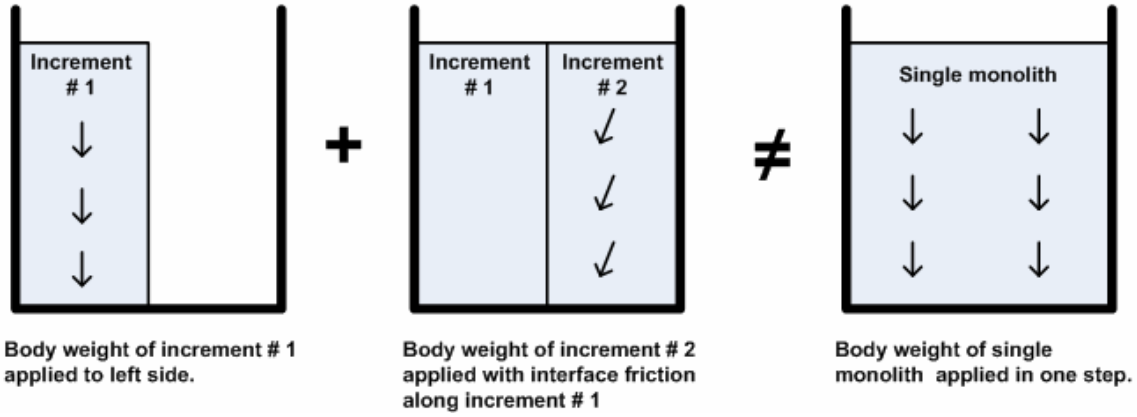

The figure illustrates that after the first construction increment is set in place with roller boundary conditions on the sidewalls, the body weight produces a uniform stress distribution properly aligned in the vertical direction as expected. However, when the second construction increment is set in place (sharing common nodes with the first construction increment), some of the second construction increment's body weight is transferred to the first construction increment's stiffness. Therefore, the resulting stress and strain distribution in the two-step system is not uniform and differs from the uniform stress distribution in the single monolith system shown on the right.

The specific point of this simple example is that the sequence of construction increments is important and influences the structural behavior of the final system. More generally, when developing a finite element model for a particular soil-structure system, the sequence of construction increments should be modeled as realistically as practical.

8.3.2 Techniques for initial construction increment

All too often the first construction increment is not modeled properly, causing incorrect deformation in the structure due to the insitu soil model. Proper modeling techniques depend on whether the insitu soil is linear or nonlinear and the assignment of body weight as discussed below.

Linear insitu soil. Generally insitu soil can be realistically modeled with a linear elastic soil model because the existing soil is pre-consolidation and/or recently unloaded from excavation. In this case, the initial construction increment may include the insitu soil, footing or bedding and the structure as illustrated in the example below.

Figure 8.3.2-1 Initial configuration for an arch-trench installation with linear insitu soil

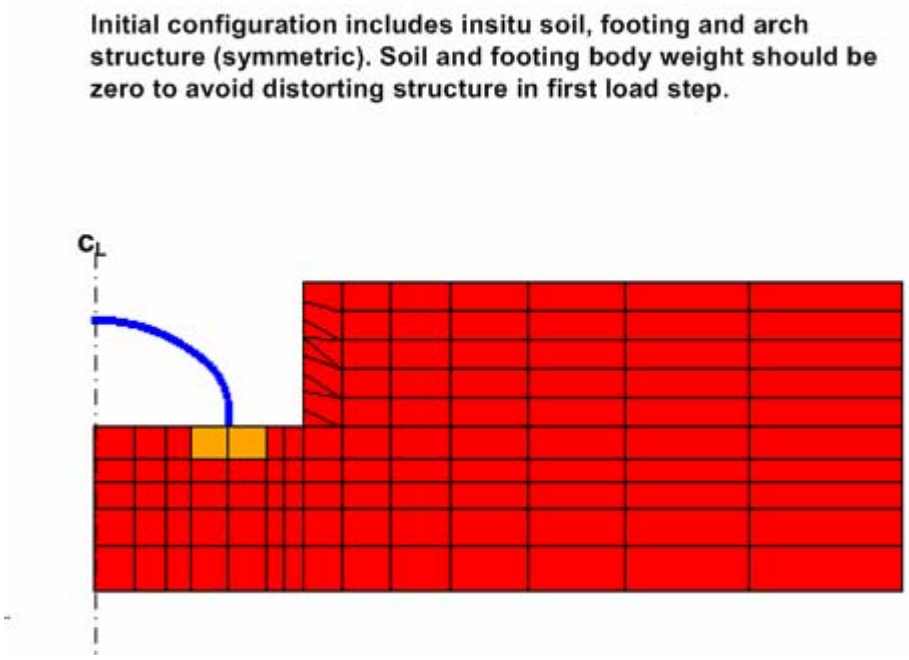

Only the arch should be assigned a non-zero body weight for this initial configuration. A common mistake made by novices is to also assign body weight to the insitu soil and footing, which causes these components to deform under there own weight and introduce fictitious distortions into the arch. Physically we know the insitu soil and footing are at rest under their own weight before the arch is attached to the footing, thus only the arch body weight cam cause deformations in the first load step.

Nonlinear insitu soil. If it is desired to model the insitu soil with a nonlinear soil model like Duncan/Selig, then the arch should be eliminated from the initial configuration and introduced in the second construction increment. In this case we need to assign the actual body weight to the insitu soil because the soil stiffness is dependent on the stress state caused by the soil body weight, requiring iteration within the load step. Figure 8.3.2-2 illustrates the proper initial configuration when nonlinear soil model is used for insitu soil.

Figure 8.3.2-2 Initial configuration for an arch-trench installation with nonlinear insitu soil

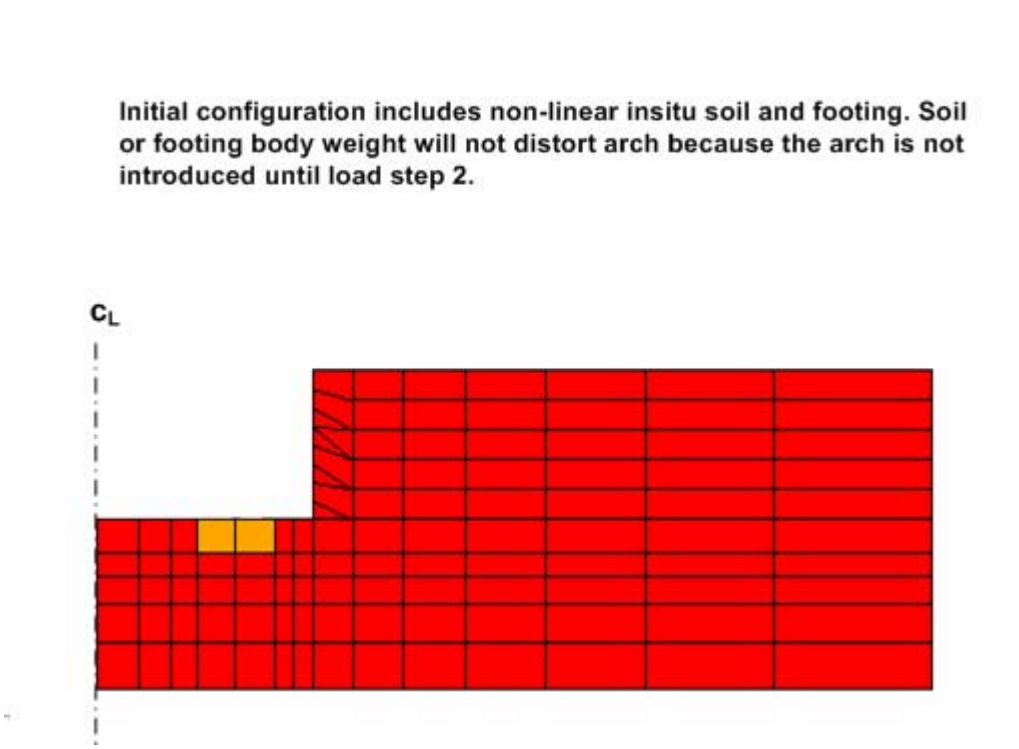

If the arch were included in the initial configuration, it would experience fictitious distortions due to deformation of the insitu soil by self-weight. Now however, after the initial configuration has converged and the insitu soil and footing are at rest in a deformed state, the arch may be correctly assigned to the second construction increment.

8.3.3 Soil compaction and construction increments

The last technique to be described is the modeling of soil compaction using the so-called squeeze layer method first introduced in Reference 18. The purpose of soil compaction is to densify soil after it is laid down in loose layers and then compacted to achieve a specified density usually stated in terms of AASHTO T-99 relative density.

Compaction equipment ranging from hand-held compactors to large-tracked bulldozers is used to compress each soil layer by creating a temporary vertical pressure to compact the soil. As the soil is compressed vertically (squeezed), it tends to expand laterally due to the Poisson effect, which creates horizontal pressure on the sides of the culvert. These lateral pressures cause inward movement of the culvert sides and peaking at the culvert crown, that is, a reverse deformation pattern from that caused by overburden loading. Large culverts such as long-span corrugated metal structures often experience as much as 2 % crown peaking as a result of compacting soil layers between the footing and the crown.

Compaction loads are beneficial not only in compacting the soil to achieve the desired soil stiffness properties but also in introducing reverse deformations and bending moments into the culvert, which provides the culvert with additional capacity to resist the opposite bending deformations that subsequently come from soil placed on top of the culvert.

The squeeze layer technique is a simple modeling concept that simulates the effect of soil compaction and is applicable to both linear and nonlinear soil models. The concept is illustrated in Figure 8.3.3-1 and discussed below.

1. To start, a uniform compaction pressure representing the compaction equipment, typically on the order 5-psi pressure, is placed on the surface of the insitu soil at the level of the footing.

2. Next, the 2nd construction increment (first layer of backfill soil with body weight) is added to the system along with another uniform compaction pressure applied to its top surface. At the same time, however, the first compaction pressure is removed by applying an equal but opposite compaction pressure to the bottom surface. These two opposing pressures squeeze the soil layer and increase the lateral pressure on the arch via the Poisson effect.

3. The intermediate construction increments 3rd, 4th and 5th are treated exactly like the 2nd construction increment so that each layer is squeezed, increasing lateral pressure on the arch and inducing more peaking. Note that after the 5th load increment (or more generally, the increment before the crown-level increment) all the temporary compaction pressures have been removed except the compaction pressure on the surface of 5th construction increment.

4. The squeeze layer process is terminated with the 6th construction increment (i.e., crown-level increment). As the 6th construction increment is added to the system with its stiffness and body weight, the last remaining compaction pressure from the 5th construction is removed.

5. All the remaining construction increments, representing soil layers above the crown, are added in the normal manner with body weight but without any compaction pressures.

Examples of applying the squeeze layer technique and the behavior of long-span culverts can be found in References 18, 26 and 27.

Figure 8.3.3-1 Squeeze-layer method for compaction loads on long-span culvert

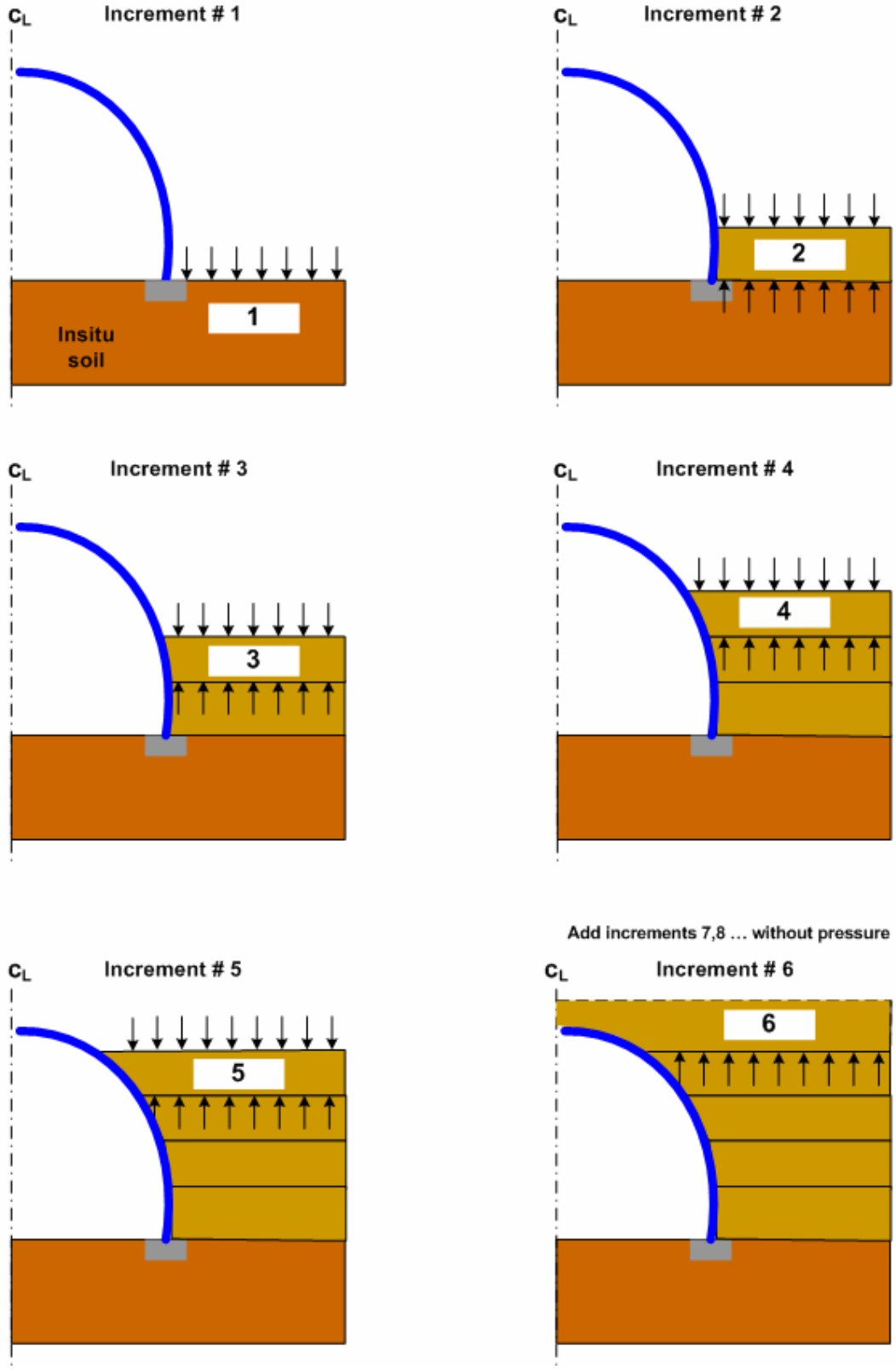

9 REFERENCES

1. CANDE: A Modern Approach for the Structural Design and Analysis of Buried Culverts, Federal Highway Administration Report No. FHWA-RD-77-5, October 1976, (Authors: M. G. Katona, J .M. Smith, R. S. Odello, and J. R. Allgood).

2. CANDE User and System Manuals, Federal Highway Administration Report No. FHWA-RD-77-6, October 1976, (Authors: M. G. Katona and J. M. Smith).

3. CANDE-1980: Box Culverts and Soil Models, Federal Highway Administration, Report No. FHWA-RD-172, May 1981 (Authors: M. G. Katona, P. D. Vittes, C. H. Lee, and H. T. Ho).

4. CANDE-89: Culvert Analysis and Design computer program – User Manual, Federal Highway Administration Report No. FHWA-RD-89-169, June 1989. (Authors: S. C. Musser, M. G. Katona and E T. Selig).

5. Predicting Performance of Buried Conduits, Report No. FHWA/IN/JHRP-81/3, Joint FHWA and Indiana State Highway Commission, June 1982. (Authors; G.A. Leonards, T.H. Wu, and C.H. Juang)

6. AASHTO (2004), *AASHTO LRFD Bridge Design Specifications*, Third Edition, AASHTO, Washington, D.C.

7. Burns, J. Q., and R. M. Richard, "Attenuation of Stresses for Buried Cylinders," In Proc., *Symposium on Soil-Structure Interaction*, University of Arizona Engineering Research Laboratory, Tucson, 1964, pp. 378-392.

8. Herrmann, L. R., "User's manual for plane strain incremental construction program," Department of Civil Engineering, University of California, Davis, 1972.

9. Katona, M. G., and A. Y. Akl, "Analysis and Behavior of Buried Culverts with Slotted Joints," Transportation Research Record, No. 1008, 1985, pp. 22-32.

10. Katona, M. G., and A. Y. Akl, "Structural Design of Buried Culverts with Slotted Joints," ASCE, Journal of Structural Engineering, January 1987.

11. Herrmann, L. R., "Efficiency evaluation of a two-dimensional incompatible finite element," Journal of Computers and Structures, vol 3, 1973, pp 1377-1395.

12. Katona, M. G., Minimum Cover Heights for Corrugated Plastic Pipe Under Vehicle Loading," Transportation Research Record, No. 1288, 1990, pp. 127-135.

13. McGrath, T.J., I.D. Moore, E.T. Selig, M.C. Webb, and B. Taleb, Recommended Specifications for Large-Span Culverts, *NCHRP Report 473,* Transportation Research Board, Washington, DC, 2002.

14. Heger, F.J., and T.J. McGrath, Shear Strength of Pipe, Box Sections, and Other One-Way Flexural Members, ACI Journal, Proceedings Vol. 79, 1982, pp. 470-483.

15. Heger, F.J. and T.J. McGrath. Crack Width Control of Reinforced Concrete Pipe and Box Sections, ACI Journal, Proceedings Vol. 81, 1984, pp. 149-157.

16. Gergely, P. and L.A. Lutz. Maximum Crack Width in Reinforced Concrete Flexural Members, SP-20, American Concrete Institute, Detroit 1968, pp. 87-117

17. Katona, M. G., and P. D. Vittes, Soil-Structure Evaluation of Buried Box Culvert Designs, Transportation Research Record, No. 878, 1982, pp 1-7.

18. Katona, M. G., D. F. Meinhert, R. Orillac, and C. H. Lee, Structural Evaluation of New Concepts for Long-span Culverts and Culvert Installations, Report No. FHWA-RD-79-115, December 1979,

19. Duncan, J. M., and C. Y. Chang, Nonlinear Analysis of Stress and Strain in Soils, Journal of Soil Mechanics and Foundations, ASCE, vol. 96, No. SM5, September 1970, pp. 1629-1653.

20. Duncan, J. M., et. al., Strength, Stress-strain and Bulk modulus Parameters for Finite Element Analysis of Stresses and Movements in Soil Masses, Report University of California, Berkeley, GT 78-02 to National Science Foundation, April 1978.

21. Selig, E. T., Soil Parameters for Design of Buried Pipelines, Proceedings, Pipeline Infrastructure Conference, ASCE, 1988, pp 99-116.

22. Hardin, B. O., Effects of Strain Amplitude on the Shear Modulus of Soils, Air Force Weapons Laboratory Technical Report AFWL-TR-72-201, Kirtland AFB, NM, March 1973.

23. Katona, M. G., and T. J. McGrath, A Guideline for Interpreting ASSHTO LRFD Specifications to Design or Evaluate Buried Structures with Comprehensive Solution Methods, Transportation Research Record, No. 2028, 2007, pp. 211-217.

24. Katona, M. G., "A Simple Contact-Friction Interface Element with Application to Buried Culverts, International Journal for Numerical and Analytical Methods in Geomechanics, Vol. 7, 1983, pp. 371-384.

25. Poulos, H. G., and E. H. Davis, Elastic Solutions for Soil and Rock Mechanics, John Wiley, New York, 1980.

26. Katona, M.G., "On the Analysis of Long-span Culverts by the Finite Element Method," Transportation Research Record, No. 678, 1978, pp. 59-66.

27. Katona, M.G., "CANDE: A Versatile Soil-Structure Design and Analysis Computer Program," Journal of Advances in Engineering Software, Vol. 1, No. 1, 1978, pp. 3-9.

10 CANDE ANALYSIS SOURCE CODE

The purpose of this chapter is to provide the reader with sufficient understanding of the CANDE Analysis Engine source-program architecture to enable the reader to modify, change and extend the program. Researchers are encouraged to modify and/or extend CANDE-2007 to investigate new soil models, pipe-material behavior and other new theories and concepts. By sharing new developments among the engineering community, CANDE will continue to grow in the future, in the same manner as it has grown in the past.

10.1 Overview of CANDE Analysis Engine Architecture

The CANDE-2007 source program is written in modern Fortran and developed with the following:

- Microsoft Visual Studio 2005, Version 8.0.50727.762 (SP.050727-7600)
- Intel Fortran Compiler version 9.1.3427.2005.
- Microsoft .NET Framework version 2.0.50727

The MVS framework permits grouping subroutines together to form projects and then grouping projects together to form a whole solution. CANDE's whole solution is composed of six projects described in the table below.

Table 10.1-1 CANDE-2007 projects contained in MVS solution

Project	Description	Number of programs or subroutines
1. Cande_dll	The primary executive routine controlling the overall solution strategy and calls to subroutines in other projects including input/output files and error messages. (dynamic link)	1
2. Engine	Contains all the engineering subroutines including all finite element formulations, equation solver, elasticity solution, soil models and pipe types with design logic and structural evaluations.	56
3. Inc	Contains all named common statements and parameter declarations whose variables are shared between subroutines by means of "Include statements".	25
4. Intel	Utility subroutines for controlling screen monitor.	3
5. IO	Utility subroutines for input/output message writing to print files and screen monitor for all output including error messaging.	27
6. Main	Dynamic link interface between Cande_dll and monitor screen to identify input file.	1

In the following discussion, the CANDE architecture is presented from a top down viewpoint, starting with the primary executive subroutine, Project Cande_dll, and then narrowing to specific subroutines in Project Engine.

10.2 Executive Routine (Cande_dll)

Overall, the executive routine is divided into three parts, input phase, solution phase and output phase. The executive routine defines the Fortran variable ICOME to communicate with other subroutines as to which phase is currently being addressed as follows.

- ICOME = 1 means input phase
- ICOME = 2 means solution phase
- ICOME = 3 means output phase

As might be expected, the solution phase is the most complicated wherein the executive routine must decide if the solution for the current load step is valid (converged) and how to proceed next. For this purpose another Fortran variable IEXIT is defined with one of four possible values as follows.

- IEXIT = 1 means entire problem is complete, normal exit from CANDE.
- IEXIT = 0 means current load step has converged, advance to next load step
- IEXIT = -1 means current load step has not converged, repeat load step.
- IEXIT = -2 means design-mode solution did not converge, repeat all load steps.

With the above understanding, Figure 10.2-1 shows a flow chart of the executive routine wherein the "ICOME divisions" are clearly evident on the left. Within each ICOME division, there are two colored boxes, one representing calls to pipe-type subroutines and one representing calls to solution-level subroutines. Both the pipe-type subroutines and the solution-level subroutines are contained in Project Engine and will be discussed in turn.

10.3 Pipe-type Subroutines

Currently there are five pipe types in CANDE's pipe library. Each pipe-type is associated with one or more subroutines to accomplish the three basic functions, input, evaluating trial solution, and updating results. Table 10.3-1 identifies the subroutines associated with each pipe type.

Table 10.3-1 Subroutines associated with each pipe-type

Pipe-type and material	Main pipe-type subroutine name	Auxiliary subroutines called by main pipe-type subroutine
Corrugated aluminum	**alum**	**emod**: calculates nonlinear section properties.
Corrugated steel	**steel**	**emod**: calculates nonlinear section properties. **jmod**: special model for slipping joints. **slpjnt**: process input/output for slotted joints.
Reinforced concrete	**concre**	**conmat**: calculates nonlinear section properties. **conend**: computes shear capacity, radial tension, and crack width.
Plastic pipe	**plasti**	**plasbro**: calculates section properties of profile wall. **plsnbk**: computes strains and local buckling losses.
Basic	**basic**	none

Each of the main pipe-type subroutines listed above performs the same three basic functions as dictated by the executive routine via the variable ICOME. Table 10.3-2 lists the basic functions for a generic main pipe-type subroutine.

Table 10.3-2 Tasks performed by main pipe-type subroutines for each ICOME value.

ICOME value	Tasks performed in main pipe-type subroutine
1 (input phase)	• Read input properties for pipe group • Compute initial linear-elastic section properties.
2 (solution phase)	• Revise section properties based on current solution • Determine if nonlinear pipe group has converged • Send IEXIT value back to executive routine (-2,-1, or 0)
3 (output phase)	• Save and update pipe-group structural responses • Print safety evaluation for pipe group

Figure 10.2-1 Executive routine flow chart: input phase, solution phase, and output phase

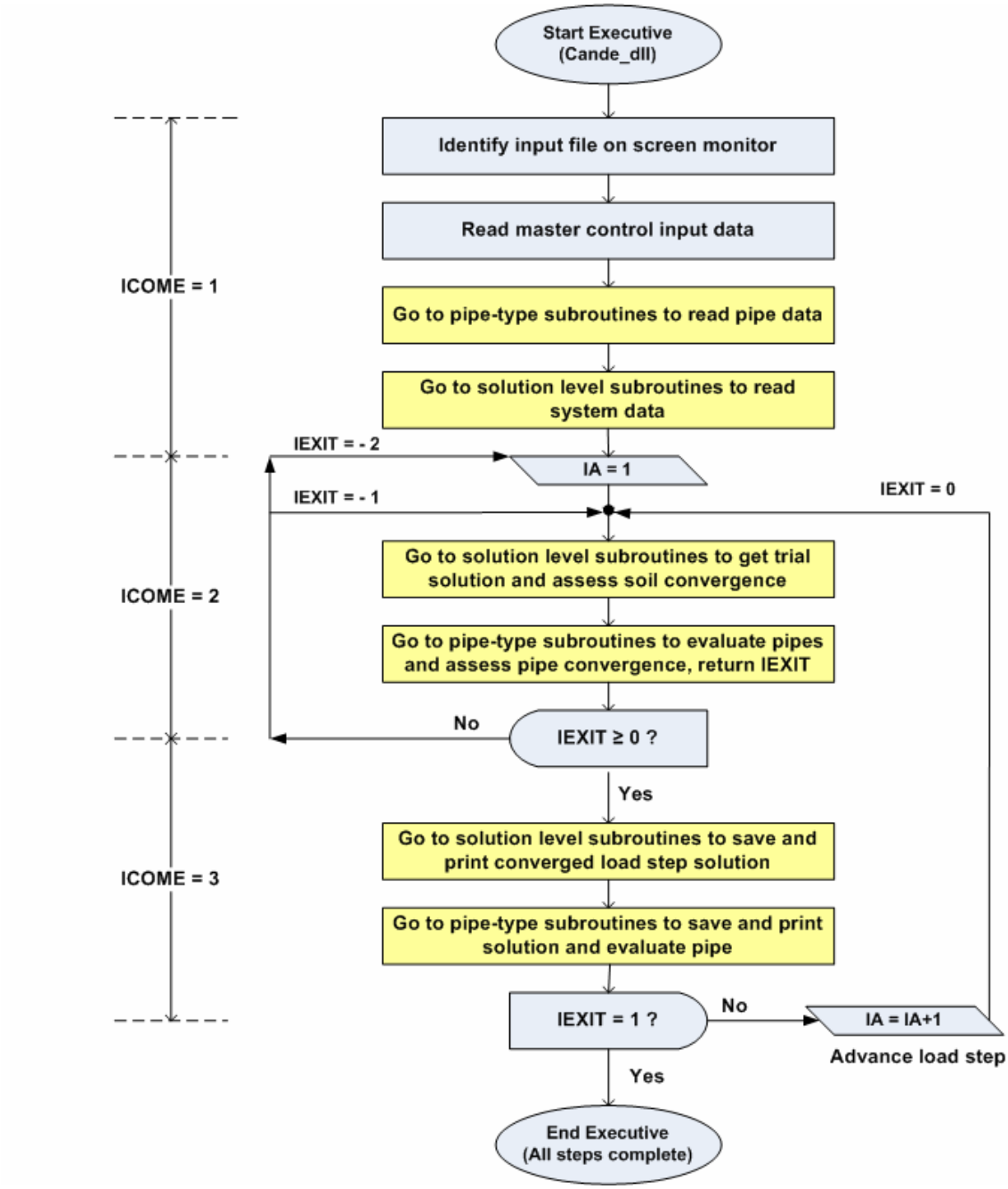

10.4 Solution-level Subroutines

For any given problem, only one of the three solution levels is operative, that is, Level 1, Level 2 or Level3. The closed-form Burns and Richard elasticity solution, Level 1, only employs one subroutine, named Burns. In contrast, the finite element solutions, Level 2 and Level 3, employ numerous subroutines. Level 2 and Level 3 share the same subroutines for the solution phase (ICOME = 2) and the output phase (ICOME = 3). For the input phase (ICOME = 1), Level 2 includes a separate set of subroutines to create an input file that is identical to a Level 3 input file. Hence, the subroutines employed for the Level 3 input phase (ICOME = 1) are also used to read the internally created Level 2 input file. The above comments are clarified in the following tables and charts.

10.4.1 Elasticity solution Level 1

As stated above, the Level 1 solution employs one subroutine called Burns that is not shared by any other solution level. The tasks performed by the Burns subroutine are shown in the table below in accordance with the calls from executive routine via the parameter ICOME.

Table 10.4-1 Burns subroutine tasks as called

ICOME value	Tasks performed by Burns subroutine
1 (input phase)	Read system input variables; pipe diameter, soil density, number of load steps, soil stiffness and fill heights, interface condition.
2 (solution phase)	Compute incremental trial solution for moments, thrusts and shear around the pipe and form trial total solutions for processing by pipe-type subroutine.
3 (output phase)	No action. (Soil responses are not computed in Burns subroutine, only pipe responses are computed which are processed in the pipe-type subroutine)

10.4.2 Finite element solutions Level 2 and Level 3

Solution levels 2 and 3 share most subroutines in common as illustrated in the following finite element flow charts. For clarity, the flow charts are broken down into the input phase (ICOME = 1), solution phase (ICOME = 2) and the output phase (ICOME = 3)

Input phase (ICOME = 1) When the executive routine calls for the finite element input phase, the sequence of subroutines shown in Figure 10.4.2-1 come into play. Note that the flow path shows a diversion path for Level 2 wherein one of the three canned-mesh subroutines are entered to create an input file identical to Level 3.

Solution phase (ICOME = 2) The sequence of subroutines that come into play for the solution phase is shown in Figure 10.4.2-2. Note there is no distinction between Level 2 and Level 3, the flow path is the same for both.

Output phase (ICOME = 3). When the executive routine determines that the load step has converged, ICOME is set equal to 3 to signal the printout of the solution. The sequence of subroutines for the output phase is shown in Figure 10.4.2-3. Again, there is no distinction between Level 2 and Level 3.

Figure 10.4.2-1 Subroutine flow chart for input phase of finite element solution Level 2 and Level 3.

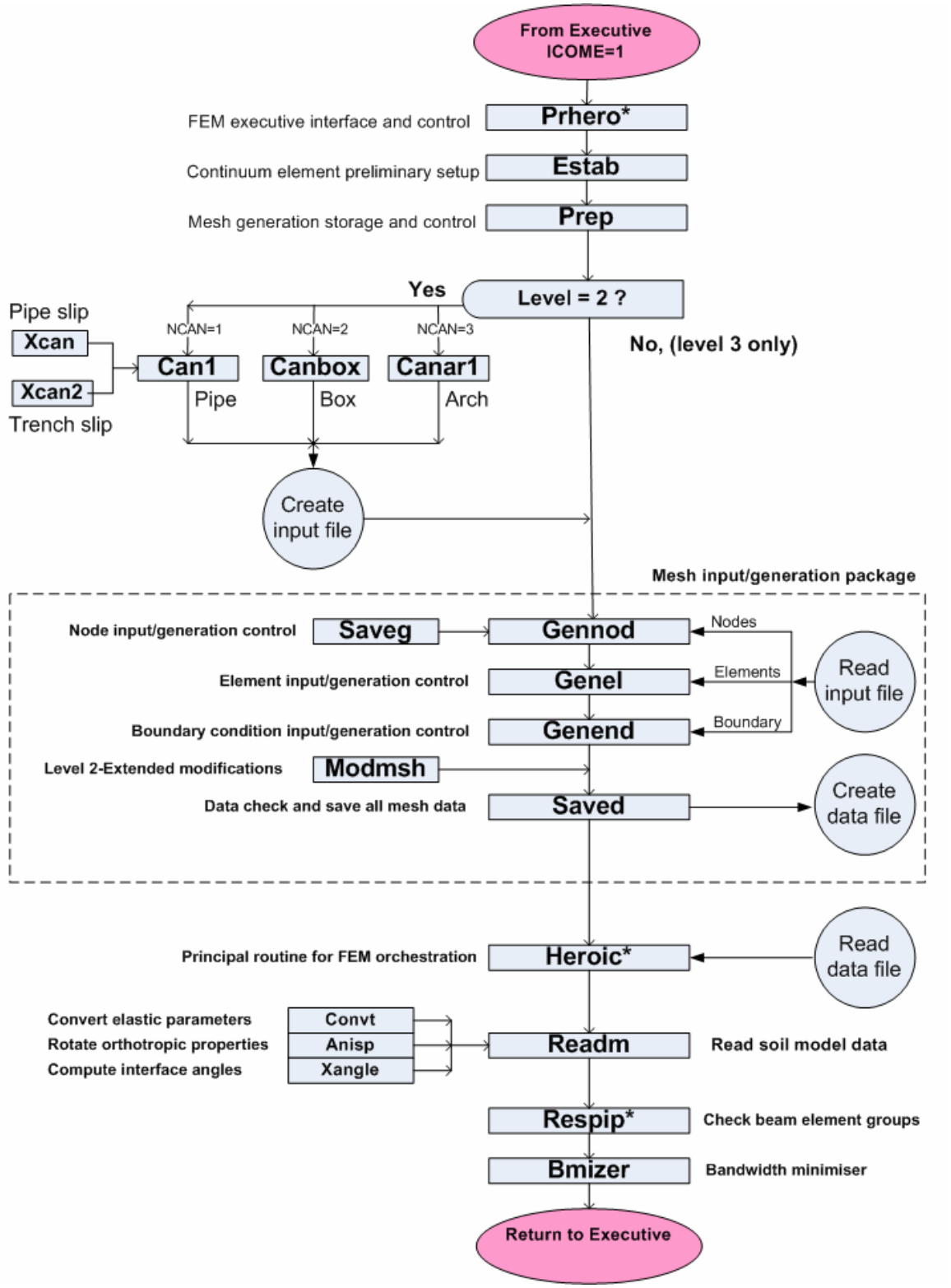

Asterisk (*) means subroutine serves in more than one phase

Figure 10.4.2-2 Subroutine flow chart for solution phase using finite element method

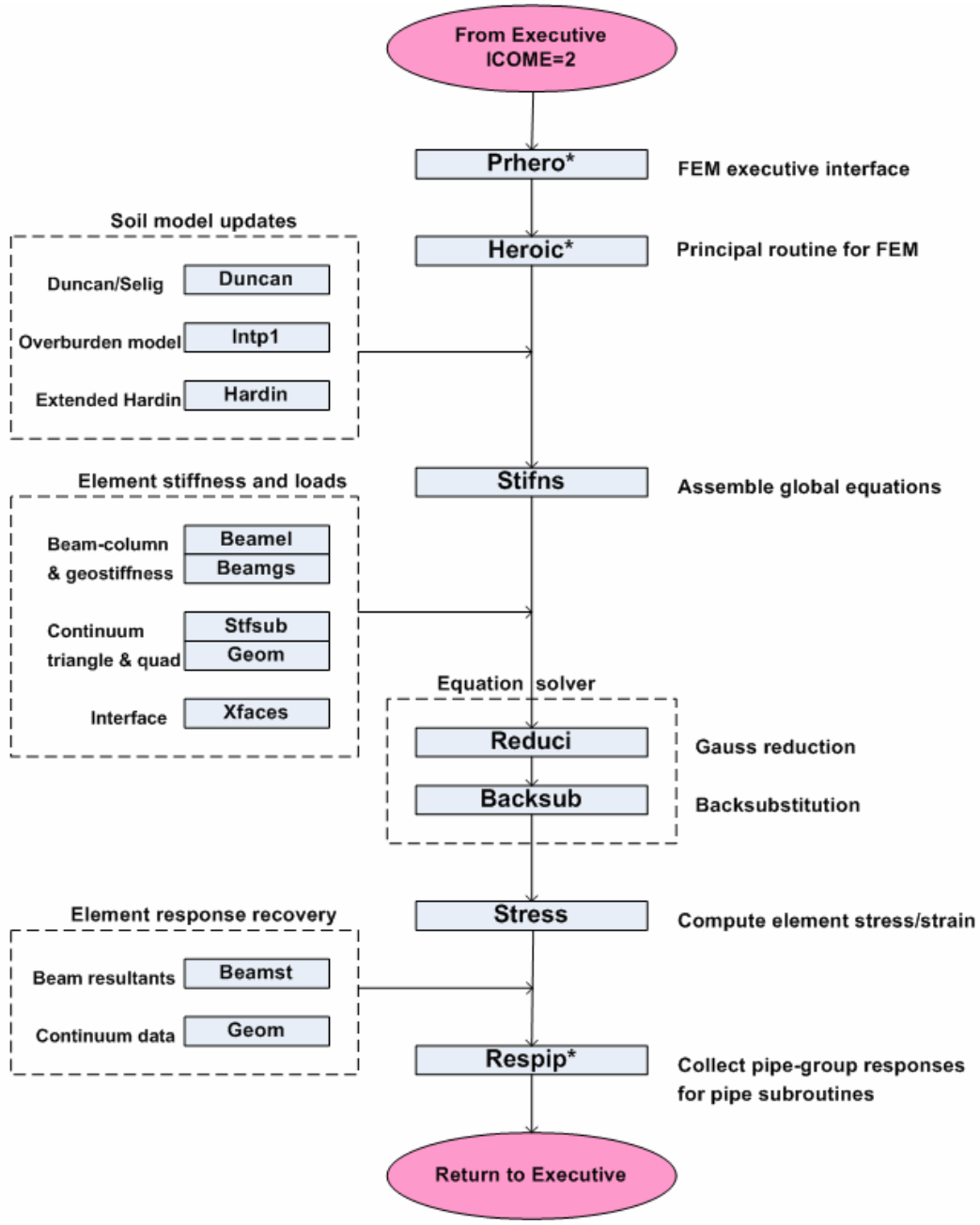

Asterisk (*) means subroutine serves in more than one phase ex

Figure 10.4.2-3 Subroutine flow chart for output phase using finite element method

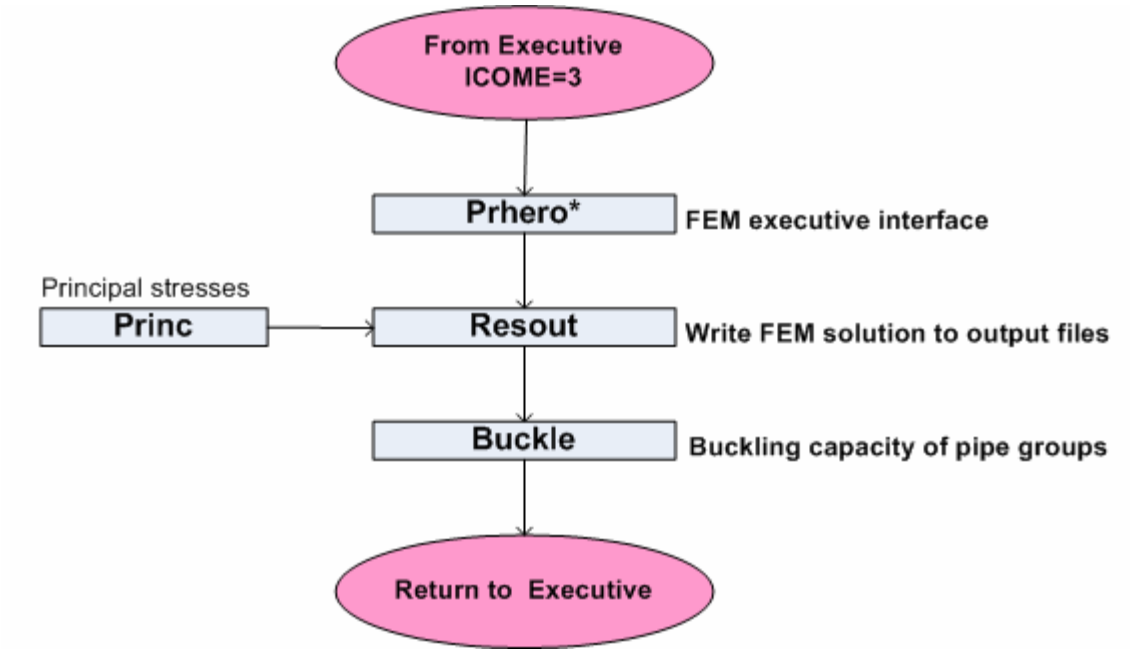

10.5 Extensions to CANDE-2007

As stated at the beginning of this appendix, modifications and extensions to CANDE's capabilities are welcomed and encouraged. Based on CANDE's history, the three areas that are most likely to be extended are: (1)new pipe-type model, (2) new soil model and (3) new canned mesh model. Brief guidance for undertaking each of these endeavors is provided below.

10.5.1 New pipe-type model

The basic programming for installing a new pipe model is already included in CANDE-2007. The executive routine contains the Fortran name NEWPIP in the list of recognized pipe-type names that may be specified in the input data file on line A-2. In addition, the executive routine is programmed with calls to a subroutine called Newpip for the three executive phases; input, solution and output (i.e., ICOME =1, 2, and 3).

The shell of subroutine Newpip along with its arguments is installed in Project Engine, therefore the researcher needs only to provide the programming within the Newpip subroutine. The programming logic should follow the structure outlined in Table 10.3-1, and the existing Basic subroutine, which is the simplest of the pipe types, is useful as a programming guide.

10.5.2 New soil models

To install a new soil model, the subroutines Readm and Heroic located in Project Engine need to be modified. Subroutine Readm is associated with the input phase wherein input parameters for all soil models are read and processed. For the first input line D-1, common to all soil models, the new soil model should be identified as ITYP = 7 because six other models already exist. The remaining input lines, D-2, D-3, etcetera, are defined as needed to read and process the input parameters associated with the new model. It is recommended to store the Fortran variables for the soil model in a new Include statement (named common statement) inserted in subroutines Readm and your new subroutine, say Newmud, called from subroutine Heroic as discussed next.

In the solution phase of subroutine Heroic (ICOME = 2), the appropriate soil-model subroutine is called to compute the updated modulus values for the element's constitutive matrix (see Chapter 3). Comment cards in subroutine Heroic identify exactly where to insert the call to subroutine Newmud (ITYP = 7). Using the element's current stress /strain values as input (ST array), subroutine Newmud's job is to update moduli values and assign values to the incremental plane-strain constitutive matrix CP(3x3) stored in the include statement, materl.fi. See subroutine Duncan as an illustration for programming and for signaling convergence using the simple logic, ICONDS = 1 or 0. Note the array STHARD may be used as desired in subroutine Newmud.

10.5.3 New canned mesh for Level 2

Installing a new canned mesh requires a trivial modification to the executive routine, inserting a call to the new subroutine, say Newcan, in subroutine Prep, and programming the Newcan subroutine. Input line A-2 contains the input variable NPCAN, which is currently input as 1, 2, or 3, corresponding to the Level 2 choice of pipe mesh, box mesh, or arch mesh. To expand NPCAN to 4 choices requires modifying line 443 in the executive routine to avoid the error check.

As indicated in Figure 10.4.2-1, subroutine Prep directs the calling to the canned mesh subroutine based on the value of NPCAN. Accordingly, a new call statement to subroutine Newcan needs to inserted in subroutine Prep immediately following line 62

Programming subroutine Newcan may seem daunting, particularly after inspecting other canned mesh subroutines. However, the fundamental goal is simple. Using physical input data describing the configuration shape being addressed, Newcan generates the entire finite element input stream and writes it to a data file (unit 11) in the same sequence and format as Level 3 input instructions. This means line C-1 (PREP), line C-2 (control), multiple lines C-3 (nodes), multiple lines C-4 (elements) and multiple lines C-5 (boundary conditions) are all written to unit 11. The mesh/generation package (Figure 10.4.2-1) reads the data file on unit 11 just the same as if it were a batch input file on unit 5.

11 CANDE GUI Source Code

The CANDE Graphical User Interface (GUI) source code is the topic of this chapter. While the source code itself is the ultimate documentation of the program, this chapter provides a simple guideline for using the code.

11.1 Overview of CANDE GUI Architecture

The CANDE-2007 source program is written in modern Fortran and developed with the following:

- Microsoft Visual Studio 2005, Version 8.0.50727.762 (SP.050727-7600)
- GUI written in .NET C# programming language
- Microsoft .NET Framework version 2.0.50727

The MVS framework permits grouping subroutines together to form projects and then grouping projects together to form a whole solution. CANDE's whole solution is composed of six projects described in the table below.

Table 11.1-1 CANDE-2007 projects contained in MVS solution

Project	Description	Files required to initiate the project
cande1	This is the primary project and can be opened by opening the cande1.sln project file. The primary functions of this project are as follow: ▪ Main CANDE GUI project that initiates the CANDE Multiple document interface (MDI) ▪ All other projects are instantiated from the main module Form1 ▪ Project also contains the input interface and all of the input screen forms ▪ Contains the help about screens and auxiliary forms	
CANDEBeamResults	Contains the form that plots the beam results using a linear graphing tool. This project uses a third party graphing tool, Graphics server. This tool is distributable royalty free, but a license must be purchased in order to develop with it.	aaa_MeshGeom.xml aaa_BeamResults.xml
CANDEGraphics	This project drives all of the mesh plotting for CANDE. The viewer permits viewing of the mesh geometry without the results file.	aaa_MeshGeom.xml(required) (aaa_MeshResults.xml) Last file is optional but must be present to view analysis results.

Project	**Description**	**Files required to initiate the project**
CANDEImport	This project provides support for importing external files into CANDE. The files currently supported are: ▪ MeshGeom.XML – the format for this file is defined in the CANDE user manual. ▪ NASTRAN – The NASTRAN commands supported by the CANDE import are described in an appendix to the CANDE user manual. ▪ CANDE-89 – The CANDE-89 plot file import is supported.	Requires an external import file of the type defined.
CANDEInputViewer	This project defines the form needed for the CANDE text input viewer. A Feature of this tool is the column-sensitive help.	Requires a CANDE input file with an extension .CID.
CANDENewInput	This project controls the CANDE input wizard screens. This form is generally made to be run in modal mode.	Generates a new CANDE input file.
CANDEOutputGenerator	The output generator project initiates the windows to dynamically generate CANDE output based on the data stored in the CANDE. The program provides the user with choices to customize the data stored in the three CANDE xml output files. The format of these files is described in the CANDE user manual.	aaa_MeshGeom.xml aaa_MeshResults.xml aaa_BeamResults.xml All three CANDE xml output files are required to run this module.
CANDEOutputViewer	This project uses the CANDE table of contents file (ctc) and CANDE output file to create an interactive browser for CANDE output files. If the CANDE table of contents file is not present, the form will still work without a browser input tree. This form performs double duty as the viewer for the standard CANDE output file and the file produced by the CANDE output generator.	CANDE output file CANDE table of contents file (ctc extension).
Utiltiy Classes		
CANDEOutputClass	Classes used to build output files for the CANDE output generator.	
AbanGeometry, absngnrl	General geometry classes	
CANDE_InputData_ClassLibrary	Group of classes that reads/write the CANDE input file using the format described explicitly in the CANDE user Manual (Chapter 5). The classes are named according to the input names defined in the user manual.	
CANDE_XML_ClassLibrary	Library of classes for reading the various XML files used by CANDE.	
RTBExCs	Expanded rich text box control that supports printing.	
CANDE Setup	Project that builds the CANDE installation.	

11.2 CANDE Files

The CANDE-2007 GUI relies on a series of files to function properly; some are generated by the analysis engine, some are soft-coded and some are produced by the GUI. This section provides a guideline for these files.

11.2.1 CANDE Input Definition

The CANDE input definition XML file provides information used by the GUI to check ranges, determine context-sensitive help tags, short help descriptions, long help descriptions, and input formatting. The file is used primarily by the GUI input system and is read in when the input system is initiated. Each input item defined in Chapter 5 of the CANDE user manual has a <Data> entry in the CANDE input definition file. A sample of the XML file is shown below.

```
<?xml version="1.0" encoding="UTF-8"?>
<CANDEInputDefinition>
	.
	.
	.
	<Data>
		<className>CLRFDLoadFactors_E1</className>
		<ShortInputName>E-1</ShortInputName>
		<CANDEVariableName>FACTOR</CANDEVariableName>
		<CANDEInputLine>E-1</CANDEInputLine>
		<shortDescription>LRFD load factor applied to the load increments INCRS
through INCRL.</shortDescription>
		<longDescription>FACTOR is the net load factor applied to the load steps
INCRS to INCRL (inclusive). It is the user's responsibility to determine the appropriate
value of FACTOR that correlates to each load step. Table E-1 provides information on
load factors based on the</longDescription>
		<inputColumnStart>11</inputColumnStart>
		<inputLength>10</inputLength>
		<inputFormat>F10.0</inputFormat>
		<ouputFormat>F10.0</ouputFormat>
		<unitsUS>.none.</unitsUS>
		<unitsSI>.none.</unitsSI>
		<defaultUS>1</defaultUS>
		<defaultSI>1</defaultSI>
		<lowerlimitUS_W>0</lowerlimitUS_W>
		<upperLimitUS_W>10</upperLimitUS_W>
		<lowerlimitSI_W>.none.</lowerlimitSI_W>
		<upperLimitSI_W>.none.</upperLimitSI_W>
		<lowerlimitUS_E>.none.</lowerlimitUS_E>
		<upperLimitUS_E>.none.</upperLimitUS_E>
		<lowerlimitSI_E>.none.</lowerlimitSI_E>
		<upperLimitSI_E>.none.</upperLimitSI_E>
		<HelpTag>5_7_1_E_1_LRFD_Net_Load_Factor_per_Load_step</HelpTag>
	</Data>
	.
	.
	.
	<Data>
		<className>CPTypeDef_AlumB2_A</className>
		<ShortInputName>B-2.Alum.A</ShortInputName>
		<CANDEVariableName>PA</CANDEVariableName>
		<CANDEInputLine>B-2</CANDEInputLine>
		<shortDescription>Area of pipe wall section per unit
length</shortDescription>
		<longDescription>The cross-sectional area of one corrugation period divided
by the period length.</longDescription>
		<inputColumnStart>1</inputColumnStart>
```

```
            <inputLength>10</inputLength>
            <inputFormat>F10.0</inputFormat>
            <ouputFormat>F10.0</ouputFormat>
            <unitsUS>in^2/in</unitsUS>
            <unitsSI>mm^2/mm</unitsSI>
            <defaultUS>.none.</defaultUS>
            <defaultSI>.none.</defaultSI>
            <lowerlimitUS_W>.001</lowerlimitUS_W>
            <upperLimitUS_W>10</upperLimitUS_W>
            <lowerlimitSI_W>.none.</lowerlimitSI_W>
            <upperLimitSI_W>.none.</upperLimitSI_W>
            <lowerlimitUS_E>.none.</lowerlimitUS_E>
            <upperLimitUS_E>.none.</upperLimitUS_E>
            <lowerlimitSI_E>.none.</lowerlimitSI_E>
            <upperLimitSI_E>.none.</upperLimitSI_E>
            <HelpTag>5_4_1_2_B_2_Aluminum_Analysis_Section_Properties</HelpTag>
        </Data>
        .
        .
        .
<CANDEInputDefinition>
```

CANDE Input Definition Tag Descriptions.

Tag	Type	Description
className	string	Class name as defined in CANDE.
shortInputName	string	Short input name description. This name is generally the command name followed by the variable description.
CANDEVariableName	string	The CANDE variable name as defined in the CANDE user manual.
CANDEInputLine	string	CANDE input line command (e.g. E-1) as defined in Chapter 5 of the CANDE user manual.
shortDescription	string	Short description of the input item.
longDescription	string	More detailed description of the input item.
inputColumnStart	integer	The column that the input item starts in the input file.
inputLength	integer	The total length of an input item as it is written to the input file.
inputFormat	string	Input format defined in Chapter 5 of the user manual for each input item. The format in general follows FORTRAN guidelines for formatting. Currently used for the persistent help shown at the bottom of the input screen.
outputFormat	(not currently used)	
unitsUS	string	This value is used in labeling the US ‘units’ field on all CANDE input menus
unitsSI	string (set by not currently used)	This value is used in labeling the SI ‘units’ field on all CANDE input menus
defaultUS	string	The value set for a CANDE input file when initially generated.
defaultSI	(not currently used)	
lowerlimitUS_W	integer, double	lower limit for CANDE input for this particular input item. CANDE allows input with range violations but provides a warning message.
upperlimitUS_W	integer, double	upper limit for CANDE input for this particular input item. CANDE allows input with range violations but provides a warning message.
lowerlimitSI_W	(not currently used)	
upperlimitSI_W	(not currently used)	
lowerlimitUS_E	(not currently used)	
upperlimitUS_E	(not currently used)	

Tag	Type	Description
lowerlimitSI_E	(not currently used)	
upperlimitSI_E	(not currently used)	
HelpTag	string	This tag is used by the GUI to set the help tag associated with the CANDE-2007.chm help file. When CANDE opens and input menu it uses this tag to search for context sensitive help.

11.2.2 CANDE analysis XML output files

The CANDE XML output files are described in detail in the CANDE User Manual and Guideline. Which modules use the files is described in a table in section 11.1 of this manual.

11.2.3 CANDE table of contents files

The CANDE analysis engine and the CANDE output generate produce a table of contents file that is used in tandem with the corresponding CANDE output files to create a 'browsable' output file. The format of the CANDE table of contents file is simple and could be applied to other programs that produce ASCII text based output. The format is as follows:

Format:

```
IIII|aaaa…
IIII|aaaa…
IIII|aaaa…
```

Where

IIII – the heading level to be used in the tree explorer
Aaaa… - represents the key text to be searched for when the tree item is clicked.

Perhaps the best way to demonstrate the use of this file is by example. The following is a snippet from a CANDE ctc file and demonstrates how it gets translated to a tree browser.

```
1|MASTER CONTROL AND PIPE-TYPE DATA FOR PROBLEM #  1
1|REVIEW SYSTEM INPUT DATA
2|LEVEL-2 DATA FOR PIPE-SHAPED CANNED MESH
2|FINITE ELEMENT INPUT CONTROLS (PREP)
2|NODAL INPUT DATA TO GENERATE COORDINATES
2|NODE COORDINATES AS GENERATED FROM INPUT DATA
2|ALL ELEMENT DATA AS INPUT "I" AND GENERATED
2|FINAL LIST OF ALL NODE COORDINATES
2|BOUNDARY CONDITIONS AS GENERATED FROM INPUT
2|EXTENDED LEVEL-2: CHANGES TO CANNED MESH
2|BEAM-NODE SEQUENCE NUMBERS FOR EACH GROUP
2|MATERIAL DESCRIPTION FOR SOILS AND INTERFACE
1|SOLUTION OUTPUT RESULTS
2|FINITE ELEMENT OUTPUT FOR LOAD STEP  1
3|ALL NODAL DISPLACEMENTS FOR LOAD-STEP   1
3|ALL BEAM ELEMENT OUTPUT FOR LOAD-STEP   1
3|INTERFACE ELEMENT OUTPUT FOR LOAD-STEP   1
3|CONTINUUM ELEMENT OUTPUT FOR LOAD-STEP   1
3|PLASTIC,  SERVICE-EVALUATION FOR GROUP  1, LOAD-STEP  1
4|STRUCTURAL RESPONSES OF PLASTIC-GROUP  1, LOAD STEP  1
4|STRAIN DIAGONOSTICS OF PLASTIC-GROUP  1, LOAD-STEP  1
4|LOCAL BUCKLING DIAGONOSTICS OF PLASTIC-GROUP  1, LOAD-STEP  1
4|ASSESSMENT SUMMARY PLASTIC-GROUP  1, LOAD-STEP  1
```

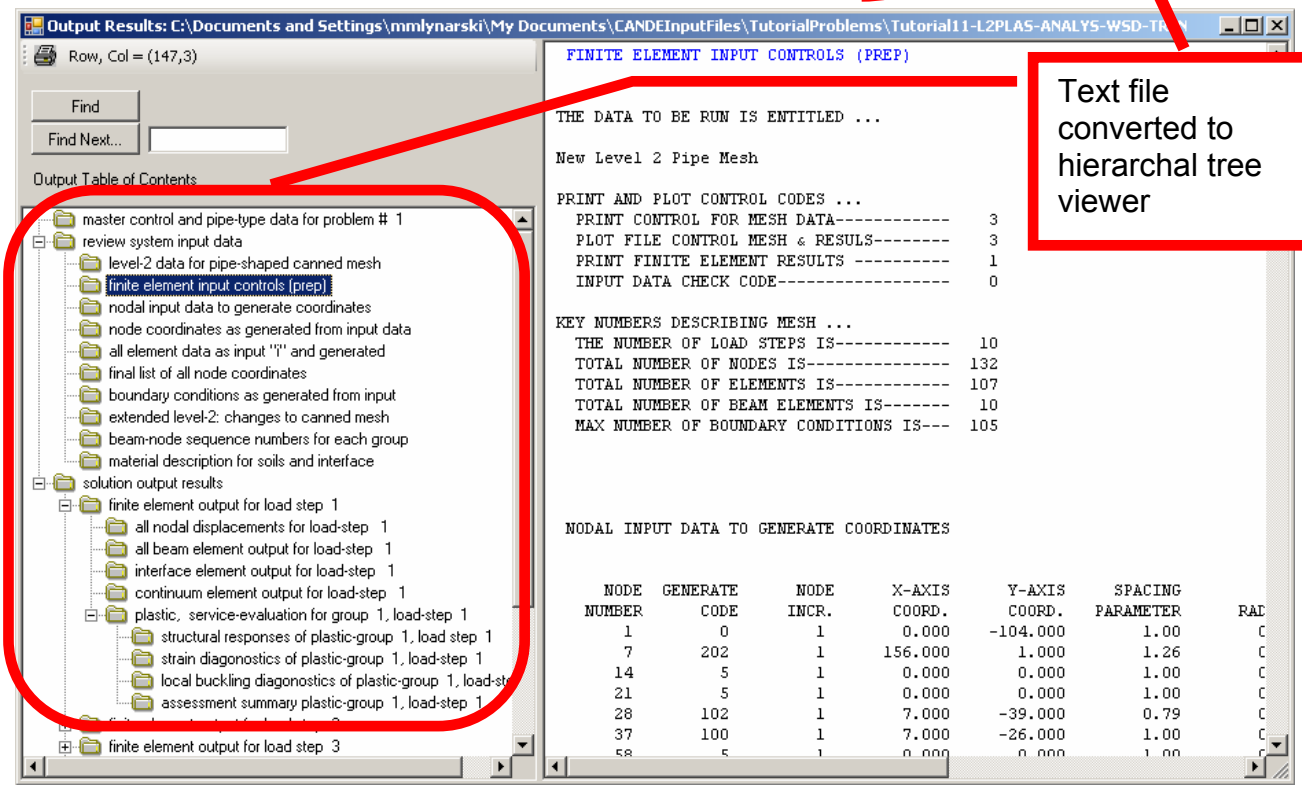

11.2.4 CANDE help files

CANDE comes with a predefined CANDE help file CANDE-2007.chm. This file was generated using Adobe RoboHelp HTML 6, Build 99. The file was produced by taking the CANDE User Manual and Guideline Microsoft Word document and importing the document into Robohelp for HTML 6. Once the document is imported a small amount of cleanup is required to finalize the document.

To create the CANDE -2007 help file following the following steps:

- Start up RoboHelp HTML
- Create a new project through 'File -> New Project'
- Select the 'Import' tab
- Select 'Word Document' as the import type
- Browse to the CANDEUserManualAndGuideline.doc file
- Import the document
- Follow the import wizard using the following settings

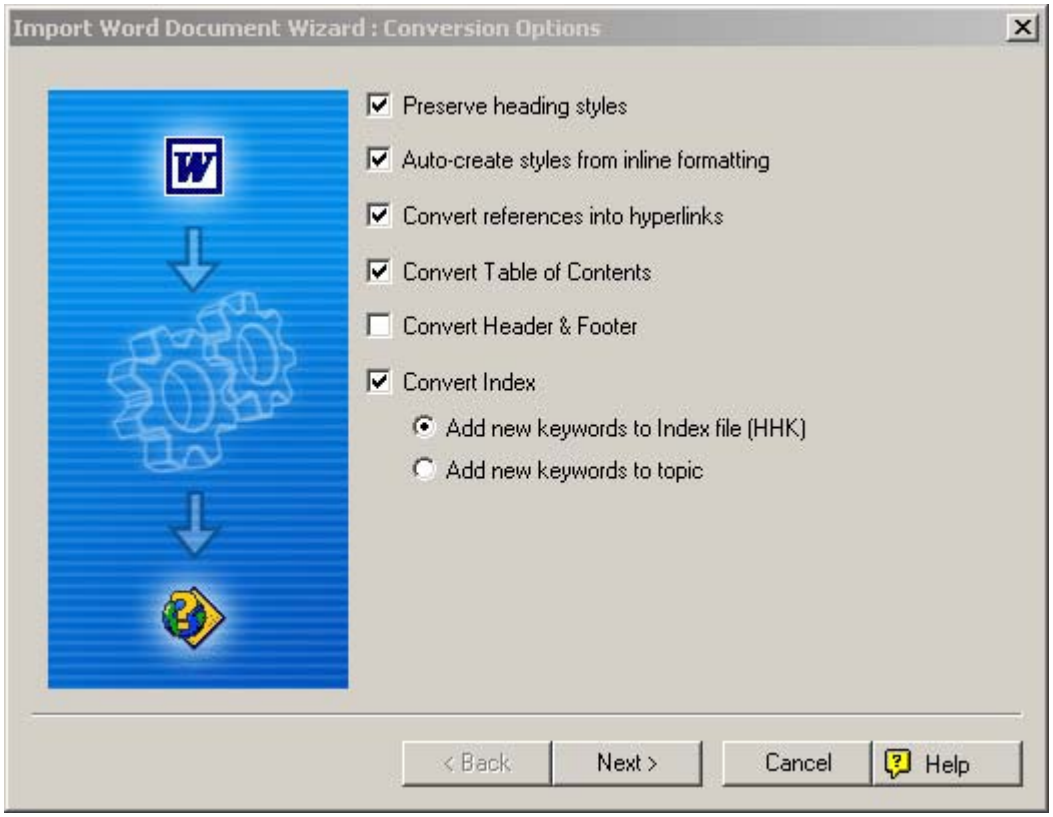

Once the project has been generated, select ‘New Window…’ by right-clicking on the ‘Windows’ icon in the RoboHelp HTML explorer (see below).

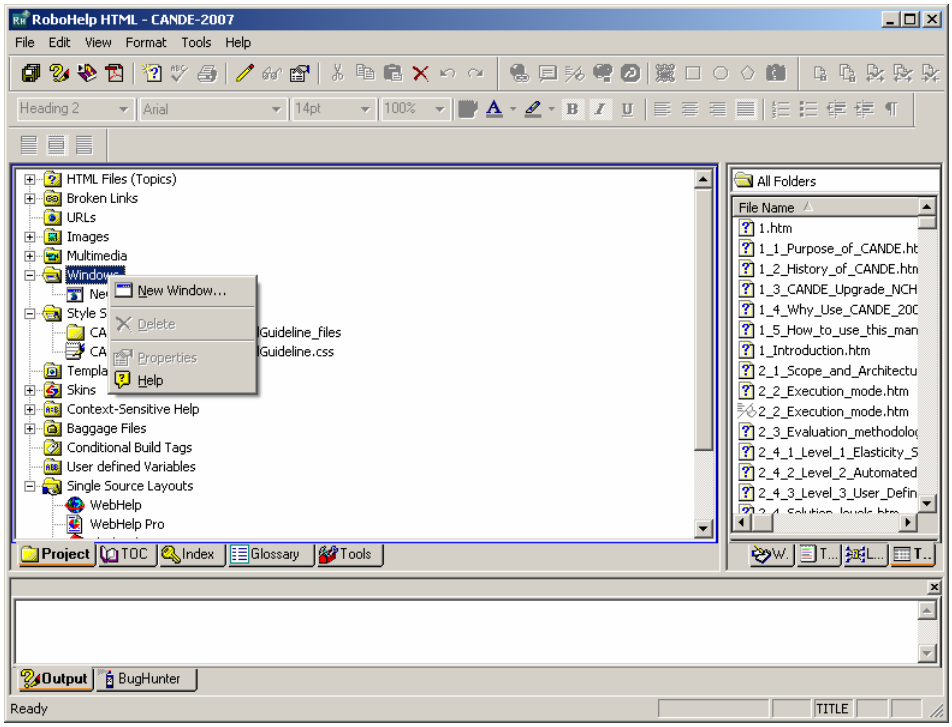

This will create a new instance of the RoboHelp project that can then be opened. Once opened select the option to ‘Remember Window Size and Position’ (see below).

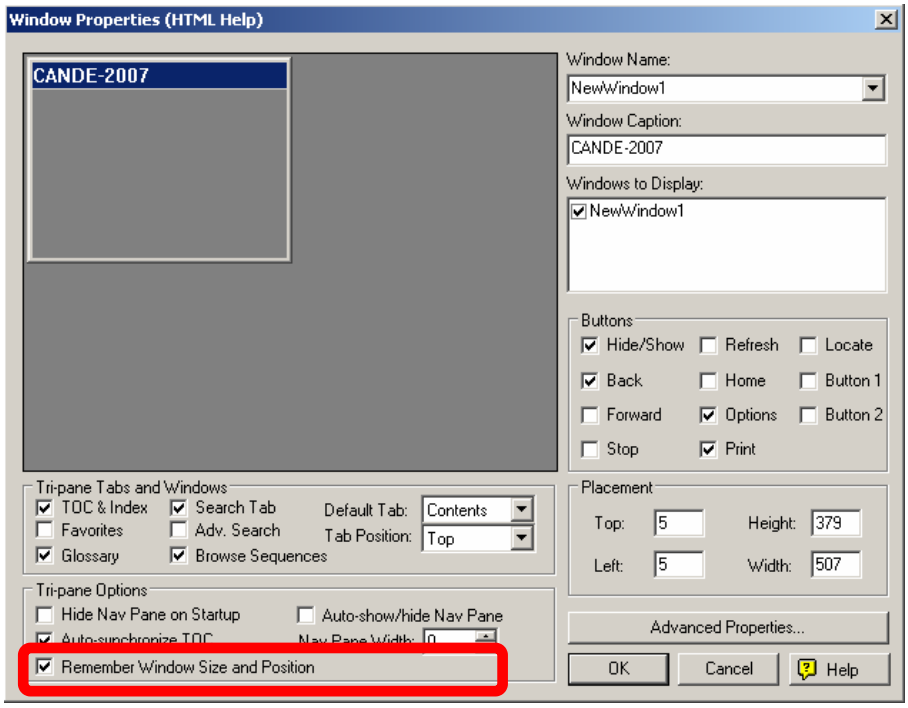

Close the window and select the ‘Generate’ option from the ‘File’ menu.